

Functional Block Copolymers As Platforms for Patterned Immobilization

Zur Erlangung des akademischen Grades eines

DOKTORS DER NATURWISSENSCHAFTEN

(Dr. rer. nat.)

der KIT-Fakultät für Chemie und Biowissenschaften

des Karlsruher Instituts für Technologie (KIT)

genehmigte

DISSERTATION

von

Hatice Turgut

aus

Istanbul, Türkei

KIT-Dekan: Prof. Dr. Willem M. Klopper

Referent: Prof. Dr. Christopher Barner-Kowollik

Korreferent: Prof. Dr. Manfred Wilhelm

Tag der mündlichen Prüfung: 14.12.2016

Die vorliegende Arbeit wurde von Juli 2013 bis Dezember 2016 unter Anleitung von Dr. Guillaume Delaittre und Prof. Dr. Christopher Barner-Kowollik am Karlsruher Institut für Technologie (KIT) – Universitätsbereich angefertigt.

Hiermit bestätige ich wahrheitsgemäß, dass ich die vorliegende Arbeit im Rahmen der Betreuung durch Dr. Guillaume Delaittre und Prof. Dr. Christopher Barner-Kowollik selbstständig verfasst und keine anderen Quellen und Hilfsmittel als die angegebenen verwendet habe. Wörtlich oder inhaltlich übernommene Stellen sind als solche kenntlich gemacht und die Satzung des Karlsruher Instituts für Technologie (KIT) zur Sicherung guter wissenschaftlicher Praxis wurde beachtet. Des Weiteren erkläre ich, dass ich mich derzeit in keinem weiteren laufenden Promotionsverfahren befinde und keine vorausgegangenen Promotionsversuche unternommen habe.

Karlsruhe, den 21.12.2016

Hatice Turgut

That which does not kill us, makes us stronger.

Nietzsche

Dedicated to my Mother and Melis

Abstract

Block copolymers (BCPs) are renowned for their microphase separation in bulk, in solution and in the form of thin films. Their ability to create various nanostructures upon phase segregation makes them beneficial materials for many applications ranging from electronics to drug delivery. The present dissertation takes an original approach at the utilization of thin films of functional/reactive block copolymers as new candidates for chemical nanopatterning. The work primarily provides insights into the preservation of phase separation behavior of well-known BCP systems upon introduction of small amounts of functional moieties, which are to be exploited as surface-displayed anchors for further immobilization. Tethering more than one type of (bio)molecules on distinct domains of BCP films could offer a high spatial resolution control, which would be highly challenging to obtain by other patterning methods.

The two first experimental Chapters of this Thesis deal with two distinct libraries of functional BCPs which were synthesized via reversible deactivation radical polymerization (RDRP) techniques. In the first one, four polystyrene-*block*-polyisoprene (PS-*b*-PI) derivatives were synthesized by nitroxide mediated polymerization (NMP), with each of them possessing approx. 5 mol% of a functional styrene derivative in the PS block. In the second part, eight functional poly(methyl methacrylate)-*block*-polystyrene BCPs were synthesized either by ATRP or RAFT polymerization, with post-polymerization modification in some cases. All block copolymers were molecularly characterized by NMR spectroscopy and size exclusion chromatography. Differential scanning calorimetry for the PS-*b*-PI library, as well as small-angle X-ray scattering for both systems were employed to evidence the ability of the BCPs to phase separate in the bulk. Subsequently, thin films were prepared by spin-coating solutions of these BCPs and analyzed by atomic force microscopy, which revealed in most cases perpendicular lamellar structures. As a first exemplary functionalization of the nanostructures, copper-catalyzed azide-alkyne coupling was performed on a PS-*b*-PI film possessing the azide functionality and assessed by X-ray photoelectron spectroscopy. Stabilization of the films was preliminarily achieved by crosslinking so as to make them suitable platforms not only for water-borne systems but also for organic media as well.

In the two further experimental Chapters of the Thesis, detailed studies on one of the ligation methods envisioned for the functionalization of the films were performed, i.e., the *para*-fluoro thiol substitution reaction (PFTR). We demonstrated the full orthogonality of PFTR with a phototriggered radical thiol-ene addition, which could therefore be used in combination for the dual functionalization of BCP films. Furthermore, we implemented the PFTR for the first time in water, which suggests its utility for functionalization of organic solvent-sensitive materials.

Zusammenfassung

Blockcopolymerer (BCPs) sind für ihre Mikrophasentrennung in Bulk, in Lösung und in Dünnschichten bekannt. Ihre Fähigkeit, verschiedene Nanostrukturen bei der Phasensegregation zu erzeugen, macht sie für viele Anwendungen zu interessanten Materialien, von der Elektronik bis hin zur Wirkstoffabgabe. Die vorliegende Dissertation verfolgt einen neuartigen Ansatz zur Verwendung von Dünnschichten aus funktionalen / reaktiven Blockcopolymeren als neue Kandidaten für die chemische Nanostrukturbildung. Die vorliegende Arbeit liefert in erster Linie Einblicke in die Erhaltung des Phasentrennverhaltens bekannter BCP-Systeme nach Einführung von geringen Mengen an funktionellen Einheiten die wiederum als oberflächenaktive Ankerpunkte zur weiteren Immobilisierung genutzt werden sollen. Die Anbindung von mehr als einer Spezies von (Bio-) Molekülen auf verschiedenen Domänen von BCP-Filmen könnte hiermit eine hohe Kontrolle der Ortsauflösung bieten, was durch andere Strukturierungsverfahren schwer zu erzielen wäre.

Die beiden ersten experimentellen Kapitel dieser Arbeit befassen sich mit zwei verschiedenen Bibliotheken funktioneller BCPs, die mittels reversibler Deaktivierungs-Radikalpolymerisationstechniken (RDRP) synthetisiert wurden. Im ersten Ansatz wurden vier Polystyrol-Block-Polyisopren (PS-*b*-PI) Derivate durch NMP synthetisiert mit jeweils 5 Mol-% eines funktionellen Styrolderivats im PS-Block. Im zweiten Teil wurden acht funktionelle Poly(methylmethacrylat)-Block-Polystyrol BCPs entweder durch ATRP oder RAFT Polymerisation synthetisiert, wobei in manchen Fällen die Polymerisation nach der Polymerisation modifiziert wurde. Alle Blockcopolymerer wurden durch NMR-Spektroskopie und Größenausschlusschromatographie auf molekularer Ebene charakterisiert. Für die PS-*b*-PI Bibliothek wurde Differential Scanning Kalorimetrie sowie Kleinwinkel-Röntgenstreuung für beide Systeme verwendet, um die Fähigkeit der BCPs zur Phasentrennung im Bulk nachzuweisen. Anschließend wurden Dünnschichten durch Spin-Coating aus Lösung dieser BCPs hergestellt und durch Rasterkraftmikroskopie analysiert, die in den meisten Fällen senkrechte lamellare Strukturen aufwies. Als erste beispielhafte Funktionalisierung der Nanostrukturen wurde die kupferkatalysierte Azid-Alkin-Kupplung auf einem azid-funktionalem PS-*b*-PI-Film durchgeführt und durch Röntgen-Photoelektronenspektroskopie nachgewiesen. Die Stabilisierung der Filme wurde zunächst durch Vernetzung erreicht, um sie als geeignete Plattform sowohl für wässrige Systeme als auch für organische Medien nutzen zu können.

In zwei weiteren experimentellen Kapiteln der Dissertation wurden eingehende Untersuchungen zur Funktionalisierung der Filme mittels der para-Fluor-Thiol-Substitutionsreaktion (PFTR) durchgeführt. Wir haben die Orthogonalität von PFTR zu einer photogetriggerten radikalischen Thiol-En-Addition gezeigt, die somit in dieser Kombination zur Doppelfunktionalisierung von BCP-Filmen verwendet werden kann. Darüber hinaus haben wir das PFTR erstmals in Wasser implementiert, was durchaus vorteilhaft für die Funktionalisierung von organischen lösemittlempfindlichen Materialien ist.

Contents

1. Introduction and Motivation	1
2. Theoretical Background and Literature Overview	4
2.1 Radical Polymerization	4
2.1.1 Free Radical Polymerization	4
2.1.2 Reversible Deactivation Radical Polymerization	6
2.1.2.1 Nitroxide Mediated Polymerization.....	7
2.1.2.2 Atom Transfer Radical Polymerization	8
2.1.2.3 Reversible Addition-Fragmentation Chain-Transfer Polymerization	11
2.2 Click Reactions/ Modular Ligations	14
2.2.1 Copper Catalyzed Azide-Alkyne Cycloaddition	15
2.2.2 Reactions of Thiols	16
2.2.2.1 Radical Thiol-Ene Addition.....	17
2.2.2.2 <i>Para</i> -Fluoro Thiol Substitution Reaction (PFTR).....	19
2.3 Block Copolymers (BCPs).....	21
2.3.1 Phase Separation and Self-Assembly of BCPs.....	21
2.3.2 BCP Thin Films.....	26
2.3.2.1 Microdomain Orientation in BCP Thin Films.....	27
2.3.2.2 Methods to Induce Perpendicular Orientation and Alignment.....	29
2.3.2.3 Techniques to Analyze BCP Thin Films.....	35
2.3.3 Applications of Block Copolymers.....	43
2.3.3.1 In Solid State.....	43
2.3.3.2 In Solution	44
2.3.3.2 BCP Thin Films as Chemical Patterning Platforms.....	45
3. Polystyrene-<i>block</i>-Polyisoprene Films as Self-Assembled Reactive Platforms	47
3.1 Introduction	48
3.2 The Idea of BCP Films as Patterning Platforms.....	48
3.3 Synthesis of Functional PS- <i>b</i> -PI Derivatives by NMP	49

3.4 Bulk Properties of PS- <i>b</i> -PI BCPs	53
3.4.1 Differential Scanning Calorimetry (DSC) Results	53
3.4.2 Small Angle X-Ray Scattering (SAXS) Results	55
3.5 Formation of Nanostructured Thin Films.....	56
3.6 Proof of Surface Reactivity: Azide-Alkyne Coupling	58
3.7 Stabilization by Photocrosslinking.....	60
3.8 Conclusion and Outlook	61
4. A Library of Functional, Nanostructured Thin Films of PMMA-<i>b</i>-PS	63
4.1 Introduction	64
4.2 General Note on the Employed Polymers	66
4.2.1 Reference Block Copolymer (RBCP): Synthesis; ATRP vs. RAFT	66
4.2.2 Characteristics of the Polymers	66
4.3 The Coating Strategy	70
4.4 Detailed Investigations of the Thin Films	71
4.4.1 AFM and SAXS Results	71
4.4.2 Microwave Annealing	75
4.4.3 Stability Tests in Water	76
4.4.4 Thermal and Photo Crosslinking to Stabilize BCP Films	77
4.4.5 Additional Polymers.....	78
4.5 Summary	79
5. Orthogonality of Two Modular Ligations: Thiol-Ene and PFTR.....	81
5.1 Introduction	82
5.2 The Orthogonality Principle.....	82
5.3 The Doubly Reactive Platform.....	83
5.4 Orthogonality Investigations	84
5.4.1 Thiol-Ene and PFTR Occurring Separately	84
5.4.2 Dual Functionalizations with Intermediate Purification	88
5.4.2.1 Direct Functionalization of BCPs Obtained in Single-Reaction Studies.....	88

5.4.2.2 Control Experiment with Ethanol	89
5.4.2.3 Changing the Thiol and Reaction Sequences	90
5.4.3 One-Pot Dual Functionalizations.....	91
5.4.3.1 One-Pot <i>Type 1</i>	91
5.4.3.2 One-Pot <i>Type 2</i>	93
5.4.3.3 One-Pot <i>Type 3</i>	96
5.5 Conclusion and Outlook	97
6. The <i>para</i>-Fluoro Thiol Substitution Reaction (PFTR) in Water	98
6.1 Introduction	99
6.2 Bringing the PFP Moiety into Water	99
6.3 Establishing a Rational Route to PFTR in Water	100
6.4 Investigations on the Effect of Different Variants on PFTR.....	101
6.5 Application of PFTR in Water on the Surface.....	107
6.6 Conclusion	110
7. Conclusion and Outlook.....	111
7.1 Summary and Concluding Remarks.....	111
7.2 Outlook.....	114
8. Materials and Characterization.....	115
8.1 Materials.....	115
8.2 Analytical Instrumentation.....	117
8.2.1 Nuclear Magnetic Resonance (NMR) Spectroscopy	117
8.2.3 Atomic Force Microscopy (AFM).....	117
8.2.4 Small Angle X-Ray Scattering (SAXS)	118
8.2.5 X-Ray Photoelectron Spectroscopy (XPS)	118
8.2.6 Ellipsometry.....	119
8.2.7 Differential Scanning Calorimetry (DSC).....	119
8.2.8 Time of Flight Secondary Ion Mass Spectrometry (ToF-SIMS)	119
8.2.9 pH Measurements.....	120
8.2.10 Water Contact Angle Measurements.....	120

9. Experimental Procedures	121
9.1 Reactive Nanostructured PS- <i>b</i> -PI Films	121
9.1.1 Syntheses	121
9.1.2 Thin Film Formation and AFM Parameters	129
9.1.3 Copper Catalyzed Azide-Alkyne Cycloaddition on the Surface	130
9.2 Functional PMMA- <i>b</i> -PS Library	131
9.2.1 Syntheses of PMMA- <i>b</i> -PS and Functional Derivatives	131
9.2.2 Synthesis of StCP by ATRP	139
9.2.3 Thin Film Formation and AFM Parameters	140
9.2.4 Film Stabilization via Thermal and Photo Crosslinking	141
9.3 Two Orthogonal Thiol Modulations: Thiol-Ene and PFTR	142
9.3.1 General Procedure for the Synthesis of P(MMA- <i>co</i> -AMA)	142
9.3.2 General Procedure for the Synthesis of P(MMA- <i>co</i> -AMA)- <i>b</i> -(S- <i>co</i> -PFS)	143
9.3.3 PFTR and Thiol-Ene Occurring Separately on P(MMA- <i>co</i> -AMA)- <i>b</i> -P(S- <i>co</i> -PFS) ...	146
9.3.4 Dual Functionalization with Intermediate Purification	147
9.3.5 One-Pot Functionalizations	149
9.3.5.1 One-Pot <i>Type 1</i>	149
9.3.5.2 One-Pot <i>Type 2</i>	150
9.3.5.3 One-Pot <i>Type 3</i>	151
9.4 PFTR in Water	153
9.4.1 Synthesis of Poly(DMAAm- <i>co</i> -PFS)	153
9.4.2 PFTR Experiments in Solution	153
9.4.3 PFTR Experiments on Surfaces	157
Bibliography	159
Abbreviations	176
List of Figures, Schemes, and Tables	179
Figures	179
Schemes	186

Tables	188
Curriculum Vitae	189
Scientific Production.....	191
Acknowledgements	193

1

Introduction and Motivation

Over the past decades, block copolymers (BCPs) have gained significant interest in a range of fields such as electronics, plastics, nanolithography, nanotemplating and many more.^[1-3] Miniaturization and/or high-resolution patterns are of special interest in the majority of these fields. BCPs constitute a unique avenue for this particular purpose as they offer readily tunable properties by simple macromolecular design, i.e., by changing the nature of the components, their distribution, and the overall molar mass, in addition to being cost-effective materials.^[4] BCPs are composed of two or more chemically distinct chains which are linked to each other through a single junction. Depending on the thermodynamic incompatibilities of the distinct blocks, BCPs phase separate to yield delicate nanostructures with feature sizes possibly as small as 5 to 50 nm.^[3]

So far, chemical patterning in sub-50 nm range has been achieved by a few methods such as dip-pen nanolithography (DPN)^[5] and e-beam lithography.^[6] Although they are sophisticated, these techniques still have limitations in terms of cost of the apparatus and large area patterning, due to their serial character. BCP phase separation presents the advantage that no expensive instrumentation is required and of being a self-assembly process, which can take place on a large scale. In this dissertation, nanostructured thin films of functionalized BCPs are presented as new alternatives for chemical patterning applications. Particularly, advances made in the last two decades in macromolecular chemistry offer a large playground. While they were traditionally synthesized using anionic polymerization, BCPs suitable for nanostructuring can now be made by functional group-tolerant radical polymerization. Overcoming the limitations of free radical polymerization (FRP), reversible deactivation radical polymerization (RDRP) techniques are indeed capable of producing BCPs with narrow molar mass distributions and

tailor-made properties. Additionally, *click* reactions/modular ligations are successful tools to modify polymers and allow modifications of materials made thereof. Well known members of the *click* family, such as thiol-ene addition and azide-alkyne cycloaddition can be employed in conjunction with RDRP methods to generate novel macromolecules and materials.

Figure 1.1 summarizes the long-term aim of the current work: producing nanostructured films which possess specific reactivity in each domain to allow ordering of molecules at the nanoscale. To achieve this, the basic idea is to utilize block copolymers known to phase separate into well-defined nanostructures and introduce specific reactive groups along the chain in each block. This way, it is envisioned that each nanodomain of BCP film would display at its surface a fraction of the reactive groups present in the corresponding block. An important detail resides in the fact that we propose to introduce a low fraction of functional monomer (typically less than 10 mol% in each block), so as to not significantly alter the phase behavior of the BCP used as a starting point. There are only a few examples in the literature that have suggested or started to present a similar strategy.^[7-11] Further grafting of molecules on these platforms via covalent attachment on functional groups paves the way for immobilizing single bio(molecules) in close proximity with each other.

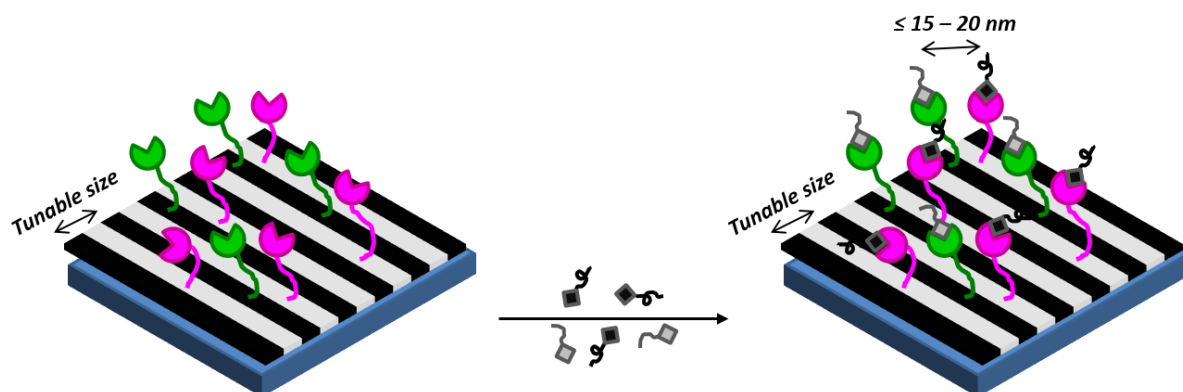


Figure 1.1 Strategy applied in this dissertation – Block Copolymers as Patterning Platforms. Black and white domains are distinct parts of a BCP, purple and green are the functional moieties. Dark grey and light grey objects represent bio(molecule)s grafted on the functional points on the BCP film.

With this in mind, two well-known phase segregating BCPs, namely PS-*b*-PI and PMMA-*b*-PS, were chosen for the present work. Two distinct Chapters of the current Thesis are devoted to these systems. For each system, a synthetic part is reported. Various RDRP techniques were employed to synthesize two corresponding small libraries with a broad range of functional

groups introduced by simple copolymerization with functional methacrylates and/or styrenics. The presented dissertation aims mostly at treating the synthetic challenges to equip the BCPs with clickable units and the influence of the latter on the formation of nanostructured films. The resulting block copolymers are characterized at the molecular level by standard techniques such as ^1H and ^{19}F nuclear magnetic resonance spectroscopy and size-exclusion chromatography, and on the physical level by differential scanning calorimetry and small-angle X-ray scattering. The corresponding thin films are investigated by means of ellipsometry, atomic force microscopy, water-contact angle measurements, and X-ray photoelectron spectroscopy.

Last but not the least, within the frame of this work, some efforts were also devoted to study in details some of the ligations which were envisioned to be used for the surface grafting onto the reactive BCP films. Particularly, the para-fluoro-thiol reaction (PFTR)^[12-14] was in the focus. Two aspects related to a later use on a BCP film were treated. First, the orthogonality with another chemistry to be performed on the same BCP film, i.e., thiol-ene addition, was evaluated. Then, the possibility of performing the PFTR in aqueous medium was examined, as it had until now been performed only in organic solvents, which is not very suitable for modifying polymeric materials.

2

Theoretical Background and Literature Overview

In this Chapter, an overview of the methods employed in the current dissertation is given. First, theories of the employed polymerization techniques are summarized. A literature review of click reactions/modular ligations are then reported with a specific focus on azide-alkyne cycloaddition, thiol-ene addition and *para*-fluoro thiol ligations. In the third section, detailed information on block copolymers (BCPs) is compiled including thermodynamics of microphase separation, BCP thin films and related studies as well as application areas of BCPs. Finally, since it is the most extensively used instrument for characterization of BCP thin films in this work, atomic force microscopy (AFM) is discussed with its background and fundamentals.

2.1 Radical Polymerization

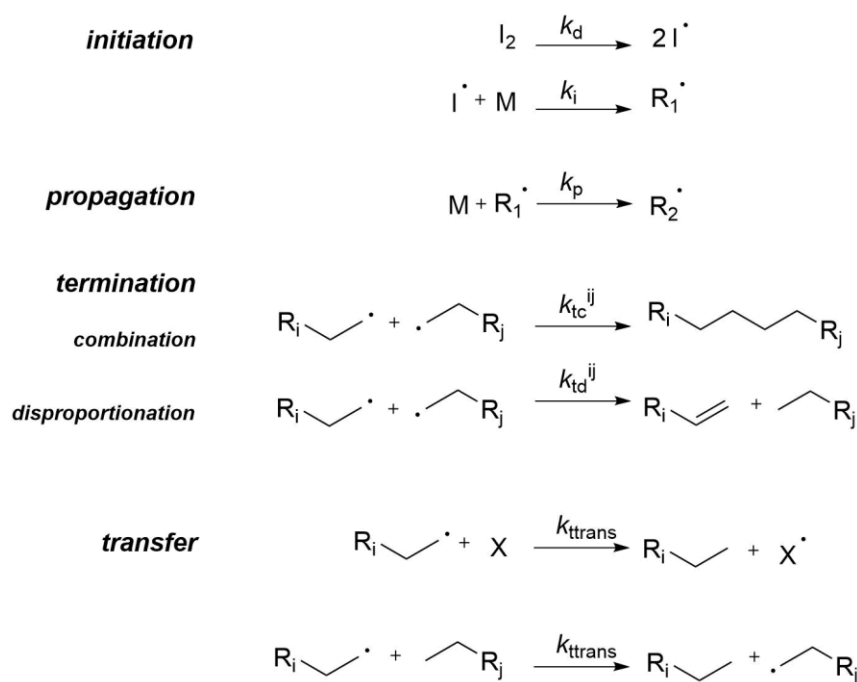
Free radical polymerization (FRP) is used in production of almost 50% of synthetic polymers, providing numerous materials for a wide range of markets.^[15] However, due to the poor control of FRP in obtaining well-defined polymers, reversible deactivation radical polymerization (RDRP) protocols are now employed at least in academia as more controlled processes to create tailor-made macromolecules.^[16] In the following part, a summary of FRP and subsequently RDRP protocols will be introduced.

2.1.1 Free Radical Polymerization (FRP)

Since many plastics, elastomers and some fibers are prepared by free radical polymerization

(FRP), this method is industrially very important. Its tolerance towards many functional moieties, applicability to a large number of monomers and the possibility to be initiated by various means render FRP a very versatile technique. The principle free radical polymerization techniques are bulk, solution, suspension, and emulsion polymerizations.^[17]

FRP proceeds via a chain growth mechanism and basically consists of four different steps: (i) initiation (ii) propagation (iii) termination (iv) chain transfer which are depicted on Scheme 2.1.^[17] The process starts with the decomposition of the initiator to generate free radicals. This can be accomplished by several means, e.g., heat, UV-light, electricity and redox reagents. Azobisisobutyronitrile (AIBN) and benzoyl peroxide (BPO) are two of the commonly used initiators in FRP. Typically, the rate of dissociation k_d is in the order of 10^{-1} to 10^{-6} s^{-1} and can change depending on the reaction conditions. In the following steps, the radical adds to a monomer that creates the first monomer radical which is regarded as initiation, governed by initiation rate constant k_i .



Scheme 2.1 The four elementary steps of the free radical polymerization mechanism.

The chain growth, i.e., propagation, occurs from an attack of the previously generated radical onto a new monomer where a new bond is formed between the monomer and the radical, which eventually elongates the growing polymer chain. In other words, propagation is the successive additions of monomer units onto a radical chain end. As propagation rate coefficient k_p regards

the addition of one monomer to a growing radical, polymerization rate is strongly dependent on the stability of the formed radicals. A slow propagation rate is hence associated with stable radicals, such as in the case of styrene and methyl methacrylate (MMA), and is close to $k_p = 10^2 \text{ L M}^{-1} \text{ s}^{-1}$. On the other hand, for instance, acrylates undergo fast polymerization with a k_p in the order of $10^4 \text{ L M}^{-1} \text{ s}^{-1}$.

Termination is a head-to-head configuration at the junction of two macroradicals which can occur either by combination of two radicals or by disproportionation that results in an unsaturated polymer chain via hydrogen abstraction and a saturated polymer chain. Typically, styrene macroradicals terminate by combination, while MMA macroradicals terminate by combination below $60 \text{ }^\circ\text{C}$ and by disproportionation at higher temperatures.^[17] Apart from these three steps, a transfer reaction can also take place during FRP. The transfer of a hydrogen atom from one end of the chain to a free-radical end of another chain is known as chain transfer. When hydrogen abstraction occurs intramolecularly or intermolecularly on a unit which is at some distance from the chain end, branching takes place in most cases.^[17] Transfer reactions also result in decreased chain length.

Despite keeping its importance in terms of mass production of industrial polymers, FRP also possesses some disadvantages such as lack of control over molar mass, polydispersity, and precise incorporation of chemical functionalities. In order to address these drawbacks, advanced polymerization techniques have been developed since the mid-1990s. Reversible deactivation radical polymerization (RDRP) methods play an important role at this point to create well-defined polymers which will be discussed in the next section.

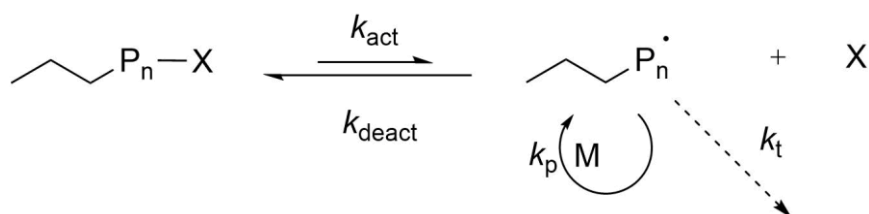
2.1.2 Reversible Deactivation Radical Polymerization (RDRP)

Reversible deactivation radical polymerization (RDRP), previously coined as controlled/living polymerization (CRP), has appeared as an alternative to eliminate the problems related to FRP. As mentioned in the previous section, FRP protocols have a major drawback of control on molar mass, dispersity and functionality which is mainly caused by the occurrence of a termination step. This leads to the accumulation of dead chains, broad polydispersities, etc. Absence of the termination step would thus solve the problems associated with FRP. The term 'living' was introduced by Szwarc in 1956, in the context of anionic polymerization. It was stated that living polymerization is a chain growth process without termination or transfer step.^[18] However, as terminations can never be entirely eliminated during a radical polymerization, IUPAC prefers to use the term RDRP rather than LRP. RDRP techniques typically fulfill the following criteria: a fast initiation step, linear increase of molecular mass in accordance with monomer conversion, narrow polydispersities and high end-group fidelity for possible chain extensions.^[19]

Most studied types of RDRP, namely, nitroxide mediated polymerization (NMP), atom transfer radical polymerization (ATRP) (and a variant of it, i.e., activators regenerated by electron transfer ATRP (ARGET ATRP)) as well as reversible addition fragmentation chain transfer (RAFT) polymerization will be further explained in the following sections.

2.1.2.1 Nitroxide Mediated Polymerization (NMP)

In all RDRP systems, a dynamic equilibrium is established between propagating radicals and dormant species. Nitroxide mediated polymerization (NMP) operates via an activation/deactivation process, governed by an equilibrium,^[20] which is depicted on Scheme 2.2. In addition, a so-called persistent radical effect (PRE) operates at the beginning of the polymerization in order to establish this equilibrium efficiently.^[21] Operating via PRE, propagating radicals (P_n^\bullet) are rapidly trapped in deactivation process by species X, which is typically a stable radical; a nitroxide in the case of NMP. The dormant species can be activated either spontaneously/thermally or with light, to recreate the radicals. It is noteworthy that growing radicals can propagate and also terminate whereas persistent radicals (X) can only (reversibly) cross-couple with growing species but can not terminate with themselves.^[22] This is the base of the PRE, leading to the accumulation of deactivating persistent radical species.



Scheme 2.2 NMP equilibrium.

NMP can have a bicomponent or monocomponent initiating system. In the first one, there exist a nitroxide radical and a conventional radical initiator (e.g., AIBN) whereas in the latter one, the reaction starts from homolytic cleavage of an alkoxyamine.^[22] Controlled polymerization of styrene in the presence of a thermal initiator such as benzoyl peroxide (BPO) and the mediating stable free radical TEMPO (2,2,6,6-tetramethyl-1-piperidynyl-N-oxy) by Georges in 1993 is the first example of NMP with a bicomponent initiating system.^[23] The concept of unimolecular initiation, which is more advantageous and more widely used, was developed by Rizzardo^[24] and Hawker.^[25-26] Structures of some commonly used nitroxides are given in Figure 2.1.

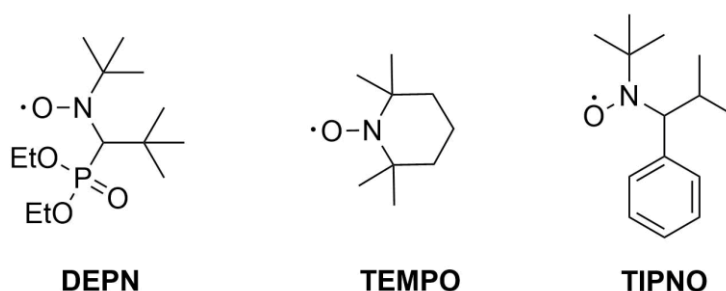
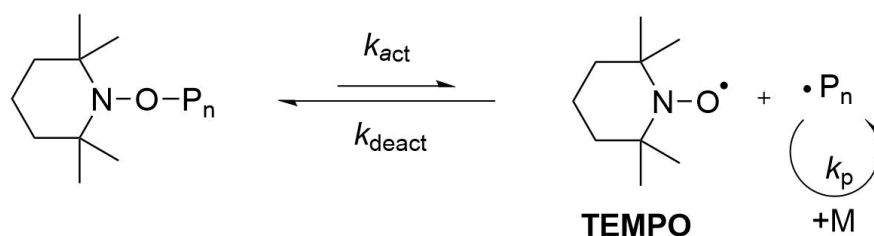


Figure 2.1 Examples of common nitroxides used in NMP.

An exemplary NMP mechanism using TEMPO as the nitroxide radical is shown on Scheme 2.3.^[27] Among all RDRP methods, NMP can be regarded as technically the simplest one especially with the use of an alkoxyamine as the initiator (monocomponent initiation). It does not require a metal catalyst, the activation-deactivation equilibrium can be reached by heating and the reaction can simply be stopped by cooling down the reaction medium. On the other hand, its versatility is limited as it is restricted to some monomers whose alkoxyamines possess adequate thermodynamic features, e.g., styrenics, acrylates, acrylamides. Particularly, less activated monomers such as vinyl acetate (Vac) and vinyl chloride (VC) are difficult to control by NMP.^[22]



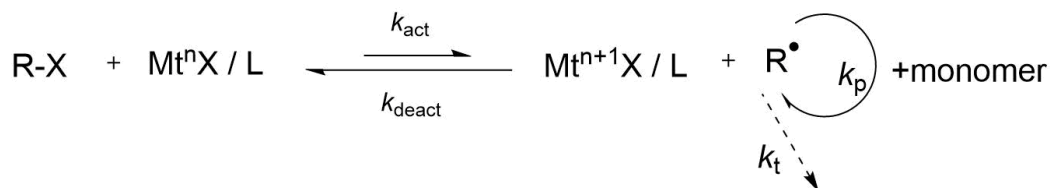
Scheme 2.3 Exemplary NMP mechanism with TEMPO.

2.1.2.2 Atom Transfer Radical Polymerization (ATRP)

Among RDRP protocols, atom transfer radical polymerization (ATRP) is one of the most powerful and widely used techniques to obtain well-defined polymer architectures along with various functionalities. The ATRP term was adapted from atom transfer radical addition reaction (ATRA)^[28-30] of alkyl halides onto alkenes, because ATRA and ATRP are mechanistically similar.^[31] In 1995, independently, Matyjaszewski,^[32] Sawamoto^[33] and Percec^[34] reported ATRP for the first time. Developments and investigations in this field are present.^[35-37]

The ATRP mechanism is based on a reversible redox process in which a metal-ligand complex ($M^{n+}X / L$) plays the role of a catalyst. This complex is elevated to a higher oxidation state (M^{n+1}

X / L) along with an halogen abstraction from the ATRP initiator (R-X) while generating alkyl radicals which react with monomers and lead to propagation to create macroradicals (Scheme 2.4). The lower oxidation state complex (Mt^nX / L) is generally termed as the activator and the higher oxidation state complex ($Mt^{n+1}X / L$) is termed as the deactivator. Overall, this process is a rapid and dynamic equilibrium, which eventually achieves to keep the radical concentration to a minimum (typically 10^{-9} - 10^{-8} M) resulting in reduced number of irreversible terminations.^[38]



Scheme 2.4 General mechanism of ATRP. Mt: metal, L: ligand, X: halide.

Although ATRP can be catalyzed by various transition metals, copper is the most frequently used and the most efficient one.^[35] Furthermore, the ligand structure has a significant effect on activation.^[36] For instance, the topology (e.g., branched > linear ~ cyclic)^[36] and the steric effects around the metal center (Me_6TREN is ~1000 times more active than Et_6TREN) play important roles.^[39] Figure 2.2 shows some exemplary ligands and ATRP initiators. The broad commercial availability of ATRP initiators renders ATRP advantageous over the other RDRP techniques. These are typically alkyl halides, which are indeed precursors of many alkoxyamines and RAFT agents as well.^[40-41] The activity of the initiator depends on several factors such as the degree of initiator substitution (tertiary > secondary > primary), leaving group (I > Br > Cl for 2-halopropionates), and the radical stabilizing groups (-CN >> OR).^[36]

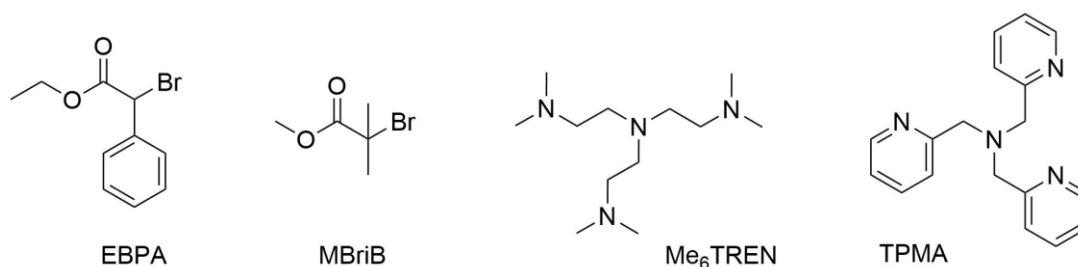
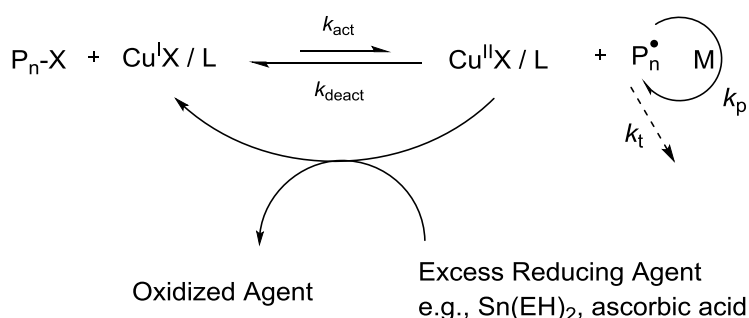


Figure 2.2 Examples of commonly used initiators and ligands for ATRP: ethyl α -bromophenylacetate (EBPA), methyl α -bromoisobutyrate (MBriB), tris[2-(dimethylamino)ethyl]amine (Me_6TREN) and tris(2-pyridylmethyl)amine (TPMA).

Despite its versatility, ATRP has some drawbacks as well. For instance, special handling procedures must be applied to deoxygenate the medium especially when considering the involvement of highly active ATRP catalysts. Many of the copper complexes are relatively toxic, their removal from the products is tedious as well as harmful for the environment.^[36, 42] To circumvent the issue regarding copper, some variants of ATRP have been developed, namely, activators generated by electron transfer (AGET) ATRP, initiators for continuous activator regeneration (ICAR) ATRP and activator regenerated by electron transfer (ARGET ATRP). As it was employed in the course of current dissertation, ARGET ATRP will be discussed in detail in the following part.

2.1.2.2.1 Activators ReGenerated by Electron Transfer (ARGET) ATRP

In classical ATRP, Cu(I) is constantly converted to Cu(II). When Cu(I) is totally consumed, and hence Cu(II) has accumulated, the reaction simply stops. Moreover, accumulation of Cu(II) slows down the polymerization rate and thus prevents high monomer conversions. In ARGET ATRP, however, a reducing agent is utilized such that the metal-ligand complex in the higher oxidation state is continuously reduced to its lower oxidation state as it forms and the activator is regenerated.^[43] An ATRP catalyst, which is stable and active enough, can be used in sufficiently reduced amounts. Depending on this fact, the amount of copper is also drastically reduced in ARGET ATRP. In other words, this variant of ATRP, makes use of minute amounts of catalyst which is continuously regenerated throughout the reaction. The mechanism of ARGET ATRP is illustrated on Scheme 2.5. The only difference between AGET and ARGET ATRP is that ARGET ATRP employs much lower quantities of copper and larger excess of the reducing agent.^[44-46] Excess reducing agent is also useful to suppress the effect of trace amounts of oxygen in the medium.



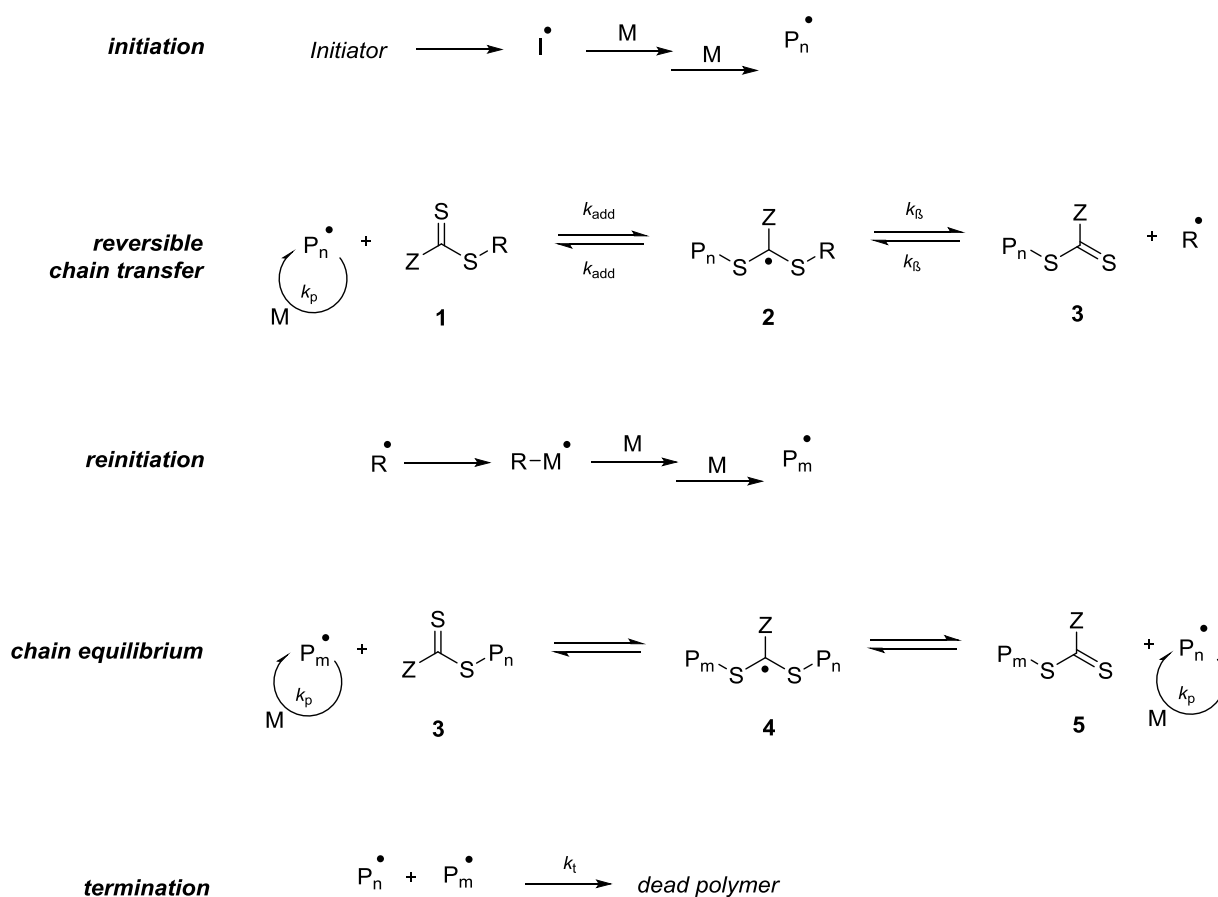
Scheme 2.5 Proposed mechanism for regeneration of the copper(I) complex in ARGET ATRP.

2.1.2.3 Reversible Addition-Fragmentation Chain-Transfer (RAFT)

Polymerization

RAFT polymerization, also being a very versatile and convenient RDRP method, mechanistically differs from the aforementioned RDRP processes. During RAFT polymerization, there exists a chain transfer agent (CTA) which reacts with a growing chain end and terminates it while releasing a radical. This radical can add onto new monomer units which react with a CTA subsequently, and simultaneously set the formerly terminated chain free again. This constant exchange process yields polymers with high end group fidelity.^[47] Typically utilized CTAs (also termed as RAFT agents) are dithiocarbonates, trithiocarbonates, and xanthates thanks to their high radical reactivity.^[48]

The general mechanism of RAFT polymerization is given on Scheme 2.6. The initial steps of RAFT is similar to FRP. Classically, an initiator is first decomposed to radicals, which attack monomers and create the first radicals that start the growth of a chain. After a short time of propagation, the growing radicals add onto the RAFT agent (**1**) and create intermediate radical (**2**) which is subsequently converted into a new CTA (**3**) and the respective radical. This step is known as reversible chain transfer.^[48] The newly generated radical starts adding onto monomer units during the reinitiation step. After a short time, the newly grown macroradical adds onto (**3**) and generates another intermediate radical (**4**), which can again release a macroradical and another macromolecular CTA reagent (**5**). The chain equilibrium step is reached when the dormant radicals (**4**) and the growing radicals repetitively undergo addition-fragmentation steps.



Scheme 2.6 Mechanism of RAFT polymerization.^[48-49]

At the end of the polymerization process, the majority of the chains are end-capped with the employed CTA though there exists a small number of dead chains terminated via conventional FRP termination mechanism.^[49-50]

A significant advantage of RAFT polymerization is preservation of radical concentration at a constant level which can make the reaction rates rather faster as compared to ATRP and NMP. Moreover, the thiocarbonyl end groups are quite versatile to undergo transformation after polymerization. The efficiency of a RAFT agent depends on several factors such as the monomer type, the free radical leaving group R, and the Z group to activate the thiocarbonyl double bond and to stabilize the intermediate radical. In general, an efficient CTA must be highly active towards radical attacks (high k_{add}) and very effective in addition and fragmentation steps.^[51] Strongly stabilizing Z groups such as a phenyl moiety efficiently control the polymerization of methacrylates and styrene. Weaker stabilizing Z groups such as dithiocarbamates and xanthates are used in polymerization of monomers which form less stable radicals.^[48]

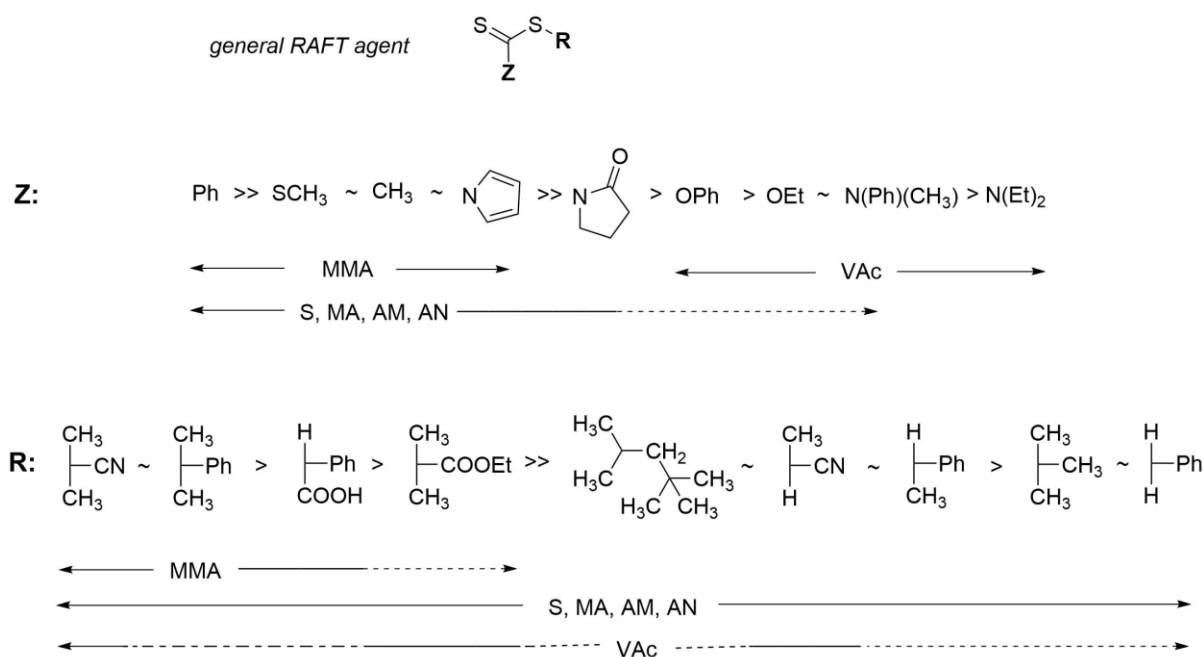


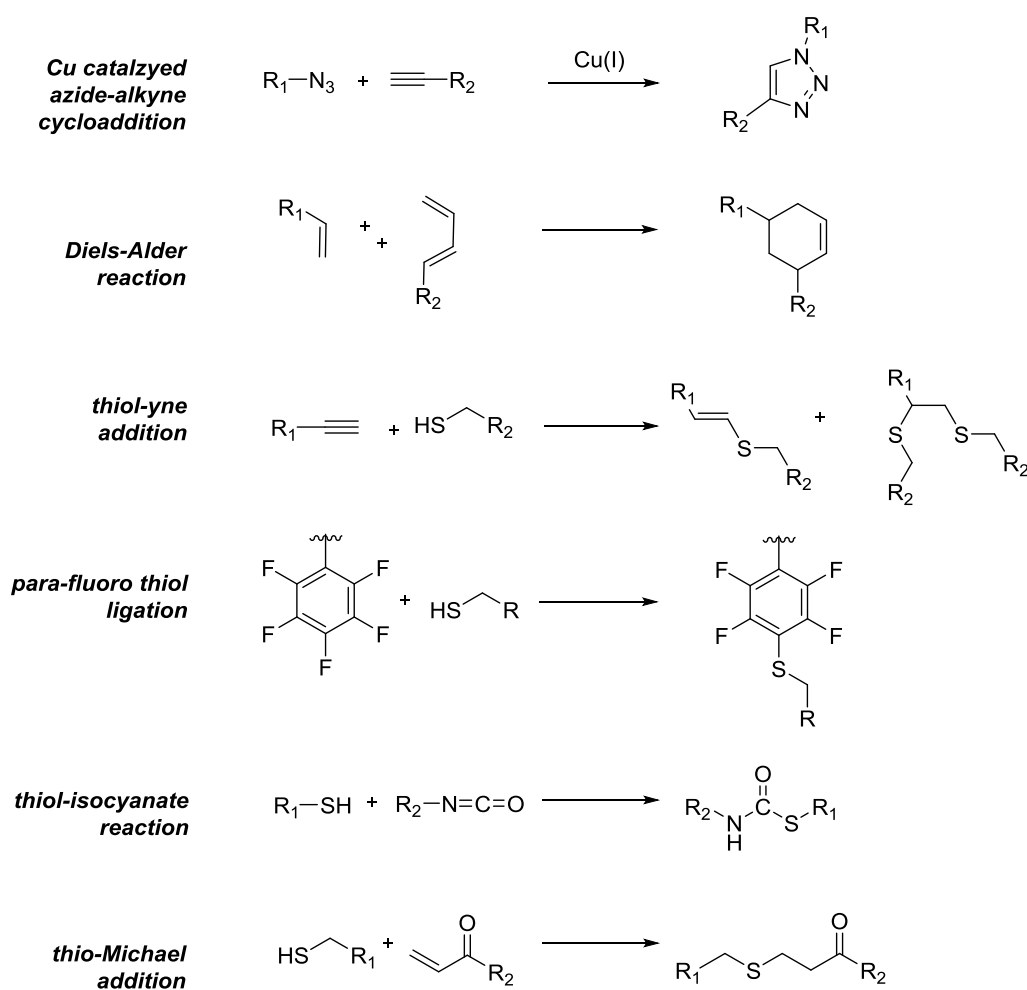
Figure 2.3 Guidelines to choose an suitable RAFT agent.^[48] Dashed lines represent poor control over the polymerization. MMA = methyl methacrylate, MA = methacrylate, St = styrene, AM = acrylamide, AN = acrylonitrile, VAc = vinylacetate.

Since most RAFT agents are colored, it can be disadvantageous in some applications. It can thus be necessary or desirable to eliminate the thicarbonylthio group not only due to the color but also due to further reactions it can undergo. The generation of thiols, on the contrary, can be used for conjugation or crosslinking, for instance.^[52]

On Figure 2.3, guidelines to choose a suitable RAFT agent are shown. As CTAs are incorporated in the product, the polymers become macro-RAFT agents and bear a living character and can also undergo chain extensions to yield block copolymers (BCPs). RAFT polymerization is hence known as one of the most versatile techniques to make BCPs. By proper selection of CTAs with suitable Z and R groups, it is possible to obtain well defined polymers and complex architectures by RAFT, as also largely utilized in the presented study.

2.2 Click Reactions / Modular Ligations

The 'click' chemistry concept was introduced by Sharpless and co-workers in 2001.^[53] This philosophy concerns reactions which can satisfy stringent criteria such as high stereoselectivity, minimum amount of byproducts, easy recovery of the products, modularity, orthogonality, insensitivity to solvents.^[53] It has already been implemented by many scientists.^[54-59] Although Sharpless envisaged the click concept to be applied mainly in biological sciences, it clearly had a great effect on polymer chemistry.^[60] Introduction of the click concept also -possibly- led to a 'paradigm shift' in the design of macromolecular materials that encouraged scientists to reevaluate the criteria to obtain well-defined polymers with various functionalities efficiently.^[61] When applied to the context of polymer chemistry, the click concept bears the following additional requirements: equimolarity of the reactants (especially in polymer-polymer conjugation), simple purification, very short reaction times, high selectivity, and high yields.^[62]



Scheme 2.7 Examples of modular ligations.

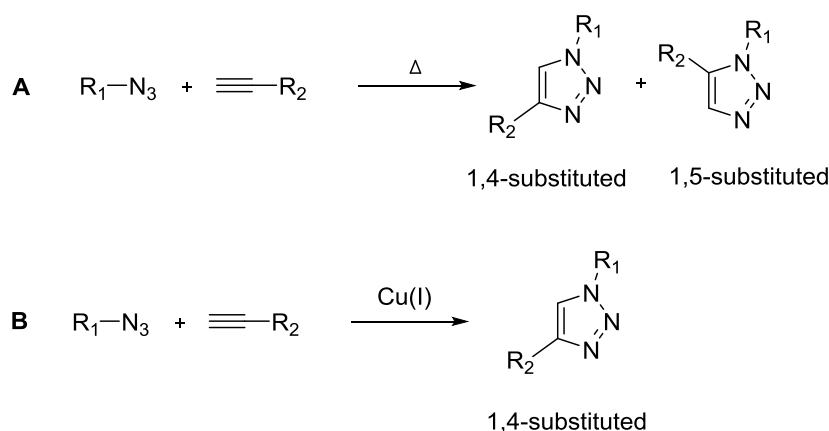
To be considered as a click reaction, conditions of a study should fulfill all the aforementioned qualifications, yet 'the click' term is abusively used in the literature. In order not to infringe it, we used the term 'modular ligation' in Chapter 5. Modular ligations span the reactions which are used to combine distinct polymers that can produce novel architectures, to bring together different polymers prepared by distinct approaches, to give new functionalities into macromolecules in an orthogonal and efficient way.^[63-65]

Some of the commonly employed click reactions/modular ligations are depicted in Scheme 2.7. The Diels-Alder reaction (DA)^[66-70] and thio-Michael addition^[71-74] are widely utilized in polymer and materials science. The DA reaction was discovered by Otto Diels and Kurt Adler in 1928 who were awarded the Nobel Prize in 1950 for this work.^[75] In a DA reaction, a diene (a hydrocarbon with two double bonds, electron rich/donating group) and a dienophile (a hydrocarbon with an isolated double or triple bond, electron poor group) form a six membered cyclic product. This reaction is effectively used in creating self-healing materials, for instance.^[76-77]

Since they were employed during the course of the presented study, CuAAC, radical thiol-ene addition and *para*-fluoro thiol ligations will be discussed in detail in the following parts.

2.2.1 Copper Catalyzed Azide-Alkyne Cycloaddition (CuAAC)

The copper catalyzed azide-alkyne cycloaddition^[53, 78] (CuAAC) is a variant of the Huisgen 1,3 dipolar [3+2] cycloaddition^[79-80] that occurs between C-C triple bonds or C-N triple bonds^[81] and also alkyl / aryl / sulfonyl azides.^[59] [3+2] notation represents the number of atoms involved in the cycloaddition reaction. Thermally induced (Huisgen type) additions are exergonic and yield a mixture of 1,4- and 1,5-substituted triazoles whereas the metal catalyzed variant is more regioselective and gives only the 1,4-substituted product (Scheme 2.8).



Scheme 2.8 Azide-alkyne cycloadditions. A) Thermally induced 1,3-dipolar cycloaddition. B) Copper catalyzed 1,3-dipolar cycloaddition.

As catalyst, generally a copper-ligand complex, for instance Cu(I) and PMDTA is utilized. However, the CuSO₄-ascorbic acid pair is less oxygen sensitive since Cu(II) is reduced to Cu(I) *in situ*,^[82] as also employed in this work (see Chapter 3). In addition, copper clusters (Cu/Cu-oxide nanoparticles),^[83] metallic Cu⁰ clusters,^[84] as well as copper/charcoal^[85] have been proven successful as catalysts in CuAAC. Despite its efficiency, a copper based catalyst system might not be favored for some systems due to its cytotoxicity.^[86] As an alternative, strain promoted azide-alkyne cycloaddition (SPAAC) is a copper free version of CuAAC.^[87] There are more, catalyst-free, photoinduced alternatives of azide-alkyne coupling that can be encountered in the literature.^[88-89]

CuAAC was first reported by Sharpless in 2001,^[53] followed by Meldal in 2002,^[90] and is still one of the most predominant type of click reactions. It has enormously been applied not only in polymer science,^[65, 91-92] to make dendrimers,^[93-94] in drug discovery,^[95] but also in carbohydrate chemistry.^[96] Furthermore, it has also been efficiently used in surface chemistry.^[97-102] More details will be discussed in Chapter 3 where CuAAC was utilized for surface reactions.

2.2.2 Reactions of Thiols

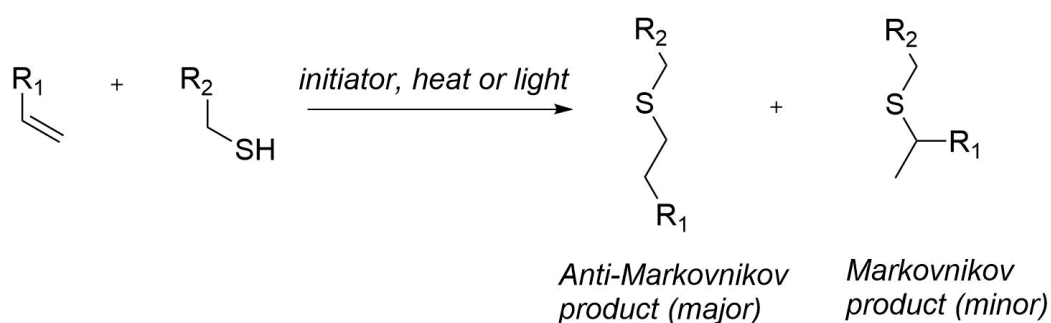
Thiols, also referred to as mercaptans in the literature, constitute a very versatile class of chemical compounds due to several reasons such as easy synthetic accessibility, high commercial availability and the ability to undergo various reactions.^[103] Thiol-containing molecules are also biologically, clinically and environmentally very critical. For instance, thiophenols are highly toxic, lack of cysteine (Cys) is involved in syndromes such as slow growth in children.^[104] Hence, sensing and recognition of thiols are also highly important aspects. On the other hand, the common, unpleasant odor of thiols is one disadvantage, particularly for low molecular weight compounds.^[105] In addition, some thiol compounds lack long term shelf stability which can be overcome with an appropriate stabilizer.^[105]

Primarily with vulcanization using natural sources of sulfur, thiols have been playing important roles in materials science and macromolecular chemistry. There are four main categories of thiols, namely, alkyl thiols, aryl thiols, thiolacetate (i.e. thioglycolate) and thiolpropionate thiols.^[105] They can undergo several reactions such as photo- or thermally-induced radical thiol-ene addition,^[106-107] *para*-fluoro thiol substitution reaction (PFTR), thiol-yne reaction,^[108-109] Michael addition,^[71, 74] and even reactions with gold.^[110] They follow either a radical initiation or a base catalysis activation. First of all, thiol-yne radical addition (alkyne hydrothiolation) is a widely utilized type of click reaction which can be regarded as sister reaction of thiol-ene addition and copper catalyzed azide alkyne coupling (CuAAC).^[111] It is a powerful tool in

monomer synthesis, network formation, site-specific functionalization,^[111-112] and surface reactions.^[113-114] Secondly, thiols can react with isocyanates upon catalysis by amines to yield thiourethanes.^[105] Thirdly, they can react with epoxy rings which is a base-catalyzed nucleophilic ring-opening reaction. As this reaction is highly effective in water and in solvent-free conditions, it is also commensurate with the *click* paradigm.^[105] Moreover, as thiols are typical soft nucleophiles, they are also able to undergo substitution with halogens. This exchange reaction has also been termed as efficient *click* chemistry.^[115] The Michael addition or the conjugate addition of thiols (i.e. thiolate anions) to electron deficient C=C bonds takes place under base catalysis with reagents such as NEt₃. The rate of this reaction can be greatly affected by the type of the base, p*K*_a of the thiol, steric hinderance of the thiol and the nature of the electron withdrawing group adjacent to the double bond.^[105] As they were employed in the course of this work, photoinduced thiol-ene addition and PFTR will be discussed more in detail in the following sections.

2.2.2.1 Radical Thiol-Ene Addition

The thiol-ene coupling, first reported more than one century ago,^[116-117] has been exclusively used in materials science and polymer chemistry, and currently qualifies as a *click* reaction due to fulfilling requirements such as orthogonality, compatibility with a wide range of solvents, high yields and short reaction times.^[118-121] The thiol-ene reaction, also known as thiylation, introduces a thioether functionality into an unsaturated compound. It can proceed photochemically or thermally and selectively gives anti-Markovnikov product (Scheme 2.9).^[122]

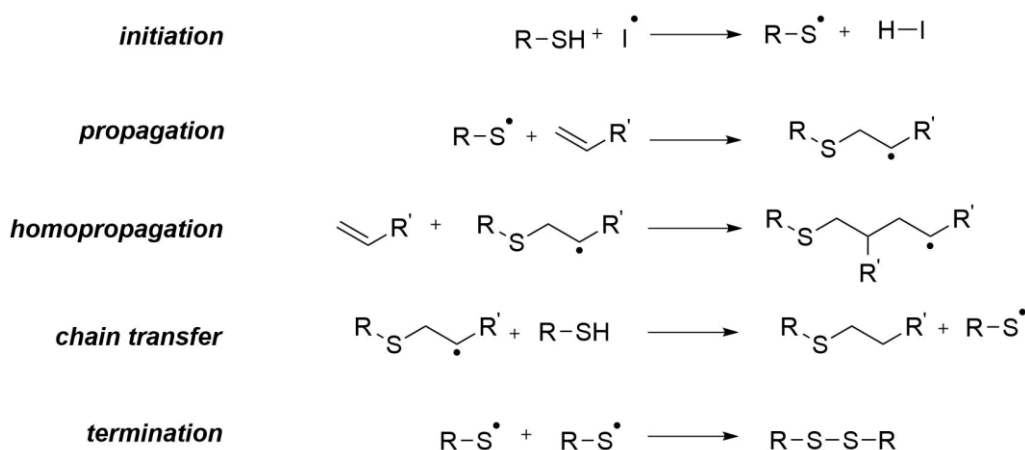


Scheme 2.9 Scheme and possible products of radical thiol-ene reaction.

The general mechanism of radical thiol-ene reaction is given on Scheme 2.10.^[119, 123] The reaction starts with the generation of a thiyl radical via proton abstraction by an initiator radical from a thiol-functional compound. Thiyl radicals subsequently react with unsaturated compounds in the propagation step while homopropagation might also take place

Radical Thiol-Ene Addition

concomitantly. The radical adduct then abstracts a hydrogen from another thiol that is present in the medium which yields the major product (chain transfer). Though thiol-ene addition is a very efficient reaction, side reactions are also observed.^[124] Head-to-head coupling of thiyl radicals and homopropagation are some of the possible undesired reactions. To be considered as a click reaction, these must be largely avoided. Radical thiol-ene follows a step-growth mechanism and its photoinduced variant is the more frequently used one.^[119, 125-126] The reactivity during radical thiol-ene addition depends on the chemical structure of the thiol and the ene components. As highlighted by Hoyle *et al.*, general reactivity with three thiol types (alkyl thioglycolates, alkylthiols and alkyl 3-mercaptopropionates) follows the order: norbornene > vinyl ether > propenyl > alkene > acrylate > acetonitrile > styrene > conjugated diene.^[119] AIBN and 2,2-dimethoxy-2-phenylacetophenone (DMPA), also known as benzyl dimethyl ketal (BDK), are the most widely used photoinitiators in radical thiol-ene addition.^[64, 127]

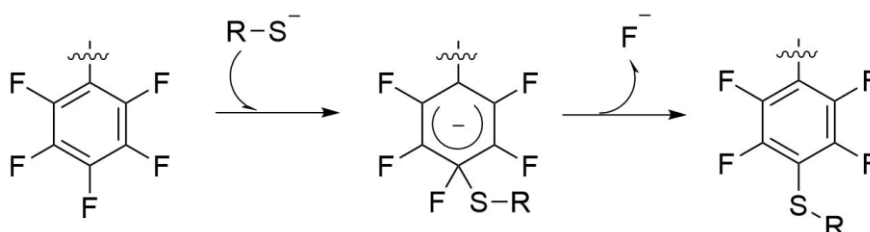


Scheme 2.10 General radical thiol-ene reaction mechanism.

Being a metal-free reaction and owing to its versatility, radical thiol-ene addition has been used in many studies in different areas of contemporary chemistry including polymer science, surface functionalization, organic chemistry, and bioconjugation since 1900s.^[118-119, 128-131]

2.2.2.2 Para-Fluoro Thiol Substitution Reaction (PFTR)

The *para*-fluoro thiol substitution reaction (PFTR) is one of the newly flourishing ligation methods which has already been referred to as 'click' reaction by some scientists,^[12-14] and its orthogonality with a radical type of thiol-ene addition has been proved by our group.^[64] As photoinitiated thiol-ene addition occurs via a radical mechanism whereas PFTR requires nucleophiles and is not oxygen sensitive, these two click type of reactions can be combined on the same molecule and/or in the same medium to take place independently. Afterwards, Cakir *et al.* presented the applicability of PFTR and radical thiol-ene to create multi-arm star polymers, not in an orthogonal way but rather in a sequential order.^[132] It is envisaged that PFTR can work in an orthogonal way with other radical processes as well. Pentafluorostyrene (PFS) was first synthesized by Wall^[133] and currently stands as a highly commercialized monomer. As a functional derivative of styrene, it can easily be copolymerized with its non-functional variant, i.e., styrene, to create functional random and block copolymers, for instance by NMP.^[134-135] The aromatic pentafluorophenyl (PFP) moiety is stable during radical polymerization^[103] and it undergoes nucleophilic substitution with a number of nucleophiles including amines,^[13, 136-137] alcohols,^[138] and particularly with thiols on the *para* position under relatively mild conditions.^[139] The reaction takes place on the *para* position as it possesses the largest activation due to its *ortho* and *meta* neighbours (See Scheme 2.11).^[103, 140-141] During PFTR, the thiols are in the thiolate state that attack the carbon to which *para*-F atom is attached, and undergoes a substitution reaction with the fluorine. The reaction is highly promoted by bases which should be chosen according to the type of thiol.^[103] For instance, DBU is an efficient base for aliphatic thiols whereas TEA would not lead to the same yields in the presence of aliphatic thiols.^[103]



Scheme 2.11 Suggested mechanism for PFTR.

Furthermore, the PFTR has been employed in porphyrin chemistry,^[138, 142-147] to create hyperbranched fluoropolymers, to make hybrid compounds for self-assembling systems,^[137] to generate glycopolymers,^[14, 134-135, 148] to perform surface reactions,^[12, 14] and to synthesize

Para-Fluoro Thiol Substitution Reaction

polymers with novel properties.^[149-150] Figure 2.4 shows an example from the literature in which PFTR was utilized for glycosylation.^[134] In this study, random and block copolymers of PFS and styrene were synthesized and some of them were employed to produce uniform nanospheres with diameters ranging from 70-720 nm upon nanoprecipitation. Noy *et al.* synthesized acrylate and methacrylate monomers containing pentafluorophenyl (PFP) moieties to make use of the thiol reactivity of PFP groups in a broader range of monomers.^[103] Unlike the previously reported PFS analogues which were prepared by NMP, these newly synthesized monomers were polymerized by RAFT polymerization. Moreover, As PFTR follows an SN2 reaction mechanism, the solvent type is highly important. It has been mostly conducted in DMF^[14, 134, 146, 148] and in some cases in THF.^[151] Protic solvents are not very feasible for this type of a reaction as they stabilize the nucleophile. However, applicability of this reaction in water is presented in Chapter 7.

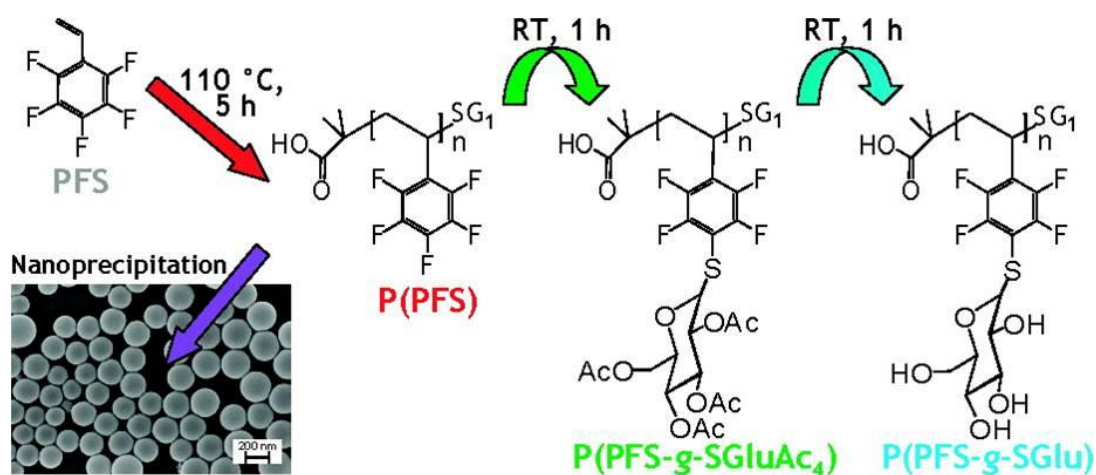


Figure 2.4 One exemplary application of PFTR in the literature. Adapted with permission from ref[134] Copyright © 2009, American Chemical Society.

2.3 Block Copolymers (BCPs)

By definition, a block copolymer (BCP) is a macromolecule that consists of at least two different segments, i.e. blocks, which are covalently attached at junction point(s). The simplest and most studied BCP architecture is linear diblock copolymers. Some other types of BCP architectures are shown on Figure 2.5. There are three categories of BCP synthesis: (i) continuous (sequential) polymerization, (ii) macroinitiation approach, and (iii) coupling of the distinct segments after synthesizing them separately.^[4] In this dissertation, only macroinitiation approach was employed using the methods introduced in section 2.1.2. Moreover, since it was also utilized in the presented work, we will devote this part to linear di-BCPs. Various aspects will be discussed: theory of their phase separation, their behaviour in the form of thin films, tools for characterization, and the application areas of BCP thin films.

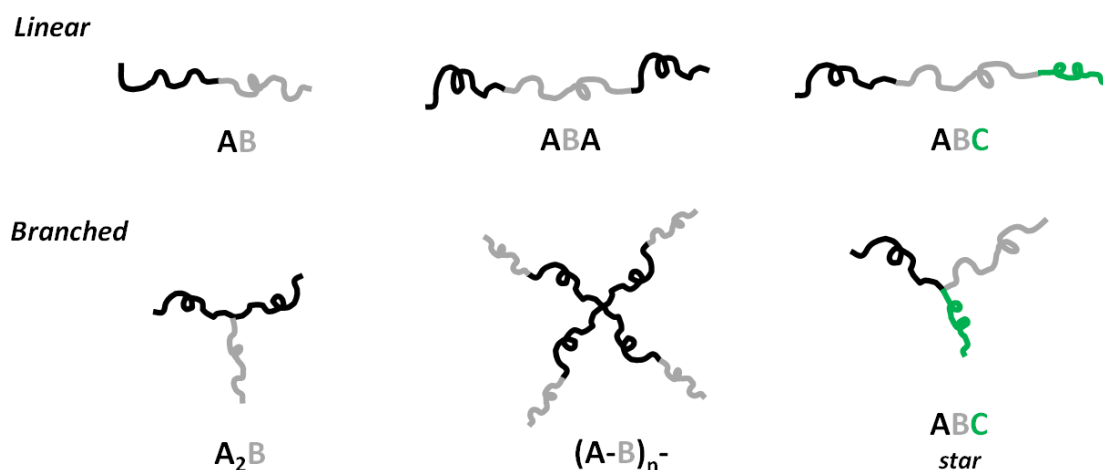


Figure 2.5 Examples of BCP architectures. A and B represent distinct blocks.

2.3.1 Phase Separation and Self-Assembly of BCPs

As BCPs consist of dissimilar segments with particular properties, they tend to demix. Yet, as opposed to a blend of homopolymers, macrophase separation does not occur since the two components are tethered with a covalent bond. Structural differences cause excess free energy contributions which make it unfavourable for the two blocks to mix.^[3] Therefore, BCPs (micro)phase separate and self-assemble into various nanostructures in bulk, in solution and in the form of thin films.^[3, 152-153]

Understanding Microphase Separation Unlike macrophase segregation in the case of homopolymer blends, the covalent bond between the blocks of a BCP hampers their separation and instead A and B segments self-assemble on opposite sides of an interface. Figure 2.6 explains this phenomenon more clearly. Thermodynamically incompatible mixture of homopolymers undergo macroscopic segregation in order to decrease surface tension, as depicted on the left of the figure. Figure 2.6 right, however, shows the microscopic phase separation with smaller feature sizes.^[154]

With the ability to microphase-separate and create a number of nanostructures, BCPs have been in the focus of intense research activities in the last decades ranging from theories to understand the thermodynamics to various applications.^[155] Di-BCPs have abilities that can be greatly utilized with functions which are not accessible by their homopolymer counterparts individually.

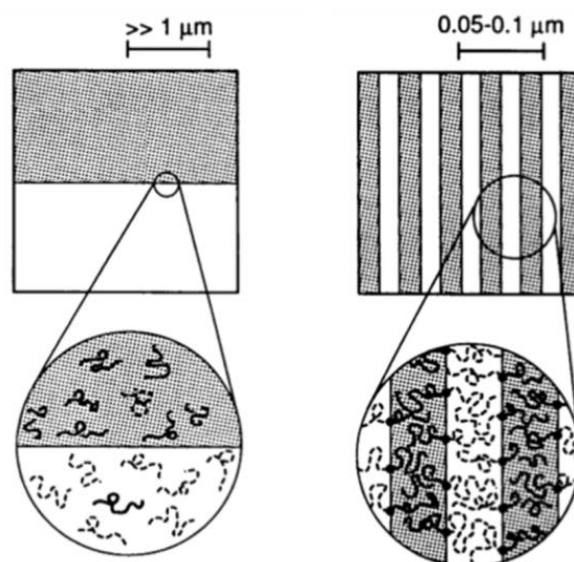


Figure 2.6 Macrophase separation of homopolymers (Left). Microphase separation of BCPs (Right). Adapted with permission from ref [154]. Copyright © 1991, 1990 by the American Association for the Advancement of Science.

Effect of Molecular Weight and Polydispersity on Microphase Separation The scale at which the constituent polymer blocks segregate is directly related to the size of the chains which results in various morphologies. One repeating unit, with lateral dimensions also known as one domain spacing or periodicity, depicted as (L_0) can be within a range down to 5-50 nm.^[153] In general, L_0 increases with increasing molar mass.^[156-157] In other words, to obtain larger periodicity, it is necessary to increase the overall molar mass of the BCP. Secondly, polydispersities might have a small effect on L_0 as well. Many studies on BCP phase separation utilized BCPs synthesized by

anionic polymerization. i.e., with low \mathcal{D} . However, RDRP protocols are utilized to obtain BCPs with narrow distributions. An increase in \mathcal{D} might increase L_0 slightly. A work of Matsushita *et al.* exemplified this phenomenon in 2003.^[158] As depicted on Figure 2.7, when \mathcal{D} increases, the longer chain compensates for the shortage of the other chain which results in increased domain spacing (L_0'). This study was performed on a PS-*b*-P2VP system. The researchers observed microphase separation up to $\mathcal{D} = 1.7$, above which macrophase segregation started to evolve. Though this is not a pronounced effect on microphase separation, it should still be noted that if there are large fluctuations in \mathcal{D} values, L_0 can be affected.

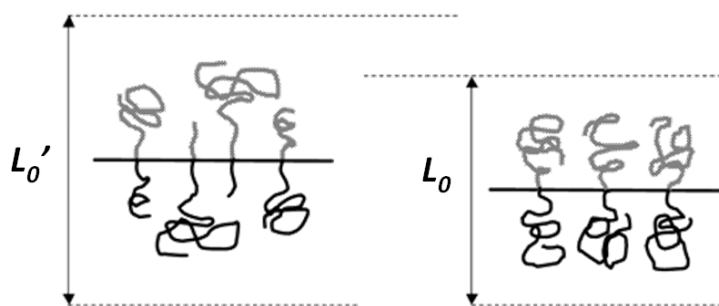


Figure 2.7 Comparison of microdomain sizes obtained by BCPs with larger (Left) and narrower (Right) polydispersities. Adapted with permission from ref [158]. Copyright © 2003, American Chemical Society.

Theory of Microphase Separation

Description of Parameters Microphase separation of BCPs is primarily driven by the incompatibilities between the individual segments. The phase behaviour of a di-BCP is governed by three factors: (i) the overall degree of polymerization N , i.e. molar mass of the BCP, (ii) the composition, f , i.e. relative volume fractions of the two blocks, and (iii) the Flory-Huggins interaction parameter χ . The first two parameters can be regulated during polymerization whereas the χ parameter is inversely related to temperature.^[152] At low temperatures, i.e., when χ is large, strong segregation is observed, which produces microdomains purely composed of A and B components.^[3] On the contrary, high temperatures are accompanied by low χ , which means that phase separation is not favorable. It is also to note that highly incompatible blocks have large χ whereas similar and compatible segments are accompanied by small χ values as χ qualifies dissimilarities between the segments.^[159] The following Equation 2.1 describes the temperature dependence of χ :

$$\chi = \alpha T^{-1} + \beta \tag{2.1}$$

α and β are the enthalpy and entropy coefficients for a particular composition. In general, these coefficients may depend on f , molar mass, and the architecture, as well as the temperature, as mentioned above.^[154]

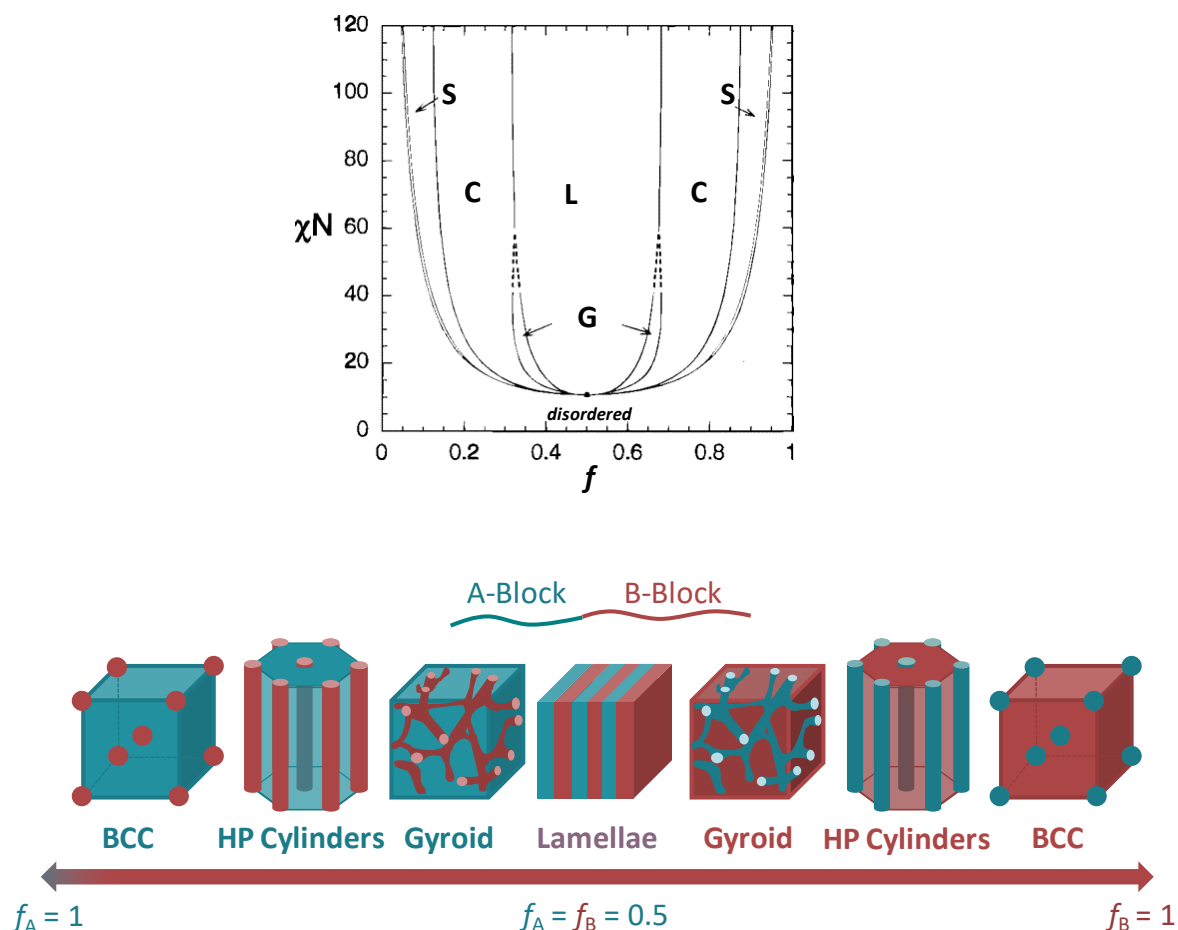


Figure 2.8 Self-consistent mean field theory^[160-162] predicting lamellar (L), cylindrical (C), spherical (S), and gyroid (G) equilibrium morphologies. Adapted with permission from ref [162]. Copyright ©1999 American Institute of Physics (top). Equilibrium morphologies predicted by the self consistent mean field theory (bottom).

To predict the phases of a BCP melt, self-consistent mean field theory (SCFT) (Figure 2.8 top) is the paramount source.^[160-163] In this method, the external mean fields acting on a polymer chain are self-consistently calculated. There are three regions regarding the phase separation: (i) strong segregation in the case of $\chi N \geq 100$, i.e., energetic factors dominate; (ii) intermediate

segregation with $\chi N \sim 10-100$, i.e., energetic and enthalpic factors are in a delicate balance; and (iii) weak segregation $\chi N \sim 10$. Below the weak segregation limit, BCPs are in the so called disordered region. In this case, entropic factors dominate and the BCP exists in a homogenous state.^[164] As it can be envisaged, at very low molar masses and/or high temperatures, BCPs can enter the disordered state and *vice versa*.

While considering enthalpic-entropic contributions, one should keep in mind that the phase state is primarily governed by enthalpic and entropic factors^[154] that together constitute Gibbs free energy (Eq. 2.2):

$$\Delta G = \Delta H - T\Delta S \quad (2.2)$$

An assembly of molecular configurations that sum up to produce the minimum overall Gibbs free energy represent the equilibrium condition in a BCP melt.^[164-165]

Morphologies Equilibrium morphologies of a di-BCP are depicted on Figure 2.8 bottom. There is a range of nanostructures from body centered cubic (BCC) to lamellar and gyroids, as explained by Bates and Fredrickson in 1999.^[3] If f_A is equal to f_B , a lamellar structure will be observed only if one is in the ordered region which is depicted in the theoretical diagram on Figure 2.8 top. Lamellae (L) is the phase in which flat layers alternate whereas in the cylindrical (C) case, one of the blocks is shorter and this minority component arranges as cylinders on a hexagonal lattice. The phase between lamellae and cylinders is called gyroid (G) which is an interesting type, basically exhibiting a more complex morphology.^[166]

Thermodynamics Considering the thermodynamics of BCP phase separation, the primary factor is the interfacial area per chain, i.e., $\Sigma = A/n$, where A is the interfacial area and n is equal to the number of molecules. The interfacial energy (F_{int}) can be explained as follows with eq. 2.3:

$$\frac{F_{int}}{nk_bT} = \rho_0 a \left(\frac{\chi}{6}\right)^{1/2} \quad (2.3)$$

where ρ_0 is segment density, k_b is Boltzmann constant, k_bT is the thermal energy and a is the statistical segment length.

The total free energy of a lamellar phase is indeed the sum of interfacial energies and the energy of stretching as demonstrated in the following Equation 2.4:

$$\frac{F_{\text{int}}}{k_b T} = \Sigma \rho_0 A a \left(\frac{\chi}{6}\right)^{1/2} + \frac{\pi^2 N}{8 \Sigma^2 \rho_0^2 a^2} \quad (2.4)$$

In this equation, the first term is the interfacial energy and the second one stands for the total stretching. Obviously, interfacial energy favors small Σ whereas stretching energy favors large Σ as the eventual target is to obtain the minimized energy.^[167] In conclusion, both interfacial and segmental energies play important roles in determination of equilibrium energies of a BCP phase segregation. As reported by Segalman,^[168] the interactions can be more simply represented with the following Equation 2.5:

$$\frac{\Delta G_{\text{mix}}}{k_b T} = \frac{1}{N_A} \ln(f_A) + \frac{1}{N_B} \ln(f_B) + f_A f_B \chi \quad (2.5)$$

where ΔG_{mix} is the Gibbs free energy, N_A is the degree of polymerization of segment A, and N_B is the degree of polymerization of segment B.

Phase Transitions In a BCP system, order-order transitions (OOT) and order-disorder transitions (ODT) can be observed as it can be followed on Figure 2.8 top. An OOT takes place between two different ordered phases, whereas an ODT occurs when a BCP moves to a disordered state from one of the ordered states. For a BCP of a given molar mass and composition, these variations might be triggered by temperature and/or pressure. To exemplify, the literature includes several studies conducted with PS-*b*-PI system. For instance, Kimishima and co-workers investigated OOT between spheres and cylinders of PS-*b*-PI systems with a PS weight fraction of 0.20. Their observations revealed that the BCP adopted a cylindrical morphology up to 114.7 °C which switched to body centered cubic (bcc) spheres at 116.7 °C, as proved by small angle X-ray scattering (SAXS).^[169]

2.3.2 BCP Thin Films

The study of BCP thin films has gained significant interest mostly due to its potential in coating surfaces and creating nanostructures.^[170-171] Although there are several techniques to obtain thin films such as dip-coating^[172] and solvent-casting,^[173] spin-coating is by far the most commonly employed method in BCP studies as it gives homogenous films with high reproducibility.^[153] During spin-coating, a volatile solvent (generally toluene), which is used for the preparation of a solution of the polymer to be coated, is evaporated and a uniform polymer film is obtained. The total spinning time, spinning rate, the concentration of the applied solution,

and even the molar mass of polymer can have influence on the film thickness.^[174] Theoretically, longer spinning times, lower concentrations of the polymer solution, and higher spinning rates lead to thinner films. In general, spin-coating is capable of producing thin films of BCPs which can be utilized for morphological studies. In addition, silicon wafers are the most commonly employed substrates in BCP studies due to their high fidelity characteristics such as flatness. In some cases, though very rarely, glass and mica can also be utilized. It is noteworthy that if the total surface energy of the polymer is much greater than that of the substrate, dewetting will occur.^[175] The total energy of a BCP film can be expressed by Equation 2.6:^[176]

$$F = F_{A-B} + F_{\text{elastic}} + F_{\text{surface}} + F_{\text{substrate}} \quad (2.6)$$

A and B are the respective two blocks of the BCP. F_{A-B} is the interfacial energy between A and B segments while F_{elastic} stands for the configurational entropy of the chains. F_{surface} represents the energy at the free surface (air) and lastly $F_{\text{substrate}}$ represents that of the polymer-substrate interface. The first three parameters are intrinsic properties of the BCP whereas $F_{\text{substrate}}$ can be modified by adjusting the substrate features. If F_{surface} and $F_{\text{substrate}}$ are dominant, the substrate and the free surface govern the film orientation and several morphologies can be observed within the same film.^[155, 176] Consequently, the behaviour of BCPs in the form of thin films differ from those in solution or in bulk, which will be discussed in detail in the following sections.

2.3.2.1 Microdomain Orientation in BCP Thin Films

As previously mentioned, there are additional factors which define the phase segregation behaviour of BCPs when they are confined in films on solid substrates, i.e., interactions with the surface and the air.^[176-177] BCP microdomains can orient either in a parallel or perpendicular fashion when they are supported on substrates (Figure 2.9). In general, the segment which has the lowest interfacial energy^[178] will be attracted to the substrate and the one with the lowest surface energy^[171] will tend to face towards air, i.e., wets the surface. The wetting and domain orientation of a BCP film depend on the chemical/energetic nature of the substrate and the type and the magnitude of the interactions of the substrate with distinct blocks.^[155] BCP thin films can result in symmetrical wetting (parallel orientation), antisymmetrical wetting (perpendicular orientation), mixed morphologies and nonpreferential wetting (perpendicular orientation). In the case of symmetrical wetting, the film thickness (d) is equal to nL_0 where n is an integer and one block preferentially wets both the interface (substrate) and top layer (the surface) due to indistinguishable energies at the substrate/air interfaces. This situation can be observed in the case of free standing films^[179] and for the those which are confined between two identical

substrates.^[180] On the contrary, during asymmetrical wetting, d is equal to $(n+1/2)L_0$ where one block wets the surface and the other block faces towards air which can be observed in substrate supported thin films of BCPs^[181]. When the film thickness is commensurate with the wetting conditions, flat and featureless top layers will be observed for a given BCP. If the as-cast film thickness is incommensurate with the equilibrium thickness, holes and islands will form.^[176] This formation depends on the film thickness: In the symmetric wetting condition, holes form when $(n-0.5)L_0 < d < nL_0$ and islands form when $nL_0 < d < (n+0.5)L_0$. These cases are depicted on Figure 2.9. The height of a typical island and the depth of a typical hole is equal to one domain spacing (L_0).^[176] Depending on substrate properties and interactions, mixed morphologies can also be observed (Figure 2.9D). Nevertheless, parallel lamellar patterns are not very useful for nanopatterning applications since only one of the blocks is present on the surface. Thus, efforts have been made to induce perpendicular orientation of BCPs on solid supports.^[168] In perpendicular arrangement, both blocks are present and accessible on the uppermost layer. As this orientation was employed in the course of this work, in the following, more detail is dedicated on perpendicular microdomain orientation.

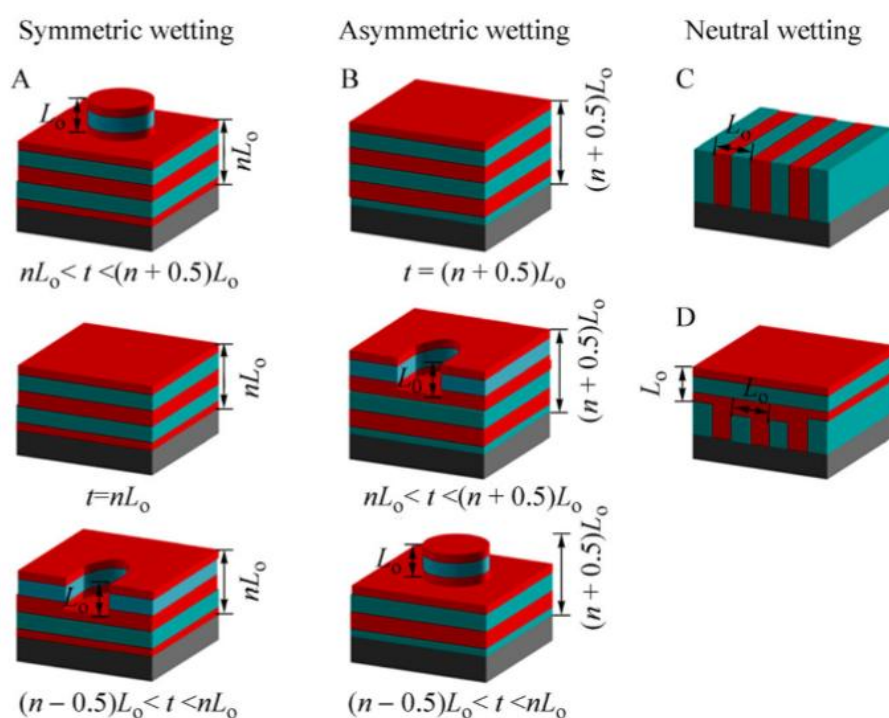


Figure 2.9 Representation of different orientations of diblock, lamellar forming BCP films. A) Parallel orientation with symmetrical wetting. B) Parallel orientation with antisymmetrical wetting. C) Neutral wetting. D) Neutral wetting-mixed morphology. Adapted with permission from ref [176]. Copyright © 2016, Chinese Chemical Society, Institute of Chemistry, Chinese Academy of Sciences and Springer-Verlag Berlin Heidelberg.

2.3.2.2 Methods to Induce Perpendicular Orientation and Alignment

Perpendicular Orientation: Relative to the Plane of the Substrate The perpendicular orientation is thermodynamically stable, which relieves entropic penalties caused by chain extension and compressions. Moreover, the free energy cost of having both blocks on the substrate is the lowest when the substrate is neutral and thus perpendicular orientation is favored.^[182] There are several methods to obtain perpendicular orientation in BCP thin films: (i) Control of the film thickness, (ii) chemical modification of the substrate to adjust substrate/polymer interactions, (iii) application of external fields such as electric, thermal, microwaves to induce long-range ordering with the desired orientation.

In majority of the work in block copolymer lithography, the film thickness (d) is almost equal to L_0 .^[183] When the thickness is commensurate with one domain spacing, it theoretically leads to the formation of perpendicularly arranged BCPs. When $d < L_0$, more complex structures can be observed as the polymer chains are compressed and confined to a certain thickness. Such systems can indeed adopt a morphology where perpendicular lamella is observed.^[153, 184] The opposite case, when the thickness is well above L_0 , also known as high aspect ratio films, is widely encountered in nanoporous template studies which makes use of external factors, e.g., electrical field to obtain perpendicular orientation.^{[183] [153]}

Chemical modification of substrates is a widely utilized technique to induce perpendicular arrangement of BCP microdomains in films. So far, for chemical modification and neutralization of substrates, self-assembled monolayers (SAMs),^[176] ethylene glycol,^[185] and alkylchlorosilane^[186] were used. Alkanethiol on gold and alkylsioxane on Si/SiO_x are the two types of SAMs.^[176] Alkanethiols are tethered on gold surfaces via thiol-gold linkages. Heier *et al.* presented a study about perpendicular orientation of PS-*b*-P2VP films on SAMs.^[187] However, SAMs of alkanethiols on gold substrates have limited stability in air at 100 °C^[188] and in BCP studies high temperatures might be required for thermal annealing. Also because this technique is only applicable for gold substrates, alternatives were required. At this point, there exists the reaction of chlorosilane with the native oxide layer of the Si substrate which results in SAMs on Si substrates. Though this method offers higher stability as compared to its previous analogue, it is still challenging in terms of reproducibility as the properties of SAMs are highly affected by deposition conditions, i.e., humidity and temperature.^[176]

In this context, a more popular technique is the use of statistical (random) copolymer to create a neutral layer for the separate segments of a given BCP. The statistical copolymer (StCP) is made up of the two (or more) monomers that comprise the distinct blocks of the BCP which will be coated as the second layer. Additionally, StCP is OH-terminated, which enables its grafting to the

Methods to Induce Perpendicular Orientation and Alignment

Si substrate. The presence of this layer equalizes interfacial energies for both blocks of the BCP and also prevents dewetting. This versatile method was first reported by Mansky *et al.* in 1997.^[189] The molar mass and the composition of the StCP can be adjusted during synthesis. In some reports, instead of endgrafting via the terminal -OH, side chain grafting was achieved by introduction of hydroxyethyl methacrylate (HEMA) as a third comonomer into the backbone.^[190-191] Furthermore, since this method was applicable only to substrates which bear an oxide layer, crosslinked mats were created by incorporation of crosslinkable units (e.g., azidomethylstyrene (AMS), benzocyclobutene (BCB), glycidyl methacrylate (GMA)) into the random copolymer so as to make it a generalized approach.^[192-197] When copolymerization of a monomer pair is challenging, blends of -OH terminated homopolymers can be employed instead of a random copolymer.^[198]

Though it was first synthesized by free radical polymerization,^[199] It is advantageous to synthesize the neutralizing StCPs via RDRP protocols which renders it possible to tune the molar mass and the composition while having narrow polydispersities.^[189] As molar masses and the composition of the random copolymer were shown to effect the orientation and perpendicular window of the BCP,^[190, 196, 200-201] it is beneficial to choose RDRP methods for the synthesis. So far, in terms of RDRP protocols, p(*S-r*-MMA) was synthesized by NMP,^[189-190, 196, 201-202] RAFT,^[203-204] ATRP,^[205] and ARGET ATRP.^[200, 206] Figure 2.10 collectively shows the structures of the random copolymers utilized in the literature. 5A depicts the structure of the StCP from the seminal work of Mansky *et al.*^[189] 5B, 5C and 5I show the cases where -OH group is on the backbone instead of at the end of the chain. 5G, 5D, and 5E are particularly useful in creating crosslinked mats. In the aforementioned seminal work of Mansky *et al.*, it was reported that with styrene fraction of 0.50-0.65 in the random copolymer ($M_n \sim 10\,000\text{ g mol}^{-1}$) layer, perpendicular orientation of the BCP microdomains were observed.^[189]

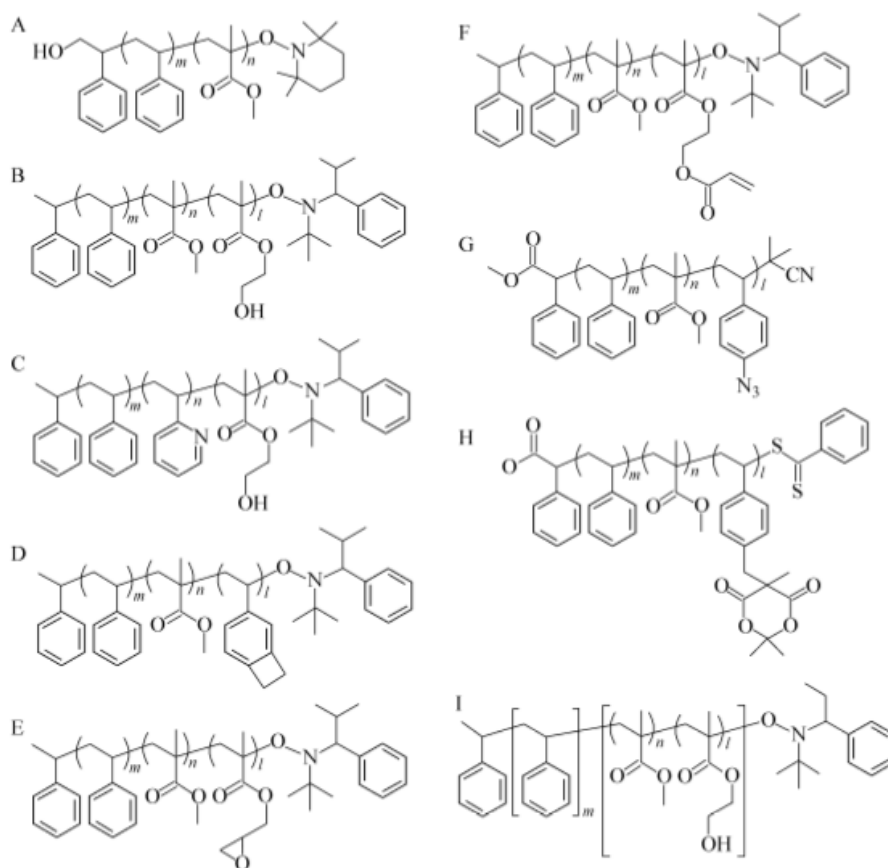


Figure 2.10 Chemical structures of various random copolymers in the literature. Adapted with permission from ref [176]. Copyright © 2016, Chinese Chemical Society, Institute of Chemistry, Chinese Academy of Sciences and Springer-Verlag Berlin Heidelberg.

Han *et al.* reported on the effects of the composition of the random copolymer and orientation of the upcoming PMMA-*b*-PS layer which is depicted on Figure 2.11 for a symmetrical PMMA-*b*-PS.^[190] It was found that for the symmetrical PMMA-*b*-PS with an overall molar mass of 104 kg mol⁻¹, a random copolymer layer with styrene mole fractions 0.45-0.57 was the range to obtain perpendicular microdomain orientation of the BCP film with 45 nm thickness. In the case of styrene fraction of 0.55, for instance, M_n of the StCP was 5400 g mol⁻¹ and the thickness of the layer was 5.4 nm which succeeded in perpendicular orientation (Figure 2.11). In 2015, Perego *et al.* performed a more detailed study about -OH terminated random copolymers of MMA and styrene. They observed that when the thickness of the random copolymer layer is more than 5-6 nm, a perpendicular orientation was always achieved due to efficient decoupling of the BCP layer with the Si substrate. However, if the thickness of the first layer is lower than 5 nm, neutralization highly depends on the molar mass of the StCP. Particularly, for a random copolymer of M_n 1700 g mol⁻¹, a 2 nm layer is sufficient to promote perpendicular

arrangement.^[200] Some results of their work are illustrated on Figure 2.12. Random copolymers with molar masses ranging from 1700-69 000 g mol⁻¹ were utilized as the first layer and a cylinder forming PMMA-*b*-PS with M_n of 67100 g mol⁻¹ and a styrene fraction of 0.70 was used as the second layer. On fig 2.12, it is shown that with a StCP of M_n 1700 g mol⁻¹, a 2 nm thickness is successful to induce perpendicular cylinders whereas in the case of StCP of M_n 3400 g mol⁻¹, 3.2 nm is the critical value to obtain the same orientation.^[200]

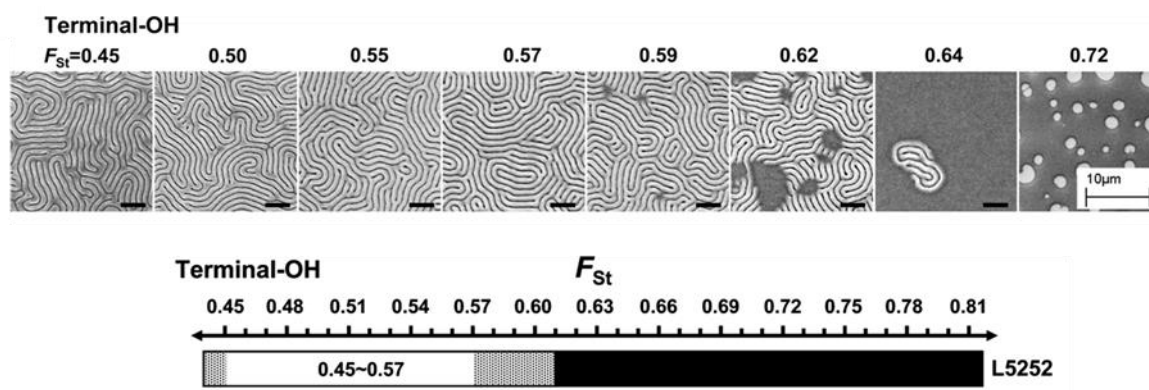


Figure 2.11 SEM images of a self-assembled, 45 nm thick, symmetrical PMMA-*b*-PS (52-52 kg mol⁻¹) film coated on OH-terminated random copolymer with different mole fractions ($F_{St} = 0.45-0.72$) (Top). Perpendicular window of a random copolymer layer bearing terminal-OH for PMMA-*b*-PS (52-52 kg mol⁻¹) (Bottom). Scale bar is 200 nm. The gray region represents mixed orientation and the black region represents parallel orientation. Adapted with permission from ref [190]. Copyright © 2008, American Chemical Society.

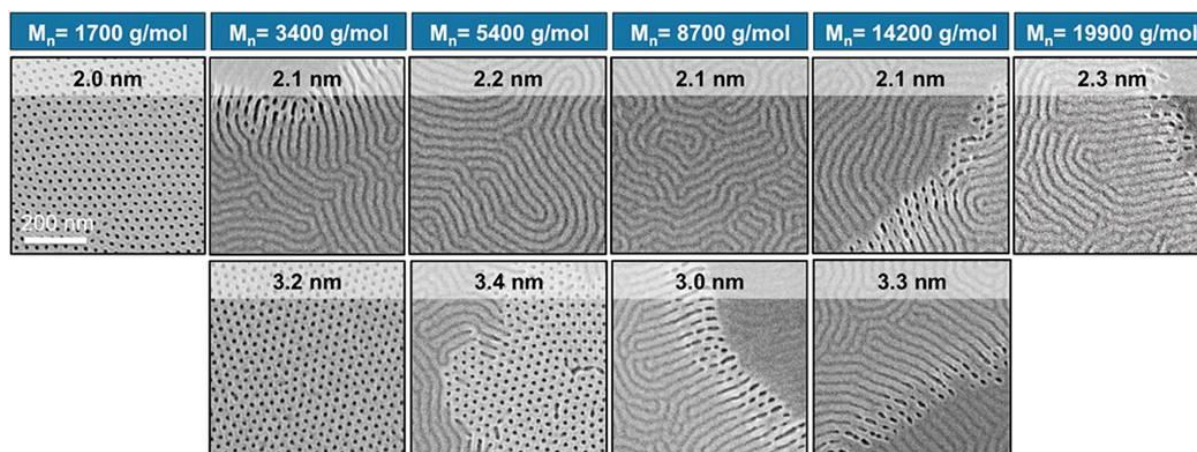


Figure 2.12 SEM images demonstrating the evolution of the nanodomain orientation in BCP films deposited on top of a ~2 nm (top) and ~3 nm (bottom) thick StCP layer with different molar masses. Adapted with permission from ref [200]. Copyright © 2015, American Chemical Society.

It should be noted that parallel cylinders resemble perpendicular lamellar orientation from the top view as depicted on Figure 2.13.^[168] Related to this, on Figure 2.12, both parallel and perpendicular orientation of cylinders are observed which should not be misinterpreted. When cylinders orient parallel to the substrate, a similar visual result is obtained as the case of perpendicular lamellar morphology.



Figure 2.13 Schematic illustration of parallel orientation of a cylinder forming BCP (Left), perpendicular orientation of cylinders (Right). Adapted with permission from ref [168]. Copyright © 2005 Elsevier B.V. All rights reserved.

In 2011, Kim *et al.* broadened the random copolymer technique to a range of substrates by treating them first with dopamine and secondly grafting poly(MMA-*co*-Sty)-OH onto the dopamine modified substrates. By doing this, they achieved perpendicular orientation of PMMA-*b*-PS on gold, Teflon and graphene planes.^[207] Apart from the listed techniques, electric field application is also a well-utilized method to obtain perpendicular arrangement.^[175, 208] Moreover, graphoepitaxy, soft lithography that makes use of a PDMS stamp, and shear alignment are some of the other sophisticated methods employed to align BCP microdomains vertically on substrates. For detailed information, readers are redirected to an excellent review by I. W. Hamley.^[175] *Alignment: The In-Plane Directionality* BCP films are mostly used after an annealing step that induces/enhances the alignment of microdomains.^[153, 183] This step increases the mobility of polymer chains and hence minimizes the non-equilibrium effects via which the film reaches its final morphology. The most common techniques for annealing are thermal and solvent annealing.^[153] During thermal annealing, the film is kept above the glass transition temperature of both blocks but below the decomposition temperature typically under vacuum or inert atmosphere for a sufficient amount of time. This technique is ubiquitous due to simple handling and is also useful in terms of removing residual solvents. However, it was found that for high molar mass polymers and for those of complex architectures, chain diffusion is slow and thus thermal annealing is not very feasible.^[209] Furthermore, some polymers have T_g values close to degradation temperature or they undergo crosslinking at high temperatures.^[210] Nevertheless, there are alternative techniques, the most common of which is solvent annealing.

In solvent annealing, the film absorbs solvent introduced as vapour in the medium. The solvent vapour behaves as a plasticizer that reduces the T_g of the blocks and thus gives mobility to the chains at RT. Many groups reported on long range ordering by this method.^[210-213] For example, Kim and co-workers demonstrated that solvent vapor treatment on cylinder forming PS-*b*-PEO resulted in highly ordered, nearly defect free cylinders.^[211] In solvent annealing, the choice of solvent is very critical. It can be chosen selectively to one block or to both blocks. In a PMMA-*b*-PS system for example, acetone is strongly PMMA selective, chloroform is slightly PMMA selective, toluene is slightly PS selective, and lastly carbon disulfide is highly PS selective.^[214] Solvent annealing is a mild method, however there exists no standard setup on the market for this treatment. Duration of annealing and the subsequent drying process are also important yet not simple to Figure out. With different solvent evaporation rates, different structures can be observed.^[215] Hence, with regards to the apparatus and the whole process, solvent vapour treatment is not as straightforward as thermal annealing. Moreover, an interesting approach is to incorporate homopolymers and blends into BCP domain and use these blends to induce self-assembly.^[216] Chevalier *et al.* reported that if the added homopolymer has a smaller molecular weight than its counterpart existing in the BCP, it is more uniformly distributed in the self-assembled structure. However, if it has a higher molecular weight, it increases the periodicity of the whole nanostructure. It was also demonstrated that despite high polydispersities, blending improved the self-assembly of PMMA-*b*-PS.^[216]

Microwave (MW) annealing is also a practical technique for BCP microdomain alignment, as depicted on Figure 2.14a.^[217-218] Another well-known technique is directed self assembly (DSA) which makes use of a lithographically created prepatter to align BCP microdomains.^[153, 183] A detailed insight into DSA related improvements were given in a perspective article.^[1]

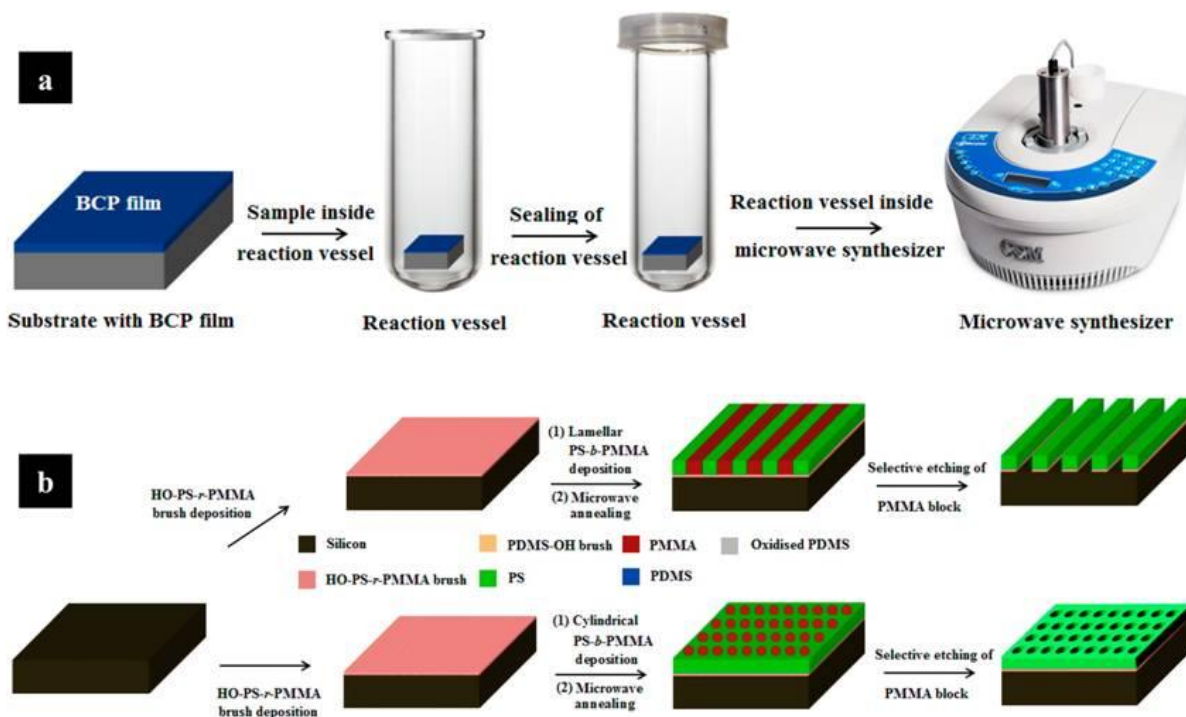


Figure 2.14 a) Demonstration of placing a BCP coated substrate into a MW system. b) Representation of an exemplary surface neutralization with OH-terminated random copolymer followed by BCP coating, annealing, and successive selective etching of PMMA block. Adapted with permission from ref [218]. Copyright © 2013 American Chemical Society.

2.3.2.3 Techniques to Analyze BCP Thin Films

The most widely employed method to characterize BCP film morphologies is atomic force microscopy (AFM). Since this technique also stands as the most crucial tool in the presented dissertation, it will be introduced separately in Section 2.4. Scanning electron microscopy (SEM) is also utilized in this context.^[218-220] However, AFM offers some advantages over SEM which will also be mentioned in section 2.4.2.5. In general, SEM is sufficient to observe a surface but transmission electron spectroscopy (TEM)^[221] is also used in BCP studies, for greater resolution or higher magnification. In both cases, staining one of the blocks might be needed to induce contrast between the blocks. Osmium tetroxide (OsO_4) and ruthenium tetroxide (RuO_4) are widely used staining agents.^[222-225] Since OsO_4 and RuO_4 are extremely toxic, metal salts such as AgNO_3 and KCl were also suggested as staining chemicals.^[223] Removing one block selectively also creates the required contrast for characterization.^[200]

Small Angle X-Ray Scattering (SAXS)

Measurement of the intensity of the scattered neutrons or X-rays give density profiles normal to the surface with Å resolution.^[175, 226] X-ray reflectivity^[227] depends on variations in electron density whereas neutron scattering depends on variations on neutron scattering length density. Small-angle X-ray scattering (SAXS) and small-angle neutron scattering (SANS) can be applied on bulk BCP samples while grazing incidence SAXS (GISAXS) and grazing incidence SANS (GISANS) can be used to probe the lateral structure of a BCP film.^[175] Furthermore, GISAXS is performed at synchrotron sources and produces fast results while GISANS can be performed at neutron sources. Both techniques, more importantly GISAXS, are gaining significance in BCP film analysis.^[175] A brief information about SAXS will be given in the subsequent section. Density profiles that can be obtained via X-ray or neutron reflectivities can also be achieved by secondary ion mass spectrometry (SIMS).^[175] Lastly, optical microscopy^[228] for imaging hole and island formations, ellipsometry^[229] for thickness measurements, and DSC to observe distinct T_g values of each segment of a phase segregating BCP^[10, 230] are also applicable characterization techniques in BCP studies.

2.3.2.3.1 Small-Angle X-Ray Scattering (SAXS)

Small-angle scattering (SAS) is a robust technique for characterization of nanostructures formed by self-assembly of BCPs in melt, in solution and in the form of crystals.^[231] One can use X-rays (SAXS) or thermal neutrons (SANS) as the source of radiation. SANS is offering the advantage of high contrast or labelling of specific regions by isotope exchange, i.e., substitution of hydrogen with deuterium. However, SAXS has the advantage of being measurable in the laboratory. Additionally, synchrotron SAXS permits rapid time resolved experiments, which are essential in probing dynamic processes.^[231] SAXS is a well-established technique for structural analysis of matter in submicrometer range.^[232] It is particularly useful for morphological characterization in BCP systems. Guinier & Fournet were the first to describe the theory of SAXS in 1955.^[233] During a SAXS experiment, a primary beam of X-rays is used to irradiate a sample. Due to fluctuations in electron density in the material, some of the X-rays are scattered and the scattering intensity I is detected as a function of either the scattering angle 2θ or the magnitude of the scattering vector:

$$q = (4\pi/\lambda)\sin\theta \quad (2.7)$$

where λ is the wavelength.^[232] A basic schematical setup of SAXS is given on Figure 2.15. As SAXS measures spatial electron density differences, it is a suitable method to analyze multiphase systems, e.g., particle dispersions,^[234] porous solids,^[235] and proteins.^[236]

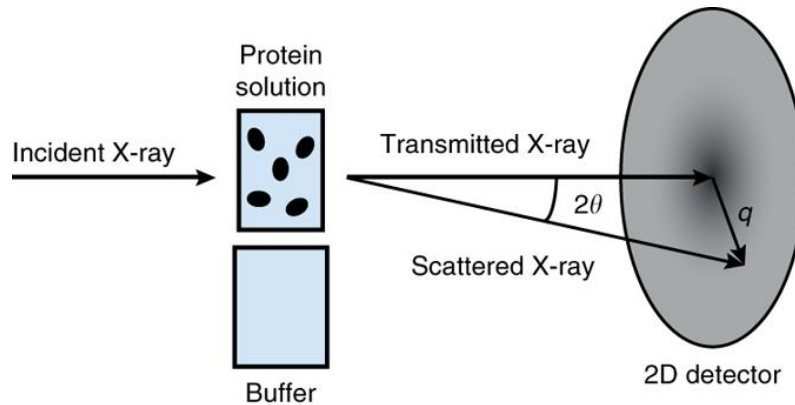


Figure 2.15 A basic setup of SAXS. Adapted with permission from ref [237]. Copyright © 2014 Nature Publishing Group.

Through SAXS, one can typically retrieve for instance particle size distribution, solid density, and molar mass of the material of interest.^[232] SAXS is largely utilized in characterization of BCPs.^[10, 238-241] Table 2.1 summarizes the positions of the peaks of equilibrium structures of a BCP melt.

Table 2.1 Peak position of Bragg reflections for possible BCP structures. q is the scattering vector, q^* is the primary peak. Adapted with permission from ref [231]. Copyright © 2004 Elsevier Ltd. All rights reserved.

Structure	Ratio q/q^*
Lam	1, 2, 3, 4, 5, 6,...
Hex ($p6mm$)	1, $\sqrt{3}$, $\sqrt{4}$, $\sqrt{7}$, $\sqrt{9}$, $\sqrt{12}$, ...
BCC ($Im\bar{3}m$)	1, $\sqrt{2}$, $\sqrt{3}$, $\sqrt{4}$, $\sqrt{5}$, $\sqrt{6}$, ...
FCC ($Fm\bar{3}m$)	1, $\sqrt{4/3}$, $\sqrt{8/3}$, $\sqrt{11/3}$, $\sqrt{12/3}$, $\sqrt{16/3}$, ...
Gyr ($Ia\bar{3}d$)	1, $\sqrt{4/3}$, $\sqrt{7/3}$, $\sqrt{8/3}$, $\sqrt{10/3}$, $\sqrt{11/3}$, ...

From the resultant sequence of Bragg reflections, SAS can be used to detect the morphology of a given BCP. In strongly segregated samples, multiple orders of Bragg reflection are observed. For a BCP exhibiting lamellar structure, domain spacing can be calculated from eq. 2.8:

$$L_0 = 2\pi/q^* \quad (2.8)$$

On the other hand, for weakly segregated structures, only low orders of Bragg reflection are observed, which might not be sufficient for a full characterization. In that case, a complementary technique such as AFM can be used to identify the morphology.^[231] Shear alignment of a sample can also increase ordering and might lead to a better identification of the peaks.^[242]

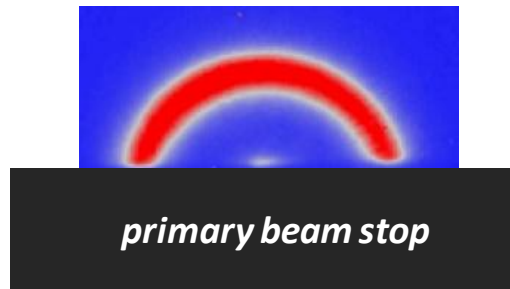


Figure 2.16 Typical 2D scattering diagram of BCPs applied listed in Chapters 3 and 4.

In Figure 2.16, one can see an experimental 2D scattering diagram of one of the BCP samples. Here typical characteristics of the system used for the experiments (Hecus S3-Micro from Hecus X-ray systems combined with a 2-D CCD detector from Photonic Science) has to be mentioned: The camera uses a horizontal block to stop the primary beam. While this system has the advantage of reducing parasitic scattering to an extremely low amount, the primary beam stop blocks the scattering in the lower half of the available space. Therefore, one can not see a full ring for an ordered structure, but only half of it. Additionally, the example shown in Figure 2.16 shows the well pronounced main ordering peak and the isotropic behaviour, justifying the latter use of radial averaged one dimensional scattering data (See Chapters 3 and 4).

2.3.2.3.2 Atomic Force Microscopy (AFM)

Atomic force microscopy (AFM), also known as scanning force microscopy (SFM), is a member of the scanning probe microscopy (SPM) family which basically makes use of a probe to investigate surface properties of materials with ultra-high resolution.^[243] This technique is principally based on interatomic forces and can produce images with a resolution down to 10^{-10} m sizes. AFM is non-destructive as compared to electron microscope and is widely utilized for characterization in polymer science.^[244] As AFM was extensively used for BCP film characterization in the current dissertation, it will be discussed in detail.

Brief History of AFM The precursor of AFM is scanning tunnelling microscopy (STM) whose preliminary invention was made by Binnig and Rohrer in 1981 at IBM Zurich research laboratories^[245] and further developed by the same researchers together with Weibel and Gerber.^[245-246] The birth of STM occurred when the scientists observed a current between a Pt sample and a tungsten tip, combined with the ability of the tip to scan against the surface.^[247] The invention of STM was also the start of SPM techniques which are based on almost all possible detectable interactions between a tip and a surface.^[247] As it made visualization of surface atoms possible in real space, STM was definitely a breakthrough in science.^[248] Binnig and Rohrer were awarded The Noble Prize in Physics in 1986 for their design of STM.

Despite the overwhelming advances that it created in surface science, STM had some drawbacks as well. The technique basically required 'conductive materials' as it works with the principle of a tunnelling current between the tip and the sample. There were some debates, however, about the possibility of additional forces acting between the tip and the sample when the distance between them was small enough.^[248] Five years after the invention of STM, AFM was eventually invented by Binnig, Quate and Gerber in 1986 proving the presence of additional forces between a tip and a surface.^[249] Unlike STM, which was limited to metals and semiconductors and even required ultra high vacuum (UHV) conditions in many cases, AFM was now able to probe at atomic scale under ambient conditions.^[248]

Working Principle of AFM In a general AFM setup (Figure 2.17), a cantilever gets in contact with the surface through a tiny tip mounted at its front. The cantilever moves with high accuracy by the control of a piezoelectric element and scans the sample. Alternatively, the sample can also be moved with a piezo element. In the AFM setup, there also exists a laser beam exposed onto the back of the cantilever. During scanning, the cantilever deflects depending on the tip-sample interactions and these motions can be monitored owing to the laser's reflection.^[248, 250] Indeed, a laser beam is reflected from the cantilever onto a photodiode (generally split into 4 parts) which amplifies the deflections of the cantilever. The tip-surface

Atomic Force Microscopy (AFM)

distance is controlled by a feedback system to keep the interactions at a fixed value. These feedback signals, collected from each and every single point measured on a 2D area, are implemented to form a 3D surface topography which is eventually obtained as an image.

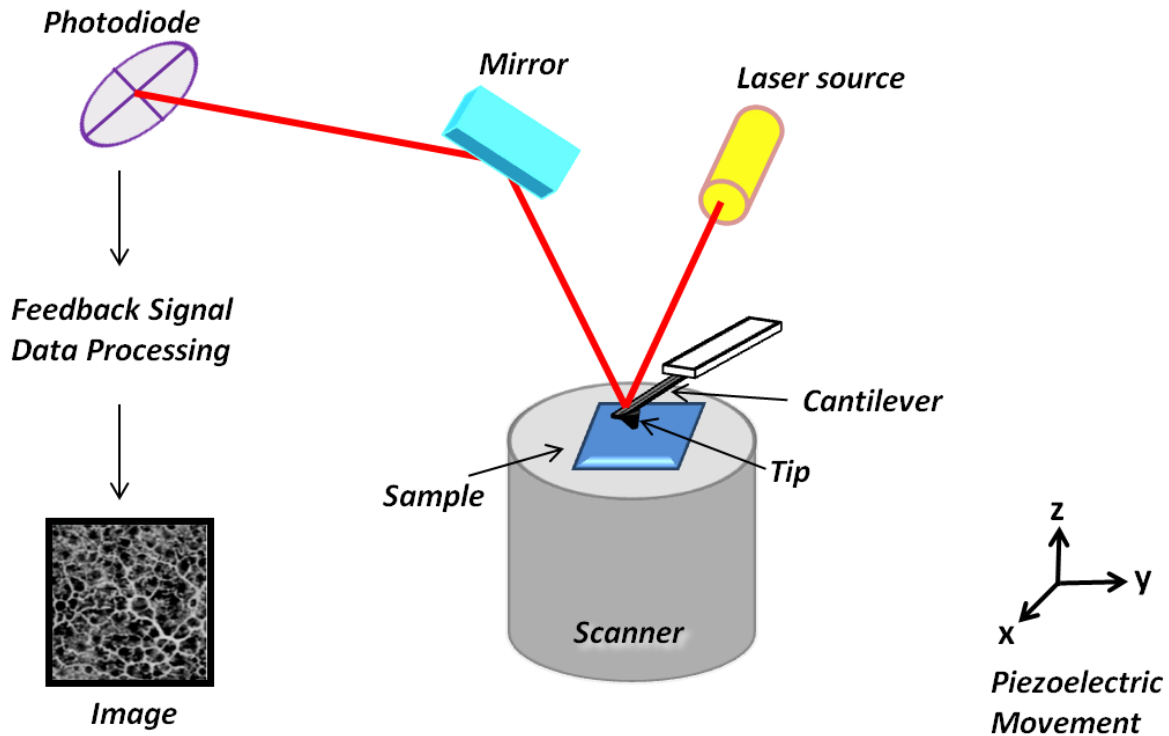


Figure 2.17 Schematic representation of a typical AFM setup.

AFM Imaging Modes In general, AFM operation is classified with 3 main modes which are namely contact, non-contact and tapping modes (Figure 2.18). In this categorization, presence of attractive (Van der Waals) and repulsive forces play an important role. For example, if the force between the cantilever tip and the surface is always repulsive and the tip is steadily in touch with the sample, the operation type is called 'contact mode'. On the contrary, if the tip senses only attractive forces and is never in direct contact with the surface, the system operates in called 'non-contact mode'. In the third case, the tip experiences both attractive and repulsive forces which is called 'tapping mode', also known as 'intermittent contact mode'.^[243] The first developed method was contact mode (static mode).^[249] During analysis by contact mode, cantilever deflection and hence the force applied onto the sample are always kept constant and images are processed by the vertical movement of piezo element.^[243] The main drawback of contact mode is the possibility to damage both the cantilever tip and the sample due to dragging

the probe all over the surface. Afterwards, tapping mode evolved which was able to overcome the disadvantages of contact mode.^[251-252] In this mode, the cantilever initially oscillates freely. Once the tip hits the surface, the amplitude of the oscillation is greatly reduced. To keep the oscillation amplitude constant, the feedback signal is recorded and is subsequently processed into an image.^[243] Contact and tapping modes are the most commonly employed techniques. In non-contact mode, on the other hand, the tip is never in touch with the surface and the cantilever can therefore not be damaged. In that case, the tip is typically 50-150 Å above the sample and topographical images can be obtained.^[253] This mode is useful to detect electrical, magnetic, and/or atomic forces of a sample. However, in this mode, image artifacts can appear, for instance due to a water layer covering the surface of the sample of interest.

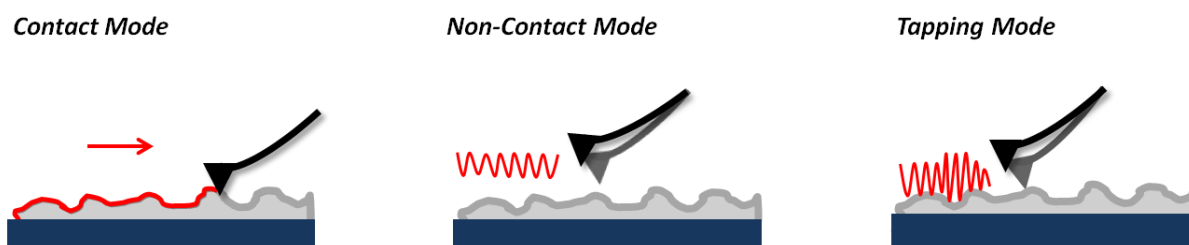


Figure 2.18 Schematic representation of the three modes of AFM: contact, non-contact and tapping modes.

AFM Cantilevers AFM cantilevers are produced by lithographical techniques with various force constants which can be chosen depending on the materials to be analyzed (hard or soft materials, e.g., proteins and polymers).^[254] They are generally made of silicon, silicon nitride, and quartz-like materials.^[255] These tips are available in many shapes, the standard one of which is pyramidal (20-30 nm). Sharper tips give higher resolution whereas they are more fragile and give more damage to cells, for instance in the biological applications.^[256-257] Commercial cantilevers have a wide range of spring constants, i.e. between 0.006-200 N/m. For very fragile samples, a spring constant of < 0.2 N/m would be appropriate whereas a stiffer cantilever of approximately 45 N/m is required during tapping mode under ambient conditions to eliminate noise.^[257] Modifications of cantilevers are also encountered with proteins or cells,^[257] for particular studies; backside or overall coating with metals or diamond, for example for creating harder, better reflecting or chemically more resistant probes.^[255]

Atomic Force Microscopy (AFM)

Application Areas of AFM AFM has applications in many fields ranging from biosystems to engineering.^[253] In biological sciences, one can utilize AFM to study DNA, DNA-protein assemblies, protein-protein interactions and enzyme interactions.^[243] Due to high resolution in lipid environment, AFM is also very useful to investigate lipid supported films or lipid membranes. Apart from these, it is very important in cell biology for imaging, binding force measurements, micromanipulation and materials property investigations. Reliable analysis can be done by AFM on metallic surfaces and to observe microstructures including determination of hardness, elasticity, and surface compositions.^[253] Furthermore, AFM played a big role in the invention of dip-pen nanolithography (DPN) which makes use of an AFM tip to pattern surfaces by essentially dipping the tip in an ink.^[5] More sophisticated applications can be encountered in the literature.^[253]

Comparison of AFM with Scanning Electron Microscopy (SEM) Although SEM is also largely used for imaging various materials at micro and nanoscale and has a longer history (invented in 1930s), AFM offers several advantages over the electron microscope. These include 3D analysis in addition to 2D measurements, no special requirement for sample preparation, recovery of the substrates after analysis (non-destructive method), possibility of measurements in ambient and liquid environment unlike vacuum environment that is crucial for SEM.^[253] Moreover, AFM is not only an imaging method but is also utilized for modification of substrates. Although SEM can image larger areas and reach greater depths, yet many signals are emitted during SEM analysis including X-rays and secondary electrons which can make it difficult to analyze the composition of materials. Thus, AFM is more reliable to determine surface compositions.^[258] There occurs no radiation damage to the samples during AFM unlike observed in SEM. On the other hand, AFM is quite complex and external factors such as contamination can also be detected during a scan.^[244] In case of hysteresis of the piezoelectric element, software enhancements might also be required in the case of AFM.

2.3.3 Applications of Block Copolymers

BCP films have garnered particular attention in view of creating nanostructures with high registry and regularity. Due to providing access to length scales which are challenging to obtain via the traditional lithographical techniques, BCP thin films are used in many fields.^[168]

2.3.3.1 In Solid State

A paramount field of BCP applications is their use as templates in top-down fabrication.^[155] Classical microelectronics fabrication techniques rely on direct patterning of layers which are limited by several factors such as the wavelength of light in the case of optical lithography, difficulty in large area patterning in e-beam lithography, or costly apparatus.^[168] Self-assembled BCPs can however be used as lithographical masks as an inexpensive alternative.^[259] They can be used as templates to transfer patterns with highly uniform structures which are valuable in areas ranging from biochips to capacitors, quantum dots, and transistors.^[168] In this context, one block of the BCP is selectively removed via plasma, ozone or chemical means and used to transfer the pattern to an underlying substrate via etching or deposition.^[155] The first example was reported by Mansky *et al.*^[260] Park *et al.* showed an example of a BCP utilized as an etch mask to transfer a pattern into an underlying semiconductor substrate.^[261] An exemplary selective etching process is depicted on Figure 2.14b. Secondly, BCPs can be used as membranes which are useful in dialysis, osmosis and filtration.^[262-263] The industrially well-established non-solvent induced phase separation (NIPS) was applied to BCP systems for creating membranes of PS-*b*-P4VP.^[264] BCPs also find applications in other areas such as photonic crystals,^[265] solar cells,^[266] blend compatibilizers^[267] and composite materials.^[268] Moreover, synthesis of nanoparticles from BCPs is an effective way to control the placement, shape and size distribution of the nanoparticles. Indeed, utilizing BCP films as a means of creating inorganic particles is well-established.^[269] This synthesis can be achieved by binding the inorganic on the BCP either before or after self-assembly of the BCP.^[168] For instance, Morkved *et al.* demonstrated self-assembly of gold islands on BCP films.^[270] Lopes *et al.* also reported on hierarchical self-assembly of metal nanostructures on BCP scaffolds.^[271] Several other reports have demonstrated that BCPs can be employed to create and/or distribute nanometer-sized magnetic,^[269] metallic^[272-274] and ceramic^[275-276] structures. More examples can be encountered in the literature.

2.3.3.2 In Solution

BCPs also offer a range of applications when considered in solution. Their self-assembly in selective solvents has been used for the formation of micelles of various geometries,^[262] which are versatile vehicles for drug delivery, for instance. A hydrophobic core can solubilize water-insoluble drugs and both the core and the corona of the BCP can be fine tuned to optimize drug uptake and release.^[262] In another case, self-assembled nanoparticles of BCPs with internal phase separation were assessed for controlled release.^[277] In this work, Hawker and co-workers synthesized poly(allyl glycidyl ether)-*b*-polylactide (PAGE-*b*-PLA), modified it with click reactions and showed controlled release via degradation of PLA. Furthermore, BCPs are also playing important roles as nanoreactors. On Figure 2.19, a work of van Hest and coworkers is depicted.^[278] In this report, a mixture of PEG-*b*-PS and PEG-*b*-PSBA (BA: boronic acid) self-assemble and create a polymersome or nanovesicle which can become porous upon addition of sugar or base. This nanoreactor is used to host *Candida Antarctica* Lipase (CALB) to catalyze its substrates which can enter the polymersome from the created pores.^[278]

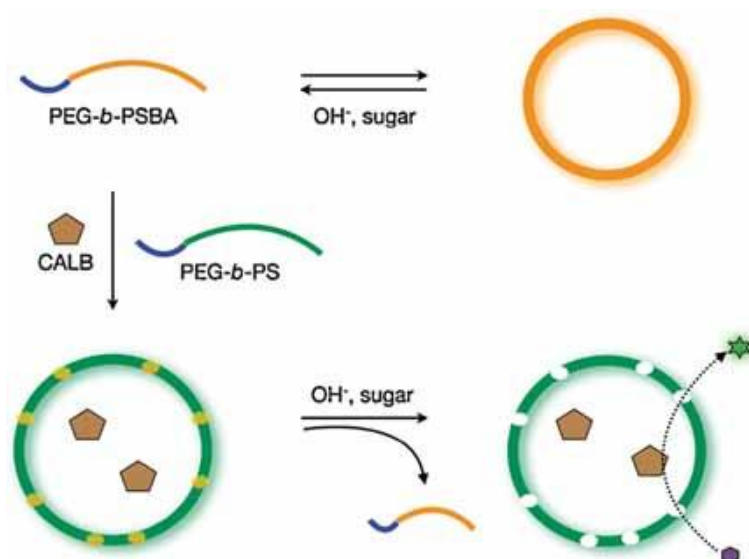


Figure 2.19 Schematic representation of stimuli responsive bioreactors with a permeable membrane responsive to sugar and base. Adapted with permission from ref [278]. Copyright © 2009 WILEY-VCH Verlag GmbH & Co. KGaA, Weinheim.

BCPs are also used for solution templating in which a BCP-metal hybrid material is first created and then the BCP is subsequently removed that allows the morphology of the BCP to be transferred to the metal species. In other words, BCP is used as a sacrificial template to create metal clusters organized in certain shapes.^[262] For more detailed information on BCP application areas, the readers are redirected to the review article of Manners.^[262]

2.3.3.3 BCP Thin Films as Chemical Patterning Platforms

Patterning and precise immobilization of (bio)molecules at highly reduced length scales is currently of interest. Apart from being mostly in the focus in electronics industry, BCP films can also be utilized in this field. Introduction of one or multiple functionalities at the end or into the backbone of a BCP will theoretically lead to the expression of these moieties at the surface of the films which can be used as tethering points on the nanostructured BCP platform. Only several examples utilizing BCPs as chemical patterning platforms appeared in the literature so far. First of all, Reynhout *et al.* synthesized a cylinder forming, biotin end-capped PS-*b*-PEO in 2013.^[8] They proved the expression of biotin moieties upon dipping a BCP film into a streptavidin solution: a regular arrangement of streptavidin on the film could be visualized by AFM. In 2014, Campos and coworkers reported a study^[9] in which they utilized the same type of BCP as Reynhout *et al.* In addition, their system possessed a crosslinking unit which rendered their films stable in organic solvents. Furthermore, by photopatterning they created hierarchical structures, i.e. both nano and micrometric features could be produced on the same substrate. Besides the non-covalent biotin-streptavidin pair, researchers also sought covalent attachment on BCP films. For example, in 2014, Lynn and co-workers reported amine reactivity placement on an azlactone containing BCP film whose underlying nanostructure could be preserved upon attachment as depicted on Figure 2.20. This work can be regarded as the first example of a reactive BCP platform for precise grafting purposes. Earlier, Stadermann *et al.*^[10] synthesized acid and alkyne functionalized BCPs and showed preservation of phase-segregating property upon introduction of these functional groups, yet no patterned immobilization was performed. In another study, the same group equipped BCPs with photolabile protected amino groups.^[11] Apart from these examples, Chae *et al.* showed lamellar formation of a PMMA-*b*-PFPPMA after being coupled with quantum dots and organic fluorophores which was also an example of conservation of self-assembly property of BCPs.^[279] The main aim of the present dissertation falls in this category: our efforts will be further discussed in Chapters 3 and 4.

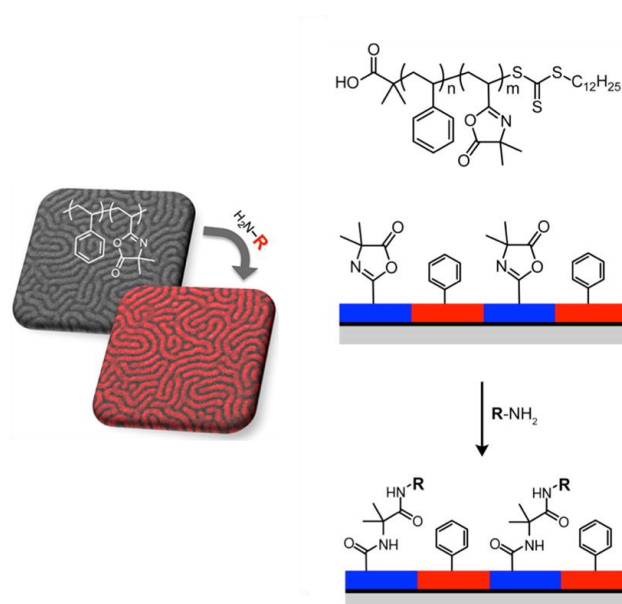
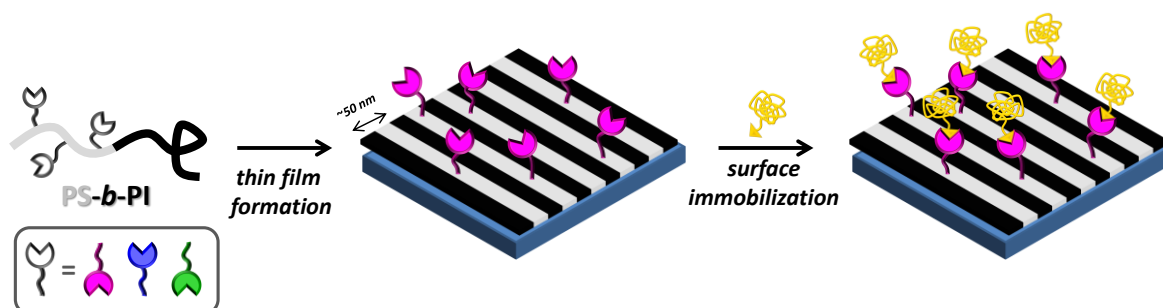


Figure 2.20 Schematic representation of the process of amine patterning on a PS-*b*-PVDMA film. Adapted with permission from ref [7]. Copyright © 2014 American Chemical Society.

3

Polystyrene-*block*-Polyisoprene (PS-*b*-PI) Films as Self-Assembled Reactive Platforms



In this project, SAXS and DSC measurements were conducted by Dr Nico Dingenouts and Helena Hoerig (Institute for Chemical Technology and Polymer Chemistry (ITCP), KIT), respectively. XPS measurements were performed by Vanessa Trouillet (Institute for Applied Materials – Energy Storage System (IAM-ESS), KIT). Dr Hartmut Gliemann (Institute of Functional Interfaces (IFG), KIT) is acknowledged for giving free access to AFM and Peter Krolla-Sidenstein (IFG, KIT) is thanked for giving extensive training and support on AFM.

3.1 Introduction

Chemical patterning in the sub-50 nm range is a difficult task and has been up-to-now been successfully addressed only by a few advanced methods, e.g., e-beam lithography,^[280-281] scanning near-field photolithography,^[282-283] dip-pen nanolithography.^[5, 280] These techniques are however costly in terms of required equipment and may suffer from long processing times in case of large-area patterning due to the serial character of top-down approaches. Another well-known technique is nanocontact printing which allows to pattern in sub-50 nm scale with high throughput.^[284] However, it is still challenging to adjust the distance between the nanostructures by this technique. Thus, there is still a great need for alternative methods.^[280] In that respect, strategies employing block copolymers (BCPs) have garnered significant attention in the last two to three decades. The ability of block copolymers to phase-separate and self-assemble into nanostructures frequently led experts to consider them as highly potent patterning/templating platforms in micro and nanotechnology.^[153, 285-286] It was also envisaged for ordering protein on surfaces.^[1, 184, 287] As extensively explained in section 2.3, the most studied BCP systems are of the linear AB type, which can exhibit various equilibrium structures, e.g., lamellae, cylinders, spheres. The segregation strength, which is proportional to the Flory-Huggins interaction parameter χ_{AB} and the overall degree of polymerization N , and the relative volume fractions of the two separate blocks ($f_A + f_B = 1$) are the two main parameters that control the microphase separation of a diblock copolymer in bulk.^[2-3, 259, 280, 288] However, when the block copolymers are processed in the form of thin films, additional factors come into play: The air/polymer and polymer/substrate interactions as well as the thickness of the films can alter the positioning of the blocks and consequently the morphology at the film surface.^[176] To date, the large majority of reports on the utilization of BCP nanostructures have focused on the so-called “block copolymer lithography” for the templating of inorganic structures for optics, electronics, or catalysis, besides a few other uses.^[159, 168, 289]

3.2 The Idea of BCP Films as Patterning Platforms

So far, Kumar and co-workers reported single-protein patterning by hydrophobic adsorption on PMMA-*b*-PS^[287] and Keddie and co-workers presented the same type of work on PS-*b*-PI films.^[184] The literature reveals some more examples of patterned molecular assemblies directed by BCPs.^[8, 271, 273, 290-292] The remarkable phase-segregating property of BCPs can be further exploited in order to align (bio)molecules in close proximity with each other in nanodimensions (5–50 nm) via introduction of functional moieties, which enables a higher level of control than simple adsorption. To elaborate more, a new chapter in this area is to

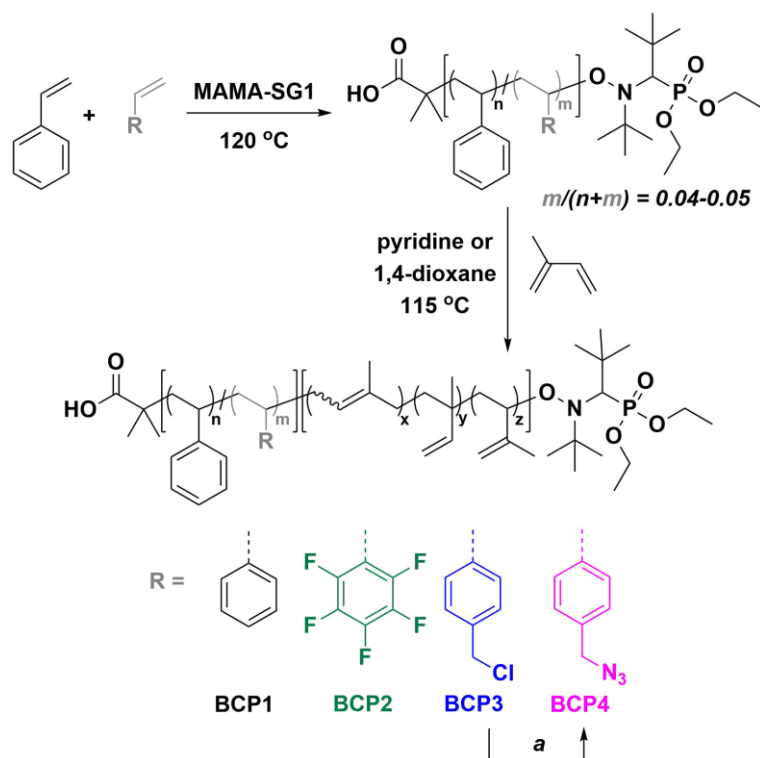
incorporate functional groups in the BCP structure. These functional moieties should be expressed at surface of the nanostructured thin films and act as anchoring points for (bio)molecules via chemical reactions. To date, only a handful of examples of this type can be encountered in the literature.^[7-9] For example, Lynn and co-workers reported amine patterning on a nanostructured BCP surface of which one block was entirely made of a functional amine-reactive monomer unit.^[7] Our idea is that it would presumably be a more versatile method to employ a well-known phase-segregating BCP system and introduce a functional monomer during the synthesis in an amount such that it is sufficient for functionalization, yet low enough not to perturb the phase behavior of the original parental system. By achieving this, every time one desires to incorporate a different functionality, it would potentially not be necessary to investigate phase separation conditions. Although some studies showed that small changes in structures can alter the morphologies and domain spacing,^[293-294] a few reports hinted at the fact that incorporation of a small percentage (< 10%) of functionalities into the polymer backbone or at its end may not influence the phase separation behavior to a considerable extent.^[9-11, 279, 295]

This Chapter of the present dissertation details an original investigation of a series of polystyrene-*block*-polyisoprene (PS-*b*-PI), a very well-known phase-segregating system,^[296-303] which have been modified with a variety of comonomers bearing a reactive group in the PS block. A range of styrenic derivatives can be either purchase or readily synthesized, while polyisoprene possesses internal double bonds which can potentially be employed as reactive handles. Our small set of functional PS-*b*-PI derivatives offers potential reactivity in ene reactions (in the PI block), nucleophilic substitution with halides, azide-alkyne 1,3-dipolar cycloaddition, and *para*-fluoro thiol reaction. Here, in addition to the synthesis and characterization of the BCPs, as well as the investigation of their self-assembly behavior, we present CuAAC variant as a preliminary and exemplary functionalization. The strategy applied in this part is demonstrated on the cover image of this Chapter.

3.3 Synthesis of Functional PS-*b*-PI Derivatives by NMP

Studies on PS-*b*-PI usually employ polymers obtained by anionic polymerization. Here, we have recourse to nitroxide-mediated polymerization (NMP) because radical polymerization is known to be tolerant to a wide range of functional moieties.^[27] Only one example of PS-*b*-PI made by NMP can be found in the literature, where Najafi-Mogaddam and Entezami used TEMPO as a controlling nitroxide derivative.^[304] However, BCPs with molar masses probably too low for phase separation were reported. Moreover, due to the low lability of the TEMPO-based alkoxyamine bond, high polymerization temperatures (125 °C) were required, yet with the

isoprene polymerization still proceeding slowly. Here, we employ SG1-mediated NMP as the nitroxide SG1 typically permits faster polymerizations and/or lower reaction temperatures. As our aim was to obtain surfaces displaying line patterns, a lamellae-forming system was targeted, i.e., a BCP with nearly equal block volume fractions. Furthermore, since we wanted to highlight the high capability of this approach to compete with other nanopatterning techniques, we aimed at a small domain size. A literature screening taught us that an overall molar mass close to 40 kg mol⁻¹ would produce sub-50 nm domains.^[184] When considering the synthesis of a di-BCP by sequential polymerization, one has to ask the question: which block should I synthesize first? In our case, either a polyisoprene or a polystyrene macroinitiator could be first synthesized. The former route may seem more logical to establish a library of PS-*b*-PI BCPs with various comonomers in the PS block and an identical PI block. From preliminary experiments, this route was found plausible. However, PI has a very low glass transition temperature (T_g) and consequently behave as a viscous oil, which was not found convenient to handle. We therefore synthesized a number of functional PS-SG1 macroinitiators, which were then used as macroinitiators for the NMP of isoprene. The general synthesis strategy for the set of functional PS-*b*-PIs is given in Scheme 3.1. The procedure was first established for plain PS-*b*-PI using MAMA-SG1 as the alkoxyamine initiator. The synthesis of PS-SG1 is classic in NMP: styrene and MAMA-SG1 are mixed, deoxygenated, and heated up to 120 °C. To maintain a high degree of livingness for the macroinitiator, monomer conversion was limited to 50%. PS-SG1 **MI1** with $M_n = 22$ kg mol⁻¹ and $\mathcal{D} = 1.1$ was first obtained (Figure 3.1A). **MI1** was subsequently chain extended with isoprene to the PS-*b*-PI block copolymer **BCP1**. For this step, we employed conditions similar to those reported for the synthesis of PI-SG1 by Nicolas and co-workers, where a benzyl-type SG1 alkoxyamine initiator (low molar mass mimic of PS-SG1) initiated the polymerization of isoprene at 115 °C in pyridine.^[305]



Scheme 3.1 Chemical structures of the PS-*b*-PI derivatives employed in the current study and corresponding synthetic route. (a) NaN_3 , DMF, RT.

A tailing in the low molar mass region was observed, which seems to indicate the presence of a fraction of non-reacted PS macroinitiator which was either “dead” after the first synthetic step or potentially extended only with a short segment of isoprene (Figure 3.1A). This distribution pattern was not seen in the study of Nicolas and co-workers, which is certainly due to the fact that a similar phenomenon occurring on a low molar mass initiator would lead to species not detectable in SEC. The presence of homopolymer should however not hamper phase separation but may only lead to domain size variations.^[306-307]

The same protocol was subsequently adapted to the synthesis of functional BCP derivatives by introducing 5 mol% of a functional styrene derivative in the synthesis of the PS macroinitiators, namely, vinylbenzyl chloride (VBC) or pentafluorostyrene (PFS) (Scheme 3.1). In all experiments we obtained polydispersities of about 1.1 (Figures 3.1B and 3.1C, Table 3.1). Using a functional derivative of the main comonomer theoretically favors simple statistical incorporation of functionality. Parallel to this, VBC exhibited an ideal behavior: A feed of 5 mol% resulted in 4.8 mol% incorporation in **MI3**. However, from a previous study^[308] and from our own experience, we knew that PFS reacts faster in its copolymerization with styrene. Therefore, to limit its concentration below 5 mol%, 3.2 mol% of PFS were introduced in the feed. While

styrene conversion was 55%, 67% of PFS polymerized. The corresponding macroinitiator **MI2** subsequently used to synthesize **BCP2** therefore contained 4 mol% PFS (Figures 3.1B, 9.1 and 9.2). As mentioned before, pyridine was used as a solvent for the synthesis of **BCP1** and **BCP4**. Pyridine is a basic solvent and a convenient medium for coordination with halogens and/or dehalogenation.^[309] Since **MI3** bears a labile chlorine atom, the synthesis of **BCP3** was performed in 1,4-dioxane, as it was reported as an alternative medium for this polymerization.^[310] To obtain **BCP4**, direct copolymerization of 4-azidomethyl styrene (AMS) was not feasible due its instability at high temperatures. Alternatively, **BCP4** originated from the azidation of **BCP3**, following a reported procedure (Scheme 3.1 and Figure 3.1C).^[311] Successful transformation was confirmed by ¹H NMR spectroscopy (Figure 9.3). All macromolecular data regarding the BCPs and their corresponding macroinitiators is compiled in Table 3.1. It is noteworthy that during chain extensions, conversion of isoprene was kept to a maximum of 10%, which obliged us to use large monomer-to-macroinitiator ratios. Indeed, we initially tried to employ lower ratios to obtain the desired chain lengths at 30% or 20% conversions, but significant shoulder formation in the high molar mass region appeared at conversions above 15% in both cases (Figure 3.2), which could be due to early termination reactions. In our optimized conditions, a slight shoulder is still present at high *M* although the conversion is only of approx. 10%.

Table 3.1 Characteristics of the polymers reported in the present study.

PS Macroinitiators				PS- <i>b</i> -PI Derivatives							
Name	$M_{n,SEC}^a$ kg mol ⁻¹	\bar{D}^a	%F ^b	Name	$M_{n,SEC}^a$ kg mol ⁻¹	\bar{D}^a	$M_{n,NMR}^b$ kg mol ⁻¹	$f_{PS}:f_{PI}$	T_g^c °C	$L_{0,SAXS}^d$ nm	$L_{0,AFM}^e$ nm
MI1	22.3	1.10	-	BCP1	57.7	1.36	44.5	0.46:0.54	-61.81/94.99	48.3	44.0
MI2	25.3	1.10	4.0	BCP2	61.9	1.32	47.3	0.50:0.50	-63.35/95.04	48.3	44.3
MI3	25.5	1.11	4.8	BCP3	61.8	1.36	49.4	0.47:0.53	-62.76/94.00	58.7	59.2
MI3	25.5	1.11	4.8	BCP4	63.5	1.33	49.4	0.47:0.53	-63.58/93.55	51.5	53.0

Values obtained by ^aSEC, ^bNMR, ^cDSC, ^dSAXS, and ^eAFM.

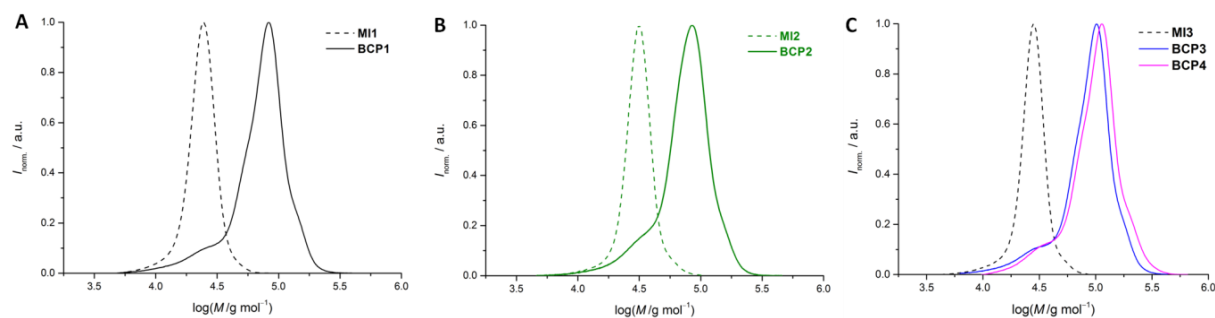


Figure 3.1 SEC traces of A) **MI1** and **BCP1**, B) **MI2** and **BCP2**, and C) **MI3**, **BCP3**, and **BCP4**.

Nevertheless, all BCPs were obtained with reasonably narrow distributions ($\mathcal{D} = 1.32\text{--}1.36$). Final volume fractions were determined by ^1H NMR and using PS and PI density values (1.05 g mL^{-1} and 0.913 g mL^{-1} , respectively) and treating the styrene derivative units as pure styrene for calculation. f_{PI} ranged from 0.50 to 0.54, which is an ideal case for lamellae formation.

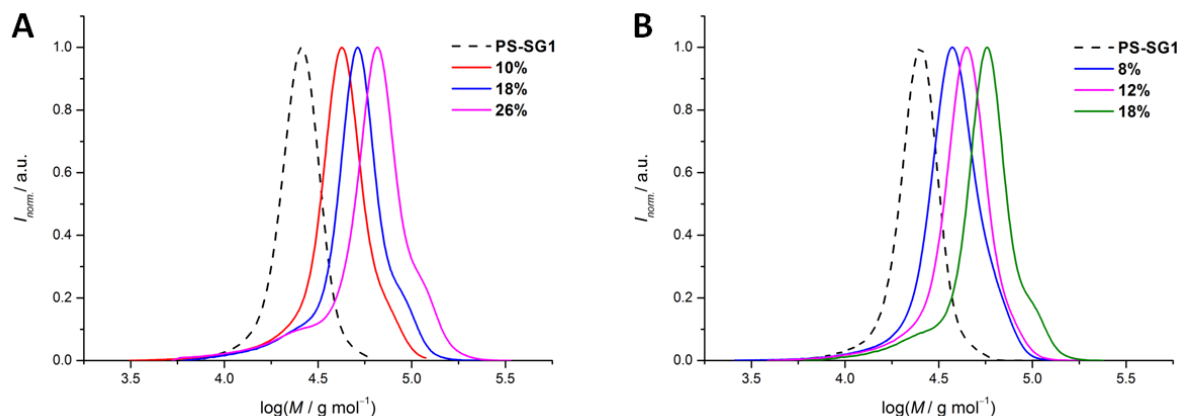


Figure 3.2 SEC traces of PI chain extension attempt from a PS-SG1: A) with a target of 30% conversion at $[\text{isoprene}]/[\text{PS-SG1}] = 1025$; B) with a target of 20% conversion at $[\text{isoprene}]/[\text{PS-SG1}] = 1335$. ($M_{n,\text{SEC}}(\text{PS-SG1}) = 23000\text{ g mol}^{-1}$).

3.4 Bulk Properties of PS-*b*-PI BCPs

In addition to NMR and SEC, DSC and SAXS were used to characterize the aforementioned set of functional PS-*b*-PI. The following section will report on these findings.

3.4.1 Differential Scanning Calorimetry (DSC) Results

Thermal characterization of block copolymers can provide information on the phase behavior. Particularly, if phase separation occurs, DSC measurements should reveal two glass transition temperatures (T_g s) corresponding to those of the independent block constituents.^[230] PS-*b*-PI is composed of a *soft* block (PI) and a *hard* (PS) block. The T_g of PS is $\sim 95\text{ }^\circ\text{C}$ which makes it glassy at room temperature.^[312-317] The T_g of polyisoprene is dependent on the distribution of repeating units ((3,4), (1,2), (1,4)), as well as of *cis* and *trans* isomers of the (1,4) unit.^[318] For example, *cis*-1,4-polyisoprene possesses a T_g of ca. $-70\text{ }^\circ\text{C}$ while that of *trans*-1,4-polyisoprene is approx. $10\text{ }^\circ\text{C}$ higher.^[312] Furthermore, when PI is synthesized by SG1-mediated NMP, the monomer unit distribution is dominated by the (1,4) motif ($> 80\text{ mol}\%$), while (3,4) units

represent 10–15 mol% with (1,2) motifs consequently being the minor component (Figure 3.3).^[319] In any case, the T_g of polyisoprene is clearly well below room temperature.

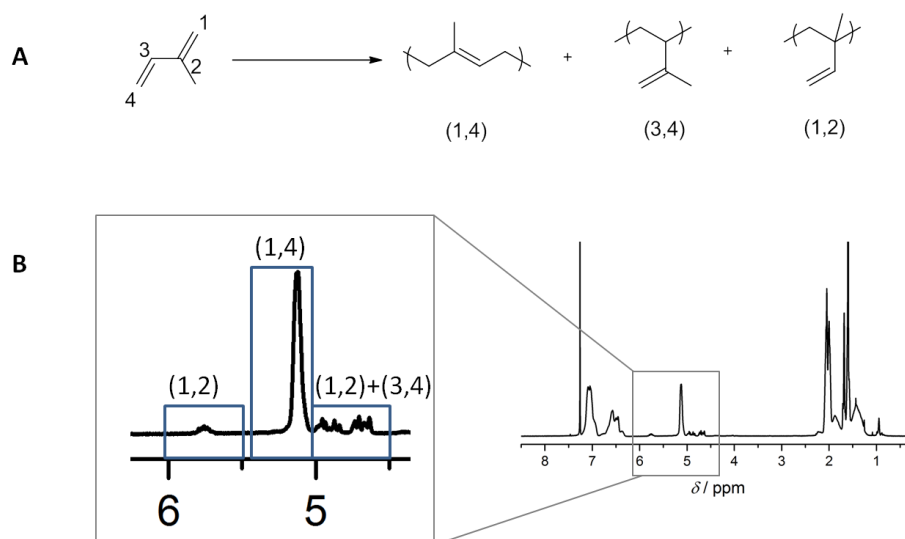


Figure 3.3 A) Representative repeating unit distribution for a PI block synthesized in the current study. B) ¹H NMR peak assignments for the ethylenic protons present in the PI block of PS-*b*-PI derivatives.

Figure 3.4A depicts the DSC thermographs of our set of PS-*b*-PI derivatives. All measurements showed two clear glass transitions ($T_{g,1} < T_{g,2}$), evidencing the ability for phase separation of the BCPs. $T_{g,1}$ falls in the -64 – (-61) °C range and corresponds to the PI block of the BCPs. Despite the incorporation of comonomers, the PS-based blocks exhibit very similar $T_{g,2}$ values, spanning a smaller range than the PI block (93.5–95 °C). The presence of functional units therefore did not significantly alter the thermal behavior of the reference PS-*b*-PI.

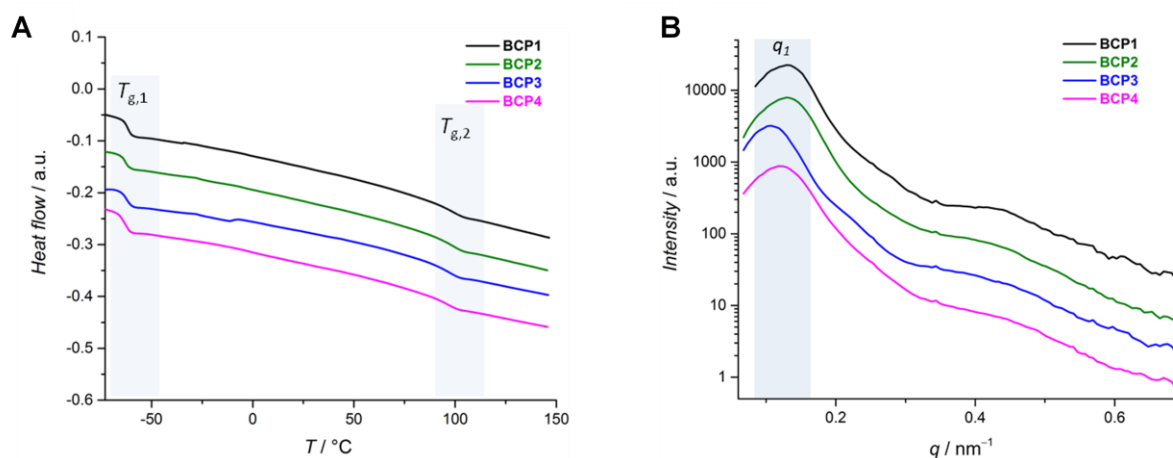


Figure 3.4 A) DSC thermographs and B) SAXS profiles of PS-*b*-PI derivatives **BCP1–4**.

3.4.2 SAXS Results

DSC can reveal the presence of two polymer phases, yet it does not give information on the nature of the phases. Therefore, our next step was to analyze the four PS-*b*-PI analogues in bulk by small-angle X-ray scattering (SAXS). SAXS enables the determination of the periodicity of the system (i.e., the mean values of the interdomain spacing) as well as the type of repeating pattern (e.g., cylinders, lamellae).^[320] Grazing-incidence SAXS (GI-SAXS) measurements could characterize the system in conditions similar to the targeted application (i.e., thin films) and particularly give information on the surface of the samples. Unfortunately, we did not have access to such an instrument. Consequently, we employed the classic SAXS variant and had in mind that parallel observation by atomic force microscopy (*vide infra*) would provide sufficient morphological information.

The obtained SAXS profiles are presented in Figure 3.4B. All four samples show a comparable behavior: a main peak at a similar position ($q_1 = 0.11\text{--}0.13\text{ nm}^{-1}$) and a shoulder at approx. three times q_1 . At two times q_1 , there is no strong indication of an existing peak. Only **BCP3** shows a clearer signal.

The absence of structural peaks at other positions than integer multiples of q_1 suggests a lamellar structure. Even without this indication of higher ordering peaks, the existence of the first ordering peak is enough to conclude a lamellar structure due to the known volume ratio of the different phase. All experimental values (from 0.46:0.54 to 0.50:0.50) lie clearly in the region where lamellar structure is expected from phase separation theory (34 vol% up to 62 vol%).^[154] The presence of the three first Bragg scattering peaks is characteristic of a rather high degree of ordering. The fact that the second-order peak q_2 is clearly less pronounced than the third-order peak suggests that the two phases have not exactly, but nearly the same dimensions. Literature indeed presents examples in which the even-ordered peaks on SAXS profiles are less pronounced than the odd-ordered ones in the presence of equal volumes of two separate blocks, i.e., for a lamellar morphology.^[156, 321-322] The first Bragg peak gives the periodicity of the system according to $L_{0,\text{SAXS}} = 2\pi/q_1$.^[320] Overall, the differences from one block copolymer to the other do not follow a clear trend with respect to molar masses. **BCP1** and **BCP2** yield an identical periodicity ($L_{0,\text{SAXS}} = 48.3\text{ nm}$), although their M_n differ of about 3000 g mol^{-1} (as determined by a combination of SEC and $^1\text{H NMR}$) and **BCP2** contains a few bulkier substituents. There is however a clear difference in periodicity with **BCP3** and **BCP4** ($L_{0,\text{SAXS}} = 58.7$ and 51.5 nm , respectively) for an increase of only about 2000 g mol^{-1} in number-average molar mass. For **BCP3**, this could potentially be attributed to an increase in polarity of the PS block due to the presence of chlorine atoms. Yet, **BCP4** also contains units of similar polarity (azides) and L_0 increases significantly less. Conclusions are difficult to draw because of the uncertainty on the

determination of the molar mass due to the presence of the functional groups in the PS macroinitiators. Nevertheless, all copolymers gratifyingly yield bulk structures containing sub-50 nm heterogeneities which can be attributed to a lamellar morphology.

3.5 Formation of Nanostructured Thin Films

Since DSC showed two T_g values and further information on the lamellar nature of this phase separation was obtained by SAXS, we proceeded to the fabrication of nanostructured thin films. Firstly, a solution of **BCP1** was spin-coated from toluene on an activated 1 cm² Si wafer. Thermal and solvent annealing are commonly utilized annealing techniques to induce BCP phase segregations. For PS-*b*-PI system, there have been some reports that used thermal annealing.^[261, 323-325] On the other hand, Keddie and co-workers used their PS-*b*-PI thin films as coated without any further annealing.^[184] To simplify the process, we followed the same approach and subsequently analyzed the films by atomic force microscopy (AFM), directly after spin-coating (Figure 3.5). Since PI is the softer block, it dissipates more energy during AFM analysis and therefore appears darker on the pictures.^[326]

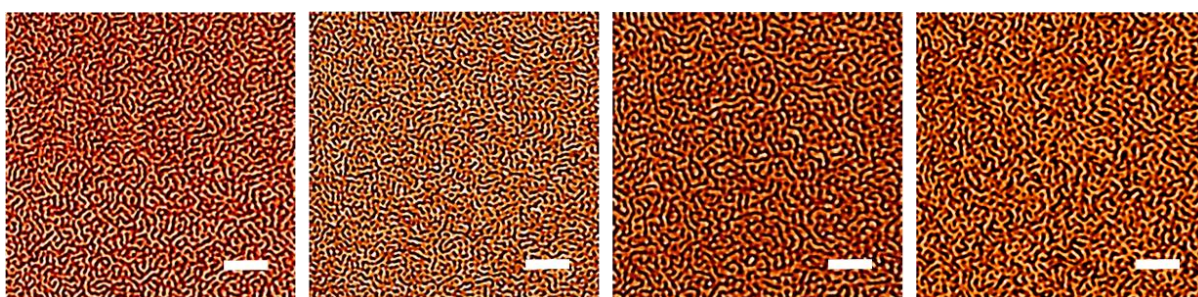


Figure 3.5 AFM phase images of A) **BCP1**, B) **BCP2**, C) **BCP3**, and D) **BCP4**. Scale bars 300 nm.

According to our SAXS measurements and NMR calculations, a lamellar structure was expected, which ideally should be perpendicular to the surface for patterning applications. At this point it should be reminded that the domain orientation depends on the interaction of the polymer segments with the substrate and air. In their report, Keddie and co-workers noted that in the case of thick PS-*b*-PI films, PI preferentially wets the substrate, leading to PI circular dot patterns on the surface. In the present case we have observed the same phenomenon for films with thicknesses of 33 and 20 nm (Figure 3.6). Reducing polymer concentration and increasing spinning rate and time in the spin-coating step resulted in a marked decrease of the film thickness. For a polymer solution with a concentration of 0.2 wt% spun at 10000 rpm for five minutes, an ultra-thin film exhibiting a thickness of ca. 7 nm (as measured by ellipsometry) was

obtained. Such a thickness is well below $L_{0,\text{SAXS}}$, which forces the phases to accommodate a perpendicular orientation, leading to so-called strip-like patterns, as observed by AFM (Figure 3.5), typical for perpendicular lamellae.^[327] Most lithographical studies employ BCP thin films with thicknesses close or equal to one domain spacing.^[183] Although more sophisticated structures can evolve when the BCP film thickness is below L_0 , lamellar microdomains can orient perpendicularly to the substrate in such cases.^[153] This type of morphology was indeed previously reported in theoretical and experimental studies,^[171, 327] particularly in the case of PS-*b*-PI.^[184] The same coating strategy was applied for the three functional PS-*b*-PIs **BCP2-4**.

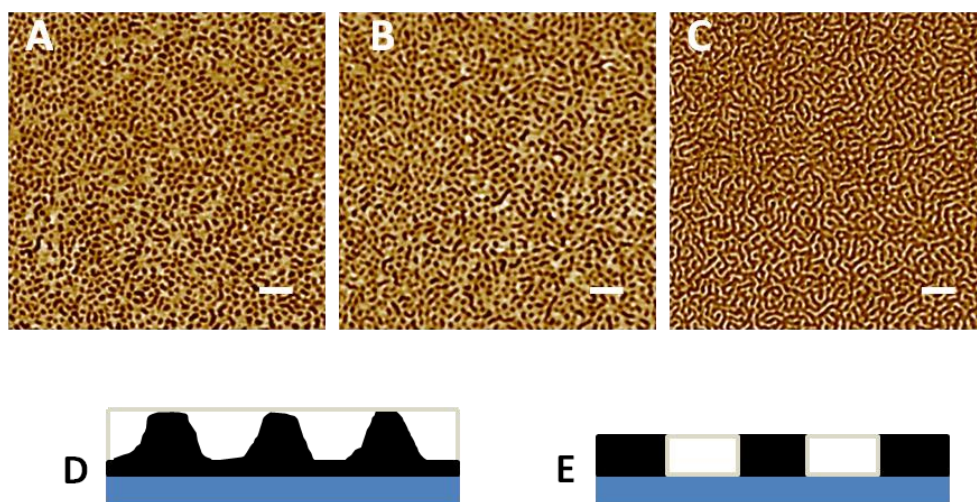


Figure 3.6 (Top row) A) AFM phase images of a 33 nm-thick film of **BCP1** spin-coated from a 0.3 wt% solution in toluene. B) 29 nm thick film of **BCP1** spin-coated from a 0.3 wt% solution in toluene. C) 7 nm thick film of **BCP1** spin-coated from a 0.2 wt% solution in toluene. (Bottom row) Schematic representations of D) PI wetting the surface in the case of thick films demonstrated on images A-B, E) BCP perpendicular orientation on Si wafer in the case of ultra thin films demonstrated on image. *Scale bar 200 nm.*

All four BCPs have evidently (almost) the same volume fractions (Table 3.1 and Figure 9.4) and are supposed to behave similarly in terms of phase separation – at least in bulk, as suggested by the SAXS data – and consequently yield analogous patterns. However, modification in interfacial interactions due to the presence of functional groups could have a major influence and alter the behavior of the BCP when confined in thin films. Working at very low thicknesses obviously prevented any issue of the sort as we observed similar morphologies for all PS-*b*-PIs (Figure 3.5). It should be noted that for the calculation of volume fractions we treated the functional styrene derivatives as if they had the same density as styrene. Although there could definitely be

slight differences, these minor fluctuations would still surely allow the BCPs to remain within the lamellar regime as it appears in a rather large window.

These films were reproduced many times and several regions were analyzed each time: comparable morphologies were consistently observed. To determine the periodicity, i.e., $L_{0,AFM}$, we measured at least 8 perpendicular segments across two adjacent domains on each characterized region and averaged these values. All copolymers yielded domains with a periodicity ranging between 44 and 59 nm. The comparison of AFM and SAXS results is congruent, with only minor fluctuations (1–10 % range).

3.6 Proof of Surface Reactivity: Azide-Alkyne Coupling

As mentioned previously, our set of functional BCPs includes reactivity in nucleophilic substitution (via $-Cl$), copper-catalyzed azide–alkyne cycloaddition (CuAAC) (via $-N_3$), *para*-fluoro thiol substitution (via PFS), and ene reactions (via the PI double bonds), among which we will here focus on CuAAC as a proof of concept. CuAAC is one of the most popular click type of reactions as explained in Section 2.2.1 and has already found a plethora of applications in surface functionalization.^[97–102] In order to probe the availability of the azide groups at the surface of the films made of **BCP4**, we synthesized a water-soluble polymer, namely poly(*N,N*-dimethylacrylamide) (DMAAm), which possesses an alkyne group as one end (Figure 3.7).

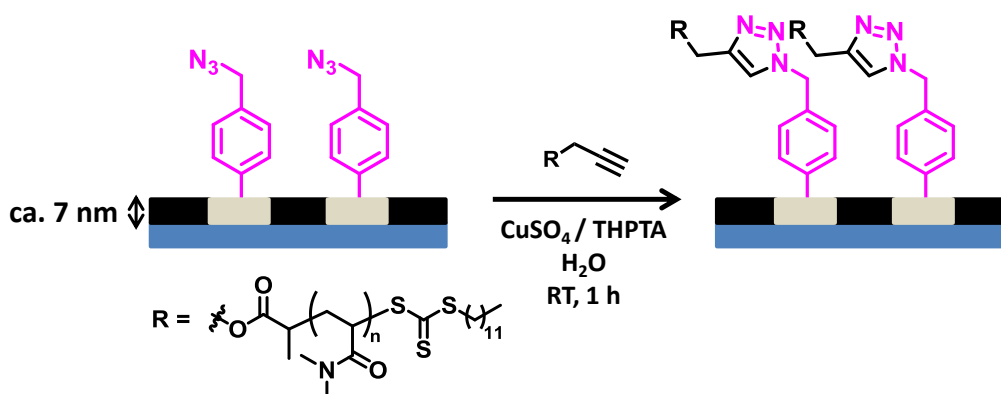


Figure 3.7 Schematic representation of the grafting of alkynyl-PDMAAm on a **BCP4** film via copper-catalyzed azide–alkyne coupling.

This PDAAm was first synthesized by RAFT with a TMS protected RAFT agent which was subsequently deprotected to yield the alkyne-PDAAm as confirmed by 1H NMR and SEC (Figures 9.5 and 9.6). As it has an amide group in each repeating unit, PDMAAm is convenient for monitoring the reaction by X-ray photoelectron spectroscopy (XPS). In addition, since the

alkynyl-PDMAAm was obtained by RAFT polymerization, XPS should also detect the presence of sulfur-related peaks arising from the trithiocarbonate end chain. In parallel to the CuAAC coupling, a control experiment was performed in the absence of copper catalyst. XPS results show a clear increase in nitrogen content upon reaction (from 0.4 to 3.8 at%) while the control sample indicates a significantly lower increase (from 0.4 to 1 at%), which could potentially suggest at limited physisorption and could be an issue for applications (Figure 3.8 Left). The S2p region of the XPS spectrum was clearly more convincing (Figure 3.8 Right). Indeed, while the control sample did not show any characteristic signal, the reaction sample exhibited a sharp peak related to sulfur species. This comparison alone proves the success of the reaction together with potential contamination with nitrogen-based species, which is not uncommon in XPS analysis.

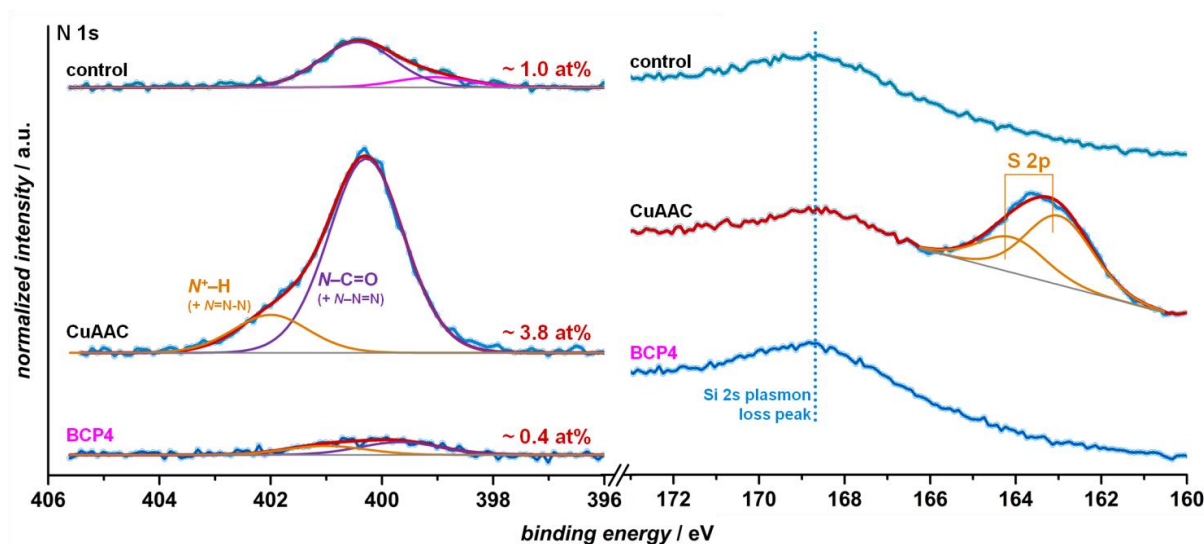


Figure 3.8 N1s (Left) and S2p (Right) selected regions of XPS spectra of an as-coated **BCP4** thin film (bottom, *reference*) and after incubation with **Alkyne-PDMAAm** in the presence (middle, *reaction sample*) or in the absence (top, *control sample*) of the copper-based catalytic system.

In addition to the successful grafting of PDMAAm onto the polymer film, it is inevitable to control that the morphology of the underlying nanostructured films is preserved. The AFM phase image after reaction (Figure 3.9 Middle) displayed very similar features as compared to those of the original film (Figure 3.9 Left). The control sample morphology was also preserved, as expected (Figure 3.9 Right).

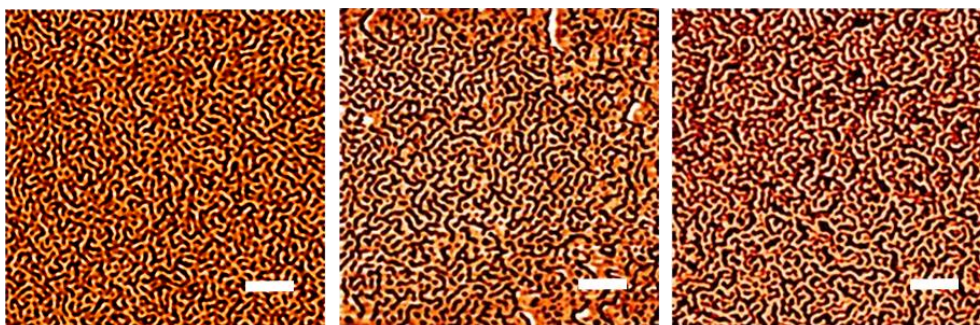


Figure 3.9 AFM phase images of a **BCP4** film before reaction (Left), after incubation with **Alkyne-PDMAAm** in the presence (Middle, *reaction sample*) or in the absence (Right, *control sample*) of the copper-based catalytic system. *Scale bar 300 nm.*

Besides AFM phase images, height images were also collected. In this case, slight changes were observed between the original **BCP4** film and the film after CuAAC (Figure 3.10). Nevertheless, the control sample presents very similar alterations, which could therefore be attributed to a poor stability of the film upon the numerous washing steps which were operated.

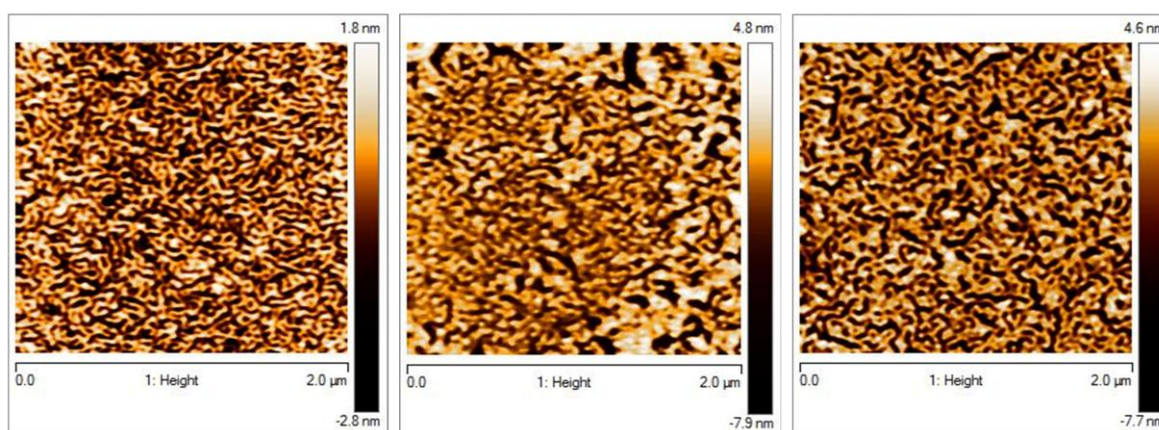


Figure 3.10 AFM height images of **BCP4** (Left), after azide-alkyne coupling (Middle), and control sample (Right).

3.7 Stabilization by Photocrosslinking

Until this point, we have been discussing reactions in water as our nanostructured materials are clearly not meant to be stable as such in organic solvents. The CuAAC investigation demonstrated that surface morphological alterations could actually also occur in aqueous media. Therefore, it is essential to stabilize the nanostructured films in order to make them applicable in a wider context. A common approach to do so is to crosslink the material. It is well known that systems bearing azides can be crosslinked thermally or by light.^[194, 328] Therefore, a **BCP4**-coated Si wafer was placed in a quartz flask and was irradiated with UV light (254 nm) for 15 min. Afterwards, the film was subjected to thorough successive washings with organic

solvents, e.g., acetone, DCM, toluene, and was finally incubated in DMSO for 30 min. AFM phase and height images of this sample are given on Figure 3.11. Clearly, 15 min of irradiation was sufficient to stabilize the film. This will allow the platform to be employed for immobilization of various molecules exhibiting a broad spectrum of solubility. This process is indeed known to be ultra-fast and hence it is possible that under optimized conditions, even few minutes of irradiation could be enough. In this case, some azides could still be available for azide-alkyne coupling after crosslinking. Furthermore, we foresee that copolymerization of 1–3% of azidomethylstyrene with for instance 4% of PFS followed by chain extension could produce stabilized PS-*b*-PI films with reactivity towards the *para*-fluoro-thiol reaction on surfaces. Moreover, one could also perform thiol-ene addition on the PI block, resulting a dual-functionalized nanostructure. Notably, these two reactions were proven to be orthogonal before.^[64] These combinations are currently being investigated in our group.

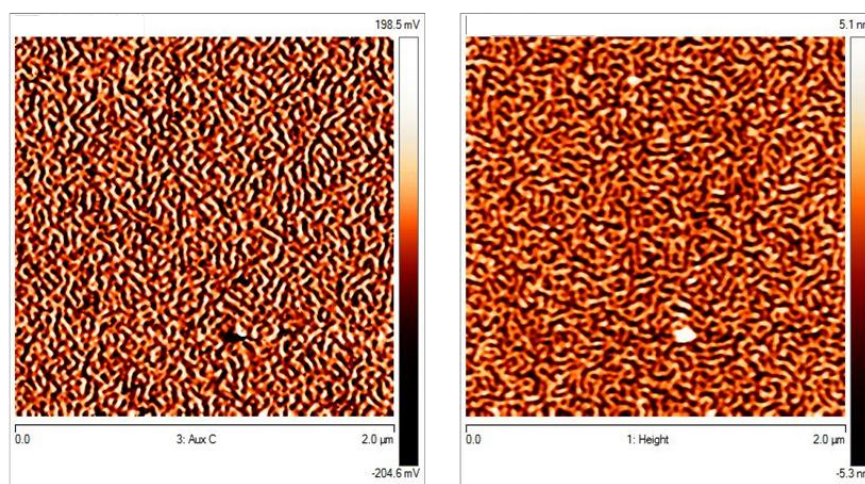


Figure 3.11 AFM phase (Left) and height (Right) images of a photocrosslinked **BCP4** film after multiple washings and incubation with organic solvents.

3.8 Conclusion and Outlook

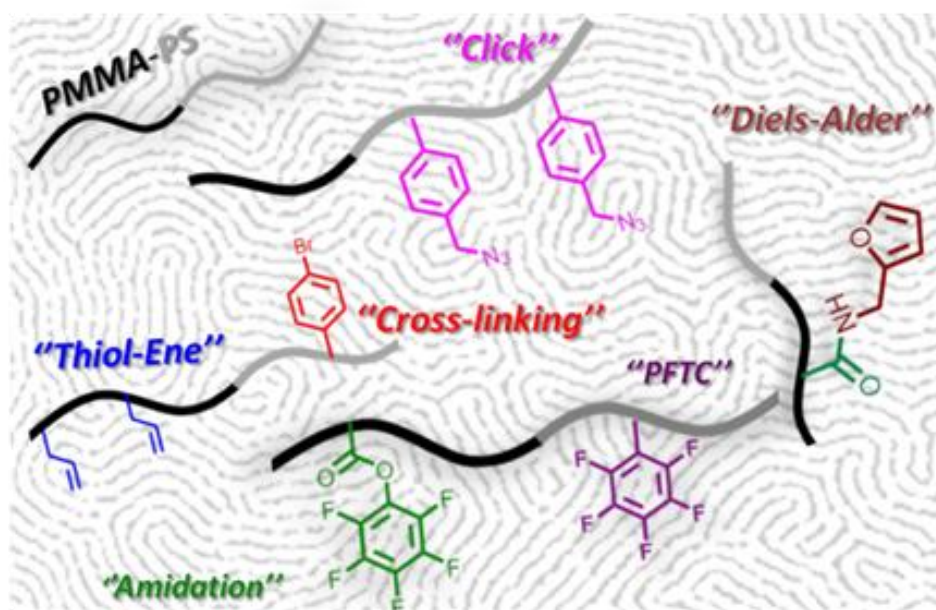
The synthesis of four PS-*b*-PI derivatives via NMP as a simple approach avoiding classic ionic polymerization setups was achieved in order to create nanostructured reactive surfaces with sub-30 nm features. While the PI block inherently possesses reactivity through internal double bonds, reactive groups were introduced into the PS block by a simple copolymerization approach. Their percentage was kept low so as to maintain the parental properties of the parent plain BCP, particularly the ability to phase separate. This small copolymer library gives access to functionalization through efficient chemical pathways such as nucleophilic substitution, azide-alkyne cycloaddition, radical thiol-ene addition, and *para*-fluoro-thiol substitution. The BCPs all exhibited 2 T_g values, which is a good indication of a phase-segregating system. All T_g s were

Conclusion and Outlook

observed to be in the very same range, irrespective of the incorporated functionality. Additionally, SAXS analysis confirmed the phase separation and revealed the lamellar morphology of the copolymers in melt, as targeted initially through the synthetic strategy. Optimized preparation conditions leading to very thin films allowed the formation of surface patterns which were characterized by AFM. All block copolymers exhibited a similar morphology, with only slight fluctuations in L_0 , which was also expected from SAXS data. Finally, a preliminary study was performed to showcase the introduction of reactivity at the surface of the films: CuAAC using a water-soluble polymer which was evidenced by XPS. Despite the hydrophobic nature and thus water stability of the individual components, the film morphology could however not be fully preserved. First photocrosslinking attempts revealed successful to stabilize the films, even in pure organic solvents, which strongly expands the scope of application of such nanopatterns to organic media. Further work should be carried out to optimize the azide-mediated UV-induced crosslinking in order to leave at least a small fraction of free azides for further surface reaction. Additional chemical routes for functionalization, i.e., ene reactions on PI and nucleophilic substitutions on PS, could also be performed, together with variation of the periodicity. We believe that employing reactive block copolymer films is a promising alternative for high-throughput chemical patterning, as most applications are based on the immobilization of two components.

4

A Library of Functional, Nanostructured Thin Films of PMMA-*b*-PS



In this work, SAXS measurements were done by Nico Dingenouts (Institute for Chemical Technology and Polymer Chemistry (ITCP), KIT). Some of the polymerizations as well as amidation reactions were performed by Divya Varadharajan.

4.1 Introduction

Block copolymer (BCP) thin films have gained significant attention in the last decades in micro and nanotechnology due to their ability to form nanostructures in sub-50 nm scale.^[153, 285] A strategy to use BCPs as patterning platforms is therefore enticing. Although chemical patterning in nanodimensions has been achieved by lithographical techniques such as dip-pen nanolithography^[5, 329] and e-beam lithography,^[281, 329] self-assembled structures of BCPs are indeed excellent candidates to substitute these methods.^[285] BCPs can create various nanostructures among which lamellae and cylinders are the most studied types. For more detailed information, the reader is redirected to Section 2.3.

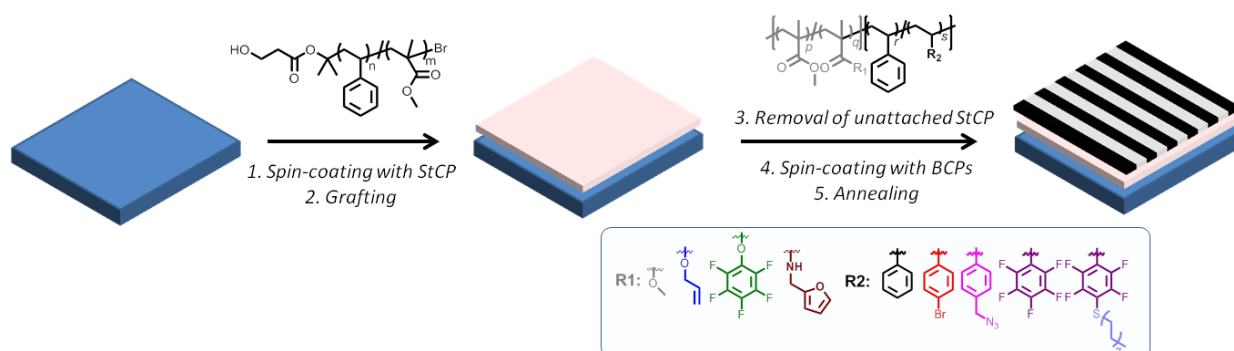


Figure 4.1 General concept employed in this project.

Particularly, nanoscale placement of (bio)molecules on precise locations on surfaces has great potential in biotechnological applications.^[330-331] Since most (bio)molecules tend to adsorb on surfaces unspecifically, it is of great importance to enhance their specific binding and minimize the background interference.^[330-331] More than this, introducing functional moieties into BCP backbones could potentially be used to tether (bio)molecules via covalent attachment on nanostructured BCP films upon their expression on the outermost surface. If the underlying nanostructure is retained during this placement, functional BCP films could be a powerful novel platform for (bio)patterning.^[7, 10]

PMMA-*b*-PS is an extensively studied system whose microphase separation behaviour can easily be predicted.^[152, 332] Nanostructured films of non-functionalized PMMA-*b*-PS have been used in different contexts with the idea of patterning in mind. For example, Lopes *et al.* presented adsorption of various metals on either PMMA or PS domains.^[271] In another report, selective

deposition of proteins on PS domain was demonstrated.^[287] Furthermore, by selective removal of PMMA upon UV exposure and crosslinking of PS domain, this BCP system has been extensively used as etch mask for lithographical applications.^[259, 333] More examples regarding different BCP systems can be found in the literature.^[8-9, 184, 273, 279, 290, 292]

In this dissertation, we chose PMMA-*b*-PS as a platform for the development of a small library of functional BCPs to be used for patterning for the following reasons: (i) functional derivatives can be easily synthesized via reversible-deactivation radical polymerization methods; (ii) various methacrylic and styrenic derivatives are commercially available, including some allowing straightforward post-polymerization modification; (iii) the fabrication of PMMA-*b*-PS films and details such as coating strategies are well documented; (iv) enhanced ordering can be achieved simply by annealing; and finally (v) well-defined PMMA-*b*-PS films have found many applications for lithography or unspecific adsorption. However there are only limited investigations for specific covalent functionalization. So far, Stadermann *et al.* showed phase-segregating PMMA-*b*-PS-based systems bearing carboxyl, alkynyl, and photocaged amino groups in the backbone, yet only with non-regular nanostructures.^[10-11] The synthetic strategies employed in the present Chapter include atom-transfer radical polymerization (ATRP), reversible addition-fragmentation transfer (RAFT) polymerization, as well as post-polymerization methods.

As highlighted in the literature, post-polymerization modifications of BCPs allow expansion of the chemical diversity and access to new applications.^[334-335] We therefore utilized pentafluorophenyl methacrylate (PFPMMA) as comonomer and a versatile group to introduce a range of moieties through functional amines.^[336-340] Our library of PMMA-*b*-PS includes reactive groups for azide-alkyne cycloaddition, thiol-ene addition, and Diels-Alder click reactions, which are ligations widely applied in polymer chemistry.^[334] In addition, we considered the *para*-fluoro-thiol ligation (see Chapters 6 and 7), which has recently drawn increasing attention.^[12-13, 64, 134, 338] The general concept is depicted on Figure 4.1.

After briefly describing synthesis of various lamellae-forming functional PMMA-*b*-PS BCPs (Scheme 4.1), we examine their phase separation behaviour in the form of thin films. It is demonstrated that upon introduction of functionalities into the PMMA-*b*-PS, the nanostructure, i.e., formation of lamellae is not perturbed. Presence of different pendant groups affect the domain spacing (L_0) only to a slight extent. By equipping the well-known PMMA-*b*-PS system with a plethora of functionalities, we are establishing practical platforms for further patterning studies.

4.2 General Note on the Employed Polymers

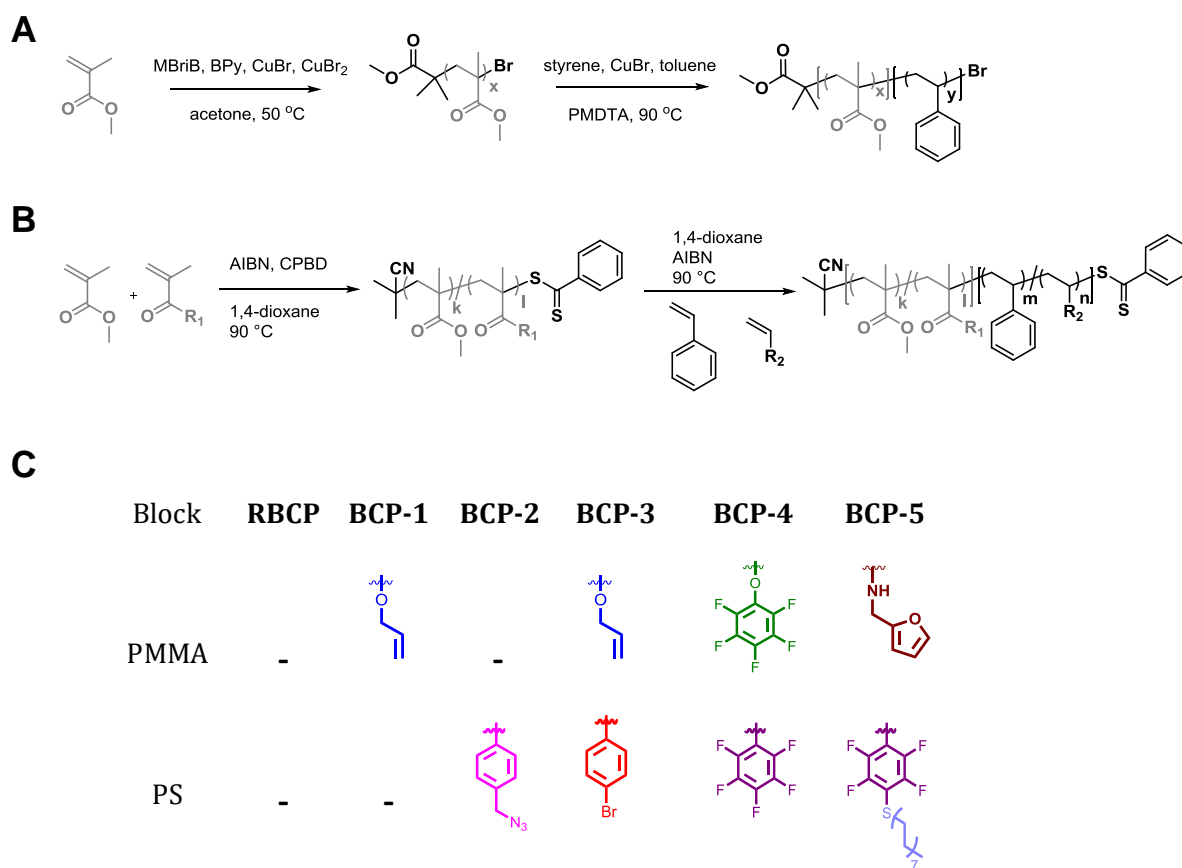
In this work, we first utilized a reference BCP, namely a non-functional PMMA-*b*-PS synthesized by ATRP. At later steps, RAFT polymerization with respective chain extensions was also employed to produce many of the functional derivatives. These extensions were achieved by using one or two different monomers. Details about synthesis and properties of the complete collection of polymers will be discussed in the following sections.

4.2.1 Reference Block Copolymer (RBCP): Synthesis; ATRP vs. RAFT

The reference, non-functional PMMA-*b*-PS (**RBCP**) was synthesized by ATRP (Scheme 4.1A) as it is a very efficient method to synthesize well-defined PMMA and chain extension with styrene also proceeds well.^[36] However, a drawback of ATRP is the employment of Cu metal, which implies a purification step. On the other hand, RAFT polymerization, that makes use of stoichiometric amounts of dithioesters as mediating agents^[341] also proceeds well in PMMA-*b*-PS systems. Therefore, during the course of this study, we switched to RAFT for the functional BCPs (Scheme 4.1B) after doing the preliminary studies with RBCP and optimizing the spin-coating and annealing conditions. It is noteworthy that RAFT is not compatible with basic monomers and those bearing primary amino groups whilst ATRP of acidic monomers needs neutralization or protection.^[341] As an alternative, NMP could be used but the commercially available reagents do not allow for a straightforward control of the polymerization of methacrylates.^[341] In short, the most advantageous method can be chosen depending on the monomers which are of interest during the particular study. To synthesize the **RBCP**, firstly, a homopolymer (**HP1**) was obtained by ATRP with M_n of 19 kg mol⁻¹ and narrow dispersity ($\mathcal{D} = 1.15$) as listed in Table 4.1. Subsequently, **HP1** was used as a macroinitiator to yield **RBCP** ($M_n = 44.4$ kg mol⁻¹) (Table 4.2). \mathcal{D} increased from 1.15 to 1.24 which is regarded as a minimal deviation.

4.2.2 Characteristics of the Polymers

For the span of monomers that we applied in this study, RAFT polymerization was an optimum method as its versatility and tolerance towards functional moieties were also reported before.^[342] Apart from the **RBCP**, our library includes 5 different functional BCPs with the 5th one being a derivative of the 4th (Scheme 4.1C).



Scheme 4.1 A) Synthesis of **RBCP**. B) Synthetic route to obtain functional BCPs. C) Functional monomers present in each BCP.

To start with, only **BCP-2** has no functionality in the first block which is made of pure PMMA (**HP2**) with M_n of 21.3 kg mol⁻¹. Copolymer 1 (**CP1**) bears 5 mole% of allyl methacrylate (AMA) copolymerized with MMA which was used as macroinitiator to synthesize both **BCP-1** and **BCP-3**. **CP2** is a copolymer of pentafluorophenyl methacrylate (PFPMA) and MMA which was subsequently used to synthesize **BCP-4**. As listed in Table 4.1, molar masses of these macroinitiators were all in a narrow range (20.9-23.5 kg mol⁻¹) with a negligible difference from **HP1** (19 kg mol⁻¹).

Table 4.1 Detailed information on the characteristics of the statistical copolymer (StCP), homopolymers (HP) and copolymers (CP).

Entry	Initiator	$M_{n,SEC}^a$ (kg mol ⁻¹)	\bar{D}^a
StCP	HEBIB	10.7	1.21
HP1	MBriB	19	1.15
HP2	AIBN	21.3	1.10
CP1	AIBN	23.5	1.20
CP2	AIBN	20.9	1.16

^aValues obtained by SEC

Polydispersities also fall in a range between 1.10-1.20, evidencing controlled polymerization. During characterization, molar masses of the first blocks (either HP or CP) were obtained from SEC with PMMA calibration (Table 4.1). Those of BCPs were also measured by SEC. However, to precisely determine the volume fractions of the BCPs, M_n values were also calculated by ¹H NMR, because no SEC calibration is available for precisely determining M_n of BCPs (Table 4.2). One can find exemplary fraction calculations in Section 9.2. For the BCPs, molar masses are between 42-47 kg mol⁻¹ with dispersities within the 1.17-1.34 range. \bar{D} values are slightly higher than those of HPs and CPs, however they are still narrow enough to exhibit a smooth distribution. In this range, it should anyway not have a significant influence on phase separation. SEC traces of **HP1** and **RBCP** are shown on Figure 4.2A, those of **CP2**, **BCP-4** and **BCP-5** are given on Figure 4.2B. For SEC traces of the rest of the library, the reader is redirected to the experimental Chapter (Section 9.2). **BCP-1** and **BCP-2** bear one functionality overall on either PS or PMMA while **BCP-3**, **BCP-4** and **BCP-5** are having one in each block. Detailed information about all BCPs is compiled on Table 4.2.

Table 4.2 Detailed information about the BCPs employed in this work.

Entry	Initiator	$M_{n,SEC}^a$ (kg mol ⁻¹)	$M_{n,NMR}^b$ (kg mol ⁻¹)	\bar{D}^a	$f_{PS}f_{PMMA}$	$L_{0,AFM}^c$ (nm)	$L_{0,SAXS}^d$ (nm)	Thickness ^e (nm)	d/L_0^c
RBCP	HP1	44.4	38	1.24	0.52:0.48	35.8	33.1	38	1.06
BCP-1	CP1	41.4	44.7	1.32	0.51:0.49	32.4	27.8	37.5	1.16
BCP-2	HP2	36.7	44.6	1.23	0.55:0.45	30.8	26	38.1	1.24
BCP-3	CP1	45.5	46.9	1.34	0.55:0.45	30.2	30.7	38.4	1.27
BCP-4	CP2	37.4	41.6	1.17	0.53:0.47	27.1	25.9	40.8	1.51
BCP-5	(Modified BCP4)	41.9	42.9	1.17	0.53:0.47	29.9	27.7	41.5	1.39

Values obtained by ^aSEC ^bNMR ^cAFM ^dSAXS ^eEllipsometry

BCP-1 bears AMA, **BCP-2** possesses azidomethyl styrene (AMS) units and **BCP-3** carries both AMA and bromostyrene (BrS). **BCP-4** includes two bulky groups, one is PFPMA in the PMMA block and the other one is PFS in the PS block. **BCP-5** is a modified version of **BCP-4** which will be discussed later in the text. The fraction of incorporated functional comonomers was kept below 10% during copolymerization: ideally at 5%, yet fluctuations occur between 5-8% depending on reactivities. The volume fraction of PS (f_{PS}) in **RBCP** is 0.52, which is theoretically leading to lamellae in bulk (Figure 9.7). For the rest of the library, f_{PS} also lie in the range of 0.51-0.55. For the calculation of volume fractions in the case of functional BCPs, the functional comonomer units were treated as MMA units in the first block and as styrene and in the second block. The density differences introduced by different pendant groups were neglected, particularly because no data or theory is available for correcting this aspect. For the corresponding NMR spectra and SEC traces, see Figures 9.8-9.15. The functional groups were chosen with the intention of bringing practical reactive handles at the surface of the BCP films. Through their allylic substituents, **BCP-1** and **BCP-3** are reactive towards thiols via radical thiol-ene addition. **BCP-3** is in addition UV-crosslinkable through BrSt units. **BCP-2** can undergo azide-alkyne cycloaddition while it can also be thermally or photo-crosslinked. As **BCP-1** and **BCP-3**, **BCP-4** is reactive towards thiols, yet via *para*-fluoro thiol ligation. At the same time, through the activated ester of the PFPMA unit, **BCP-4** can be modified via a range of amines. Depending on the type of amine, many new functions can thus be introduced into the BCP. For instance, **BCP-5** was obtained by reaction of **BCP-4** with furfuryl amine, thereby introducing reactivity towards Diels-Alder reaction. Finally, *para*-fluoro-thiol ligation was performed on the PFS units of **BCP-4** with octanethiol to further investigate its effect on phase separation.

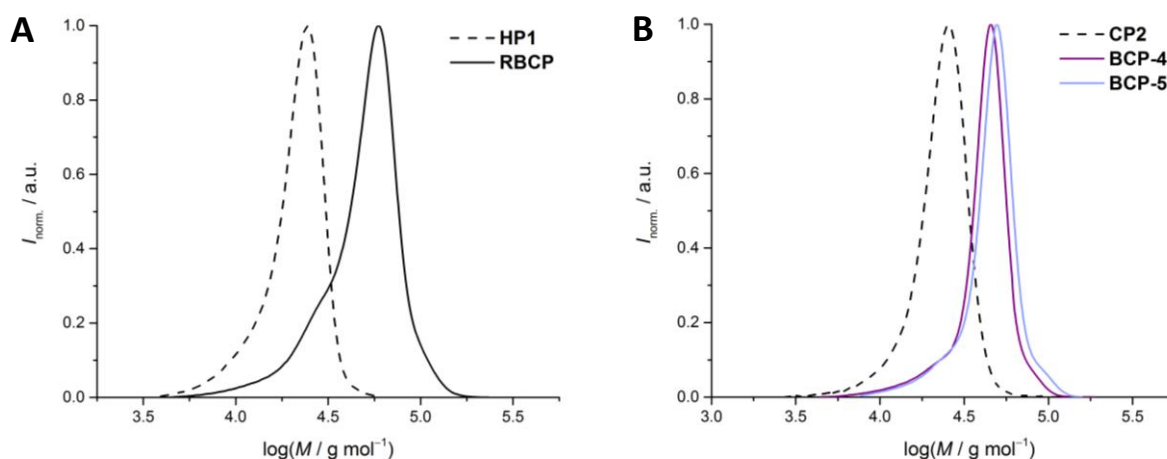


Figure 4.2 SEC traces of A) **HP1** and **RBCP** B) **CP2**, **BCP-4** and **BCP-5**.

4.3 The Coating Strategy

One of the challenges in obtaining perpendicular lamellar structure in BCP thin films is to have a neutral substrate with balanced interfacial energies for both blocks. As discussed in Section 2.3.2.1, there are several ways to achieve this. Among the listed techniques, in this part of the work, we employed the ‘random copolymer’ approach,^[189] as it is widely encountered in PMMA-*b*-PS systems.

Overall, a two-layer coating strategy is applied (Figure 4.1). The first layer is made of a statistical copolymer (StCP) of styrene and MMA which bears an –OH end group. Firstly, an OH-functionalized ATRP initiator (2-hydroxyethyl 2-bromo-2-methylpropanoate; HEBIB) was synthesized according to a reported procedure.^[343] It was then used to initiate the atom transfer radical copolymerization of styrene and MMA ($M_n = 12900 \text{ g mol}^{-1}$, $D = 1.21$) (Figure 4.3). Although it is not highlighted in the literature, the optimal M_n for StCP is $\sim 10000 \text{ g mol}^{-1}$, which produces $\sim 5\text{-}8 \text{ nm}$ thicknesses.^[259] Through the hydroxyl end, the polymer is anchored onto the SiO_2 layer of the Si substrate. The grafting step is achieved by heating up to $170 \text{ }^\circ\text{C}$ for a total time of 24 h. After this period, nongrafted chains are removed by sonication and extensive washing, leaving a $\sim 7 \text{ nm}$ thick layer of the StCP, as measured by ellipsometry. As stated in previous reports,^[192-193, 200] with a neutralization layer thickness greater than 5 nm, perpendicular orientation is always observed thanks to the efficient decoupling of BCP from SiO_2 surface. The final styrene molar fraction f_{Sty} in the StCP was 0.56 (Figure 9.16). In the original report of Mansky,^[189] it was demonstrated that $\text{P}(\text{S-}r\text{-MMA})$ brushes with $0.50 < f_{\text{Sty}} < 0.65$, one can achieve perpendicular orientation for a symmetrical BCP, though processing conditions can also play roles.

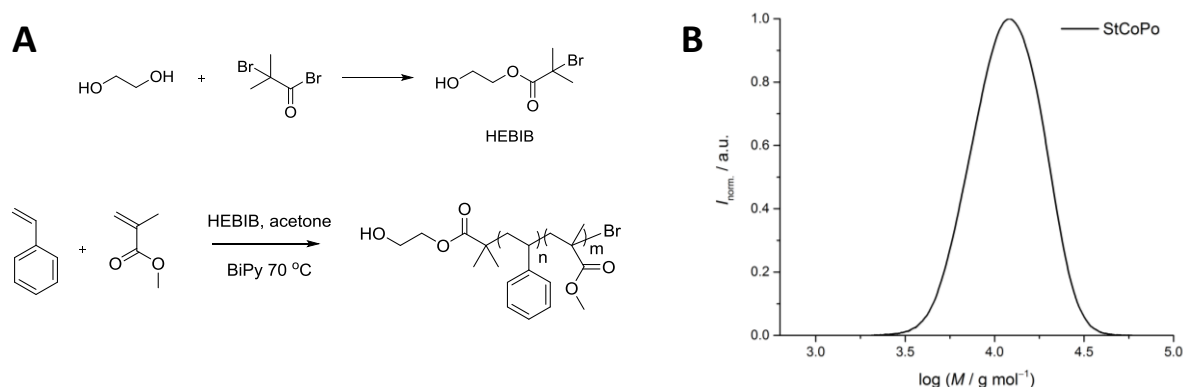


Figure 4.3 A) Synthetic steps to obtain HEBIB and the StCP used in the first layer of the coating. B) SEC traces of the StCP.

In terms of molar mass, composition of the polymer, and thickness of the film, our StCP matches adequate literature values. The second layer coated on top of the neutralized Si substrate was made of the BCPs. The same StCP was used in all coatings with the same processing conditions. In other words, the only difference between the samples was the type of BCP which was spin-coated on top of the StCP layer, with its relevant functionality. Characterization of these films will be discussed in the next section.

4.4 Detailed Investigations of the Thin Films

In this section, analysis of film morphologies by AFM and SAXS will be provided. This will be followed by an alternative methodology for annealing, i.e., microwave irradiation. Water stability investigations of the films as well as crosslinking studies will subsequently be reported.

4.4.1 AFM and SAXS Results

The BCP films were created by spin-coating on 1 cm² Si wafers and were thermally annealed at 170 °C for 24 h prior to analysis, adopted as optimum conditions from previously reported systems.^[189, 192, 201, 344] Although there exist other potentially milder methods such as solvent annealing^[211] and application of electric field,^[345] we opted for traditional thermal annealing as it is simpler to apply. On AFM images, the PS domains appear darker whereas the PMMA domains are the lighter area as PMMA shows a slight height difference upon moisture uptake as compared to PS.^[346] Although both PMMA and PS are well below their T_g values at RT and thus not expected to exhibit significant contrast in AFM, the difference is attributed to preferential absorption of moisture by PMMA.^[347] The thickness of the films (d) was measured by ellipsometry and listed in Table 4.2. They vary between 37.5-41.5 nm: this 4 nm negligible difference can be attributed to small experimental errors and uncontrollable loss of the solution during spin-coating process, as encountered in other systems as well.^[348] As shown on Figure 4.4, all 6 BCPs exhibit similar perpendicular lamellar structure in AFM phase images. On the phase image of **BCP-5** a mixed morphology could be suspected since it exhibits a rather discontinuous stripe patterns with what could seem to be dots. However, we would attribute this as a visual effect due rather to AFM scanning parameters since one can clearly see a lamellar structure on the height image (Figure 4.5). Note that the color gradient difference between phase and height images is only a visual adjustment, arbitrarily chosen to demonstrate better contrast of the two distinct phases). With confidence, from the typical ‘fingerprint’ pattern and relevant literature, it can be claimed that perpendicular lamella are obtained.

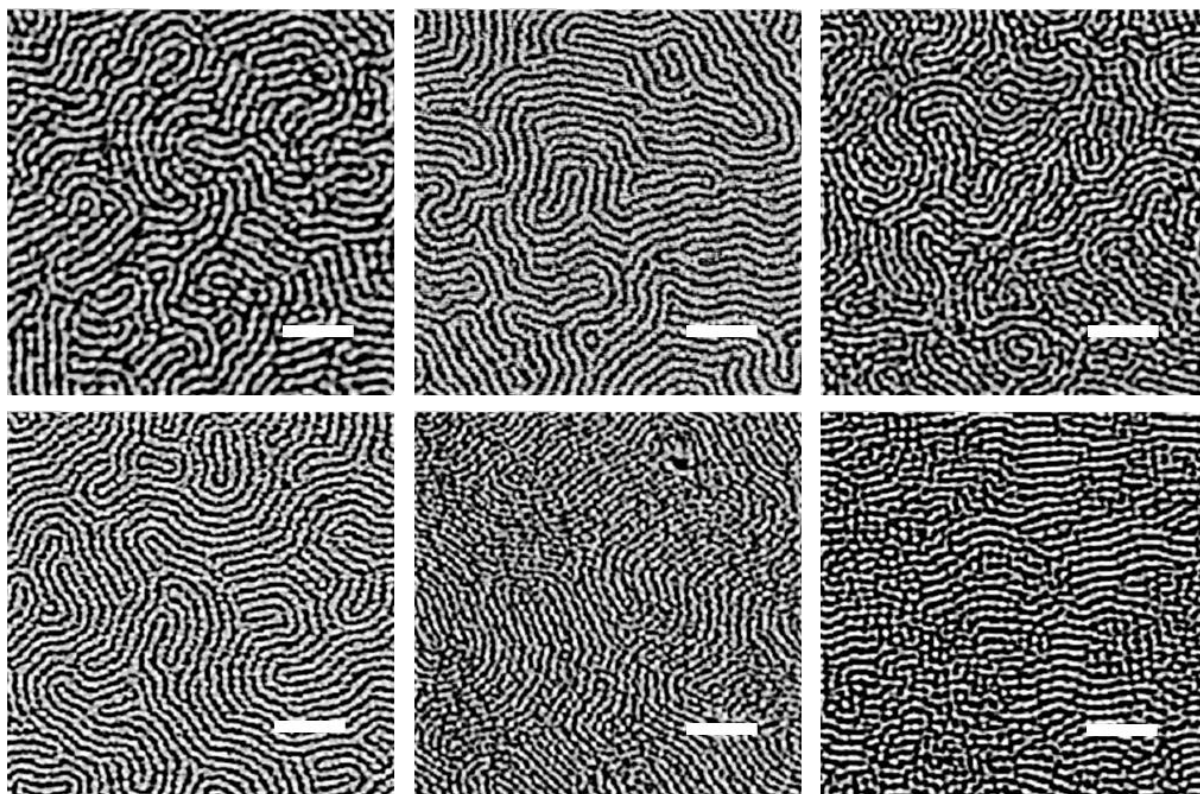


Figure 4.4 AFM phase images of all 6 BCPs employed in this work. The order is as follows: Top row from left to right: **RBCP**, **BCP-1**, **BCP-2**. Bottom row from left to right: **BCP-3**, **BCP-4**, **BCP-5**. Scale bar 200 nm.

In one study conducted by Ham *et al.*,^[201] it was demonstrated that on a random copolymer layer with $f_{\text{Sty}} = 0.55$, the BCP ($M_n = 55 \text{ kg mol}^{-1}$, $f = 0.50$) orients perpendicularly up to a thickness of 39 nm. Considering that a few nanometers of difference can source from different experimental setups, our parameters are in the same vicinity of these values. In another study by Borah *et al.*, two different lamella forming PMMA-*b*-PS (36 kg mol^{-1} and 74 kg mol^{-1}) were coated on a random copolymer layer ($M_n = 13.2 \text{ kg mol}^{-1}$, $f = 0.58$) and annealed with all similar conditions as applied in our work. They obtained thicknesses varying around 45 nm and proved that the structures for both BCPs were perpendicular lamella.^[348] One can simply conclude that with such an established procedure from the literature, our **RBCP** is exhibiting perpendicular lamella while the functional ones are only showing slightly decreased L_0 values and keep the same microdomain orientation. Additionally, the thickness-to-domain spacing ratio (d/L_0) is an important parameter to predict the BCP orientation. As seen in Table 4.2, for **RBCP** this ratio is 1.06, which is in perfect agreement with perpendicular arrangement. Furthermore, the film thickness is rather invariant in our BCP library. Only L_0 is varying – consistently being lower for functional BCPs, leading to a variation of d/L_0 , being slightly larger in the case of functional BCPs.

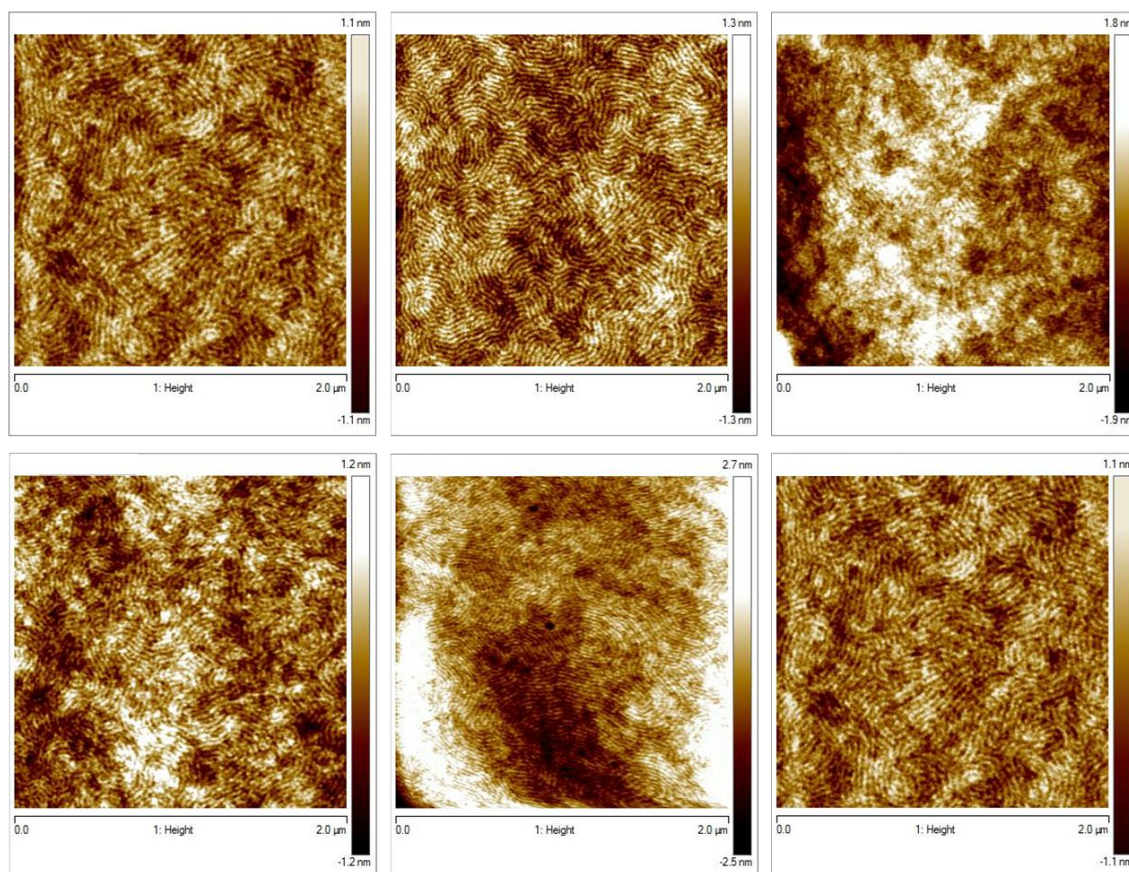


Figure 4.5 AFM height images of all 6 BCPs employed in this work. The order is as follows: Top row from left to right: **RBCP**, **BCP-1**, **BCP-2**. Bottom row from left to right: **BCP-3**, **BCP-4**, **BCP-5**.

Nevertheless, referring to the aforementioned report,^[348] if the thickness is equal or close to $1-2 L_0$, thermodynamic stability for vertical orientation is preserved. L_0 was measured by AFM and also calculated from SAXS. It is to note that the values obtained by AFM are slightly different from those calculated via SAXS. However, this type of result was also observed in another study.^[201] The SAXS profiles of all 6 BCPs are given on Figure 4.6. The series is split in two for easier observation. All 6 BCPs exhibit a first maxima (q^*) which is a direct proof of phase segregating behaviour. The first maximum peaks are marked with a vertical line on each curve with the respective color. Theoretically, L_0 is calculated from $2\pi/q^*$ which gives us 33.1 nm in the case of **RBCP**, for instance. In a lamellar system, one could observe second and third order peaks ($2L_0$ and $3L_0$) as well, without any additional peak in between. In our case, the 2nd and 3rd peaks are rather broad and thus not very pronounced. However, the third order peak is more pronounced than the second order peak (especially more obvious in the case of **RBCP**) and this occurs only in the case of a lamellar system, as also discussed in the previous Chapter., Combining the volume fraction calculations by NMR and the AFM phase images, one can conclude that the system clearly presents a lamellar structure, without perpendicular orientation in the chosen preparation conditions. Only in the case of **BCP-2** is it difficult to

undoubtedly state the system is lamellar from its SAXS profile, which probably stems from the experimental setup and a lack of material to be analysed in the present case.

Since it is simpler to measure the lateral length by AFM as the stripes exhibit a well ordered conformation, we prefer to discuss L_0 obtained via AFM ($L_{0,AFM}$). Although the radius of gyration, thus the molar mass for a BCP of the same composition, is the main factor influencing L_0 , the presence of functional groups can potentially play a role, as they may alter the density of the block where they are located, as well as the Flory-Huggins interaction parameter χ and even interfacial energies with the supporting substrate or the atmosphere. In the following, some side-by-side comparisons are highlighted:

- **BCP-1** and **BCP-2** have a very similar molar mass (44.7 and 44.6 kg mol⁻¹, respectively) and their $L_{0,AFM}$ exhibit only a 1.6 nm difference. Considering that AMA and AMS are both small pendant groups, they do not seem to strongly affect L_0 .
- The largest L_0 was observed for **RBCP** which has the lowest M_n and no functional group. On the contrary, the lowest L_0 was surprisingly observed for **BCP-4**, which bears two bulky groups on its backbone.
- From a different point of view, though **RBCP** has the lowest M_n (38 kg mol⁻¹) and **BCP-3** has the highest M_n (46.9 kg mol⁻¹), L_0 of **RBCP** is 5.6 nm bigger than that of **BCP-3** by AFM (2.9 nm by SAXS).
- A clear effect of the substituent nature can be observed after the modification of **BCP-4** to yield **BCP-5**. While the overall structure of the BCP should remain the same during the side-chain modification (indeed M_n and \bar{D} do not significantly change), an increase of 2.5-3 nm in L_0 is witnessed in both AFM and SAXS measurements.
- **BCP-1** bears AMA and **BCP-3** bears BrS together with AMA. Furthermore, **BCP-3** has a slightly higher M_n as compared to **BCP-1** (2.2 kg mol⁻¹ difference), while its $L_{0,AFM}$ is 2.2 nm smaller than that of **BCP-1**. This shows that presence of BrS reduces L_0 to a small degree. As observed on **BCP-4** as well, halogenated monomers seemed to lower L_0 .

Clearly, the molar mass of the BCP is not the only parameter that governs the domain spacing of a BCP thin film, when even a low fraction of functional comonomer is introduced.

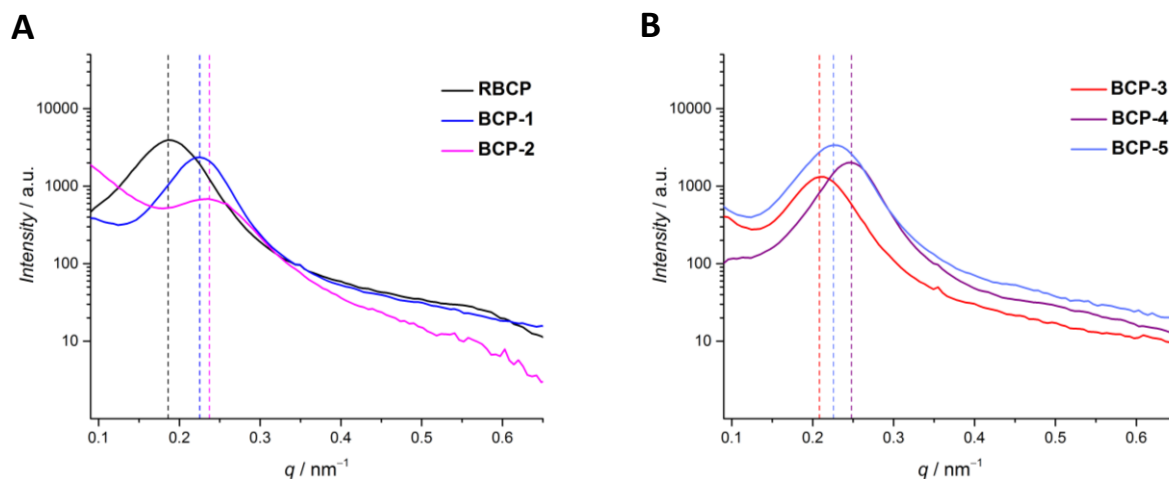


Figure 4.6 SAXS profiles of A) RBCP, BCP-1 and BCP-2 B) BCP-3, BCP-4, BCP-5.

4.4.2 Microwave Annealing

Among the well-known annealing methods, we chose thermal annealing in our initial studies. However, high temperatures can be harmful to some of the functional groups: for instance, crosslinking could occur through the azide groups. As a very simple, alternative method, microwave (MW) assisted annealing was introduced in the literature. MW annealing is able to induce BCP self-assembly within 30 s to few minutes at RT (Section 2.3.2.2).^[217-218] To show the applicability of this method to our systems, we arbitrarily picked up one BCP, namely **BCP-3**. In our hands, phase separation by this technique was obtained after MW treatment in 2 minutes at 30 °C as shown in Figure 4.7 left. Obviously, the MW-induced phase separation is very similar to that obtained by thermal treatment (Figure 4.7 right). It is noteworthy that in this technique, we used 0.5 cm² wafers instead of 1 cm² so as to reproduce the literature reports.

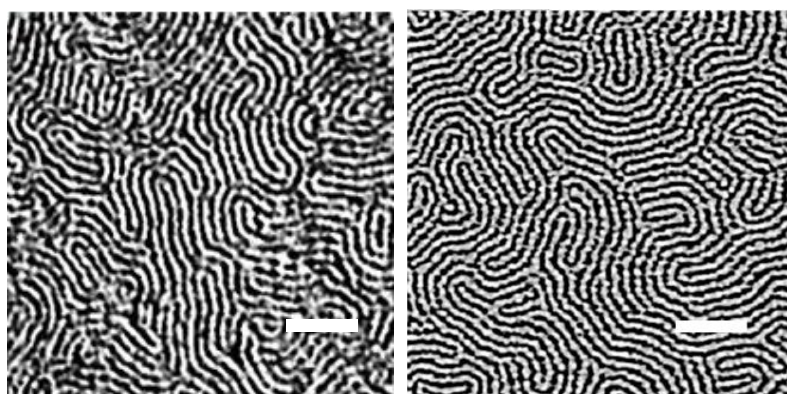


Figure 4.7 AFM phase image of (Left) **BCP-3** after MW annealing, (Right) after thermal annealing. Scale bars 200 nm.

4.4.3 Stability Tests in Water

As both blocks of the PMMA-*b*-PS are hydrophobic (water contact angle (WCA) of ca. 90°), we initially assumed they would be stable in aqueous media (water contact angles of the functional BCPs are not shown here since there is no detectable difference as compared to **RBCP**). However, since PMMA is more hydrophilic than PS, it is possible that swelling can occur over extended time periods, which could disrupt the nanostructuration. To investigate this, stability tests were performed. The first test was carried out on **RBCP**. As presented on Figure 4.8 middle, **RBCP** nanostructures were rather well maintained in water (1.5 mL water per sample) at RT for at least to 6 h. However, after 2.5 days, it was observed that the morphology was totally adrift and the WCA was drastically reduced (Figure 4.8 right).

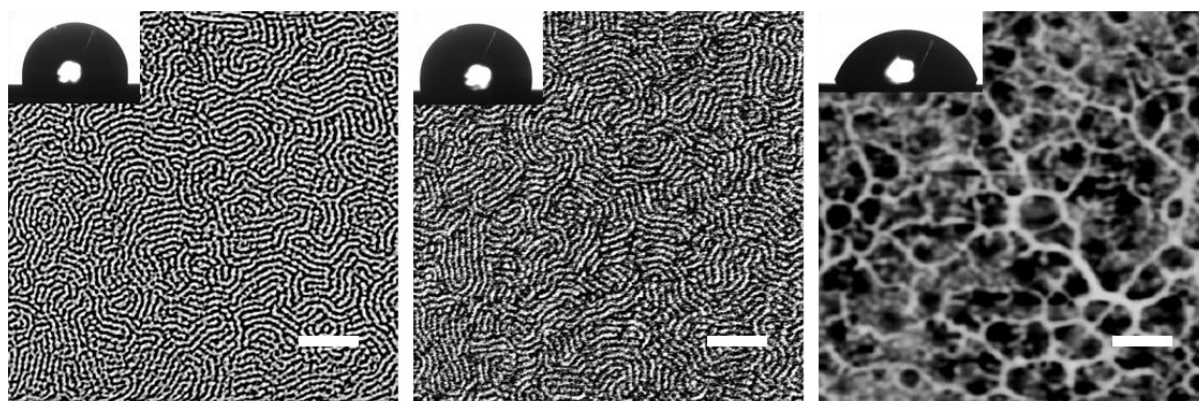


Figure 4.8 AFM phase image of (Left) **RBCP**, (Middle) After incubation in water for 6 h at RT, (Right) after incubation in water for 2.5 days at RT. The insets of the top row depict the water contact angle images obtained for the respective films. *Scale bars 300 nm.*

For further stability tests, we investigated **BCP-2**, **BCP-3**, and **BCP-4**. Figure 4.9 shows that the film morphologies were also maintained until at least 6 h in water at RT, although a cracked structure appeared. Since **BCP-4** has the lowest L_0 , it was challenging to obtain a good contrast between domains during AFM measurement in this case. It can be concluded that surface homogeneity of the surface is damaged in the case of functional BCPs faster than in the case of **RBCP**. Arguably, it might be different in the presence of another type of functionality, especially for those which are very hydrophobic or strongly hydrophilic. However, fundamentally, we do not expect drastic changes as the percentages of the functionalities are intentionally kept below 5% to preserve the parental properties. All in all, for water-borne experiments, it is advisable not to exceed a few hours of reaction time with these type of BCPs in order to preserve the underlying morphology.

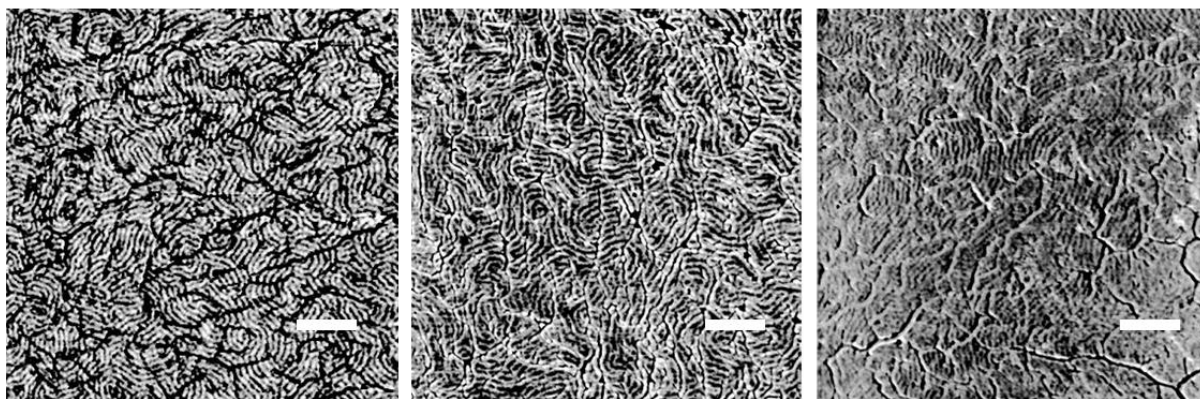


Figure 4.9 AFM phase image after incubation in water for 6 h of (Left) **BCP-2**, (Middle) **BCP-3**, and (Right) **BCP-4**. Scale bars 300 nm.

4.4.4 Thermal and Photo Crosslinking to Stabilize BCP Films

Many of the click-type reactions have already been reported in aqueous media. Recently we completed a study on the applicability of PFTR in water as well (see Chapter 6).^[349] Although click-type reactions are generally fast, the efficiency of attachment is still highly dependent on reaction conditions and might require extended times, which will potentially suppress the nanostructuring of our films, as shown above. In order to use these functional PMMA-*b*-PS films for extended periods of time in aqueous media but also to possibly extend their applicability in organic media, it is crucial to stabilize them. Crosslinking is a widely applied method to obtain hard mats and preserve film morphologies. It can be achieved either thermally or by UV irradiation. AMS and BrS are particularly suitable for this purpose.^[9, 194, 328] In the case of AMS, both thermal and photocrosslinking are possible while BrS is known to undergo crosslinking upon UV irradiation. For photocrosslinking, **BCP-3** was irradiated with UV light at 254 nm for 30 min under vacuum. After that, the film was washed with several organic solvents such as acetone, toluene, and THF. An AFM phase image recorded after these steps and is given on Figure 4.10 right, showing that the film is stable with the preserved nanostructure. For thermal crosslinking the **BCP-2** film was heated up to 250 °C for 2 h under vacuum. After rinsing with several organic solvents, AFM analysis was performed and revealed a preserved morphology, as depicted on Figure 4.10 right. In conclusion, both methods, i.e., photo and thermal crosslinking, were found to be applicable on such systems for film stabilization.

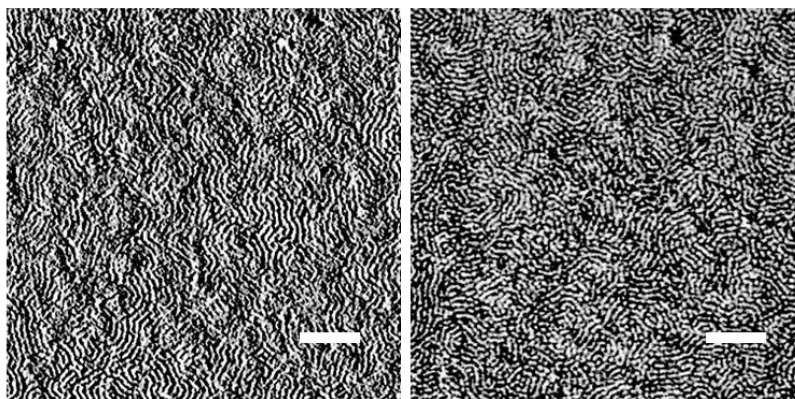


Figure 4.10 AFM phase image of (Left) **BCP-3** after photo-crosslinking and (Right) **BCP-2** after thermal crosslinking. Scale bars 300 nm.

4.4.5 Additional Polymers

In addition to the aforementioned BCPs, we investigated two more BCPs which are in fact the monofunctionalized counterparts of **BCP-4**, which carries on both blocks a pentafluorophenyl derivative. **BCP-6** possesses a plain PS block, while in **BCP-7** the PMMA block is devoid of functionality. Details are compiled in Table 4.3.

Table 4.3 Characteristics of **BCP-6** and **BCP-7**.

Entry	Initiator	$M_{n,SEC}^a$ (kg mol ⁻¹)	$M_{n,NMR}^b$ (kg mol ⁻¹)	\mathcal{D}^a	$f_{PS}:f_{PMMA}$	$L_{0,SAXS}^c$ (nm)
BCP-6	CP2	38.5	40.6	1.19	0.52:0.48	25.9
BCP-7	HP2	41.5	43.3	1.16	0.54:0.46	25.5

Values Calculated by ^aSEC ^bNMR ^cSAXS. *BCP-6 has PFPMA in the PMMA block and BCP-7 has PFS in the PS block.*

Interestingly, when the aforementioned coating strategy was applied with these two BCPs, it was not possible to obtain homogeneous films on the neutralized substrates. The films tended to dewet from the substrate, creating a layer with many gaps and holes (data not shown). In other words, **BCP-6** and **BCP-7** were not able to cover the substrates homogeneously. This is attributed to incompatibility of the surface energy of the BCP with the substrate. It is known that when the surface energy of the polymer is much higher than that of the substrate, the polymer is dewetted.^[175] In contrast, when both functionalities are present in the BCP, i.e., PFS is in the PS block and PFPMA is in the PMMA block, the energies seem balanced and one can obtain

homogeneous films with perfect nanostructuration as we reported in the case of **BCP-4**. Importantly, SAXS measurements were done on these two samples (Figure 4.11). In the case of **BCP-6**, the results prove the occurrence of a lamellar structure. The 1st maxima proves nanostructuration. There is a 2nd maxima which is less pronounced than the 3rd one which is extremely well-pronounced, altogether evidencing a lamellar phase. In the case of **BCP-7**, similar observations were made however the 3rd maxima is not very clear. Thus we can conclude that there is 'indication of lamellar' phase for **BCP-7**. To conclude, although **BCP-6** and **BCP-7** are shown to create lamellar structure, to utilize these polymers in the form of thin films, it is certainly necessary to apply a different coating strategies. For instance, another neutralizing random copolymer could be employed for the first coating step.

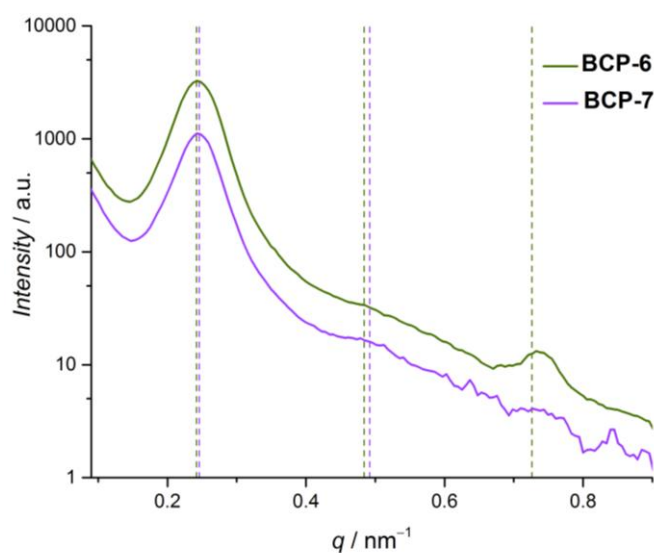


Figure 4.11 SAXS profiles of **BCP-6** and **BCP-7** with q , $2q$ and $3q$ values indicated with vertical dashed lines.

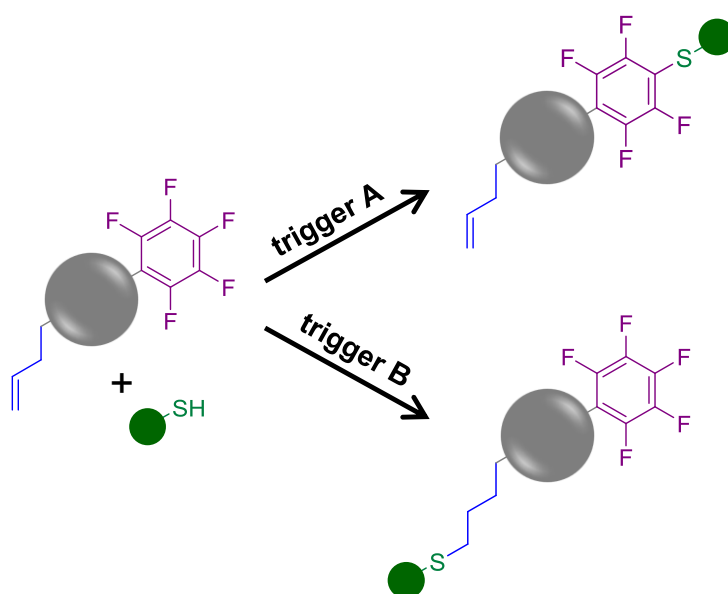
4.5 Summary

In this Chapter, we present the first study on the effect of the presence of functionalities on the phase separation behavior and L_0 values for a widely studied BCP system, namely PMMA-*b*-PS. We first showed the synthesis of several PMMA-*b*-PS, either with a single functionality in one block or with one in each block. The functionalities are introduced through derivatives of styrene and/or MMA which were copolymerized with their corresponding main monomer (e.g., pentafluorostyrene with styrene, allyl methacrylate with MMA). The percentages of the functional monomers are kept small (~5 mol%) so as to favor the conservation of the parental properties, particularly the phase segregation behaviour of the main backbone, while bringing

clickable moieties into them. First blocks were used as macroinitiators or macromolecular chain transfer agents that underwent chain extensions to create the second blocks. Initially, a non-functional PMMA-*b*-PS was produced by ATRP to be used as reference as it is the widely employed technique in the literature to synthesize PMMA-*b*-PS. However, since RAFT polymerization is more tolerant to functional groups and easier in terms of purification, we also employed it for the synthesis of some of the functional BCPs. Subsequently, we analyzed the phase separation behavior of these BCPs. Applying a two-layer coating strategy which includes a first layer of neutralizing random copolymer of styrene and MMA and a second layer made of the BCP, we managed to observe perpendicular lamellar structure in most cases. The molar mass, composition, and thickness of the random copolymer layer together with the thickness and volumic fractions of the BCP were all set in agreement with the previous findings of the literature that are known to exhibit perpendicular lamellar structures. With percentages below 10 mol%, we showed that these clickable moieties do not fundamentally perturb the nanostructure of the BCP thin films, in most cases. The outcomes were evidenced by AFM and SAXS. There exist only small fluctuations in L_0 in the presence of each monomer. The films were classically thermally annealed while microwave treatment also proved useful for milder annealing in the view of preserving thermally sensitive chemical groups. The non-functional, reference BCP was found to exhibit the biggest L_0 which decreases in the presence of functional handles, especially with that of halogenated monomers. The films were shown to be suitable for water borne experiments only a limited period of time (at least 6 hours). Moreover, crosslinking using heat or UV light was preliminarily evaluated and suggested the applicability in organic media as well. This investigation is the first step towards a versatile BCP platform which could be used to produce nanoscale patterns for the co-immobilization of (bio)molecules in very close proximity.

5

Orthogonality of Two Modular Ligations: Thiol-Ene and *para*-Fluoro-Thiol Substitution



Parts of this Chapter were reproduced with permission from H, Turgut, G. Delaitre, *Chem. Eur. J.* **2016**, 22, 1511-1521. Copyright © 2016 WILEY-VCH Verlag GmbH & Co. KGaA, Weinheim.

5.1 Introduction

Enrichment in chemical diversity of BCPs is crucial to create multifunctional polymers and to broaden the range of potential applications, in addition to improvements in synthetic efficiencies and structural control. The versatility of BCPs can be enhanced by introducing functional elements either into the backbone or on the side chains. This type of modifications allow postpolymerization chemistries to be applied, while inheriting the parental properties from the main backbone.^[334] There are covalent and noncovalent strategies to perform postpolymerization modifications on BCPs. Despite a great potential in applications ranging from drug delivery to electronics and nanotechnology, only a limited number of reports regarding postpolymerization modifications of BCPs appeared so far.^[334] In this part of the dissertation, we present a dual orthogonal fully thiol-based modular ligation combination on a functionalized BCP. The strategy is depicted on the cover image of this Chapter.

Why thiols? The importance of thiols was explained in Section 2.2.2. The types of reactions that thiols undergo were also summarized. The readers are kindly redirected to that part for detailed information. Among these reactions, in the present section, we report on the orthogonality of photo-initiated radical thiol-ene and PFTR. As it is suggested on Scheme 5.1, two distinct means are applied to trigger the reactions: base triggered PFTR takes place on the pentafluorophenyl (PFP) moieties in one case without consuming the alkenes and in the second case, photoinduced thiol-ene addition occurs with no effect on pentafluorophenyl moieties. The overall process exhibits ‘orthogonality’ which will be discussed in the subsequent section.

5.2 The Orthogonality Principle

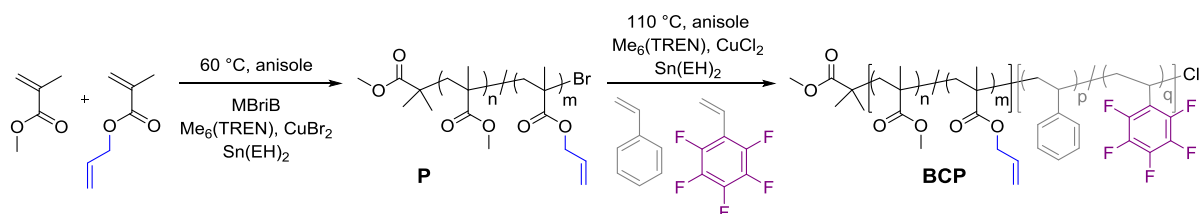
Thiols undergo numerous reactions as discussed in Section 2.2.2. In this study, we were interested in combining the PFTR with UV triggered thiol–ene reaction since both can be carried out at ambient temperature and under mild conditions without a metal catalyst. Principally, as these reactions can be triggered by distinct activators/catalysts, it should be possible to develop protocols for which the two reactions can take place in the presence of all reaction partners, i.e., thiols, pendant double bonds, and pentafluorophenyl moieties, thereby fulfilling the requirements of orthogonality.

The orthogonality concept generally includes a set of chemical reactions that occur without interfering with other chemical functionalities present in the surroundings.^[350] In biological sciences, it means that the reaction partners do not interfere with unmodified biomolecules, such as carbohydrates, peptides, or proteins.^[351] In a more synthetic context, two reactions can

be considered orthogonal if one occurs with no alteration of the chemical functionalities involved in the other one. For instance, copper-catalyzed 1,3-dipolar cycloadditions and Diels-Alder reactions can obviously be considered orthogonal.^[63] While the orthogonality concept usually concerns two pairs of reactive groups (A reacts with B, C, reacts with D), we address here a different type: one reactive group (i.e., thiol) is placed in the presence of two reaction partners (i.e., pentafluorophenyl and allyl groups). Our main purpose can thus be summarized as follows: guiding thiol molecules to either a PFP moiety or a nonactivated double bond; consequently enabling spatial and temporal control over the functionalization of scaffolds bearing both functionalities, for instance in BCP films such as those reported in the previous Chapters of this Thesis.

5.3 The Doubly Reactive Platform

We employ a diblock copolymer, namely poly(MMA-*co*-AMA)-*b*-poly(styrene-*co*-PFS) (P(MMA-*co*-MMA)-*b*-P(S-*co*-PFS)), as a platform for our orthogonality investigations.



Scheme 5.1 Synthesis of the doubly reactive platform: poly(MMA-*co*-AMA)-*b*-poly(styrene-*co*-PFS). MBriB: methyl 2-bromoisobutyrate, Me₆(TREN): tris[2-(dimethylamino)ethyl]amine, Sn(EH)₂: tin(II)2-ethylhexanoate.

The synthetic steps to obtain p(MMA-*co*-AMA)-*b*-p(S-*co*-PFS) by ARGET ATRP are shown in Scheme 5.1. MMA was copolymerized with AMA (5 mol%) by ARGET ATRP to yield the first block (denoted as **P**), in which reactive allyl groups were incorporated in view of radical thiol-ene addition (Figure 9.17). Monomer conversions were kept low to avoid potential side reactions with the allyl group.^[352] The purified macroinitiator was chain-extended by ARGET ATRP with styrene and PFS (5 mol%) to generate the doubly reactive **BCP** (Figures 9.18-9.20). A series of polymers with similar molar masses and compositions were made and used in this study (Table 5.1). Incorporation of high amounts of reactive handles could alter the intrinsic features of the polymer, e.g., phase separation behaviour (aspect related to Chapters 3 and 4) as well as thermal, mechanical, or optical properties. Therefore, we kept the amount of

functional monomers below 10 mol%, considering that the properties of the main backbone could be preserved with such a low amount, while introducing new features.

Table 5.1 Detailed information on the reactive BCPs employed herein.

Entry	Initiator	$M_{n,SEC}^a$ (kg mol ⁻¹)	\bar{D}^a	AMA content		PFS content	
				mol% ^b	wt%	mol% ^b	wt%
P1	MBriB	10.80	1.15	5.5	6.8	-	-
P2	MBriB	10.58	1.18	5.4	6.7	-	-
P3	MBriB	10.30	1.18	5.3	6.6	-	-
P4	MBriB	9.98	1.20	5.3	6.6	-	-
P5	MBriB	9.97	1.20	5.6	6.9	-	-
BCP[1]	P1	20.52	1.17	3	3.5	4.4	8
BCP[2]	P2	18.50	1.15	3.1	3.7	4.2	7.8
BCP[3]	P3	17.20	1.15	3	3.6	4.1	7.7
BCP[4]	P4	18.10	1.16	2.96	3.5	4.6	8.4
BCP[5]	P5	18.90	1.21	2.75	3.2	5.5	9.9

Values obtained by ^aSEC ^bNMR

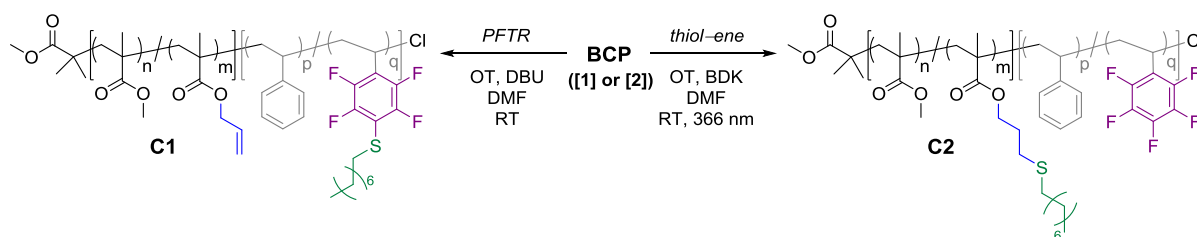
5.4 Orthogonality Investigations

Conditions for PFTR and thiol-ene to occur independently, sequential functionalizations, and 3 types of *one-pot* reactions are here reported. Previously, a few studies addressed the concept of orthogonality or two thiol ligations; however, only partial orthogonality was established as the sequences presented could only occur in one direction^[353-355] (one reaction had to be completed before the other) and/or a protection/deprotection strategy was used.^[353, 355] In our study, all reactive groups are present in the medium from the start, with no protection chemistry. The system is fully bidirectional, i.e., an identical final product structure can be achieved starting with PFTR or with thiol-ene addition, followed by the other reaction.

5.4.1 Thiol-Ene and PFTR Occurring Separately

During the course of this Thesis, the teams of Roth^[103] and Boyer^[356] reported relevant results on the PFTR and phototriggered thiol-ene reactions, respectively, which highlighted the suitability of a broad spectrum of thiols for both ligations. In this work, we selected 1-octanethiol (OT) and mercaptoethanol as model compounds because aliphatic thiols are

ubiquitous. We first focused on establishing the conditions for each reaction to occur with the fastest kinetics without causing any changes in the other part of the BCP (Scheme 5.2). DMF was chosen as the common solvent in our experiments for both reactions since the nucleophilic PFTR had previously been exclusively reported in nonprotic polar solvents, with bases as activators.



Scheme 5.2 Chemical routes to direct thiols towards either PFS units or allylic double bonds for the PFTR or thiol-ene addition, respectively. DBU: 1,8-diazabicyclo[5.4.0]undec-7-ene, BDK: benzyl dimethyl ketal.

As highlighted by Noy et al.,^[103] and as opposed to most previously reported studies on PFTR in which triethylamine (TEA) is used as the base, DBU yields ultra fast substitution with aliphatic thiols. In our setup, ¹⁹F NMR spectroscopy measurements revealed that the PFTR could be completed in 2 min with one equivalent of DBU and five equivalents of OT (according to PFS units) at ambient temperature (C1). The original PFS units exhibit three distinct characteristic signals corresponding to the fluorine atoms in the *ortho*, *para*, and *meta* positions of the PFP motif in the order of decreasing chemical shifts (Figure 5.1, top). Upon PFTR, the *para*-fluorine signal completely vanishes, while the *meta* peak shifts towards a higher chemical shift (Figure 5.1, middle). Analysis of the ¹H NMR spectra revealed the appearance of a signal corresponding to the two protons in the α position of the sulfur atom (signal a in Figure 5.2A), which was then used to confirm the quantitative transformation by integration of the peaks (Figure 9.21). Importantly, at the same time, the pendant double bonds of the PMMA block do not undergo any reaction, as shown by the intact allylic proton signals a, b, and c (Figures 5.2A and 9.21).

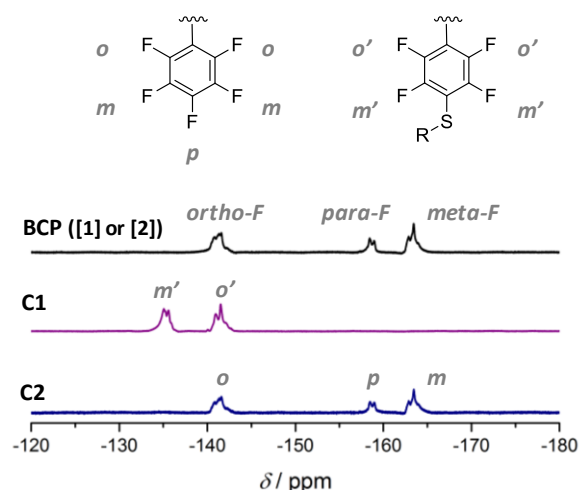


Figure 5.1 ^{19}F NMR spectra of **BCP** (top), **C1** (middle), and **C2** (bottom).

In addition, only a slight shift towards higher molar masses was detectable upon comparison of the size exclusion chromatograms of **BCP** before and after the PFTR (Figure 5.3B). Nevertheless, post-polymerization modifications on a few units of a polymer with heavier modules does not necessarily call for an increase in molar mass measured by SEC: potential changes in the hydrodynamic behavior of the polymer chains could lead to an opposite shift or even in no shift. Conservation of the overall shape of the molar mass distribution is more important, which suggest a clean transformation with no modification of the polymer backbone (e.g., no cross-linking reaction).

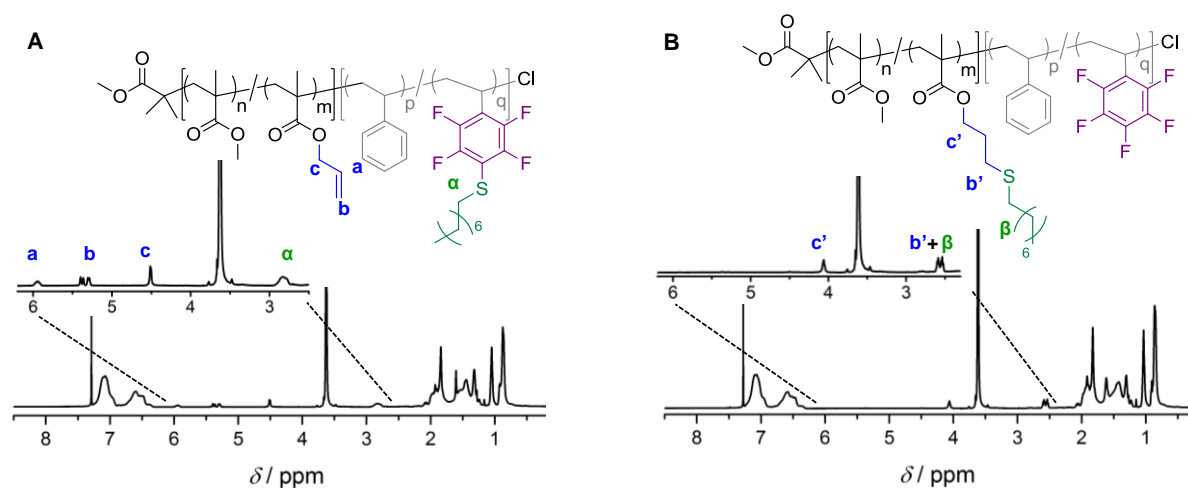


Figure 5.2 A) ^1H NMR spectrum of **BCP[1]** after PFTR with OT (**C1**). B) ^1H NMR spectrum of **BCP[2]** after thiol-ene reaction with OT (**C2**). Adapted with permission from ref [64]. Copyright 2016 Wiley.

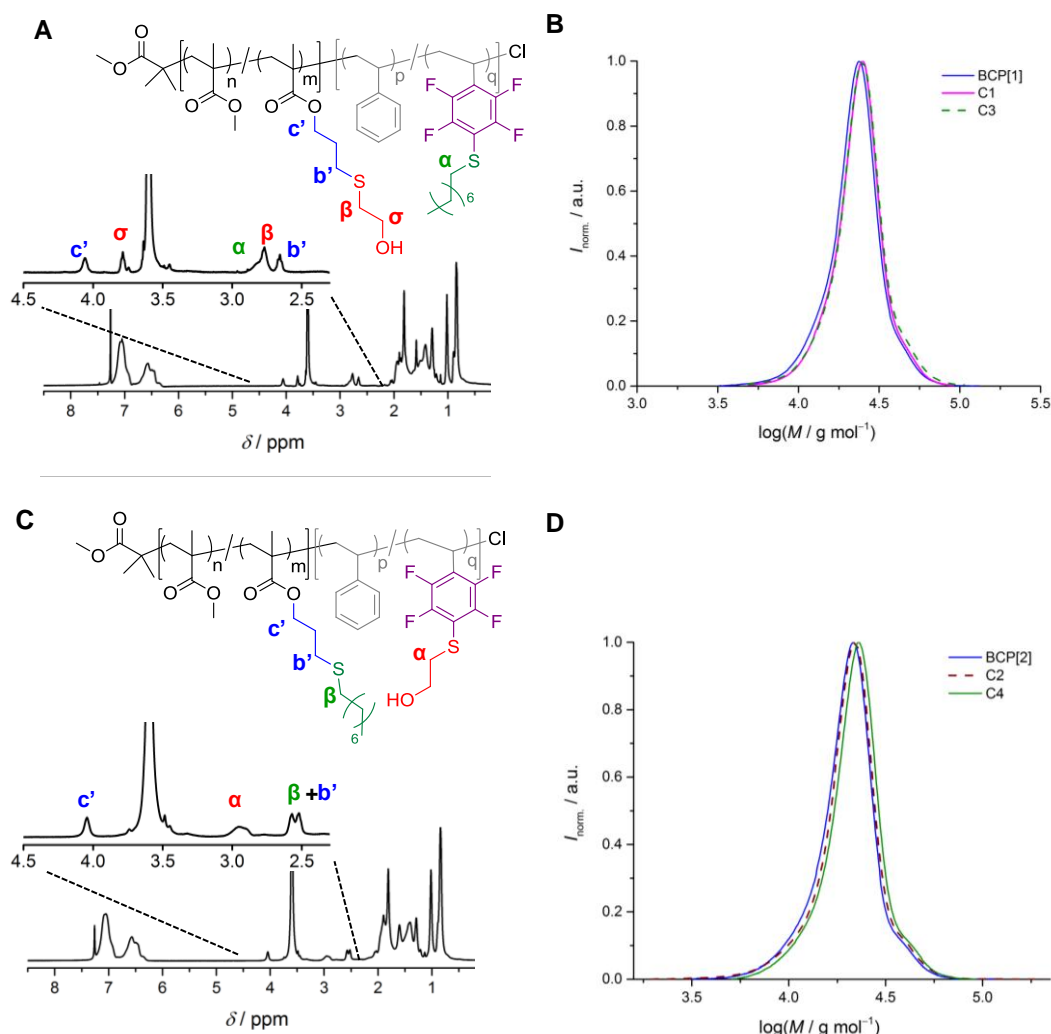


Figure 5.3 A) ^1H NMR spectrum of C3. B) SEC traces of BCP[1], C1, and C3. C) ^1H NMR spectrum of C4. D) SEC traces of BCP[2], C2, and C4. Adapted with permission from ref [64]. Copyright 2016 Wiley.

As a next step, the influence of DBU concentration on the PFTR was assessed through the same procedure and lower amounts of DBU (Table 5.2). Just 0.4 equivalent of DBU allowed full conversion to be achieved in a reasonably short time (30 min).

As a continuation, radical thiol-ene addition onto the allylic groups incorporated in the PMMA block of BCP[2] was investigated. We selected the phototriggered variant of the radical thiol-ene addition as it can also take place at ambient temperature. Particularly, we opted for a conventional radical photoinitiator (BDK) because, in contrast to other reported efficient systems such as photocatalysts,^[356] it provides an economical, metal-free, and additive-free alternative. A basic, handheld UV lamp generally employed for TLC analysis was utilized, at $\lambda = 366$ nm. Pleasantly, BDK permitted quantitative conversion of the allyl groups into thioethers in

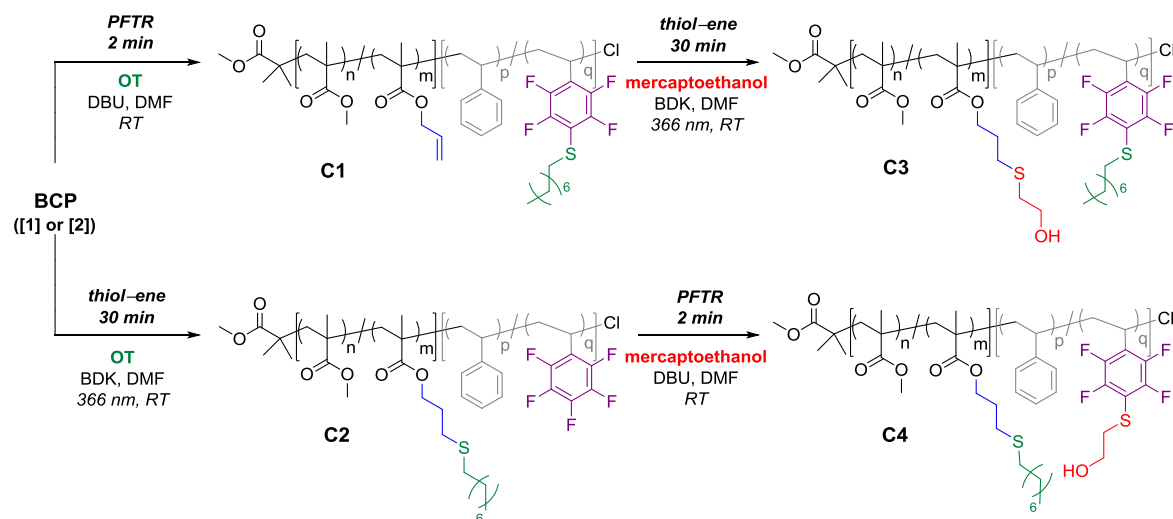
30 min under classical thiol–ene conditions, i.e., 5 equivalents of thiol and 0.5 equivalent of photoinitiator (Figure 5.2B). Notably, the SEC chromatogram (Figure 5.3D) and the ^{19}F NMR spectrum of **BCP[2]** (Figure 5.1, bottom) remained unaltered after the thiol–ene addition, which brought the PFTR/photo-thiol–ene pair closer to qualifying as orthogonal.

Table 5.2 Conversions of PFTR with different amounts of DBU.

OT eq.	DBU eq.	T	Result
5	0.15	50 °C	4 h, 48% conv.
5	0.2	RT	4.5 h, 50% conv.
5	0.3	RT	1 h, 78% conv.
5	0.4	RT	30 min, full conv.
5	1	RT	2 min, full conv.

5.4.2 Dual Functionalizations with Intermediate Purification

5.4.2.1 Direct Functionalization of BCPs Obtained in Single-Reaction Studies



Scheme 5.3 Chemical routes towards dual functionalization by sequential PFTR and thiol–ene addition. Adapted with permission from ref [64]. Copyright 2016 Wiley.

After showing the possibility of engaging both thiol-reactive segments independently, we subsequently aimed to achieve dual functionalization. A methodology involving intermediate purification was first considered. Monofunctionalized BCPs **C1** and **C2**, previously obtained by PFTR and thiol–ene addition with OT, respectively (see above), were therefore reutilized to

perform the complementary reaction with another model thiol on the non-reacted segment. As depicted in Scheme 5.3, the thiol-ene reaction was quantitatively performed on **C1** with mercaptoethanol in 30 min to cleanly obtain **C3**, as evidenced by NMR spectroscopy and SEC results (Figures 5.3A, 5.3B, and 5.4). In parallel, compound **C2** underwent full PFTR with mercaptoethanol in 2 min to produce **C4**, in agreement with previous results (Figures 5.3C, 5.3D, and 5.4). This pair of experiments highlights the opportunity of grafting distinct thiols onto distinct parts of a single scaffold, with no concern regarding the reaction sequence order.

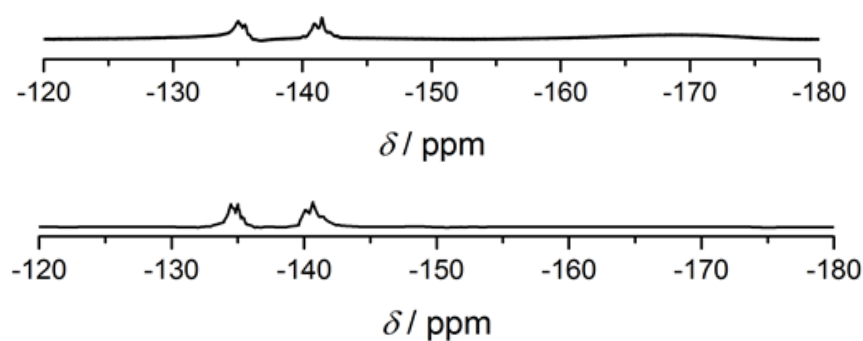


Figure 5.4 ^{19}F NMR spectra of **C3** (top) **C4** (bottom).

5.4.2.2 Control Experiment with Ethanol

As it is known that pentafluorophenyl units are susceptible to reaction with alcohols and amines besides thiols, it is essential to prove in the case of PFT with mercaptoethanol that the substitution takes place exclusively at the thiol moiety. For this, a control experiment with ethanol, which is the analogue of mercaptoethanol without the thiol moiety, was carried out: no ^{19}F NMR spectroscopy revealed no change in the pentafluorophenyl peak pattern, leading to conclude that only substitution by the thiol moiety took place in the presence of mercaptoethanol (Figure 5.5)

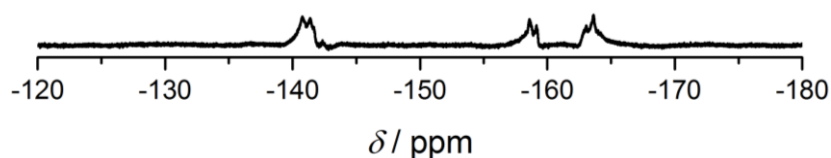
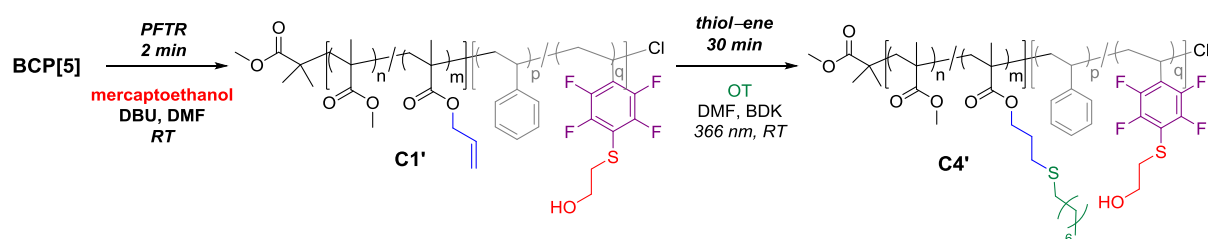


Figure 5.5 ^{19}F NMR spectrum obtained after the PFTR control experiment with ethanol.

5.4.2.3 Changing the Thiol and Reaction Sequences

In Section 5.4.2.1, two sequences were carried out with a different reaction order, yet with a reversed thiol order (OT first, then mercaptoethanol), which yielded different products (**C3** and **C4**). We here show that it is possible to produce identical products by inverting both the reaction sequence and the thiol order at the same time. More simply, compound **C4'**, strict image of **C4**, could be produced by grafting mercaptoethanol by PFTR first (**C1'**) followed by thiol-ene addition with OT (Scheme 5.4). ^1H NMR spectra of **C1'** and **C4'** are given on Figure 9.22. ^{19}F NMR spectra and SEC traces of the final product **C4'** exhibit strictly identical features as for **C4** and prove the success of this reaction sequence (Figure 5.6).



Scheme 5.4 Synthetic conditions for obtaining **C4'**, equivalent product to **C4**, with inversion of the reaction sequence and an intermediate purification step.

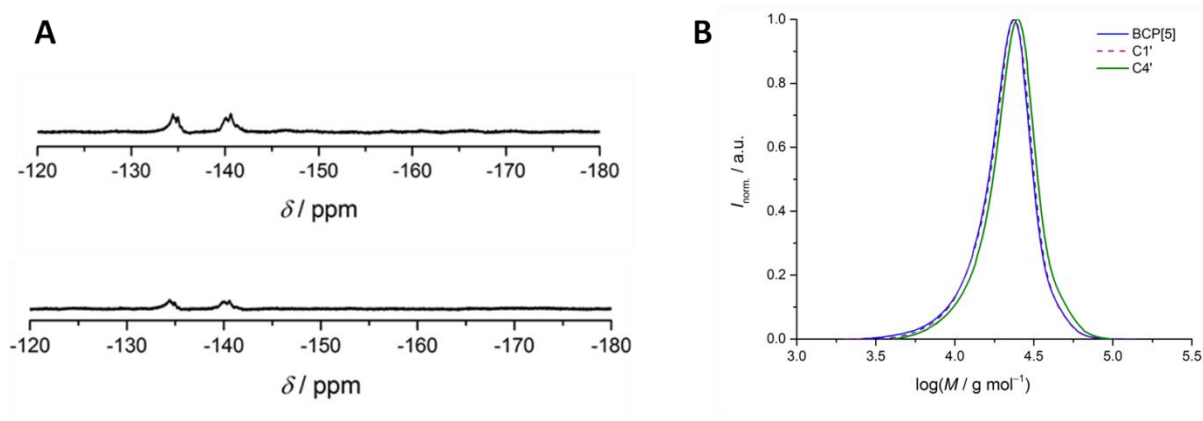


Figure 5.6 A) ^{19}F NMR spectra of **C1'** (top) and **C4'** (bottom). B) SEC traces of **BCP[5]**, **C1'**, and **C4'**. Adapted with permission from ref [64]. Copyright 2016 Wiley.

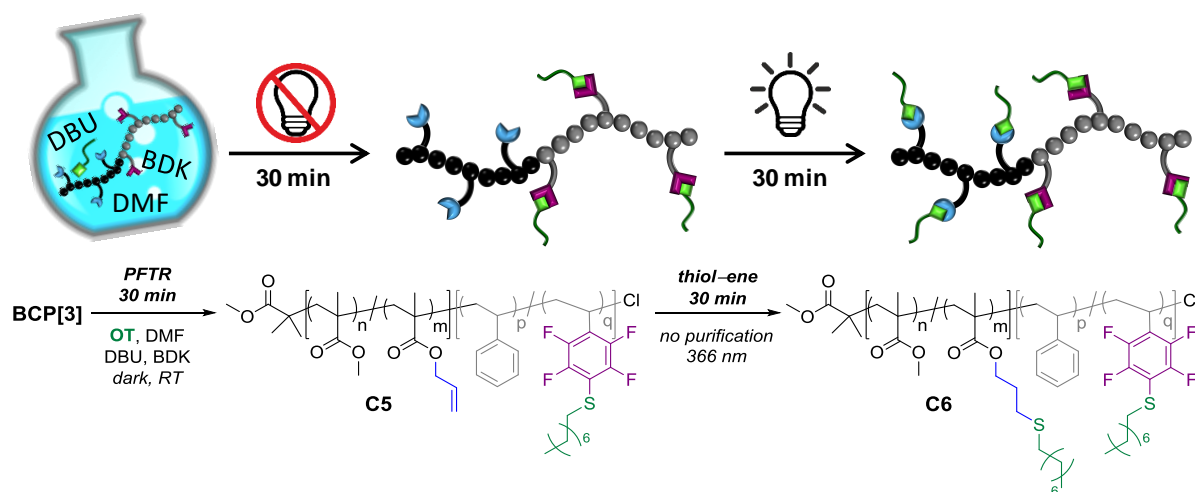
These successful series of dual functionalization experiments prove the bidirectionality of this modular ligation pair and consequently true orthogonality.

5.4.3 One-Pot Dual Functionalizations

To reduce the overall synthetic effort, it is usually advisable to eliminate purification procedures. Accordingly, we investigated three different variants of one-pot synthesis. For characterization purposes, each experiment was initially performed in an identical manner in two separate vessels: one flask served for the characterization of the first step, while the second one underwent the entire sequence and led to the final dual-functionalization product.

5.4.3.1 One-Pot *Type 1*

Type 1 is a batch process where all components involved in the PFTR and thiol-ene addition are present from the start and in which an external stimulus, i.e., light, is applied at a later stage. The mixture is firstly stirred in the dark to let the nucleophilic substitution occur, which happens without any energy input. Then, a UV light source is turned on to trigger the thiol-ene reaction (Scheme 5.5). Disappointingly, when all components for the PFTR and thiol-ene reactions were combined from the start in the same stoichiometry as previously employed, the thiol-ene addition could however not take place. This could be explained by the presence of DBU, which is a tertiary amine capable to engage in radical processes such as hydrogen abstraction and eventually addition onto alkenes.^[357-358] Furthermore, a large fraction of thiols are in a deprotonated thiolate state and are consequently not available for thiyl radical formation. Indeed, increasing the photoinitiator concentration (up to [BDK] = [OT]) did not solve this issue. Since the PFTR step was already extremely fast with [DBU]/[PFS] = 1, we decided to decrease the amount of DBU in the medium to overcome this issue. Based on the aforementioned investigations on PFTR alone (see Section 5.4.1), a DBU/PFS molar ratio of 0.4 was employed, as it allowed completion of the first step in a reasonably short time (30 min, see Table 5.2). This was combined with a 0.5 molar ratio of BDK to pendant double bonds.



Scheme 5.5 Representation of *Type 1* dual functionalization. (Top) Simplified cartoon. (Bottom) Synthetic route for the one-pot batch sequential procedure. Adapted with permission from ref [64]. Copyright 2016 Wiley.

Since the PFS molar content is slightly higher than that of AMA in **BCP[3]** (4.1 vs. 3.0 mol%, see Table 5.1), a 5-fold excess of OT with respect to PFS units guarantees a similar excess for the second step (i.e., thiol-ene addition): after 1 equivalent has been consumed in the first step, 4 equivalents are left, which leads to a remaining 5.5-fold excess with respect to the allylic groups. Under these conditions, quantitative PFTR with OT was completed in 30 min, as demonstrated by ^{19}F NMR spectroscopy (Figures 9.23 and 9.24), while full persistence of the allylic bonds was confirmed by ^1H NMR spectroscopy (similar ^1H NMR spectrum as that of **C1**, see Figure 5.2A). Afterwards, exposing the reaction medium to UV light for 30 min induced full transformation of the allylic groups into thioethers (Figure 5.7A). One-pot *Type 1* thus allows controlled and quantitative conversion of all reactive groups separately, with an overall reaction time of one hour. Molar masses of **C5** and **C6** slightly increased and, more importantly, their molar mass distributions remained as narrow as that of the originally non-reacted BCP (Figure 5.7B).

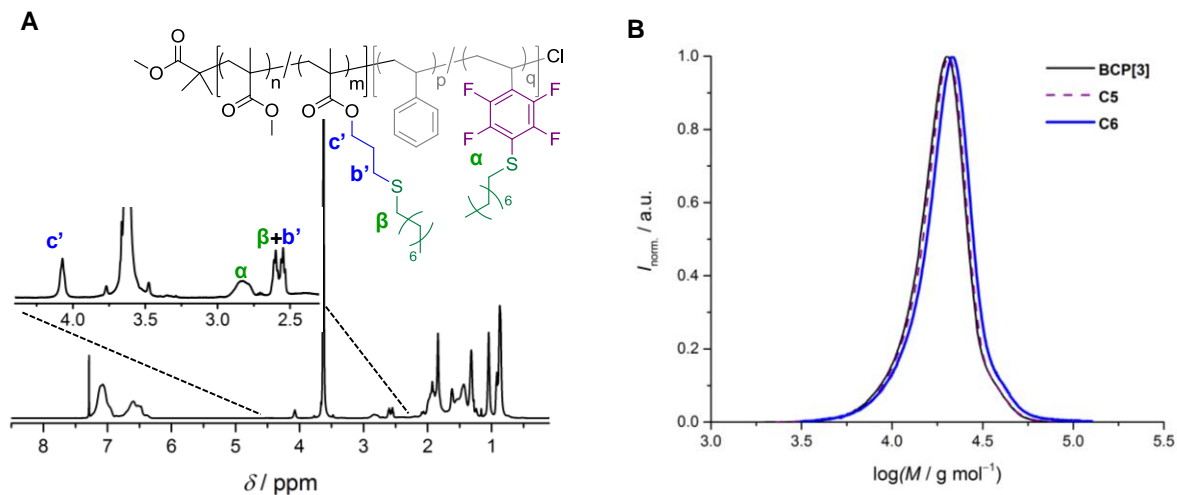


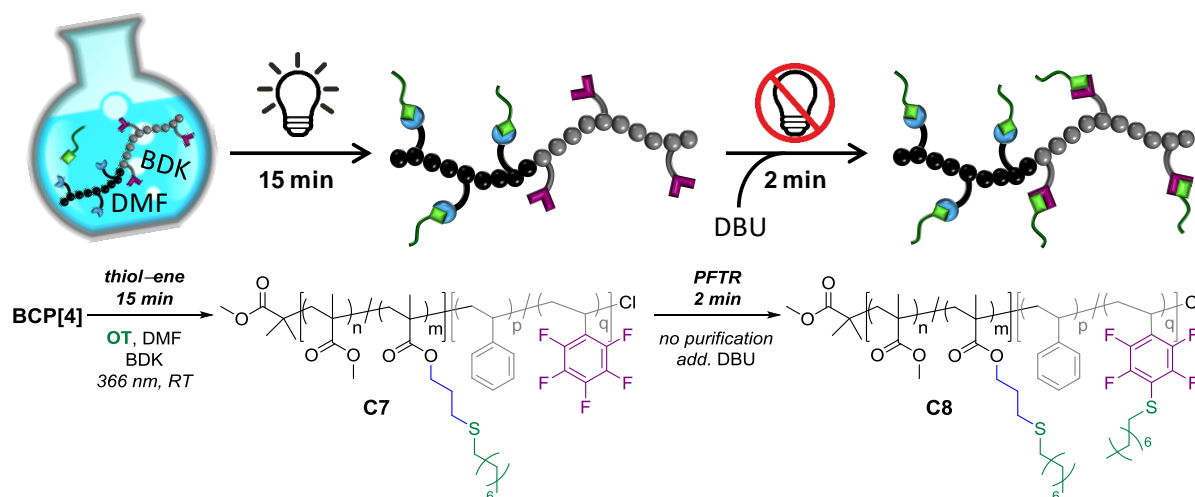
Figure 5.7 A) ^1H NMR spectrum of **BCP[3]** after undergoing *Type 1* dual functionalization with OT (overall reaction time = 1 h, **C6**). B) Size-exclusion chromatograms of BCP before the reaction, after the *Type 1* PFTR step (30 min, **C5**), and after the complete *Type 1* dual functionalization (overall reaction time = 1 h, **C6**). Adapted with permission from ref [64]. Copyright 2016 Wiley.

5.4.3.2 One-Pot Type 2

In this Section, we assess the possibility of reversing the sequence employed in *Type 1*, i.e., carrying out the thiol–ene addition before the PFTR, again in one-pot. To achieve this, it is necessary to slow down the PFTR step because under the previously employed conditions it is not possible to complete the thiol–ene addition before any thiol grafting starts onto the PFS units. Our first idea was to decrease the amount of DBU. For example, an amount of DBU as low as 0.15 equivalent could allow the thiol–ene reaction to be achieved in a few tens of minutes. However, we found that even after 5 h the PFTR could not be completed with this amount of DBU (see Table 5.2). A second idea was to use a base that induces a slower PFTR, e.g., TEA. In that case, another issue arises: The required amount of TEA, which is a weaker activator for alkanethiols in PFTR, is so high that the thiol–ene addition rate is drastically reduced. For instance, the combination of 90 equivalents of TEA (with respect to PFS units, i.e., a typical amount for TEA-induced PFTR) with 0.5 equivalent of BDK resulted in incomplete thiol–ene addition after 3 h, time after which the first indications of PFTR already appeared (Table 5.3). More problematic, under these conditions, the PFTR actually does not reach full conversion, even at 60 °C for 24 h. This alternative is therefore not conclusive either.

Table 5.3 Thiol–ene reaction results with various quantities of TEA and BDK.

TEA eq.	OT eq.	BDK eq.	Thiol-ene outcome
100	5	0.5	74% conv., 1 h
90	5	0.5	98% conv., 3h
90	5	0.6	100% conv., 3h



Scheme 5.6 Representation of *Type 2* dual functionalization. (Top) Simplified cartoon. (Bottom) Synthetic route for the one-pot batch sequential procedure. Adapted with permission from ref [64]. Copyright 2016 Wiley.

Eventually, we designed the second dual functionalization route (*Type 2*) by delaying the addition of DBU. The reaction sequence still takes place in the same vessel and without intermediate purification, yet in this case, qualifies as a one-pot, semibatch reaction (Scheme 5.6). This way, it was possible to perform the first step under the same conditions as for the independent thiol–ene functionalization (Section 5.4.1, synthesis of **C2**). This first step was completed in only 15 min to yield **C7** (Figure 9.26). Indeed, as five equivalents of OT with respect to PFS units were initially added and since the number of PFS units was slightly higher than that of allyl groups in the employed BCP (**BCP[4]**, see Table 5.1), the [thiol]/[allyl] ratio was slightly higher than that in our previous independent thiol–ene investigations (7.8 vs. 5; see Section 5.4.1). Importantly, after UV irradiation, there was no difference between the ^{19}F NMR spectra of **C7** and of the starting BCP, i.e., **BCP[4]** (Figure 5.1 top and Figure 9.25), which proved that no PFTR had occurred in parallel. After 15 min of irradiation, the lamp was turned off and DBU (1 equivalent with respect to allyl groups) was introduced. After two minutes, a ^{19}F NMR

spectrum was recorded and revealed integral loss of the *para*-fluorine atom signal, along with the expected shifts of the *meta* signal (Figure 9.25).

Again, the molar mass distribution of the intermediate and final products, respectively **C7** and **C8**, slightly shifted towards higher molar masses and remained as narrow as that of the starting **BCP[4]** (Figure 5.8B). The ^1H NMR spectrum of **C8** was similar to that of **C6**, evidencing a similar outcome for both *Type 1* and *Type 2* routes (Figure 9.27). Nevertheless, the delayed addition of DBU in the medium allowed both reactions to be carried out at full rate, leading to a dual functionalization completed in only 17 min, as opposed to one hour for the *Type 1* one-pot reaction.

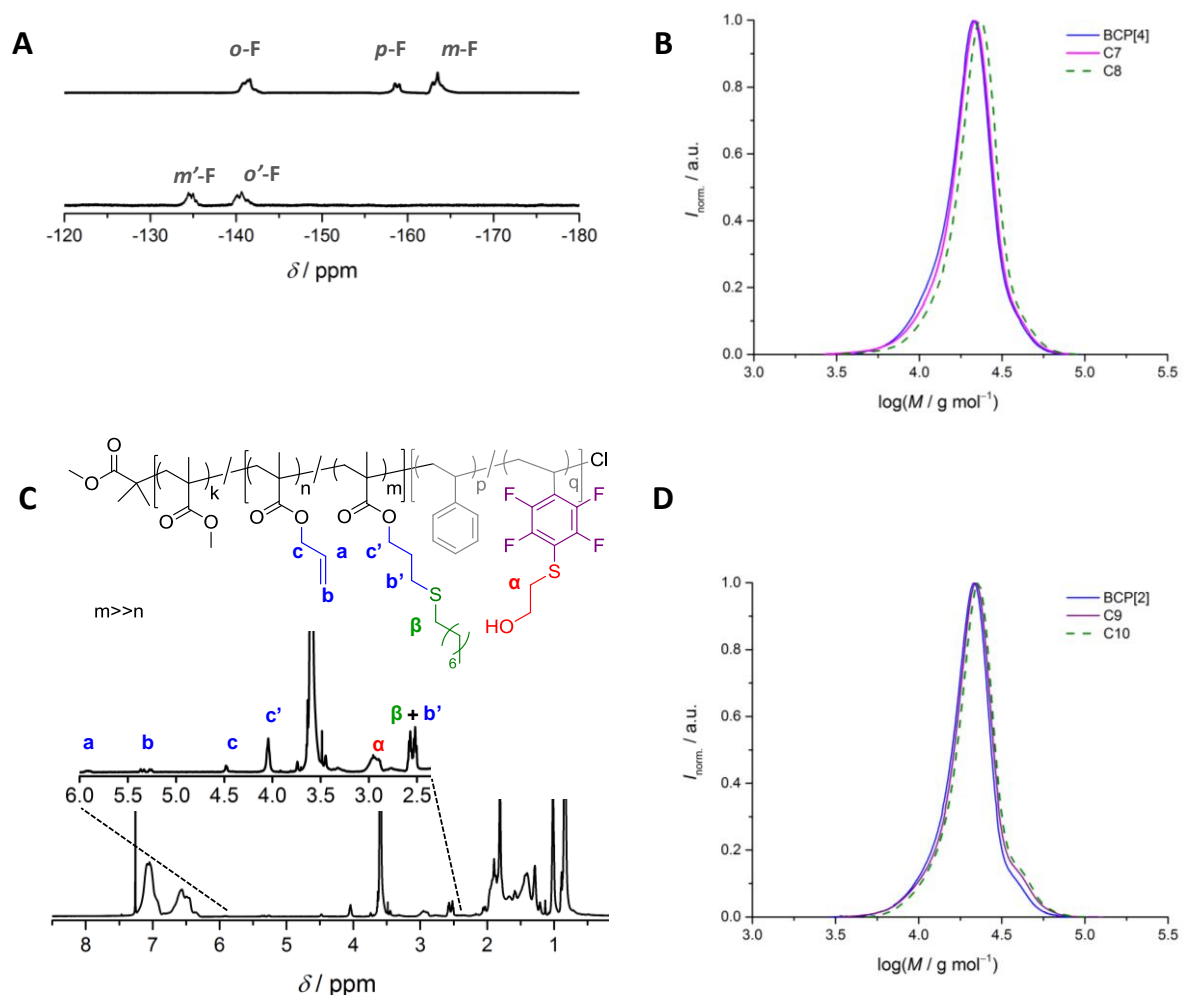
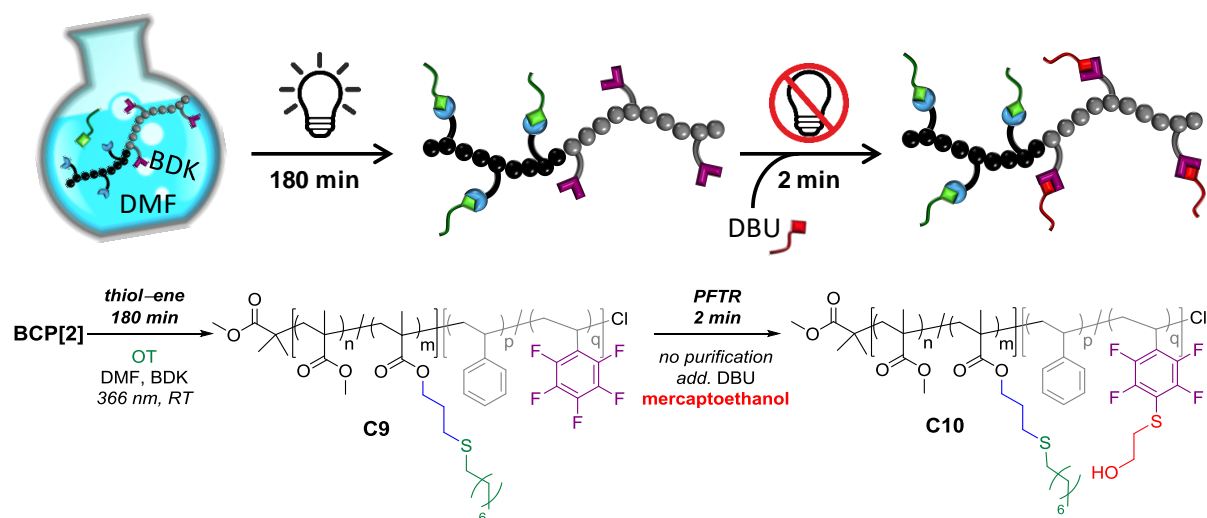


Figure 5.8 A) ^{19}F NMR spectra of (top) **C9** and (bottom) **C10**. B) SEC traces of **BCP[4]**, **C7**, and **C8**. C) ^1H NMR spectrum of **C10**. D) SEC traces of **BCP[2]**, **C9**, and **C10**. Adapted with permission from ref [64]. Copyright 2016 Wiley.

5.4.3.3 One-Pot Type 3

We eventually developed a third one-pot route (*Type 3*), to synthesize a BCP with two distinct grafted thiols (first by thiol-ene, then by PFTR), which is clearly more interesting in terms of applications (Scheme 5.7). We hypothesized that, if only a slight excess of a first thiol (e.g., 1.1–1.2 equivalents) were added in the first step, the introduction of a second thiol in an excess similar to what was described before (typically five equivalents), the remaining amount of the first thiol in the second step would largely be overcome by the second one.



Scheme 5.7 Representation of *Type 3* dual functionalization. (Top) Simplified cartoon. (Bottom) Synthetic route for the one-pot batch sequential procedure. Adapted with permission from ref [64]. Copyright 2016 Wiley.

With a method adapted from *Type 2* functionalization (DBU not present from the start), 1.1 equivalent of OT was first introduced along 0.5 equivalent of BDK in a decreased volume of DMF, so as to keep the radical concentration at an adequate level. Nevertheless, under these conditions, thiol-ene addition was slower than previously (88% conversion in 3 h, see Figure 9.28), yet PFS units all remained intact (Figure 5.8A, top). The light source was then switched off and PFTR was started by the addition of DBU and OT (1 and 5 equivalents with respect to PFS units, respectively). As previously observed, this step was completed in just two minutes (Figure 5.8A, bottom). Minor shifts of the SEC distributions, yet with similar breadths, were witnessed upon completion of both steps (Figure 5.8D). The one-pot *Type 3* route permitted to functionalize both blocks with distinct thiols, with yet only a minimal amount of residual non-reacted double bonds and no apparent cross-contamination (Figure 5.8C).

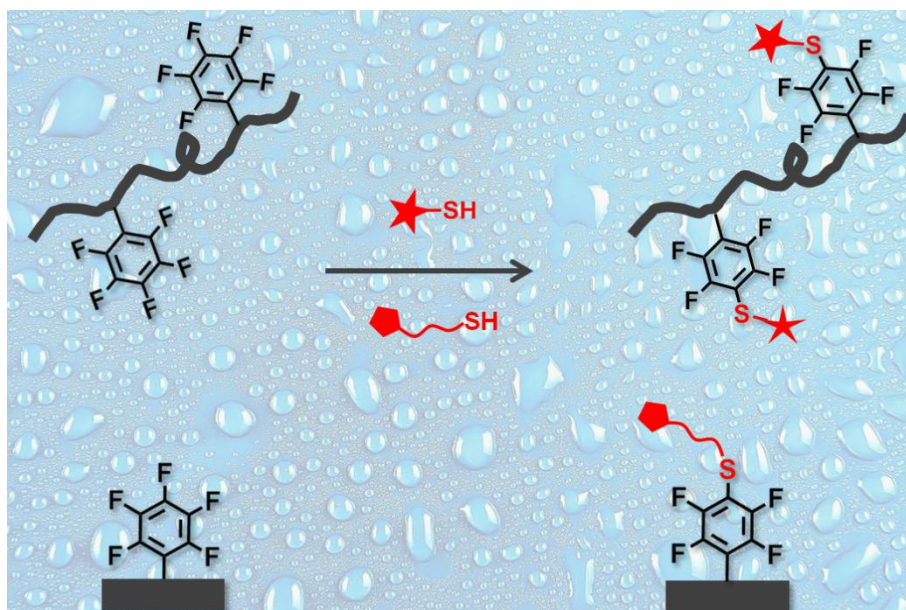
5.5 Conclusion and Outlook

This study shows that for a scaffold possessing two distinct moieties that are reactive towards the same species, here thiols, it is envisageable to address one of the former without altering the other without a protecting group strategy; which is the principle of chemical orthogonality. We employed two thiol based chemistries, namely, radical thiol–ene addition and *para*-fluoro thiol substitution, which can be independently set off and proceed under ambient conditions. Each transformation carried out separately may proceed to full completion within minutes. When all reagents are initially present, the use of light as an external trigger for thiol–ene addition enables clean and quantitative sequential dual modification in one hour. However, since PFTR with reasonable kinetics could not be delayed, a reverse sequence with thiol–ene addition occurring first could not be achieved in batch mode. A potential alternative would be to have recourse to a photobase generator operating at a different wavelength from that of the photoinitiator employed to also externally trigger the PFTR step. This would be certainly beneficial as the presence of a base undoubtedly affects the kinetics of thiol–ene addition. Nevertheless, the delayed addition of DBU allowed us to perform both reactions in a sequential fashion in the same vessel, with fast kinetics. This way, fully controlled dual grafting was achieved in 17 min. While these two one-pot methodologies were based on grafting of the same thiol on each part of the scaffold, a final one-pot procedure led to modification with distinct thiols through the reduction of the amount of thiol involved in the thiol–ene first step and delayed addition of DBU to start the PFTR step.

Since a wide range of thiols were previously shown to be suitable for these two chemistries, the methodology presented herein paves the way for numerous functional materials. This reaction pair is a powerful alternative to the recently reported thio-Michael addition/radical thiol–ene combination because it does not require external heating and possibly operates with faster kinetics.^[359] Here, a bifunctional BCP was employed as a convenient platform for establishing orthogonality conditions, yet it can certainly be envisioned that this work is applicable to smaller molecules as well as to perform advanced surface functionalization, such as that of BCP thin films presented in Chapter 4, for which orthogonal ligation methods are crucial.

6

The *para*-Fluoro Thiol Substitution Reaction (PFTR) in Water



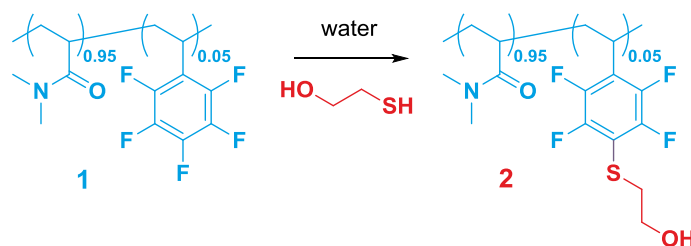
In this project, a set of initial kinetic studies were performed by Aaron C. Schmidt in the frame of a *Vertiefungspraktikum* and a Master Thesis. Peptide synthesis was carried out by Dr Parvesh Wadhvani (Institute for Biological Interfaces (IBG), KIT). ToF-SIMS analysis was done by Dr Alexander Welle at Institute for Applied Materials – Energy Storage System (IAM-ESS), KIT. Rouven Mueller (Institute for Chemical Technology and Polymer Chemistry (ITCP), KIT) is thanked for his valuable ideas.

6.1 Introduction

Thiols constitute a rich class of compounds as addressed in detail in Section 2.2.2. Besides other well-known *click*-type reactions, another thiol-based reaction, namely *para*-fluoro-thiol reaction (PFTR) has recently gained attention. PFTR corresponds to the nucleophilic substitution of the *para* fluorine atom of the pentafluorophenyl (PFP) motif by thiols. The reader is redirected to Section 2.2.2.2 for more details on this reaction. PFTR is triggered by the presence of a base and was reported exclusively in polar solvents in the literature. In contrast to the widely employed, well-known thiol-based reactions such as thiol-ene or thiol-yne additions, PFTR has never been applied in aqueous conditions until now. Using water as a reaction medium is obviously advantageous in terms of environmental and financial costs and enlarges the scope of application of PFTR to water-borne systems. In this Chapter, we show that PFTR can occur in basic water (pH = 11-13), using a macromolecular platform. Polymers are multifunctional materials and constitute ubiquitous scaffolds to assess kinetics, yields, and potential side reactions which would usually lead to molar mass alterations. In addition, polymers allow for solubilizing insoluble moieties through copolymerization.

6.2 Bringing the PFP Moiety into Water

In this work, a poly(*N,N*-dimethylacrylamide) (PDMAAm) was utilized as it is a water-soluble polymer that can be synthesized by an RDRP method. Specifically, we copolymerized DMAAm with a small amount of pentafluorostyrene (PFS) by nitroxide-mediated polymerization (NMP). A well-defined water-soluble polymer bearing PFP pendant groups was obtained (Scheme 6.1, compound **1**) ($M_n = 9700 \text{ g mol}^{-1}$, $D = 1.35$). The targeted PFS content of the copolymer was 5 mol%, a value intentionally low in order to preserve the water solubility of PDMAAm. PFS polymerizes slightly faster as compared to DMAAm (95% vs 75% conversion, respectively, in the corresponding polymerization; see Figure 9.29). Therefore, it was decided beforehand to introduce only 3.9 mol% of PFS in the initial feed. This way, the final copolymer **1** contained ca. 4.9 mol% of PFS units.



Scheme 6.1 Structure of poly(DMAAm-*co*-PFS) **1** and model reaction carried out in this work.

6.3 Establishing a Rational Route to PFTR in Water

Mercaptoethanol was selected as a water-soluble thiol for the PFTR investigations (Scheme 6.1). The experimental pK_a of mercaptoethanol is approx. 9.7,^[360] which is an intermediate value for aliphatic thiols.^[361-363] Owing to its low cost and great water-solubility, it was thus envisaged as an ideal model thiol to be utilized.

As presented in Chapter 5, DBU is a strong base used in the presence of aliphatic thiols to mediate PFTR and allows the reaction to reach full completion in a few minutes in DMF.^[64] Therefore, we first used DBU in water to perform PFTR with mercaptoethanol on copolymer **1**. However, no reaction was observed in the presence of 1.1 equivalents or even 5 equivalents of DBU and 1.1 equivalents of mercaptoethanol (with respect to PFS units) at RT after 24 h (Figure 6.1B). The PFP moiety exhibits 3 distinct signals on ^{19}F NMR spectra, corresponding to the *ortho*, *meta*, and *para*-fluorine atoms, as also explained in Chapter 5. Upon PFTR, the *para* peak should disappear and the *meta* peak shift to a higher chemical shift. As demonstrated on Figure 6.1B, no change was detected in the ^{19}F NMR spectrum of **1** when using DBU in water. An explanation of this can be the protonation of the base by water,^[364] which prevents the generation of the reactive thiolate species. Likewise, the reaction occurred neither in methanol nor in ethanol (Figure 6.1B). As the pK_a of thiols is typically not larger than 11,^[361-363] it was envisaged that simply working at pH higher than this value would provide a means to produce thiolates, hence to trigger the reaction. The pH was initially adjusted by addition of NaOH. Although a reaction finally did occur, high yields could not be reached (Figure 6.1A).

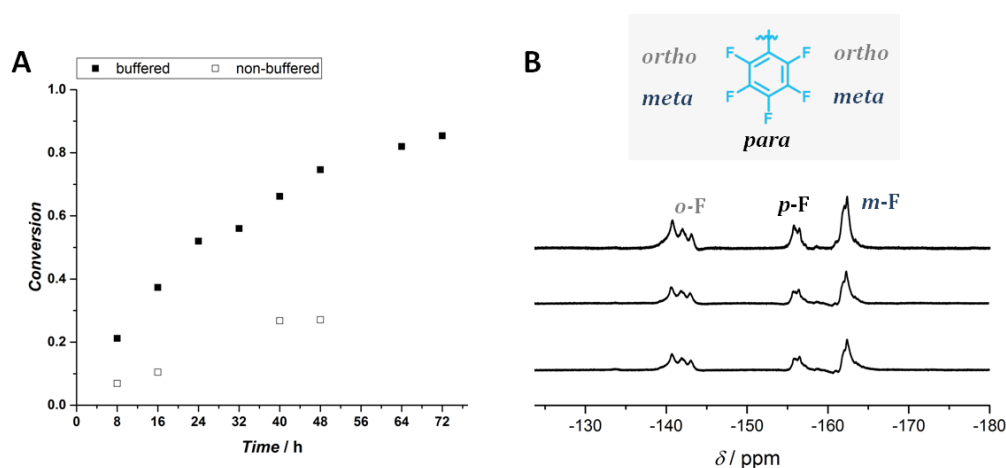


Figure 6.1 A) Conversion vs. time plot for the PFTR on **1** in buffered and non-buffered pH 12 solutions, conducted at 40 °C with 10 eq. of mercaptoethanol. B) ^{19}F NMR spectra of **1** upon PFTR conducted at RT with (top) 5 eq. DBU and 1.1 eq. mercaptoethanol in deionized water, (middle) 1.1 eq. DBU and 1.1 eq. mercaptoethanol in methanol, and (bottom) 1.1 eq. DBU and 1.1 eq. mercaptoethanol in ethanol.

At this point, it was found that the pH of the NaOH solution was actually not stable and steadily decreased. Hence, buffered pH solutions were used for subsequent experiments. For a similar initial pH, significantly faster kinetics were observed with the use of buffered solution (Figure 6.1A and Table 6.1). The rest of the study was therefore conducted in buffered solutions set at various pH values. PFTR is theoretically not an oxygen sensitive reaction and could thus be performed under ambient conditions. However, since thiols are prone to oxidation and may lead to disulfide formation over long time periods, we conducted all studies in deoxygenated media as our initial studies yielded lower conversions under ambient conditions (data not shown).

Table 6.1 Conversion values for the PFTR of **1** in buffered and non-buffered pH 12 solutions at 40 °C with 10 eq. of mercaptoethanol.

time / h	Conversion	
	Buffered	Non-buffered
8	0.21	0.069
16	0.37	0.1
24	0.52	
32	0.56	
40	0.66	0.26
48	0.75	0.26

6.4 Investigations on the Effect of Different Variants on PFTR

The effects of pH, temperature, and thiol stoichiometry on the rate of aqueous PFTR were investigated (Table 6.2). Samples were collected periodically to track the kinetics by ¹⁹F NMR spectroscopy. A 1M HCl solution was used to quench the reaction before analysis.

Table 6.2 Summary of all conditions applied in the present study for the PFTR of **1** with mercaptoethanol.

Entry	pH	T (° C)	Thiol eq.
★	12	40	20
■	12	40	10
▶	12	40	5
▲	13	40	10
☆	12.5	40	10
⬠	11	40	10
◐	13	50	10
◆	13	RT	10

One exemplary set of kinetics is provided in Figure 6.2 where one can visualize the disappearance of the *para* fluorine signal of **1** and the apparition and progressive increase of the *meta* signal of compound **2**. Integrations of the peaks before reaction and after full completion of the reaction are given on Figure 9.30. Additional spectra can be found on Figure 9.31. To calculate conversions, the *meta* peak integral of **2** was divided by the sum of the integrals of the *ortho* peaks of both **1** and **2**.

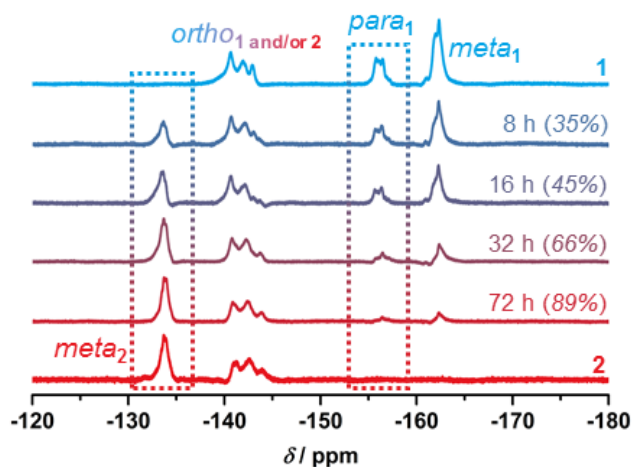


Figure 6.2 Exemplary kinetics monitored by ^{19}F NMR spectroscopy of the experiment conducted at pH 12 and 40 °C with 20 eq. of thiol. Note that for the spectrum of **2**, the final sample of the experiment at 50 °C, pH 13, and 10 eq. thiol was plotted as a reference for full conversion.

Referring to our previous study (Chapter 5), we initially used 5 equivalents of mercaptoethanol. Since PFTR is generally not carried out at RT when weak activators are used,^[12, 14, 103, 149, 365] the initial set of experiments was run at 40 °C. We chose to start at pH 12, which is a value sufficiently higher than the $\text{p}K_{\text{a}}$ of mercaptoethanol. Unfortunately, under these conditions, the reaction proceeded rather slowly, reaching only 40% conversion after 3 days (Figure 6.3, black series and Table 6.3). The $[\text{thiol}]/[\text{PFS}]$ ratio was then increased to 10 and 20. At any reaction time, the conversion was approximately doubled when 10 equivalents were employed (Figure 6.3, green series). However, in spite of a higher initial rate, 20 equivalents did not lead to a drastic difference, as compared to the 10 equivalents experiment (89 vs. 85% in 72 h, Figure 6.3, yellow series).

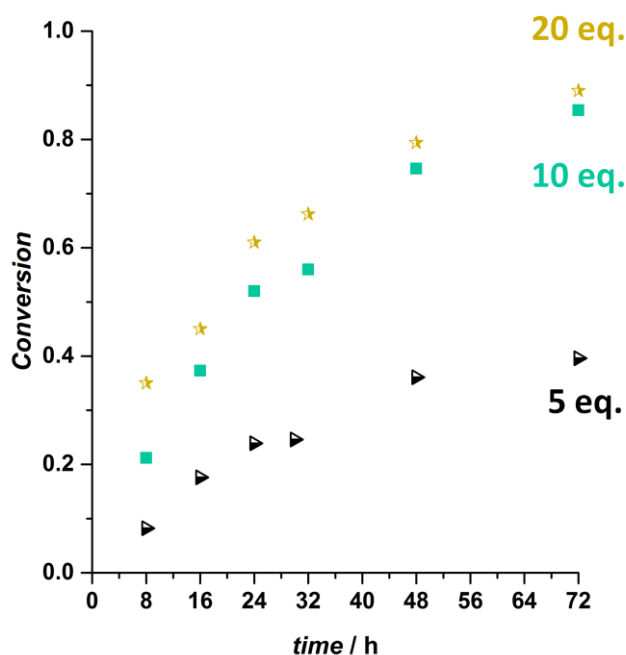


Figure 6.3 Kinetics studies for the PFTR of **1** with various quantities of mercaptoethanol, at 40 °C and pH 12 (buffered).

Table 6.3 Conversion values for the PFTR of **1** with various quantities of mercaptoethanol, at 40 °C and 12 (buffered).

time / h	Conversion		
	5 eq.	10 eq.	20 eq.
8	0.08	0.21	0.35
16	0.17	0.37	0.45
24	0.24	0.52	0.61
32	0.24	0.56	0.66
48	0.36	0.75	0.79
72	0.40	0.85	0.89

A possible reason for the reduced effect upon increasing $[\text{mercaptoethanol}]/[\text{PFS}]$ from 10 to 20 would be that at higher thiol concentrations, competition between PFTR and disulfide formation becomes more important, despite the preliminary deoxygenation of the reaction solution. In fact, basic conditions are known to enhance disulfide formation.^[310, 366-369] As a consequence, and to reduce the efforts for the purification of excess thiols, it was decided to utilize 10 equivalents for the rest of the investigations.

The influence of the pH on the PFTR rate was then examined. Four reactions were performed using 10 equivalents of mercaptoethanol at 40 °C: at pH 11, 12, 12.5, and 13. As expected, the higher the pH values the faster the kinetics. The reaction at pH 11 did happen but was remarkably slow, reaching 54% conversion after 6 days (Figure 6.4, Table 6.4). Moreover, while pH 12 reached 52% conversion in 24 h, pH 12.5 and 13 attained 78% and 95% conversion in

the same period of time. It was expected that pH values lower than 11 would lead to even slower kinetics. Thus, no attempt was made below this value. Additionally, experiments could not be conducted at pH 13.5 since the polymer would not dissolve at this pH, possibly due to a salting out effect.

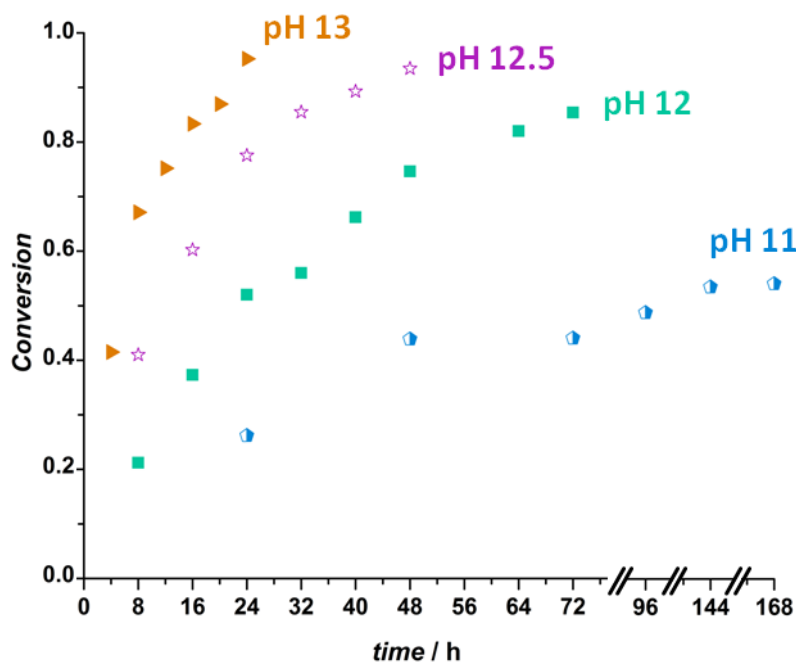


Figure 6.4 Kinetics studies for the PFTR of **1** at various pH values (buffered), with 10 equivalents of mercaptoethanol at 40 °C.

Table 6.4 Conversion values for the PFTR of **1** at various pH values (buffered), with 10 equivalents of mercaptoethanol at 40 °C.

time / h	Conversion			
	pH 11	pH 12	pH 12.5	pH 13
4				0.41
8		0.21	0.41	0.67
12				0.75
16		0.37	0.60	0.83
20				0.87
24	0.26	0.52	0.78	0.95
32		0.56	0.85	
40		0.66	0.89	
48	0.43	0.75	0.93	
64		0.82		
72	0.44	0.85		
96	0.49			
120				
144	0.54			
168	0.54			

Finally, the effect of temperature was investigated at pH 13 with 10 equivalents of mercaptoethanol. As it can be observed on Figure 6.5 (see values in Table 6.5), temperature has a major impact on the reaction rate: the reaction was very slow at RT while full conversion was reached at 50 °C in 16 h (vs. 95% in 24 h at 40 °C). It is noteworthy that the reaction at RT seemed to reach a plateau after 72 hours, which could also potentially be attributed to disulfide formation over extended periods of time.

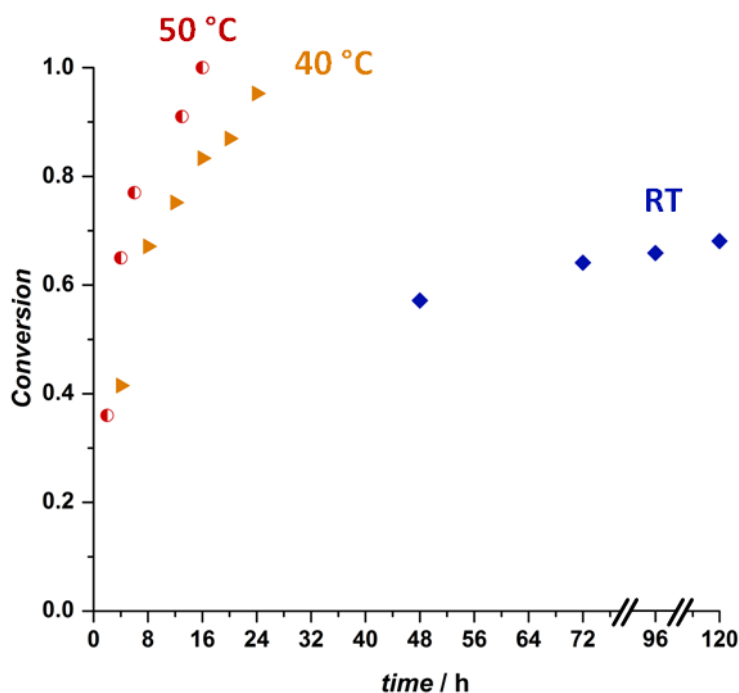


Figure 6.5 Kinetics studies for the PFTR of **1** at various temperatures, at pH 13 (buffered) and with 10 equivalents of mercaptoethanol.

Table 6.5 Conversion values for the PFTR of **1** at various temperatures, at pH 13 (buffered) and with 10 equivalents of mercaptoethanol.

time / h	Conversion		
	RT	40 °C	50 °C
2			0.36
4		0.41	0.65
6			0.77
8		0.67	
12		0.75	
13			0.91
16		0.83	1
20		0.87	
24		0.95	
48	0.57		
72	0.64		
96	0.66		
120	0.68		

A size-exclusion chromatogram of the polymer after full PFTR in some of the most stringent conditions (pH 13, 50 °C) showed a small increase in molar mass from polymer **1** to polymer **2**, while there was no change in polydispersity ($M_n = 10800 \text{ g mol}^{-1}$, $D = 1.36$) (Figure 6.6A). This suggests that such basic conditions are not harmful to the employed polymer. ^1H NMR spectra of **1** and **2** can also be found in Figure 6.6B with indication of grafting of mercaptoethanol via the newly appearing peak, with the rest of the spectrum remaining essentially unchanged.

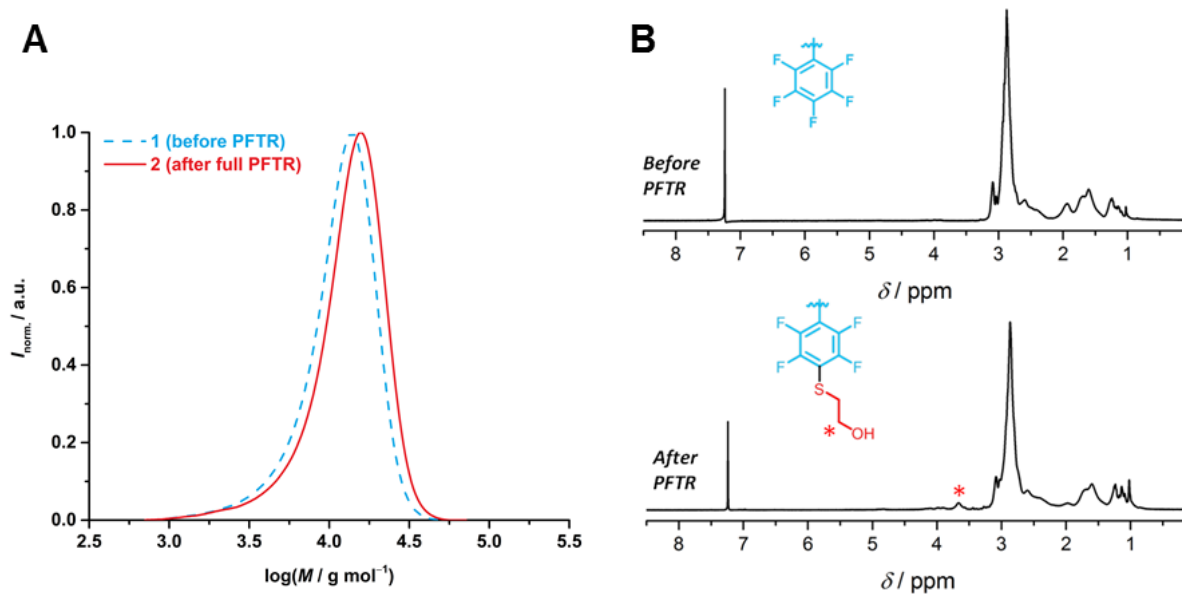


Figure 6.6 (A) Size-exclusion chromatograms of polymer precursor **1** and its counterpart **2** after full PFTR at pH 13 and 50 °C. (B) ^1H NMR spectra of **1** (top) and **2** (bottom).

Besides their reaction with thiols, the PFP moiety may also react with alcohols (and amines). Since mercaptoethanol bears both sulfhydryl and hydroxyl groups, it could have potentially reacted from the hydroxyl side as well. To avoid this possibility and in parallel to our previous study (Chapter 5), a control experiment was conducted to prove that the substitution exclusively proceeds only through the thiol moiety. For this purpose, ethanol was chosen as a thiol-free mercaptoethanol substitute. Under comparable conditions (pH 13, 40 °C, 10 eq. ethanol, and even 4 days) the ^{19}F NMR spectrum showed no change (Figure 6.7), thereby confirming that mercaptoethanol was undoubtedly grafted through its thiol part to yield a thioether linkage.

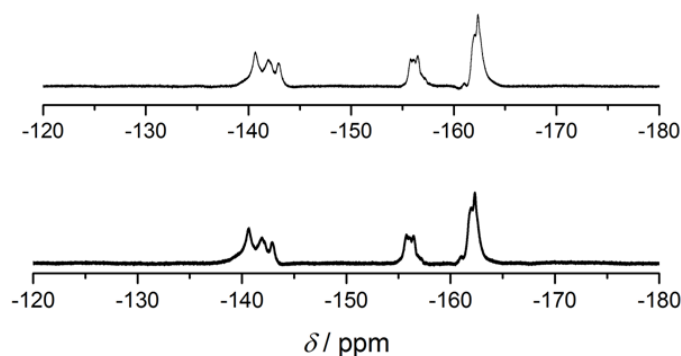


Figure 6.7 ^{19}F NMR spectra of **1** (top) and **1** after incubation during 4 days with 10 eq. ethanol at pH 13 and 40 °C (bottom).

6.5 Application of PFTR in Water on the Surface

One of the motivations to investigate the PFTR in water was to endow its application for the surface modification of polymeric materials, which would usually dissolve in organic solvents but not in aqueous media, such as the films developed in Chapters 3 and 4. For example, polystyrene is a constituent of various items employed for biological investigations. Therefore, we set out to demonstrate the utility of our new protocol for the modification of widely used tissue culture polystyrene (TCPS) Petri dishes with peptides. The surface modification of TCPS has indeed been widely employed for decades.^[370-372] Peptides, as functional subunits of proteins, are potential candidates for creating novel bioactive materials by conjugation to various types of polymeric substrates (e.g., flat surfaces, nanoparticles, hydrogels).^[373] Here, we utilized a 22-amino acid long water-soluble antimicrobial peptide^[374-376] (Cys-PGLa, CGMASKAGAIAGKIAKVALKAL-amide, $M = 2071.73 \text{ g mol}^{-1}$) possessing a cysteine (thiol-containing) residue at its *N*-terminus. To introduce PFP groups at the surface of TCPS dishes, we had recourse to a mild and straightforward photografting strategy based on a hydrogen abstraction mechanism by benzophenone derivatives.^[377] To achieve this, an aqueous solution of polymer **1** and a water-soluble benzophenone derivative was placed in a TCPS dish and irradiated with UVA light for 30 min under ambient conditions (Figure 6.8, first arrow). Successful attachment of the polymer on the dish was evidenced by time-of-flight secondary ion mass spectrometry (ToF-SIMS) with the presence of C_6F_5^- and $\text{PO}_2^-/\text{PO}_3^-$ fragments arising from the PFS units and the NMP initiator employed for synthesizing the polymer, respectively (Figures 6.9).

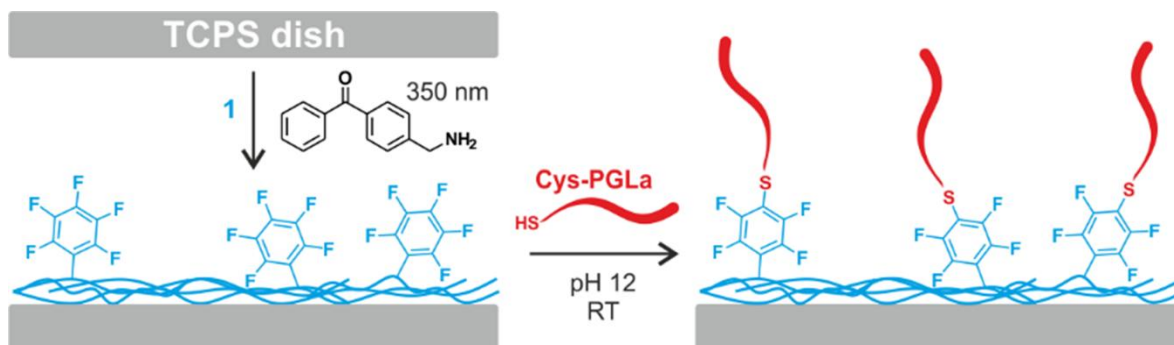


Figure 6.8 Schematic representation of the surface modifications.

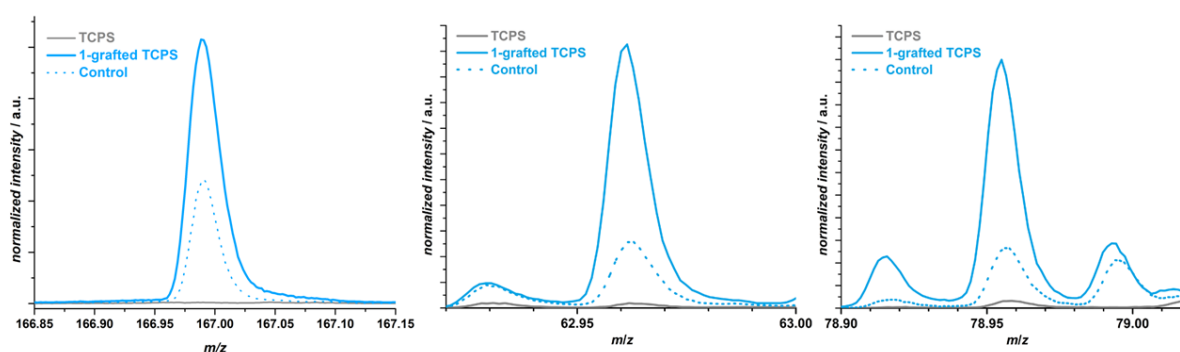


Figure 6.9 Secondary ion mass spectra obtained for the original TCPS Petri dish (grey, solid), after photografting of **1** (blue, solid), and the control experiment of the photografting step (blue, dashed). (Left) Pentafluorophenyl-specific region, theoretical m/z value ($C_6F_5^-$): 166.9. (Middle) First phosphonate-specific regions (PO_2^-), theoretical m/z value: (PO_2^-): 62.96. (Right) Second phosphonate specific region (PO_3^-), theoretical m/z value: (PO_3^-): 78.96.

During surface functionalization, the concentration of the reagents present in solution is far greater than that of the surface functionality. Therefore, we carried out the peptide immobilization at pH 12 and room temperature for a total time of 24 h. In other words, although at pH 12, the reaction was found not to proceed very fast in solution, it is envisaged to occur faster on surfaces. Also, the PFTR through the thiol of the cysteine motif is envisaged to occur more easily as compared to mercaptoethanol at the same pH (i.e., 12 here) since the pK_a of cysteine is approximately 8.5,^[378-379] which is one unit lower than that of mercaptoethanol. Since kinetics of surface reactions might differ from those conducted in solution, comparing efficiencies is quite challenging. Nevertheless, ToF-SIMS is a versatile technique which achieves unambiguous detection of peptide fragments on surfaces. As mentioned, the Cys-PGLa peptide sequence includes a cysteine at the *N*-terminus which is exploited here for conjugation to PFS

units. Additionally, the peptide possesses other residues which are readily detectable by ToF-SIMS; [380-382] four lysine and four leucine/isoleucine.

In order to avoid unspecific physisorption of peptides, thorough washings with a surfactant (Tween 20) were carried out. Moreover, control experiments were accomplished at neutral pH, where PFTR does not occur. Figure 6.10 shows selected regions of the secondary ion mass spectra obtained by ToF-SIMS. The polymer **1** coated-TCPS does not contain any significant amount of sulfur, while the sample after incubation of the peptide solution at pH 12 clearly showed intense peaks corresponding to negative fragments S^- and HS^- (Figure 6.10, left and middle), as well as for CHS^+ (Figure 6.10, right), characteristic of the cysteine residue. In addition, a strong signal characteristic of lysine is detected for the reaction sample, while it is absolutely absent from the PFS polymer-coated Petri dish (Figure 6.11, left). A similar finding stands for a lysine-specific fragment (Figure 6.11, right). Overall, the reaction was successful and it can be seen from the control experiment that limited peptide nonspecific adsorption occurred.

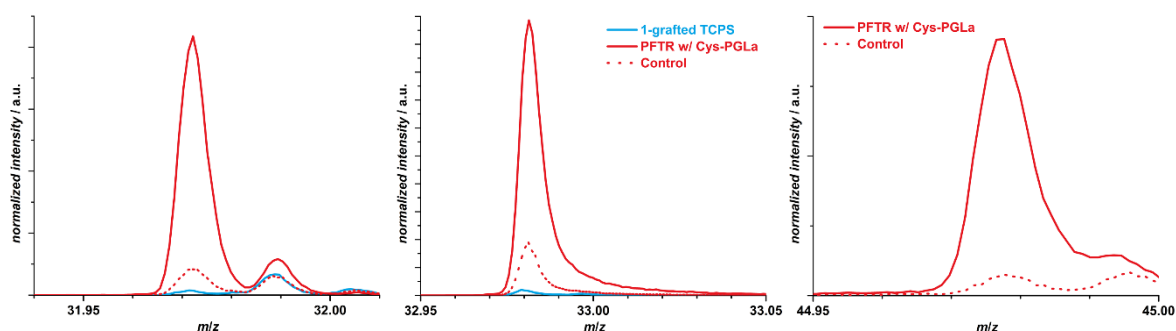


Figure 6.10 Cysteine-specific regions of the secondary ion mass spectra obtained after photografting of **1** (blue plain line), PFTR with peptide Cys-PGLa (red plain line), and control of PFTR (red dashed line). (Left and middle) negative mode. (Right) positive mode. Theoretical m/z values: (S^-) 31.97; (HS^-) 32.98; (CHS^+) 44.98.

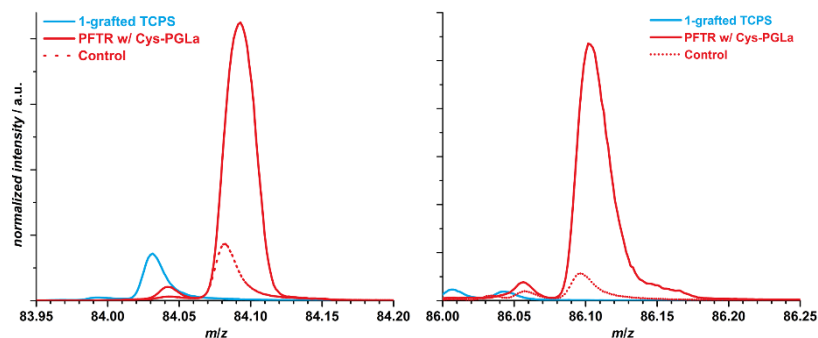


Figure 6.11 Secondary ion mass spectra obtained after photografting of **1** (blue, solid), PFTR with peptide Cys-PGLa (red, solid), and PFTR control (red, dashed). (Left) Lysine-specific region; theoretical m/z value ($C_5H_{10}N^+$) 84.08. (Right) Leucine/Isoleucine-specific region; theoretical m/z value ($C_5H_{12}N^+$) 86.10.

6.6 Conclusion

The study detailed in this Chapter is the first report on the *para*-fluoro–thiol reaction (PFTR) in aqueous medium. The reaction occurs at pH 11 and above in buffered solutions. The reaction rates increase with increasing pH values. PFTR was also found to be highly sensitive to temperature: It proceeds significantly faster at 50 °C as compared to room temperature. As opposed to the previous studies on PFTR carried out in organic solvents, the reaction is slower under the reported conditions with completion in hours rather than minutes. This is possibly due to the relatively lower concentrations of reagents used in the present case, resulting from the limited solubility of pentafluorophenyl moieties in water. Although there exist some limitations due to the relatively high pH conditions, this method can potentially be applied to many classes of materials which are free of base-labile ester groups, which is the case of aromatic vinyl polymers, polyureas, polyacrylamides, and many more.



Conclusion and Outlook

In the last decades, block copolymers (BCPs) have been in the focus of many fields ranging from electronics to drug delivery systems. With the ability to microphase separate and self-assemble into various structures from several hundreds to a few nanometers, BCPs stand as precious materials in micro- and nanotechnology. In this dissertation, studies towards exploitation of BCP thin films as cost-effective platforms for nanopatterned immobilization were presented. Indeed, the chemical flexibility offered by macromolecular synthesis led us to investigate the incorporation of functional moieties into the BCPs employed to fabricate surface-reactive nanostructured films through self-assembly. The surface-expressed functionalities are thought to be used as tethering points for immobilization applications. Furthermore, by varying the molar mass of the BCPs, it could be possible to tune the feature size of the nanostructures. Therefore, thanks to the bottom-up nature of this approach, BCP-based chemical nanopatterning could lead to applications, where other nanotechniques such as dip-pen nanolithography would not be able to compete in terms of throughput. As a primary step, the current work was devoted to the establishing protocols for the synthesis of the functional BCPs and to analyzing their behavior in thin films. As the literature presented only few examples in this area so far,^[7-10] we chose two well-known phase-separating BCP systems, equipped them with functional/reactive groups, and investigated various aspects such as solid-state behavior, nanostructuration, surface reactivity, and – as a secondary focus – orthogonality between some of the functional groups.

7.1 Summary & Concluding Remarks

The first studied system was based on PS-*b*-PI (Chapter 3). Nitroxide-mediated polymerization was employed for this purpose: functional PS macroinitiators were chain-extended with isoprene. Corresponding copolymers with overall molar masses of approximately 45 kg mol⁻¹ were contained functional styrene derivatives, namely chloromethylstyrene, azidomethylstyrene, and pentafluorostyrene in the PS block. Differential scanning calorimetry

Conclusion and Outlook

(DSC) showed two T_g values for each derivative, which is a clear sign of a phase separating system. Small-angle X-ray scattering (SAXS) characterization results pointed at the presence of a lamellar structure, which was the targeted morphology through macromolecular design. Thin films obtained by a simple spin-coating step were characterized by ellipsometry and atomic force microscopy (AFM): ultra-thin films consistently exhibited a stripe-like pattern characteristic of perpendicular lamellae, which is a useful morphology for patterning purposes. Domain spacing (L_0) values were determined both by AFM and SAXS and were in close agreement with each other. In short, introduction of the aforementioned functionalities into a parent backbone did not perturb the phase segregation ability. In the second step, as a preliminary step to prove the presence and reactivity of the functional moieties at the surface of the BCP films, we selected the azide-containing derivative and performed the attachment of a model water-soluble polymer by copper-catalyzed azide-alkyne cycloaddition. XPS was utilized to prove the occurrence of the surface reaction. Importantly, the underlying morphology was protected as demonstrated by AFM.

Chapter 4 focuses on a second BCP system, that is PMMA-*b*-PS. In the previous system, the PI block bears inherent double bonds and only PS block could be arbitrarily functionalized. In this system however, both MMA and styrene can be readily copolymerized with various commercial derivatives of similar reactivity in copolymerization, which thus allows one to functionalize both blocks at will. Following the same strategy as before, yet employing ATRP and RAFT as the polymerization techniques, we developed a larger library of BCPs which can undergo a broader range of reactions such as thiol-ene, Diels-Alder, *para*-fluoro-thiol reaction (PFTR), and amidation reactions. Many of the BCPs were able to produce thin films composed of perpendicular lamellae, as evidenced by AFM and SAXS. In both systems, the films were all hydrophobic and hence applicable in aqueous media for at least a few hours. Nevertheless, long-term stability was problematic. Therefore, first experiments for stabilization by crosslinking (either by heat or by light) were performed and led to films which were even resistant in organic media.

In the latter part of this dissertation, some of the functionalities introduced in the block copolymers were investigated in terms of reactions conditions and orthogonality, having in mind the current context: (i) if a BCP contains two functionalities, they must be independently addressable (which is related to orthogonality) and (ii) the film functionalization should ideally be performed in aqueous media. Particularly, we focused on PFTR. In Chapter 5, we showed the orthogonality of this mild *click* type of reaction with phototriggered radical thiol-ene addition. The system under investigation contained both pentafluorophenyl (for PFTR) and allylic (for thiol-ene coupling) groups, i.e., two groups potentially amenable to react with the same type of

compounds, i.e., thiols. In the presence of two thiol-reactive groups, it is essential to direct the thiol to either of the moieties selectively. This was possible to achieve by selecting appropriate mild triggers. PFTR could be performed independently at RT within a few seconds to minutes with DBU as an activator, without triggering any reaction on the allylic groups. Thiol-ene addition could also be achieved independently using a photoinitiator. Dual orthogonal functionalization sequences as fast as being completed in 17 min were demonstrated.

In Chapter 6, we reported for the first time the PFTR in aqueous medium. Being a nucleophilic substitution reaction, PFTR is highly promoted by polarity and basicity of the medium. We showed that by simply tuning the pH of the medium, the reaction could be triggered. The higher the pH, the faster the reaction. To show the applicability of PFTR on surface reactions in water, we successfully coupled a peptide onto a pentafluorophenyl-functionalized polystyrene Petri dish, as evidenced by ToF-SIMS. It is believed that PFTR could be utilized both in biology and materials related contexts.

To conclude, the presented dissertation shows that the introduction of less than 10% of clickable units into phase separating BCPs does not necessarily perturb significantly this inherent property, yet instead increases the applicability of BCPs in different areas, particularly for immobilization purposes. Proving the surface reactivity as well as stabilization of the films via crosslinking, we open a way for utilization of BCPs as next-generation patterning platforms.

7.2 Outlook

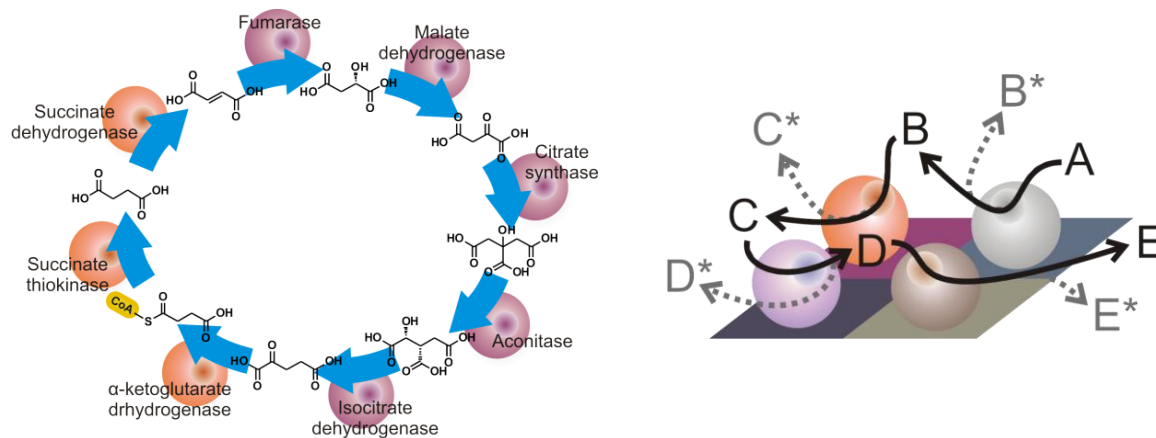


Figure 7.1 (Left) The Krebs cycle. (Right) Representation of enzyme cascades on a surface with a nanostructuring.

As a future work, reactivities of all the existing functionalities in the films should be assessed. Variation of the characteristic features of the films, i.e., morphology and domain spacing should also be carried out. This can be done by macromolecular design, that is synthesizing block copolymers with different molar masses and block ratios. Particularly, for some applications, the perpendicular cylinder morphology can also be of interest.

Potential applications should then be investigated. One possible direction is enzyme immobilization, which is one of the research focuses of our group. Indeed, immobilization of enzymes offers several advantages such as decreased sensitivity to environment, increased stability, tolerance to high pH and easy recovery of the products.^[383-384] In many cases, enzymes work cooperatively in so-called cascades: the product of one enzyme is the substrate of a second one, and this process can take place with many more than just two enzymes. A well-known example from nature is the Krebs cycle (Figure 7.1 left). In that case, there is even an additional effect created by the proximity between some of the enzymes (in purple): a phenomenon called “metabolic channeling” takes place, in which the product/substrate are passed from enzymes to enzymes with no or very few diffusion in the environment. There have been some efforts to create this sort of multienzyme systems.^[385-387] To artificially create this phenomenon, coimmobilization onto surfaces with features in the lengthscales of single enzymes (5-15 nm) could be a solution (Figure 7.1 right) and BCP films therefore appear attractive.

Materials and Characterization

8.1. Materials

Methyl methacrylate (MMA; 99%, Acros), allyl methacrylate (MMA; 98%, Sigma Aldrich), styrene (99%, Acros), pentafluorostyrene (PFS; 98%, ABCR), and *N,N*-dimethylacrylamide (DMAAm; 99%, Acros) were passed through a short basic alumina column prior to use. 4-Vinyl benzyl chloride (97%, Sigma-Aldrich), pentafluorophenyl methacrylate (PFPMA; 95%, Sigma Aldrich), 4-bromostyrene (BrS; 97%, Sigma Aldrich) were used as received. Azidomethyl styrene (4-vinylbenzyl azide) was synthesized from 4-vinylbenzyl chloride via a procedure adapted from the literature.^[311] Isoprene (99%, ABCR) was distilled at 40 °C prior to use.

CuBr (99%, abcr), CuBr₂ (99%, abcr), CuCl₂ (97%, Sigma Aldrich), methyl α -bromoisobutyrate (MRiB; 99%, Sigma Aldrich), PMDTA (99%, Acros), tin(II) 2-ethylhexanoate (Sn(EH)₂; 95%, Sigma Aldrich), tris[2-(dimethylamino)ethyl]amine (Me₆(TREN); 97%, Sigma Aldrich), bipyridine (\geq 99%, abcr), octanethiol (OT; 98.5%, Sigma Aldrich), mercaptoethanol (99%, Roth), 2-cyano-2-propyl benzodithioate (CPDB; 97%, Sigma Aldrich), triethylamine (TEA; > 99%, Fisher Scientific), furfuryl amine (\geq 99%, Sigma Aldrich), copper(II) sulfate pentahydrate (CuSO₄·5H₂O; \geq 99.5%, Roth), tetrabutylammonium fluoride solution (TBAF; 1.0 M in THF, Sigma Aldrich), butylated hydroxytoluene (BHT; 99%, Alfa Aesar), benzyl dimethyl ketal (BDK; 99%, Sigma Aldrich), sodium azide (NaN₃; \geq 99%, Roth), magnesium sulfate (MgSO₄; \geq 99%, Roth), 4-benzoyl benzylamine hydrochloride (ABCR), Tween 20 (molecular biology grade, VWR), ethanol (99.8%, Acros), sodium hydroxide (NaOH; \geq 99%, Roth), hydrochloric acid (HCl; 37%, Roth), sodium dihydrogen phosphate (NaH₂PO₄; \geq 99%, Roth), and glycine (\geq 99%, Roth) were used as received. 1,8-Diazabicyclo[5.4.0]undec-7-ene (DBU; > 98%, Merck) was distilled prior to use. Azobisisobutyronitrile (AIBN) was crystallized from methanol.

Materials and Characterization

N-tert-Butyl-N-[1-diethylphosphono-(2,2-dimethylpropyl)] nitroxide (SG1)^[388] and 2-methyl-2-[*N-tertbutyl-N*-(1-diethoxyphosphoryl-2,2-dimethylpropyl)aminoxy]propionic acid (MAMA-SG1)^[389] were synthesized according to the literature.

HEBIB was synthesized according to a procedure from the literature.^[343] The RAFT agent reported in Chapter 3 was a leftover from Dr. Christoh Duerr.^[390] THTPA was donated by Dr. Ana Beloqui which was synthesized according to literature.^[391]

Methanol, acetone, and toluene were purchased from Fisher with high purity. Isopropanol, pyridine, and pH standards for calibration were purchased from Roth. 1,4-Dioxane, DCM, DMF, anisole (99%, Acros), and THF were purchased from VWR with high purity.

Ace pressure tubes (Ref. 8648-75) equipped with a PTFE plug (Ref. 5845-47) were purchased from Sigma Aldrich.

Petri dishes (100% USP VI crystal virgin polystyrene, Ø 35 mm, ref. no. 734-2317) were bought from VWR.

Si wafers (p-type, boron-doped, <100>, $\rho = 1\text{--}30 \Omega \text{ cm}$) were purchased from Si-Mat (Kaufering, Germany).

A CAMAG dual-wavelength UV lamp was used for irradiation at $\lambda = 366 \text{ nm}$, placed at a 2 cm distance from the reaction flask for thiol-ene additions in Chapter 5. The same UV lamp was used at $\lambda = 254 \text{ nm}$ at a 1 cm distance from the substrates for photocrosslinking PMMA-*b*-PS in Chapter 4 and PS-*b*-PI in Chapter 3. A PL-L lamp (310-400 nm, max. 350 nm) was used in a custom built photoreactor to irradiate Petri dishes in Chapter 6.

8.2. Analytical Instrumentation

8.2.1 Nuclear Magnetic Resonance (NMR) Spectroscopy

NMR spectroscopy measurements (^1H -NMR and ^{19}F -CPD NMR) were performed on a Bruker AM 500 spectrometer at 500 MHz. The analytes were dissolved in CDCl_3 and acetone- d_6 and the residual solvent signals were employed for shift correction. For the ^{19}F -CPD NMR spectra, 600-1000 scans were recorded and at least one of the following corrections was carried out: baseline correction with the method Bernstein polynomial fit (with polynomial order of 14), manual correction, or multipoint baseline correction.

8.2.2 Size Exclusion Chromatography (SEC)

THF/SEC measurements were performed on a TOSOH Eco-SEC HLC-8320 GPC system, which comprised of an autosampler, a SDV 5 μm bead size guard column (50 \times 8 mm, PSS) followed by three SDV 5 μm columns (300 \times 7.5 mm, subsequently 100, 1000, and 105 \AA pore size, PSS), and a differential refractive index (DRI) detector with THF as the eluent at 30 $^\circ\text{C}$ with a flow rate of 1 mL min^{-1} . The SEC system was calibrated by using linear polystyrene standards ranging from 266 to 2.52×10^6 g mol^{-1} , with linear PMMA standards ranging from 800 to 1.82×10^6 g mol^{-1} . Calculation of the molecular weight proceeded by using the Mark-Houwink-Sakurada (MHS) parameters for PMMA ($K = 12.8 \times 10^{-5}$ dL g^{-1} , $\alpha = 0.69$)^[392] and for PS ($K = 14.1 \times 10^{-5}$ dL g^{-1} , $\alpha = 0.70$)^[393].

DMAc/SEC measurements were performed on a Polymer Laboratories (Varian) PL-GPC 50 Plus Integrated System, comprising an autosampler, a PLgel 5 μm beads size guard column (50 \times 7.5 mm) followed by three PLgel 5 μm Mixed-C columns (300 \times 7.5 mm) and a differential refractive index detector using DMAc containing 0.3 wt% LiBr as the eluent at 50 $^\circ\text{C}$ with a flow rate of 1 mL min^{-1} . The SEC system is calibrated using linear polystyrene standards ranging from 160 to 6×10^6 g mol^{-1} and linear poly(methyl methacrylate) standards ranging from 700 to 2×10^6 g mol^{-1} . SEC calculations are carried out applying an effective calibration by using the Mark-Houwink-Kuhn-Sakurada (MHKS) parameters for polystyrene ($K = 14.1 \times 10^{-5}$ dL g^{-1} and $\alpha = 0.7$).

8.2.3 Atomic Force Microscopy (AFM)

AFM measurements were done on a MultiMode2 Bruker instrument (MMAFM-2) equipped with an E-scanner using tapping mode. The probes used during AFM analysis were n-type silicon

based probes, namely HQ: NSC14/Al based with typical values for resonance frequency of 160 kHz and spring constant of 5 N/m and HQ: NSC35/No Al with typical values for resonance frequencies of 150-300 kHz and spring constants of 5.4-16 N/m which were purchased from Micromash. NSC14 was mostly used for PS-*b*-PI system and NSC35 for PMMA-*b*-PS. However, since their frequencies and force constants are in the same range, both cantilevers were observed to be efficient for both systems at times and gave similar results. Scan size: 2 μm , engage setpoint: 0.9, z-limit: 1-3 μm , samples/line: 512, scan angle: 0°, aspect ratio: 1:1, scan rate: 1.97 Hz and tip velocity of 7.88 $\mu\text{m/s}$ were default values. A Nanoscope software was used for image processing. On the images, at least one of the followings was applied: lowpass, planefit, median-3 filters and color contrast enhancement/adjustment.

8.2.4 Small Angle X-Ray Scattering (SAXS)

The block copolymer morphology and its orientation were determined via SAXS using a S3-Micro from Hecus X-ray systems combined with a 2-D CCD detector from Photonic Science, respectively. The distance between sample and detector is 280.1 mm, the pixel size of the detector is 29 μm in each dimension. With this combination, a q range from 0.08 to 5 nm^{-1} is accessible.

For SAXS measurements, the polymers were annealed for 24 h at 150 °C under vacuum in O-rings (2 mm diameter) serving as sample supports. Measurements were directly performed in these O-rings with the X-ray beam position adjusted to the middle of the polymer. Both the background signal of the CCD detector and the scattering of the system itself were subtracted after radial averaging of the data. No correction for the final dimension of the beam has been performed, therefore the scattering peaks are broadened compared to a measurement at a large research facility.

8.2.5 X-Ray Photoelectron Spectroscopy (XPS)

XPS investigations were performed on a K-Alpha+ spectrometer (ThermoFisher Scientific, East Grinstead, UK) using a microfocused, monochromated Al $K\alpha$ X-ray source (400 μm spot size). The kinetic energy of the electrons was measured by a 180° hemispherical energy analyzer operated in the constant analyzer energy mode (CAE) at 50 eV pass energy for elemental spectra. Data acquisition and processing using the Thermo Advantage software is described elsewhere.^[394] The K-Alpha+ charge compensation system was employed during analysis, using electrons of 8 eV energy, and low-energy argon ions to prevent any localized charge build-up. The spectra were fitted with one or more Voigt profiles (BE uncertainty: +/- 0.2 eV). The

analyzer transmission function, Scofield sensitivity factors and effective attenuation lengths (EALs) for photoelectrons were applied for quantification.^[395] EALs were calculated using the standard TPP-2M formalism. All spectra were referenced to the C 1s peak (C-C,C-H) at 285.0 eV binding energy controlled by means of the well-known photoelectron peaks of metallic Cu, Ag and Au, respectively

8.2.6 Ellipsometry

The thicknesses of films were determined by a spectroscopic ellipsometer (J. A. Woollam) in a wavelength range of 400-800 nm at 75° angle of incidence. The SiO₂ layer was measured to be 3 nm. The ellipsometric angles (and psi) were fitted using a model consisting of a 3 nm SiO₂ layer and a Cauchy layer for the PS-*b*-PI system. For the PMMA-*b*-PS system, the random copolymer layer thickness was determined using a model consisting of a 3 nm SiO₂ layer and a Cauchy layer. For determination of BCP thicknesses in the PMMA-*b*-PS system, a 3 nm SiO₂ layer, a Cauchy layer for the first layer and a second Cauchy layer for the second layer were applied.

8.2.7 Differential Scanning Calorimetry (DSC)

Thermographs were obtained using a Q200 differential scanning calorimeter from TA Instruments. Each sample was heated first to +150 °C at a rate of 10 °C min⁻¹ to erase the thermal history of the sample, then cooled down to -90 °C. For determination of the glass transition temperatures, samples were then heated from -90 to +150 °C at a rate of 10 °C min⁻¹.

8.2.8 Time of Flight Secondary Ion Mass Spectrometry (ToF-SIMS)

ToF-SIMS was performed on a TOF.SIMS⁵ instrument (ION-TOF GmbH, Münster, Germany). This spectrometer is equipped with a bismuth cluster primary ion source and a reflectron type time-of-flight analyzer. UHV base pressure was < 5 × 10⁻⁹ mbar. For high mass resolution the Bi source was operated in the “high current bunched” mode providing short Bi₃⁺ primary ion pulses at 25 keV energy and a lateral resolution of approx. 4 μm. The short pulse length of 1.1 to 1.3 ns allowed for high mass resolution. The primary ion beam was rastered across a 500 × 500 μm² field of view on the sample, and 128 × 128 data points were recorded. Primary ion doses were kept at 10¹¹ ions/cm² (static SIMS limit) for all measurements. Due to the highly insulating nature of the use polystyrene substrates charge compensation during spectrometry was necessary. Therefore, an electron flood gun providing electrons of 21 eV was applied, and the secondary ion reflectron tuned accordingly. Spectra were calibrated on the omnipresent C-, CH-

CH_2^- , C_2^- , C_3^- ; or on the C^+ , CH^+ , CH_2^+ , and CH_3^+ peaks. Based on these datasets the chemical assignments for characteristic fragments were determined.

8.2.9 pH Measurements

pH measurements were conducted using a Mettler Toledo SevenCompact™ pH/Ion S220 pH-meter, calibrated using standard solutions of pH 2.0, pH 4.0, pH 7.0, pH 9.0, and pH 12.0 purchased from Roth.

8.2.10 Water Contact Angle (WCA) Measurements

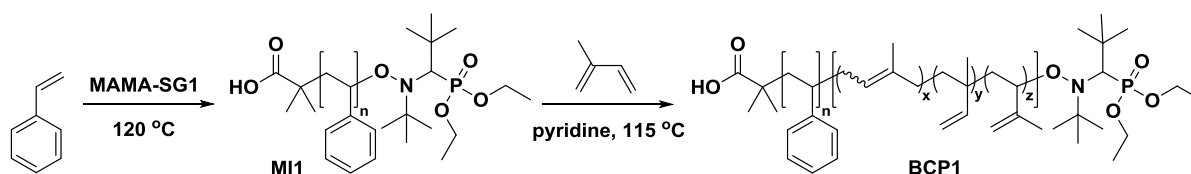
5 μL of deionized water droplets were used to measure the static WCA of the surfaces. Images were taken with a UK 1115 digital camera from EHD Imaging GmbH (Germany). Image J software with a Dropsnake plugin was used to determine the WCA.

Experimental Procedures

9.1 Reactive Nanostructured PS-*b*-PI Films

In this section, experimental procedures and the related content for Chapter 3 will be provided.

9.1.1 Syntheses



Scheme 9.1 Synthetic route to obtain **MI1** and **BCP1**.

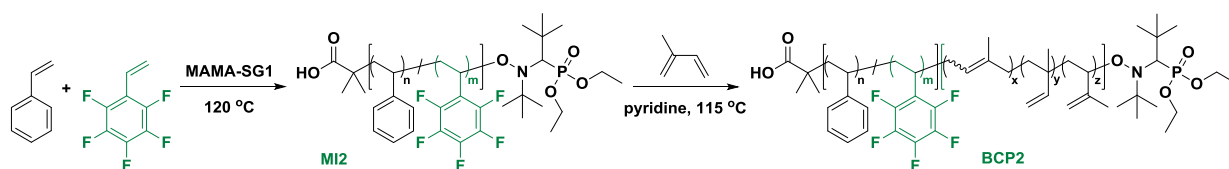
Synthesis of polystyrene (Macroinitiator 1 (MI1)) by NMP: Styrene (10.36 g, 99.4 mmol) was mixed with MAMA-SG1 (98.1 mg, 0.26 mmol) in a 25 mL round bottom flask. The flask was sealed with a rubber septum, the content was purged with N₂ for 30 min and then placed in a preheated oil bath at 120 °C. After 2 h, the reaction was stop by cooling to ambient temperature. The resulting polymer was precipitated twice in cold methanol and recovered as white powder. SEC (THF): $M_n = 22\ 300\ \text{g mol}^{-1}$; $D = 1.10$.

Synthesis of polystyrene-*block*-polyisoprene (PS-*b*-PI) (BCP1) by NMP: MI1 (100.6 mg) was dissolved in 1280 μL pyridine in a pressure tube which was sealed with a rubber septum and the content was purged with N₂ for 30 min. A large amount of distilled isoprene was previously taken in a big flask, sealed with a rubber septum and purged with nitrogen in an ice bath. The isoprene flask and the pressure tube were taken into glovebox. Isoprene (1280 μL , 870.4 mg, 12.78 mmol) was added into the pressure tube and the tube was very quickly closed with its

Experimental Procedures

own cap instead of rubber septum eventually. The pressure tube was placed in a thermostated oil bath at 115 °C. After 13 h 40 min, the reaction was cooled to ambient temperature. After removing pyridine under vacuum, the product was dissolved in a minimum amount of THF and precipitated in a mixture of methanol:isopropanol (3:1 v/v) which contained a tiny amount of BHT as stabilizer against oxidation of isoprene double bonds. The resultant PS-*b*-PI was recovered as white powder. SEC (THF): $M_n = 57\,700\text{ g mol}^{-1}$; $\bar{D} = 1.36$.

Synthesis of MI2 by NMP: In a 10 mL round bottom flask, styrene (4.63 g, 44.5 mmol), and PFS (449 mg, 2.3 mmol) were mixed to which MAMA-SG1 (46.1 mg, 0.12 mmol) was added. The flask was closed with a rubber septum and placed in a preheated oil bath at 120 °C after being purged with N₂ for 30 min. The reaction was stopped after 135 min. The same purification steps were applied as for the previously mentioned MIs and the product was recovered as white powder. SEC (THF): $M_n = 25\,300\text{ g mol}^{-1}$; $\bar{D} = 1.10$.



Scheme 9.2 Synthetic route to obtain **MI2** and **BCP2**.

Synthesis of BCP2 by NMP: **MI2** (200.6 mg) was dissolved in pyridine (2560 μL) in a pressure tube. The same procedure was applied as for the synthesis of **BCP1** with addition of isoprene (2560 μL). The reaction was quenched after 13 h 55 min. The same purification steps were applied as in the case of previous BCPS. SEC (THF): $M_n = 61\,900\text{ g mol}^{-1}$; $\bar{D} = 1.32$.

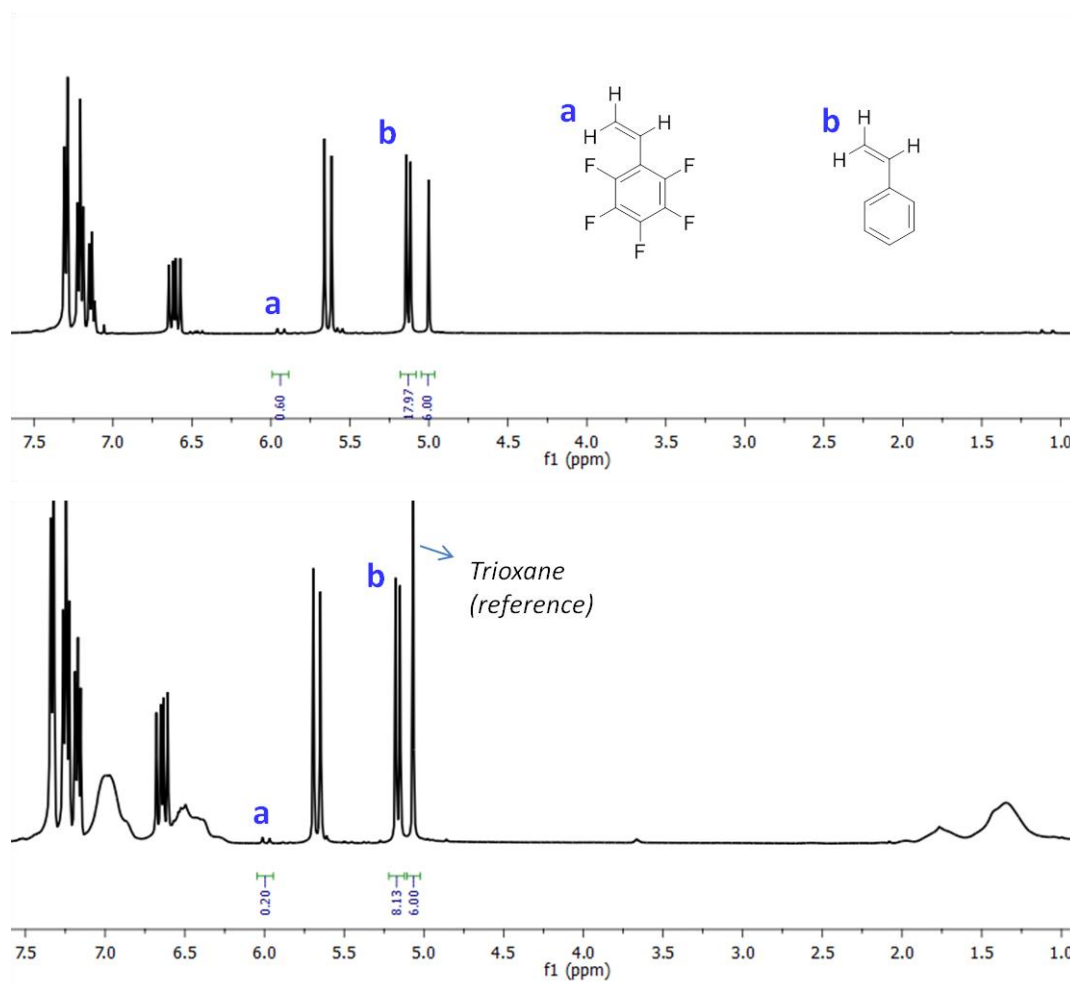


Figure 9.1 ^1H NMR spectra of samples taken during the synthesis of **MI2** at t_0 (top) and t_{end} (bottom), with integrals indicated that were used for conversion and comonomer composition calculation.

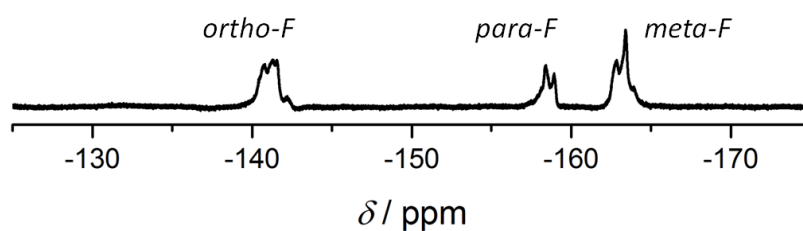
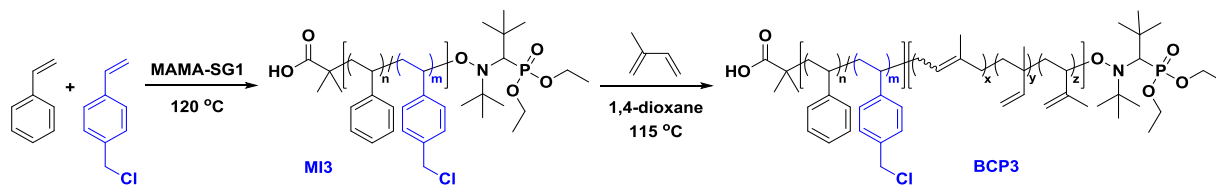


Figure 9.2 ^{19}F -NMR spectrum of **BCP2**.

Synthesis of MI3 by NMP: Styrene (3.67 g, 35.1 mmol), 4-vinylbenzyl chloride (282 mg, 1.84 mmol) were taken in a 10 mL round bottom flask. MAMA-SG1 (35.5 mg, 0.09 mmol) was added. The flask was sealed with a rubber septum, purged with N_2 for 30 min and then was placed in a

Experimental Procedures

preheated oil bath at 120 °C. The reaction was stopped after 135 min. The same purification steps were applied as applied for the previous polymers and the product was recovered as white powder. SEC (THF): $M_n = 25\,500 \text{ g mol}^{-1}$; $\mathcal{D} = 1.11$.



Scheme 9.3 Synthetic route to obtain **MI3** and **BCP3**.

Synthesis of BCP3 by NMP: **MI3** (200.4 mg) was dissolved in 1,4-dioxane (2560 μL) in a pressure tube. The same procedure was applied as for the synthesis of **BCP1** with addition of isoprene (2560 μL). The reaction was run for a total time of 15 h. The same purification steps were applied as for BCP1. SEC (THF): $M_n = 61\,800 \text{ g mol}^{-1}$; $\mathcal{D} = 1.36$.

Conversion of BCP3 into BCP4: **BCP3** (100.8 mg) was dissolved in 3 mL THF and diluted with 50 mL DMF in a 100 mL round bottom flask. NaN_3 (10 mg, 0.15 mmol) was added to this solution. The flask was stirred at RT for 4 days. After removing DMF in vacuum, the product was dissolved in 20 mL CH_2Cl_2 and extracted with water (80 mL) ($\times 3$). The organic layer was dried over MgSO_4 , filtered and was concentrated in vacuum. The product was precipitated in a mixture of methanol:isopropanol (3:1 v/v) including a tiny amount of BHT and finally obtained as white powder. SEC (THF): $M_n = 63\,500 \text{ g mol}^{-1}$; $\mathcal{D} = 1.33$.

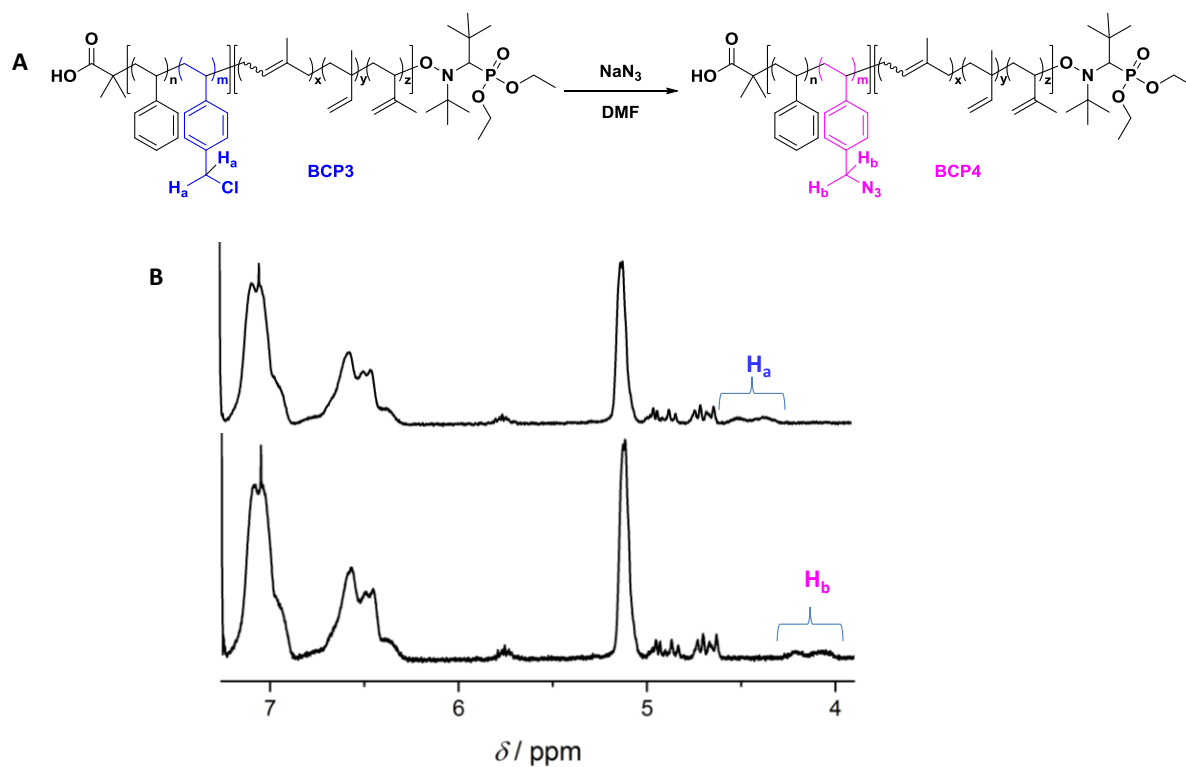


Figure 9.3 A) Synthetic route for the conversion of 4-chloromethylphenyl group into 4-azidomethylphenyl to obtain **BCP4** from **BCP3**. B) Selected region of the ^1H NMR spectra of **BCP3** (top) and **BCP4** (bottom) to show the shift of the methylene protons after chloride-to-azide transformation.

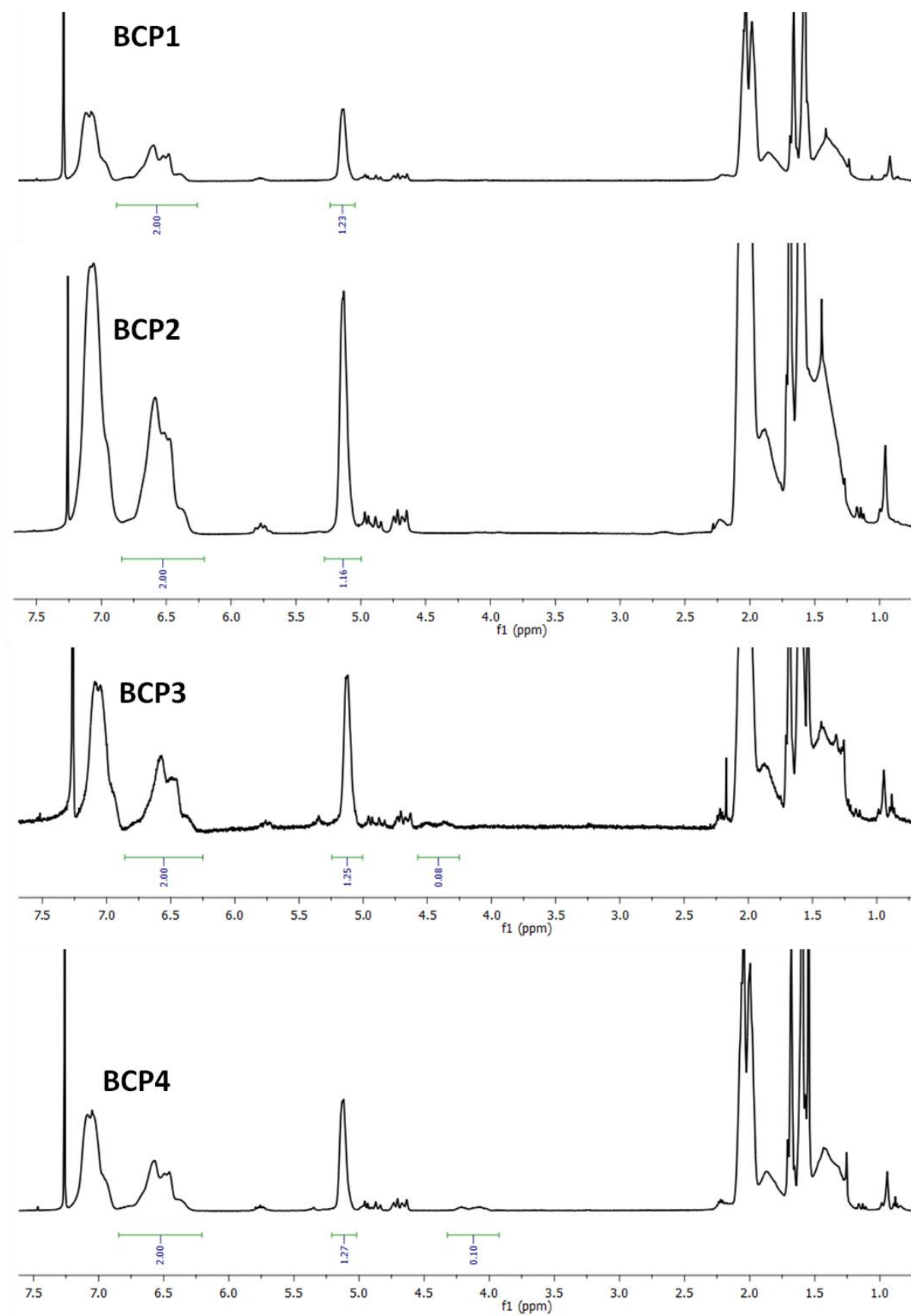
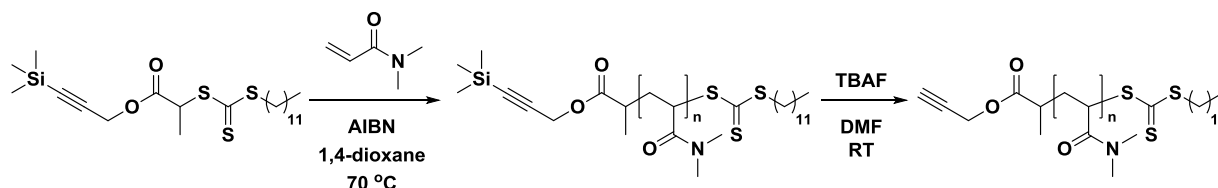


Figure 9.4 ¹H NMR spectrum of **BCP1-4** showing similar integral values for styrene and isoprene repeating units.

Synthetic Part for the Functional PDAAm:**Scheme 9.4** Synthetic route to obtain **TMS-Alkyne PDAAm** and **Alkyne-PDAAm**.

Synthesis of TMS-Alkyne-functionalized poly(*N,N*-dimethylacrylamide) TMS-Alkyne-PDAAm by RAFT: TMS protected DOPAT (43 mg, 0.093 mmol) and *N,N*-Dimethylacrylamide (461.1 mg, 4.65 mmol) were taken in a 5 mL round bottom flask. AIBN (6.1 mg, 0.037 mmol) and 1,4-dioxane (1.857 mL) were added. The flask was sealed with a rubber septum and the content was purged with N_2 for 30 min. After 15 min of reaction time at 70 °C, the flask was cooled to ambient temperature. Solvent was removed, the product was dissolved in THF and precipitated twice in cold pentane. The product was recovered as a sticky yellow polymer. SEC (DMAC): $M_n = 4090 \text{ g mol}^{-1}$; $D = 1.09$.

Deprotection of TMS end group of Alkyne-PDAAm: TMS-Alkyne PDAAm (155 mg) was dissolved in 865 μL THF. TBAF solution (1.0 M in THF) (80 μL) was added dropwise. The content was stirred for 1 h at RT. After that, the product was precipitated in cold pentane and alkyne-PDAAm was recovered as sticky yellow polymer. SEC (DMAC): $M_n = 4180 \text{ g mol}^{-1}$; $D = 1.08$.

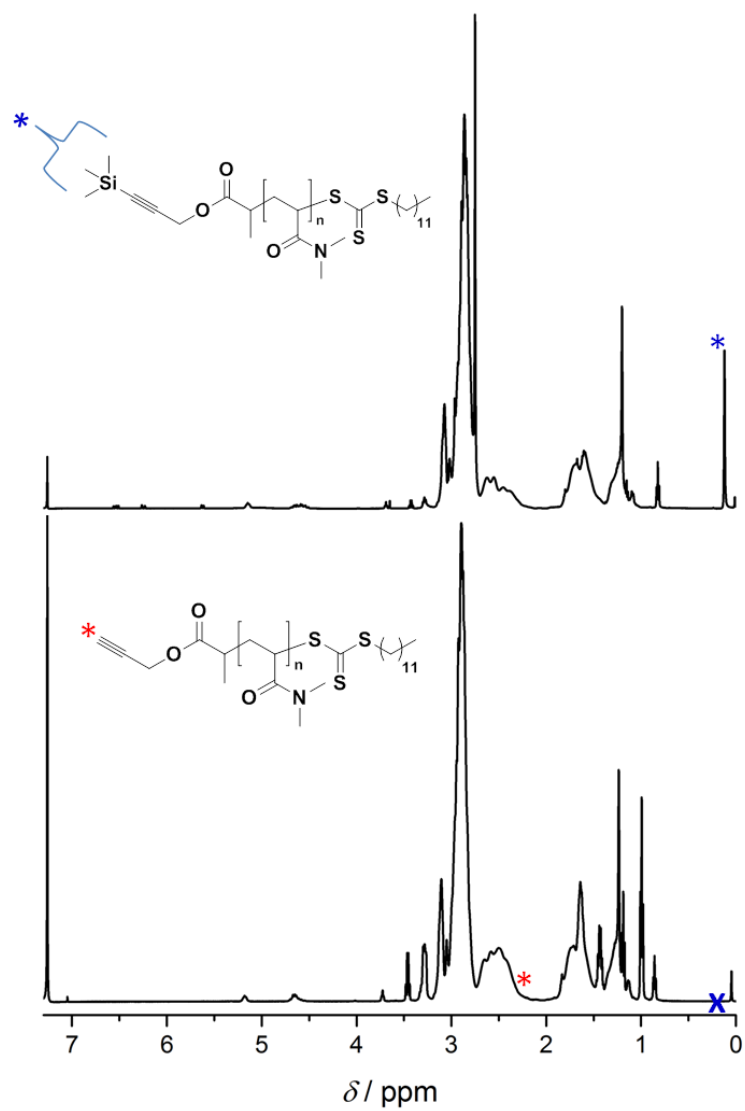


Figure 9.5 ¹H NMR spectra of (top) TMS-Alkyne-PDMAAm (bottom) Alkyne-PDMAAm.

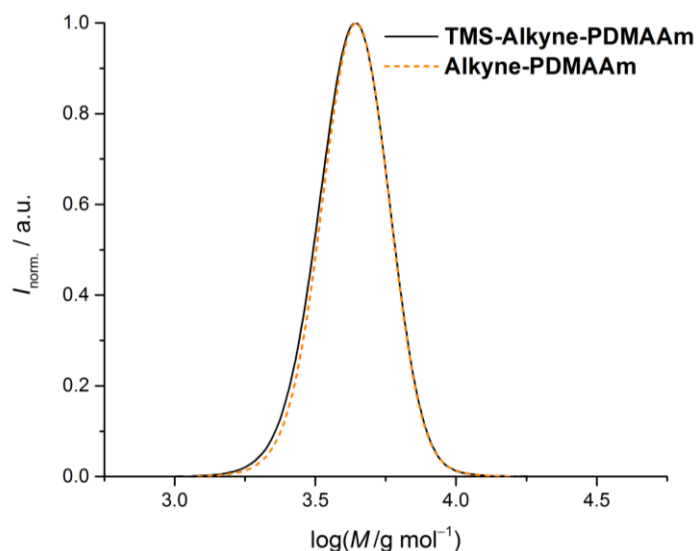


Figure 9.6 SEC traces of **TMS-Alkyne-PDMAAm** and its deprotected counterpart **Alkyne-PDMAAm**.

Example of volume fraction calculation using BCP3:

According to ^1H NMR data, for 1u styrene, there exist $1.25/0.8 = 1.5625\text{u}$ isoprene and 0.04 CMS (u is an arbitrary number)

$$f_{\text{PI}} = \frac{\frac{68.12 \times 1.5625}{0.913}}{\frac{104.15 + (0.04 \times 152.62)}{1.05} + \frac{68.12 \times 1.5625}{0.913}} = 0.53$$

9.1.2 Thin-Film Formation and AFM Parameters

Pretreatment of Silicon Wafers. A fresh silicon disc was cut into 1 cm² pieces with a diamond cutter. These wafers were put in piranha solution ($\text{H}_2\text{SO}_4:\text{H}_2\text{O}_2$ 3:1 v/v) (*Caution! Explosive when in contact with organic solvents!*) at room temperature for 45 min for activation of the SiO_2 layer. The wafers were then rinsed thoroughly with distilled water and consecutively with ethanol and dried under a stream of N_2 .

Spin-Coating Conditions: A solution of PS-*b*-PI was prepared in toluene (0.2 wt%; 2 mg polymer in 1152 μL toluene) and filtered with an SEC filter. 100 μL of this solution was spin-coated on piranha activated, 1x1 cm² Si substrates at 3000 rpm for 1 min resulting in a film thickness of ~ 7 nm. It is to note that different spin-coating conditions such as 3000 rpm, 3 min or in extreme cases 10000 rpm, 10 min also created same type of films at different times.

The important parameter is the film thickness which will bear the desired film morphology. More concentrated solutions need to be spin-coated faster and/or for longer time to obtain thin films and vice versa. Depending on small experimental errors, different conditions should be tried.

AFM Parameters: Apart from the default AFM parameters mentioned in section 8.2.3, here are some exemplary additional parameters that were used in PS-*b*-PI and led to the images presented in this thesis: (1) Integral gain: 0.1, proportional gain: 2, amplitude setpoint: 0.4 V, drive frequency: 264 kHz (NSC35 used), drive amplitude: 150 mV.

(2) Integral gain: 0.1, proportional gain: 2, amplitude setpoint: 0.4 V, drive frequency: 159 kHz (NSC 14 used), drive amplitude: 150 mV.

(3) Integral gain: 0.1, proportional gain: 2, amplitude setpoint: 0.3 V, drive frequency: 157 kHz (NSC 14 used), drive amplitude: 53.20 mV.

(4) Integral gain: 0.2, proportional gain: 0.2, amplitude setpoint: 0.4 V, drive frequency: 159 kHz (NSC 14 used), drive amplitude: 200 mV.

(5) Integral gain: 0.1, proportional gain: 2, amplitude setpoint: 0.5 V, drive frequency: 160 kHz (NSC 14 used), drive amplitude: 30 mV.

9.1.3 Copper Catalyzed Azide-Alkyne Cycloaddition on the Surface

0.4 M CuSO₄, 1.4 M sodium ascorbate and 0.4 M THPTA solutions were prepared in water. BCP3 coated Si wafers were placed in 5 mL vials (x2). The first vial was used for the reaction and the second one was used as control experiment. Onto the first film, 550 μL water was added which was followed by the addition of 200 μL fDMAAm solution (1mg/mL in water). The aforementioned CuSO₄ and THPTA solutions were mixed in equal volumes and 30 μL of this mixture (including 15 μL of each) was added to the first vial. Lastly, 70 μL of sodium ascorbate solution was added and the total volume of solution in the first vial was 850 μL. The lid of the vial was closed and the sample was totally dipped into the solution while the coated side was facing upwards. Secondly, onto the control sample, 650 μL water and 200 μL of the fDMAAm (1 mg/mL) solution were added. Vial was sealed. Both vials were placed on a bench top shaker at a speed of 150 rpm and left for 1 hour at room temperature. Afterwards, samples were removed from the solutions and rinsed thoroughly with water for ~30 sec. Afterwards, they were placed in falcom tubes filled with 14 mL water and placed back onto the shaker at 150 rpm for 15 min for excessive washing (x2). Finally, they were dried with a stream of air gun and analyzed by AFM and XPS.

9.2 Functional PMMA-*b*-PS Library

Synthetic procedures for Chapter 4 as well as related content such as NMR spectra and SEC traces will be given in this section.

9.2.1 Syntheses of PMMA-*b*-PS and Functional Derivatives

Synthesis of the First Block (PMMA, HP1) by ATRP: 8.8 ml MMA (83 mmol, 377 eq.) was mixed with acetone (10.4 mL) in a 50 mL round bottom flask. BiPy (78 mg, 0.5 mmol, 2.3 eq) and MBriB (28.5 μ L, 39.9 mg, 0.22 mmol, 1 eq.) were added to this mixture and the content was then deoxygenated with N₂ for 30 min. CuBr (29.85 mg, 0.21 mmol, 0.94 eq) was taken into a Schlenk tube together with CuBr₂ (5.5 mg, 0.025 mmol, 0.11 eq.). The tube was deoxygenated with 5 cycles of evacuation and backfilling with nitrogen. The content in the first flask was transferred to the Schlenk tube using a cannula. Afterwards, the Schlenk tube was placed in a thermostated oil bath at 50 °C. After 6 h, the flask was cooled to ambient temperature (MMA conv. 49%). The product was passed through a short neutral alumina column, precipitated in cold methanol (\times 2), and the polymer was recovered as a white powder. SEC (THF): $M_n = 19000$ g mol⁻¹; $D = 1.15$.

Synthesis of the Second Block (RBCP) by ATRP: HP1 (590 mg, 0.031 mmol, 1 eq.) was dissolved in toluene (964 μ L) and styrene (888 mg, 8.53 mmol, 275 eq.) was added to this. PMDTA (7.14 μ L, 5.92 mg, 0.034 mmol, 1.1 eq.) was also added with a glass microsyringe. CuBr (4.9 mg, 0.034 mmol, 1.1 eq.) was taken in a Schlenk tube which was deoxygenated by 5 cycles evacuation and backfilling with nitrogen. The content of the first flask was transferred to the Schlenk tube via a cannula after being deoxygenated for 30 min with N₂. The Schlenk tube was placed in a preheated oil bath at 90 °C. The flask was cooled to ambient temperature 24h later (styrene conv. 59%). The product was passed through a short neutral alumina column and precipitated in cold methanol (\times 2) and it was recovered as a white powder. SEC (THF): $M_n = 44400$ g mol⁻¹; $D = 1.24$

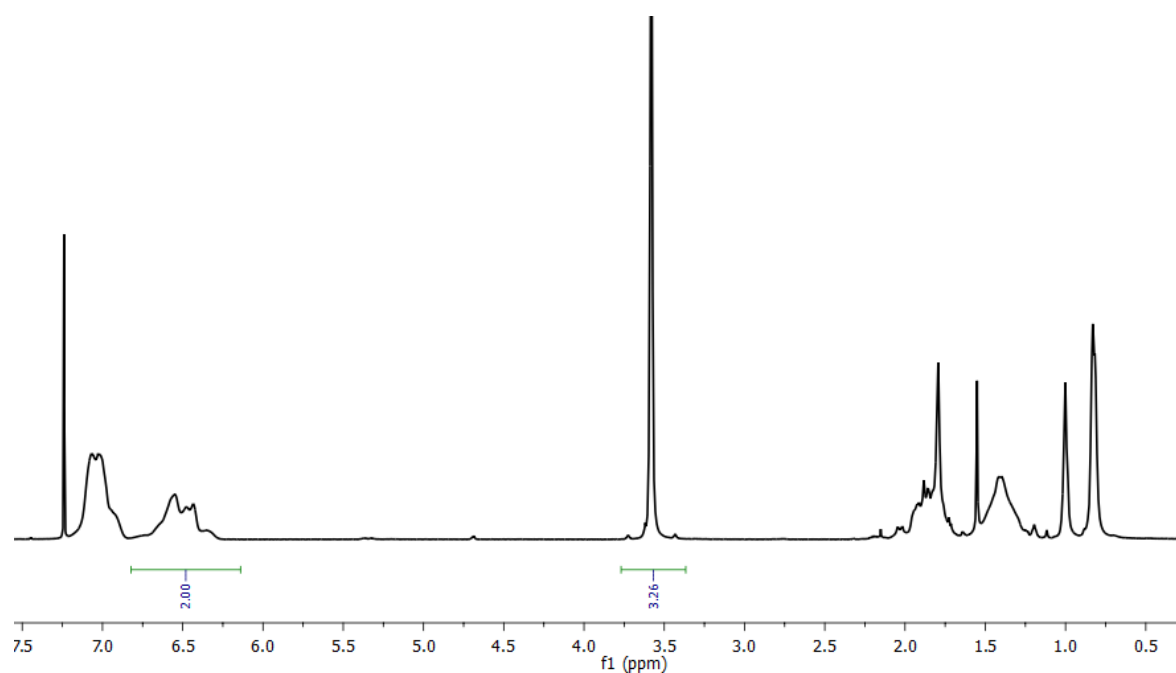


Figure 9.7 ^1H NMR spectrum of RBCP.

Volume Fraction Calculation on RBCP:

As shown on Figure 9.7, The $-\text{OCH}_3$ peak belonging to MMA appears at around 3.5 ppm (3H): $3.26/3 = 1.08$ for one MMA.

The aromatic peaks of styrene appear at 6.5-7.2 ppm (5H), which includes 2 of the protons between 6.5-6.8 pp ($2/2 = 1$ styrene)

There thus exists 1.08k MMA units in the presence of 1k units styrene (k is an arbitrary number).

$$\text{Volume fraction of styrene is equal to } f_{\text{PS}} = \frac{\frac{M(\text{PS})}{d(\text{PS})}}{V(\text{tot})} = \frac{\frac{1 \cdot 104.15}{1.05}}{\frac{1 \cdot 104.15}{1.05} + \frac{1.08 \cdot 100.12}{1.18}} = 0.52$$

Synthesis of Poly(MMA-co-AMA) (CP1) by RAFT: MMA (1.7 g, 16.7 mmol, 382 eq.) and AMA (114.6 mg, 0.91 mmol, 21 eq.) were taken in a round bottom flask. AIBN (0.89 mg, 0.005 mmol, 0.12 eq.) and CPDB (9.7 mg, 0.044 mmol, 1 eq.) were added together with 1,4-dioxane (1.754 mL). After deoxygenation with nitrogen for 30 min, the flask was placed in a thermostated oil bath at 90 °C. The reaction flask was cooled to ambient temperature after 107 min. Dioxane was removed under vacuum. The product was then diluted with a minimum amount of acetone and precipitated in cold methanol ($\times 2$). The polymer was obtained as a pink powder. SEC (THF): $M_n = 23\,500 \text{ g mol}^{-1}$; $D = 1.20$.

Synthesis of Poly(MMA-co-AMA)-*b*-PS (BCP-1) by RAFT: CP1 (400 mg, 0.017 mmol, 1 eq.) was dissolved in styrene (6.8 g, 65 mmol, 3824 eq.) and 1,4-dioxane (6217 μ L). To be handled more easily, AIBN (2 mg) was dissolved in 1,4-dioxane (2 mL) previously. From this solution, 555 μ L was taken and added to the reaction flask which provided 0.555 mg AIBN into the mixture (0.0034 mmol, 0.2 eq.) (Total solvent volume in the reaction flask was 6772 μ L). After deoxygenation with N₂ for 30 min, the flask was placed in a preheated oil bath at 90 °C and it was cooled to ambient temperature after 60 min. Dioxane was removed under vacuum. The product was then diluted with a minimum amount of acetone and precipitated in cold methanol ($\times 2$). The polymer was obtained as a pink powder. SEC (THF): $M_n = 41\,400\text{ g mol}^{-1}$; $D = 1.32$.

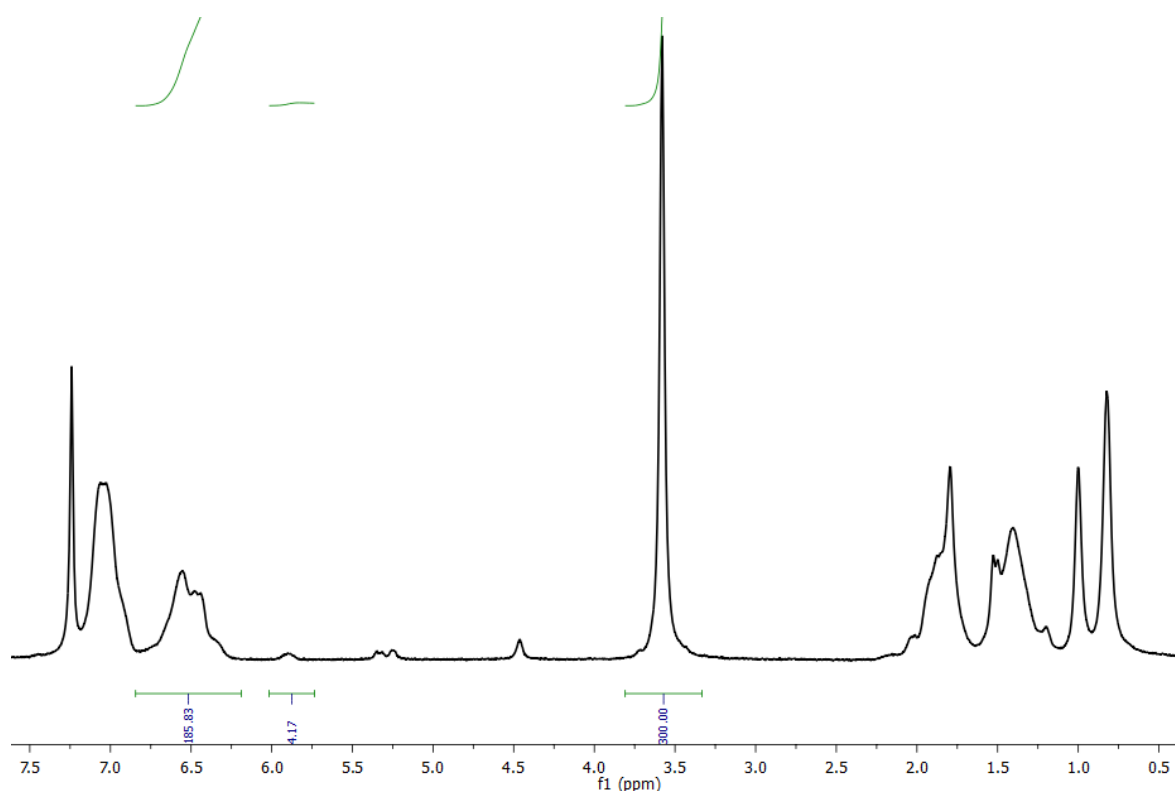


Figure 9.8 ¹H NMR spectrum of BCP-1

Volume Fraction Calculation on BCP-1:

As given on Figure 9.8, for 100m MMA, there exist 92.9m styrene and 4.17m AMA, m being an arbitrary number. (Peak assignments were done according to the literature)^[64]

$$\text{Volume fraction of styrene is equal to } f_{\text{PS}} = \frac{M(\text{PS})}{V(\text{tot})} = \frac{\frac{92.915m \cdot 104.15}{1.05}}{\frac{92.915m \cdot 104.15}{1.05} + \frac{100m \cdot 100.12}{1.18} + \frac{4.17m \cdot 126.15}{1.18}} = 0.51$$

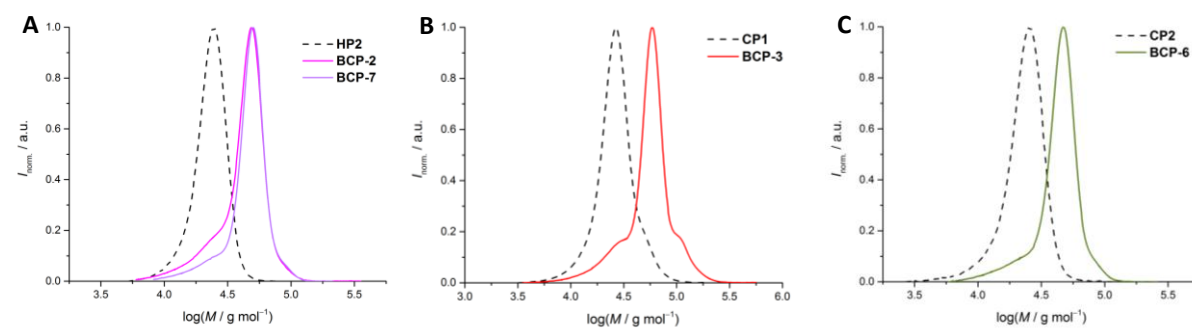


Figure 9.9 SEC traces of (A) HP2, BCP-2, and BCP-7; (B) CP1 and BCP-3; and (C) CP2 and BCP-4.

Synthesis of HP2 by RAFT: CPBD (55.3 mg, 0.25 mmol) was dissolved in 1,4-dioxane (9 mL) in a 50 mL round bottom flask. MMA (10 g, 99.9 mmol) was subsequently added. In a 5 mL vial, AIBN (5.13 mg, 0.03 mmol) was dissolved in 1,4-dioxane (1 mL) which was transferred to the round bottom flask. A t_0 sample was taken and the flask was sealed with a septa. The flask was deoxygenated by bubbling nitrogen through a needle for 1 h. The reaction was run in a preheated oil bath at 90 °C which was cooled to ambient temperature after 150 min. The resulting polymer was precipitated twice in cold methanol and dried under vacuum at 40 °C overnight. SEC (THF): $M_n = 21\,300 \text{ g mol}^{-1}$; $\mathcal{D} = 1.10$.

Synthesis of PMMA-*b*-Poly(Sty-*co*-AzMeSty) (BCP-2) by RAFT: Macro-RAFT agent HP2 (89.26 mg, 0.004 mmol) was dissolved in 1,4-dioxane (1 mL). Styrene (1.7 g, 16.3 mmol) and AMS (136 mg, 0.96 mmol) were added. AIBN (0.14 mg, 0.0008 mmol) that was dissolved in 1,4-dioxane (560 μL) was added. The flask was deoxygenated by bubbling nitrogen through a needle for 1 h. The reaction was run in a preheated oil bath at 90 °C which was cooled to ambient temperature after 90 min. The resulting polymer was precipitated twice in cold methanol and dried under vacuum at 40 °C overnight. SEC (THF): $M_n = 36\,700 \text{ g mol}^{-1}$; $\mathcal{D} = 1.23$.

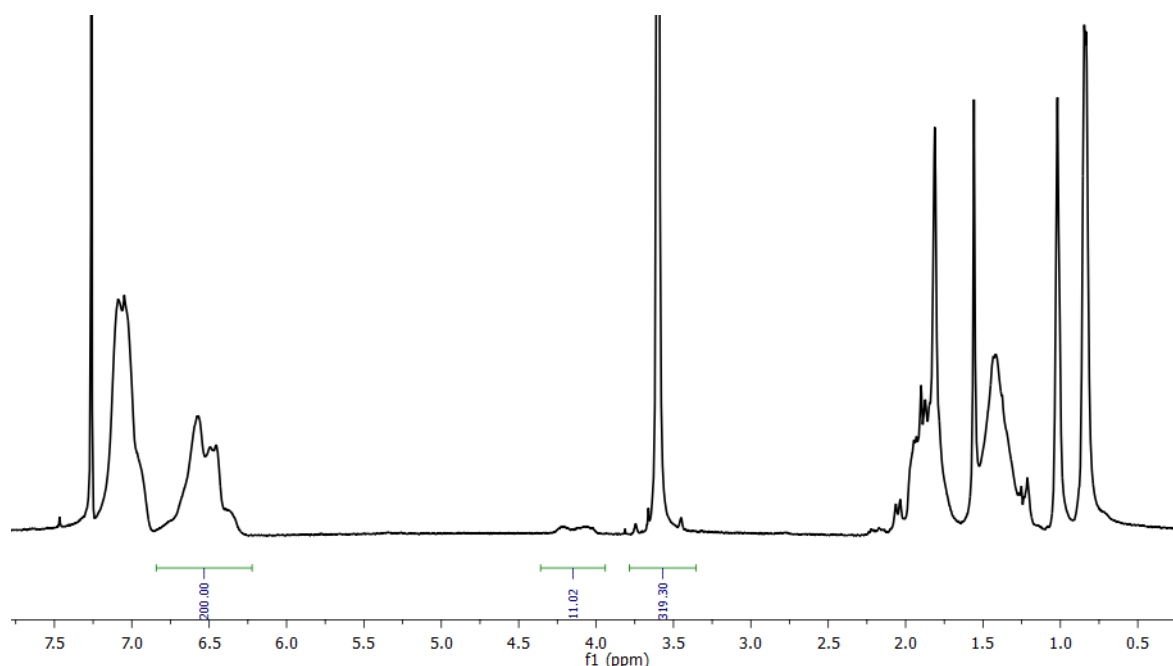


Figure 9.10 ^1H NMR spectrum of **BCP-2**.

Volume Fraction Calculation on BCP-2:

The peak at 4.1 ppm belongs to 2H of the methylene unit adjacent to the azide. This means, for 100m number of styrene, there exist 106.4m MMA and 5.50m of azidomethylstyrene (m is an arbitrary number).

$$\text{Volume fraction of styrene is equal to } f_{\text{PS}} = \frac{M(\text{PS})}{d(\text{PS})} = \frac{V(\text{tot})}{\frac{100\text{m} \cdot 104.15}{1.05} + \frac{106.4\text{m} \cdot 100.12}{1.18} + \frac{5.50\text{m} \cdot 159.188}{1.05}} = 0.55$$

The same type of calculations were conducted for the rest of the study.

Synthesis of Poly(MMA-co-AMA)-*b*-Poly(Sty-co-BrS) (BCP-3) by RAFT: Macro-RAFT agent CP1 (569 mg, 0.024 mmol, 1 eq.) was dissolved in styrene (9.2 g, 88 mmol, 3667 eq.). BrS (846 mg, 4.62 mmol, 193 eq.) and 1,4-dioxane (9650 μl) were also added. AIBN (0.8 mg, 0.005 mmol, 0.21 eq.) was finally added. After deoxygenation with nitrogen for 30 min, the flask was placed in a thermostated oil bath at 90 °C. After 90 min, the flask was cooled to ambient temperature. After removing 1,4-dioxane under vacuum, the product was diluted with a minimum amount of acetone and precipitated in cold methanol ($\times 2$). The resulting polymer was recovered as a pink powder. SEC (THF): $M_n = 45\,500 \text{ g mol}^{-1}$; $D = 1.34$.

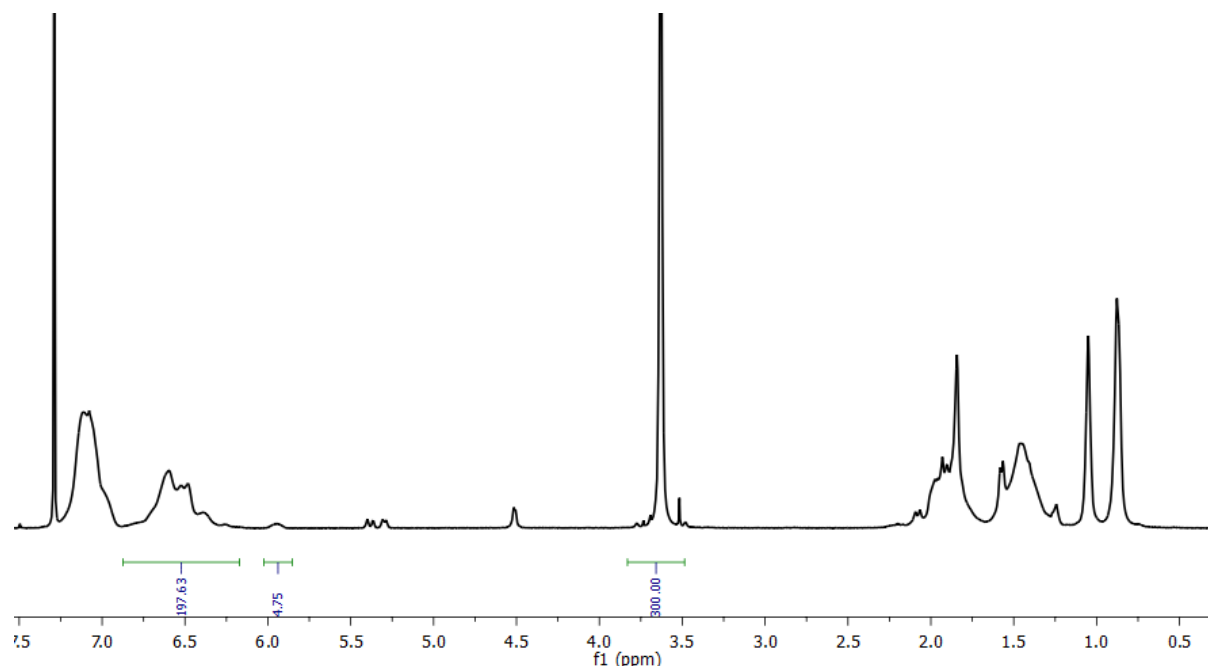


Figure 9.11 ^1H NMR spectrum of **BCP-3**.

Synthesis of CP2 by RAFT: CPBD (55.3 mg, 0.25 mmol) was dissolved in 1,4-dioxane (9 mL) in a 50 mL round bottom flask. MMA (9.5 g, 94.9 mmol) and PFPMA (1.26 g, 0.5 mmol) were added to this. In a 5 mL vial, AIBN (5.13 mg, 0.03 mmol) was dissolved in 1,4-dioxane (0.5 mL) which was then added into the reaction flask. The flask was sealed with a rubber septum after a t_0 sample was withdrawn, deoxygenated by bubbling nitrogen for 1 h, and subsequently placed in a pre-heated oil bath at 90 °C. After 3 h, the flask was cooled down to ambient temperature. ^1H NMR was used to determine the conversion of both comonomers. The resulting polymer was purified by precipitation in cold methanol ($\times 2$) and dried under vacuum at 40 °C overnight. The macro-RAFT agent was obtained as a pink powder. The incorporation of PFPMA was confirmed by ^{19}F NMR. The amount of PFPMA incorporated was estimated via conversion calculation of the non-purified polymer since PFPMA does not have any identifiable peaks in ^1H NMR. MMA (conv.) = 44%, PFPMA(conv.) = 67%. SEC (THF): $M_n = 20\,900\text{ g mol}^{-1}$; $\mathcal{D} = 1.16$.

Synthesis of Poly(MMA-co-PFPMA)-b-Poly(Sty-co-PFS) (BCP-4) by RAFT: Macro-RAFT agent CP2 (525 mg, 0.0025 mmol) was dissolved in 1,4-dioxane (9.5 mL) in a 50 mL round bottom flask. To this solution, styrene (9.7 g, 93.1 mmol) and PFS (559.1 mg, 2.8 mmol) were added. AIBN (1.64 mg, 0.001 mmol) was separately dissolved in 1,4-dioxane (0.5 mL) which was subsequently added into the round bottom flask. The flask was sealed with a rubber septum and the content was deoxygenated with nitrogen for 1 h. The reaction was run in a thermostated oil bath at 90 °C for 80 min. After this, the flask was cooled to ambient temperature. The resulting

polymer was purified by precipitation in cold methanol ($\times 2$) and dried under vacuum at 40 °C overnight. The product was recovered as a pink powder. SEC (THF): $M_n = 37\,400\text{ g mol}^{-1}$; $D = 1.17$.

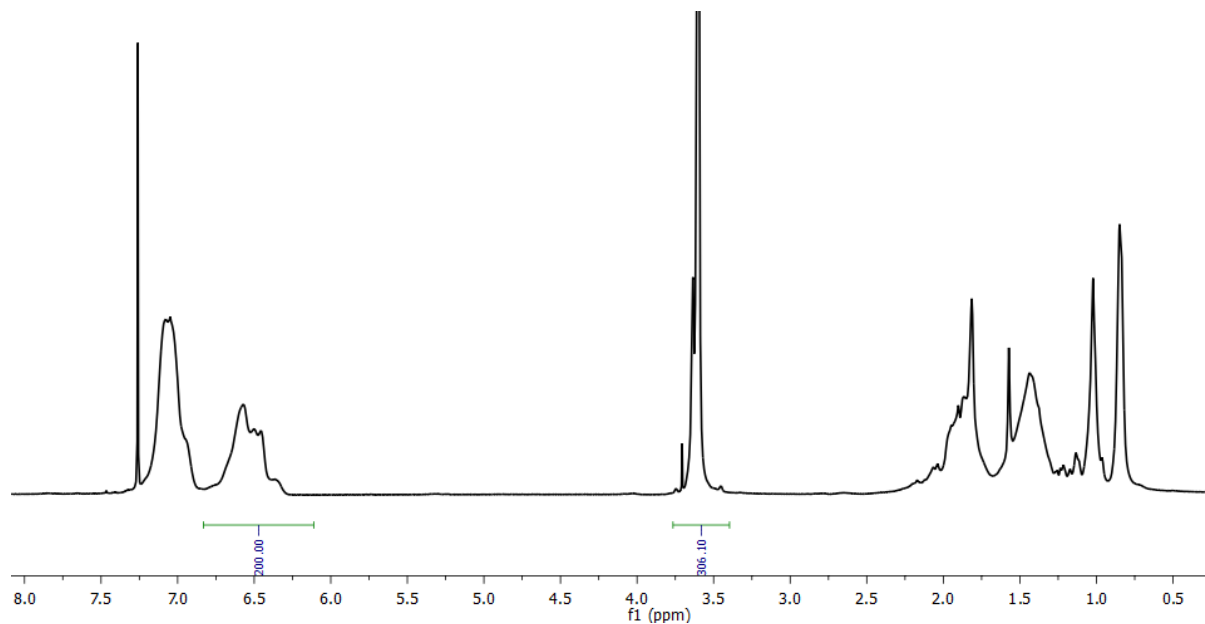


Figure 9.12 ^1H NMR spectrum of BCP-4.

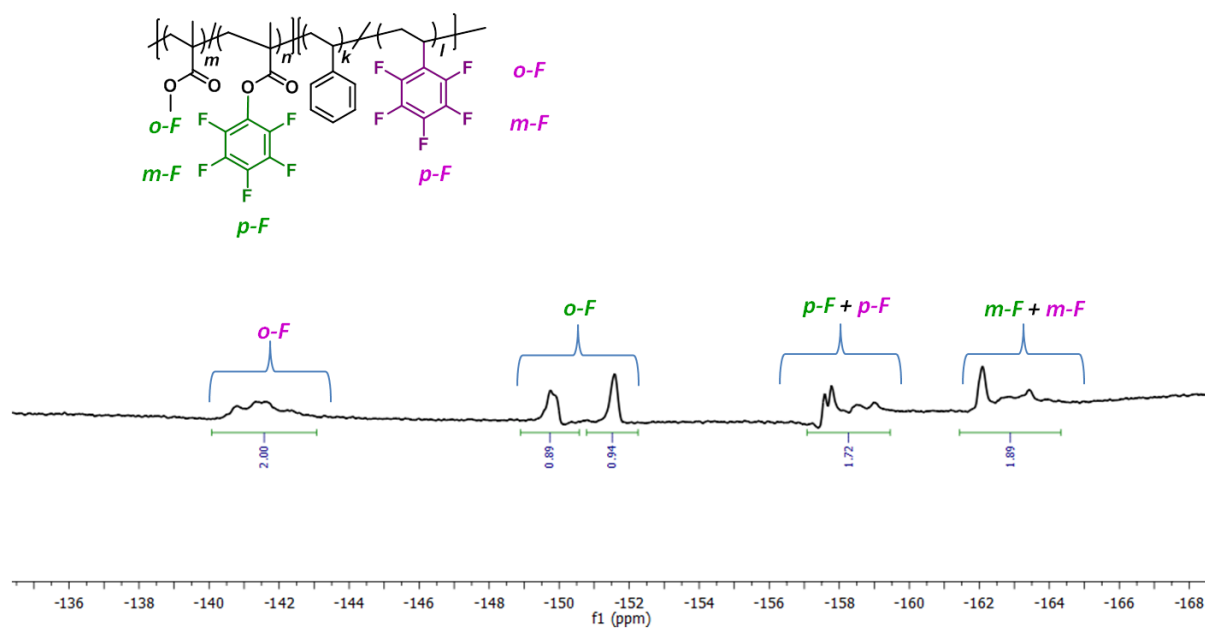


Figure 9.13 ^{19}F NMR spectrum of BCP-4.

Synthesis of BCP-5

Step 1 Amidation Reaction on BCP-4: End capping of the RAFT group was done according to the literature.^[338] In a 5 mL round bottom flask, the end group capped **BCP-4** (100 mg, 0.0023 mmol, 1 eq.) of the polymer was prepared in DMF and placed in a pre-heated oil bath at 50 °C. In another flask, furfurylamine (180.69 mg, 1.86 mmol, 50 eq. per unit of PFPMA) and triethylamine (18.83 mg, 0.186 mmol, 5 eq. per unit of PFPMA) were mixed together and added to the polymer solution. After stirring for 24 h, the reaction mixture was cooled down to room temperature and excess DCM was added. The organic layer was extracted with distilled water (20 mL) followed by brine (2 × 20 mL). Excess dichloromethane was then removed under vacuum and the polymer was precipitated in excess cold methanol and washed extensively with cold methanol. The polymer was then dried under vacuum at 40 °C overnight to obtain the modified polymer as a white powder.

Step 2 PFTC Reaction on BCP 4: This reaction was performed according to the literature.^[64]

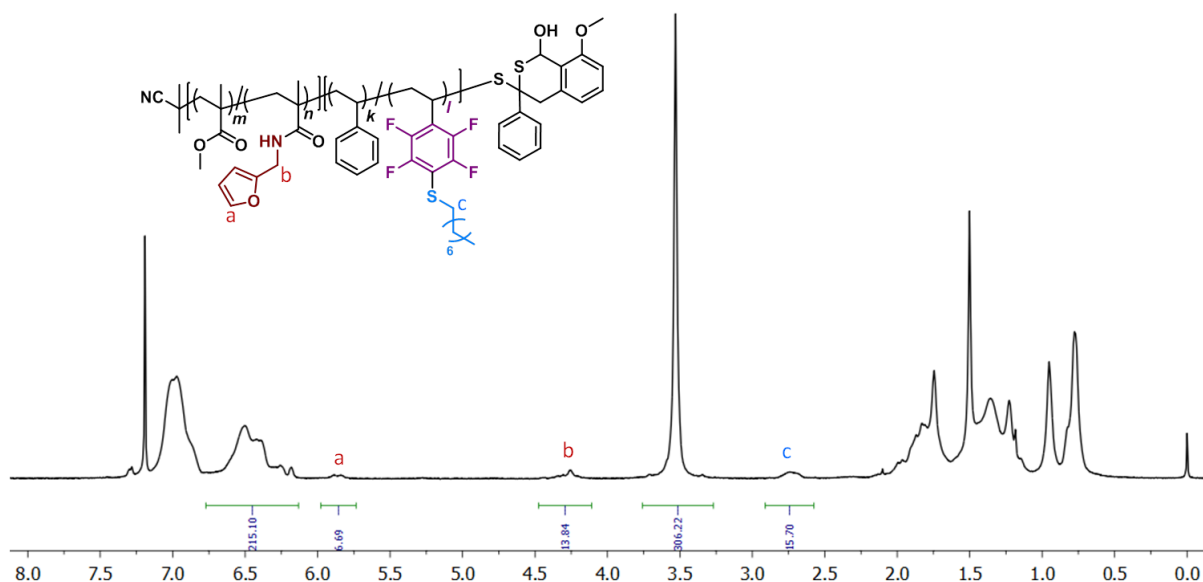


Figure 9.14 ¹H NMR spectrum of **BCP-5**.

Volume Fraction Calculation for BCP-4 and BCP-5:

f_{PS} of BCP5 (and that of BCP4 as well) is calculated with the following formula:

$$f_{PS} = \frac{M(PS)}{V(tot)} = \frac{\frac{100.85k * 104.15}{1.05} + \frac{7.85k * 194.10}{1.05}}{\frac{100.85k * 104.15}{1.05} + \frac{7.9k * 194.10}{1.05} + \frac{102k * 100.12}{1.18} + \frac{6.7k * 252.14}{1.18}} = 0.53$$

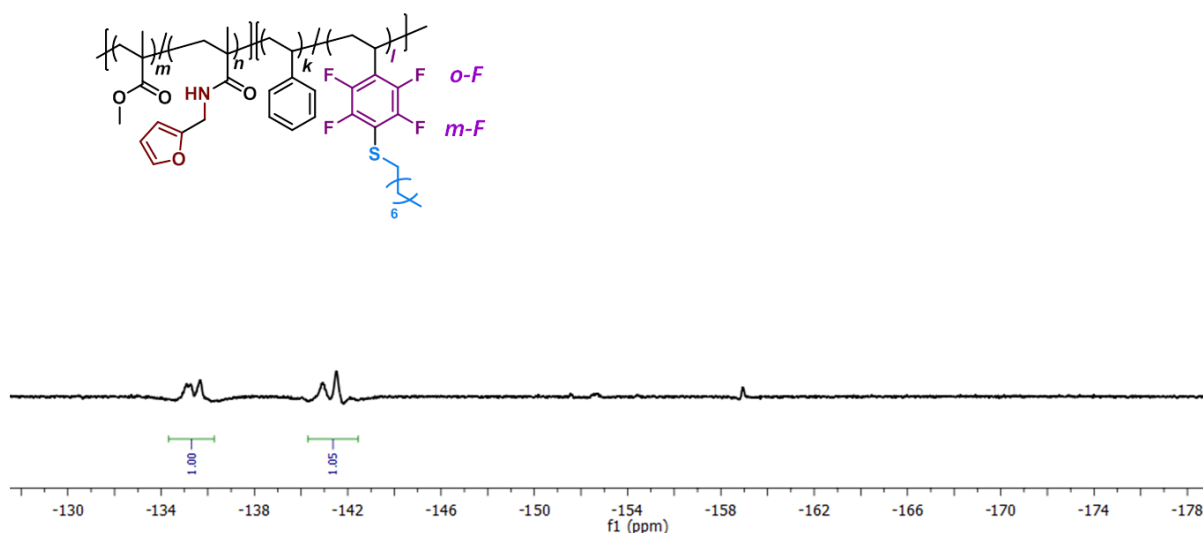


Figure 9.15 ^{19}F NMR spectrum of **BCP-5**.

Synthesis of BCP-6: In a 50 mL round bottom flask, CP2 (525 mg, 0.0025 mmol) was dissolved in 1,4-dioxane (9.18 mL). To this, styrene (10 g, 93.1 mmol) was added. AIBN (0.82 mg, 0.005 mmol) (820 μL was taken from a 1 mg/mL stock solution of AIBN in dioxane) was subsequently added. The flask was sealed with a rubber septum and the contents were deoxygenated by bubbling with nitrogen for 30 min and placed in a pre-heated oil bath at 90 $^{\circ}\text{C}$ for 80 min. After this, the flask was cooled down to ambient temperature. The same purification steps were applied as for the previous BCPs.

Synthesis of BCP-7: In a 50 mL round bottom flask, HP2 (509 mg, 0.024 mmol) was dissolved in 1,4-dioxane (9.18 mL). To this, styrene (9.7 g, 93.1 mmol) and PFS (300 mg, 1.54 mmol) were added. AIBN (0.82 mg, 0.005 mmol) (820 μL was taken from a 1 mg/mL stock solution of AIBN in dioxane) was also added. The same steps were repeated as for **BCP-6**.

9.2.2 Synthesis of StCP by ATRP

The OH-terminated initiator was synthesized according to the literature.^[343] Styrene (3.64 g, 35 mmol, 4 mL, 404 eq.) was mixed with 1.7 g MMA (17 mmol, 1.83 mL, 196 eq.) in a 25 mL round bottom flask. BiPy (27.2 mg, 0.174 mmol, 2 eq.) and HEBIB (18.4 mg, 0.087 mmol, 1 eq.) and toluene (5 mL) were also added to the same flask and the content was deoxygenated with N_2 gas for 30 min. CuBr (12.7 mg, 0.088 mmol, 1.01 eq.) was taken in a Schlenk tube which was deoxygenated with 5 cycles evacuation and backfilling with nitrogen. The content of the first flask was transferred to the Schlenk tube using a cannula and the tube was immediately placed in a thermostated oil bath at 90 $^{\circ}\text{C}$. The flask was cooled to ambient temperature after 15h. The

resulting polymer was passed through a short neutral alumina column to remove copper residues and then precipitated in cold methanol ($\times 2$). The product was recovered as a white powder. SEC (THF): $M_n = 12\,900\text{ g mol}^{-1}$; $D = 1.21$.

Calculation of the Composition of StCP

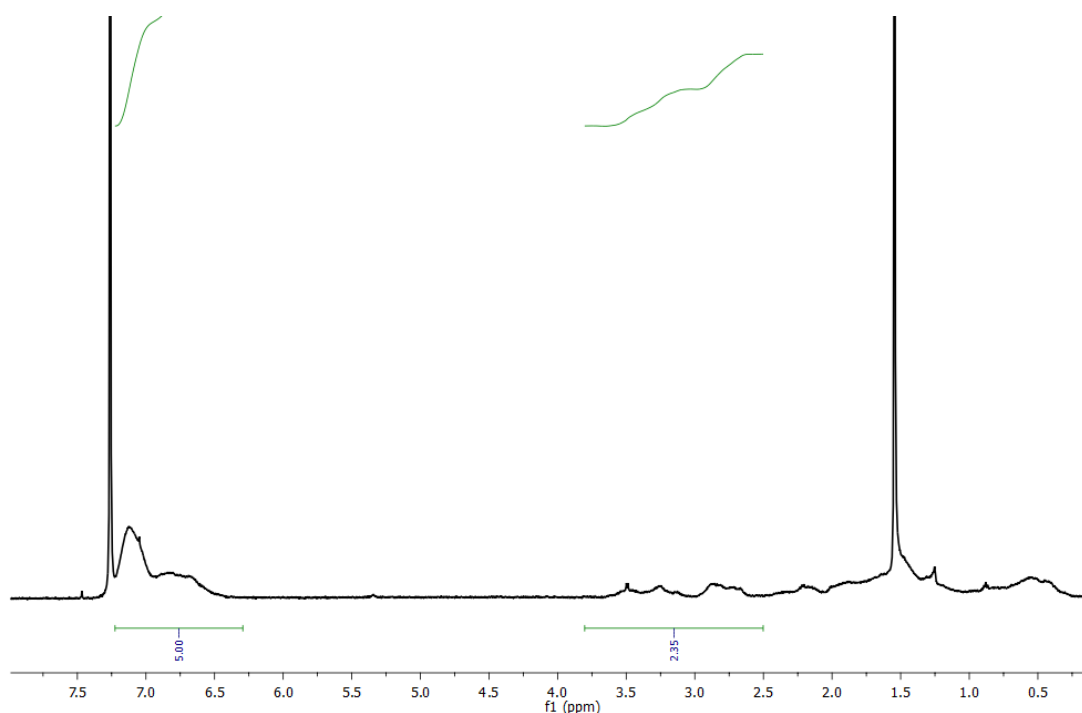


Figure 9.16 ^1H NMR spectrum of the StCP.

$-\text{OCH}_3$ peaks belonging to methyl methacrylate units appear between 2.5 ppm-3.8 ppm ($2.35 / 3 = 0.78$ stands for 1 H) as depicted on Figure 9.16.

The aromatic peaks of styrene are present between 6.5 ppm-7.3 ppm ($5 / 5 = 1$ stands for 1H).

Mole fraction of styrene is equal to $1 / (1+0.78) = 0.56$, that of MMA is 0.44.

9.2.3 Thin Film Formation and AFM Parameters

Formation of First Layer (Surface Neutralization): 100 μL of a 1 wt% solution of the StCP (1 mg polymer per 100 μL toluene, filtered) was spin-coated at 3000 rpm for 1 min as previously done in another report.^[348] Coated wafers were then placed on glass Petri dishes and left in vacuum oven at 170 $^\circ\text{C}$ for 2.5 days in order to graft the StCP onto the substrates via the $-\text{OH}$

end group. Afterwards, samples were brought to RT and each wafer was placed into a small vial filled with approx. 5 ml toluene. To remove unattached chains, they were sonicated for 5 min. Finally, surfaces were dried with N₂ gun after rinsing with toluene for 5 seconds.

Thin Film Formation with BCPs (Formation of Second Layer): 1 wt% solution of a BCP solution in toluene (100 μ L, filtered) was added on a neutralized Si substrate and spin-coated at 3000 rpm for 1 min. The films were subsequently thermally annealed in a vacuum oven at 170 °C for 1 day. After 24 h, the samples were quickly quenched to RT.

AFM Parameters: Apart from the default AFM parameters mentioned in section 8.2.3, here are some exemplary additional parameters that were used for analyzing PMMA-*b*-PS thin films and led to the images presented in this thesis:

(1) Integral gain: 0.1, proportional gain: 2, amplitude setpoint: 0.4 V, drive frequency: 264 kHz (NSC35 used), drive amplitude: 810 mV.

(2) Integral gain: 0.1, proportional gain: 0.1, amplitude setpoint: 0.7 V, drive frequency: 273 kHz (NSC 35 used), drive amplitude: 180 mV.

(3) Integral gain: 0.4, proportional gain: 0.4, amplitude setpoint: 0.6 V, drive frequency: 279 kHz (NSC 35 used), drive amplitude: 60.15 mV.

(4) Integral gain: 0.2, proportional gain: 0.2, amplitude setpoint: 0.4 V, drive frequency: 157 kHz (NSC 14 used), drive amplitude: 74 mV.

(5) Integral gain: 0.2, proportional gain: 2, amplitude setpoint: 0.8 V, drive frequency: 159 kHz (NSC 14 used), drive amplitude: 1200 mV.

9.2.4 Film Stabilization via Thermal and Photo Crosslinking

Photocrosslinking: A thermally annealed **BCP3** film was placed in a quartz flask and connected to a vacuum pump. Connected to the vacuum the entire time, the surface was irradiated with UV light ($\lambda = 254$ nm) at 1 cm distance for 30 min, with a simple TLC hand-held lamp (CAMAG).

Thermal Crosslinking: A thermally annealed **BCP2** film was placed in a Schlenk tube which was closed with a glass stopper. The tube was under vacuum for 30 min and then backfilled with N₂. Afterwards, it was placed in oven at 250 °C for 2 h to be crosslinked.

9.3 Two Orthogonal Thiol Modulations: Thiol-Ene and PFTR

In this section, detailed procedures will be given for the experiments discussed in Chapter 5. Related NMR spectra will also be provided.

9.3.1 General Procedure for the Synthesis of P(MMA-co-AMA)

MMA (9.5 g, 95 mmol) and AMA (0.63 g, 5 mmol) were mixed in anisole (4.4 mL) in a 50 mL round-bottom flask. MBriB (64.7 μ L, 0.5 mmol) was added to this mixture. Me₆(TREN) (13.4 μ L, 0.05 mmol) and CuBr₂ (11 mg, 0.05 mmol) were provided from a previously prepared stock solution in anisole. Sn(EH)₂ (101.28 mg, 0.25 mmol) was added from a solution prepared in anisole. The total volume of anisole in the main flask was completed to 9.2 mL. The flask was sealed with a rubber septum and the content was purged with nitrogen for approximately one hour. Afterwards, it was placed in a preheated oil bath at 60 °C. The flask was cooled to ambient temperature after 2 h of reaction time. The resulting product was passed through a short neutral alumina column to remove residual copper. It was subsequently dried under vacuum and precipitated twice in cold methanol by dissolution in a small amount of acetone. The polymer was recovered as a white powder. Several polymers were synthesized with a similar procedure and employed for this study. Their characteristics are summarized in Table 5.1.

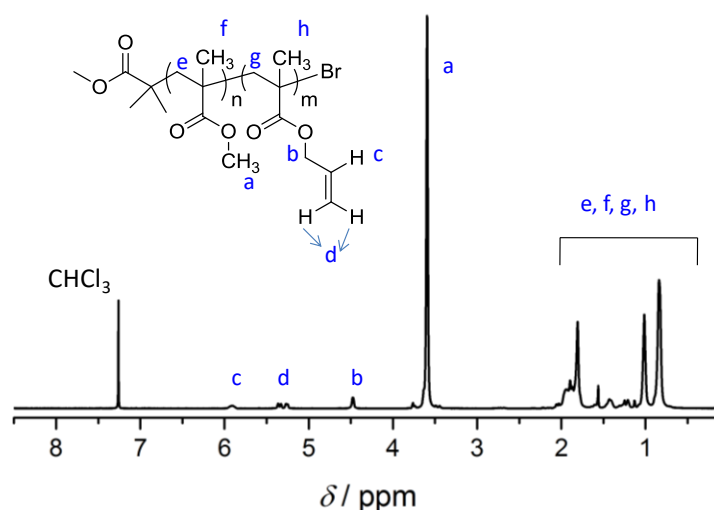


Figure 9.17 Exemplary ¹H NMR spectrum of a P(MMA-co-AMA) macroinitiator (**P3**).

9.3.2 General Procedure for the Synthesis of P(MMA-co-AMA)-*b*-(S-co-PFS)

P(MMA-co-AMA) (1 g, approx. 0.1 mmol) was mixed with styrene (4.2 g, 40 mmol), PFS (0.440 mg, 2.3 mmol), and anisole (3.5 mL). Me₆(TREN) (2.7 μ L, 0.01 mmol) and CuCl₂ (1.3 mg, 0.01 mmol) and were added from a previously prepared stock solution in anisole. Sn(EH)₂ (20 mg, 0.05 mmol) was added from a solution prepared in anisole. The volume of anisole in the reaction flask was 4.5 mL in total. A time zero (t_0) sample was withdrawn for ¹H NMR spectroscopy analysis and the flask was immediately sealed with a rubber septum. The content was purged with nitrogen for 1 h before being placed in a preheated oil bath at 110 °C. After 80 min, the reaction was stopped by cooling the flask to ambient temperature. The resulting product was passed through a short neutral alumina column to remove copper residues, successively dried under vacuum and precipitated twice in cold methanol after dissolution in a minimum amount of acetone. P(MMA-co-AMA) was recovered as a white powder. Several block polymers were synthesized with the same procedure and employed for the current study. Their characteristics are compiled in Table 5.1.

Calculation of PFS Content

As there is no distinguishable peak of PFS in the ¹H NMR spectrum of BCP, direct calculation of the PFS content is not possible and is therefore determined indirectly via its consumption during the synthesis of BCP.

¹H NMR spectra of the initial and final raw (unpurified) polymerization mixtures (BCP synthesis) are recorded. Since PMMA does not undergo any change during the synthesis of the styrenic block, one of its characteristic peaks is used as an internal standard (around 3.6 ppm) and monomer conversions of styrene and PFS are calculated accordingly. Figure 9.18 shows exemplary initial and final raw ¹H NMR spectra. The corresponding calculations were made as follows.

For an integration of the methoxy peak of MMA units set to 3.00 in the initial and final samples, the initial integration values for one vinylic proton of styrene are 5.18 and 4.45, respectively. This gives a styrene conversion of 14% $([5.18-4.45]/5.18)$. A similar calculation gives 37% conversion for PFS $([0.27-0.17]/0.27)$.

Subsequently, a ¹H NMR spectrum of the precipitated BCP is acquired and the molar ratios of MMA-AMA-styrene are obtained by integration (Figure 9.19): 100-5.3-66.

Experimental Procedures

Combining calculations from Figures 9.18 and 9.19, the overall compositional ratios are obtained as:

MMA-AMA-styrene-PFS = 100-5.3-66-9

To double-check the PFS content, quantitative grafting of octanethiol onto BCP is exploited. To this aim, ^{19}F NMR is first employed to verify the full disappearance of the *para*-fluorine atom. Integration of distinct OT peaks in the ^1H NMR spectrum of the purified product enables another indirect calculation of the PFS content (1 OT = 1 initial PFS). For grafting OT, the procedure explained for the synthesis of compound **C1** is applied (see 9.3.3). The results obtained by this method match the values obtained by indirect PFS conversion calculation as listed on Table 5.1.

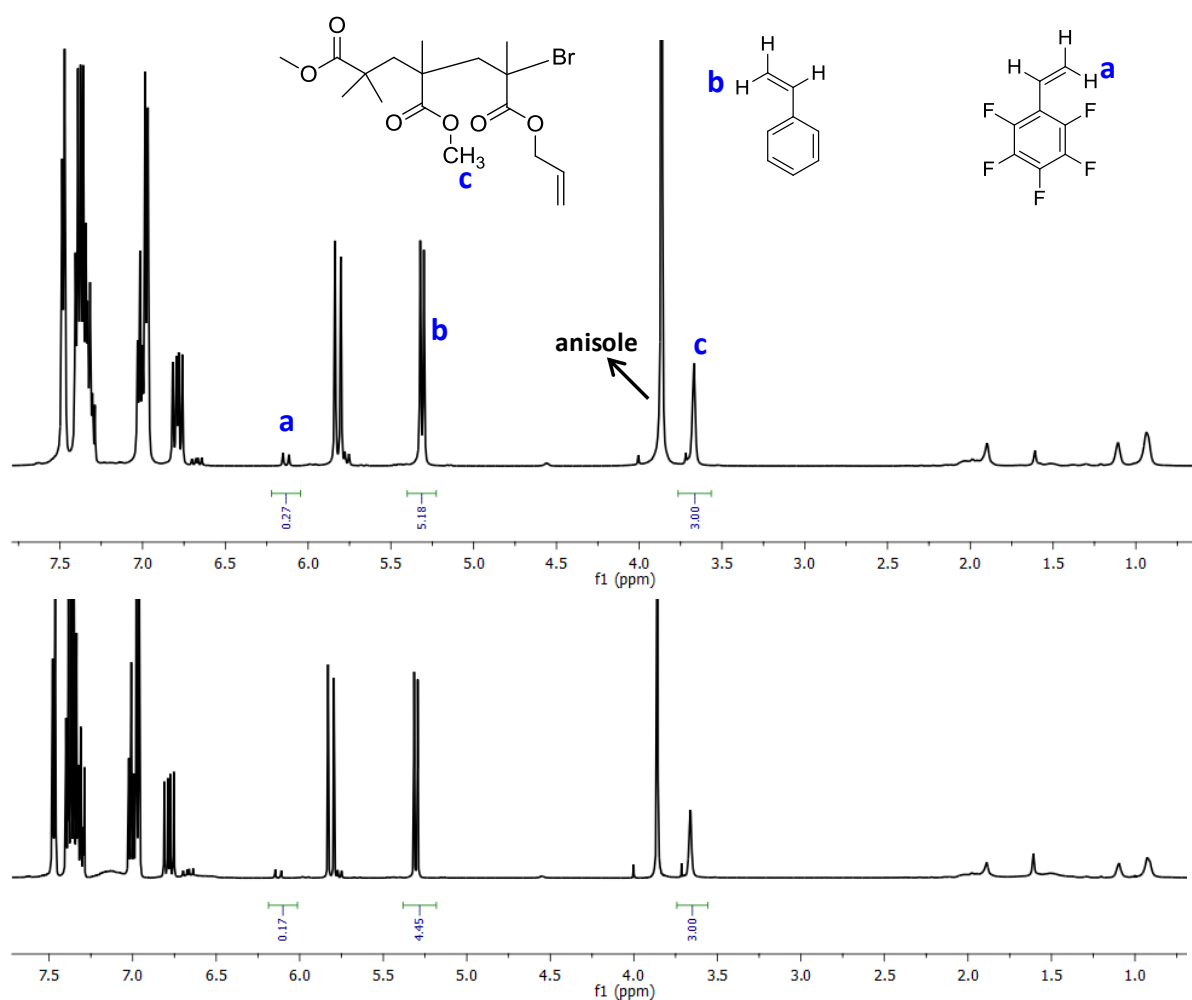


Figure 9.18 Exemplary ^1H NMR spectra for the calculation of PFS content using **BCP[4]** initial (top) and final (bottom) raw polymerization mixtures.

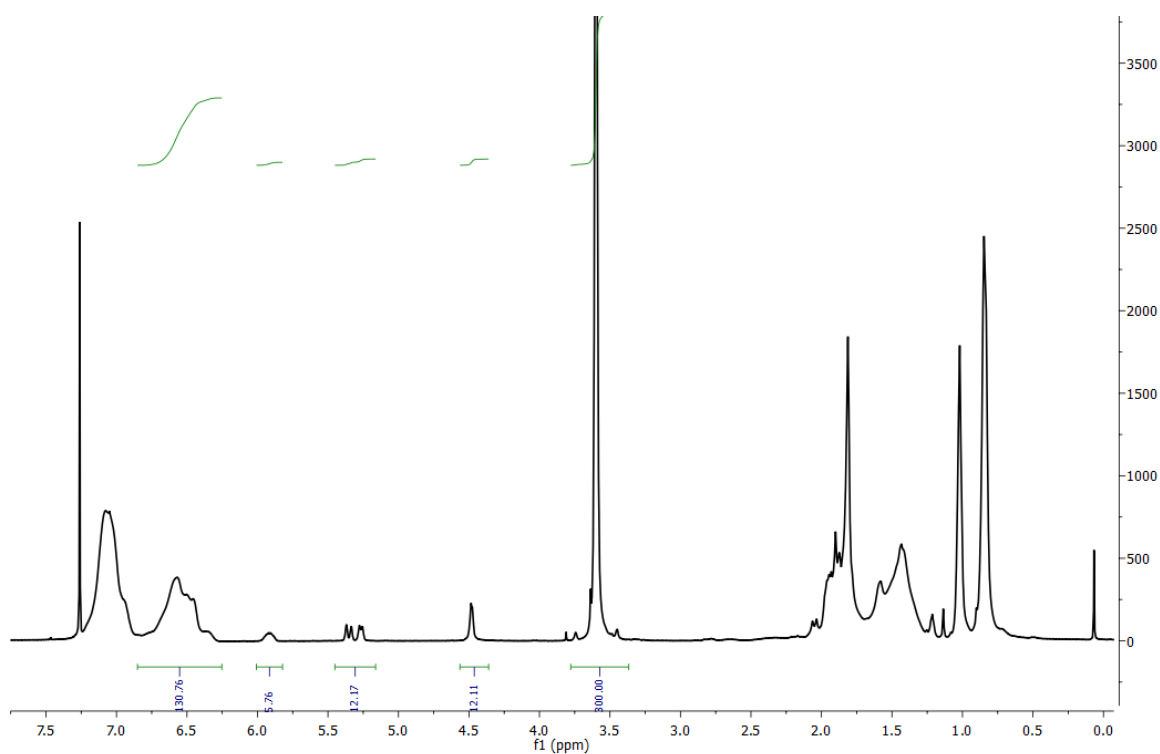


Figure 9.19 ¹H NMR spectrum of BCP[4] with peak integral values.

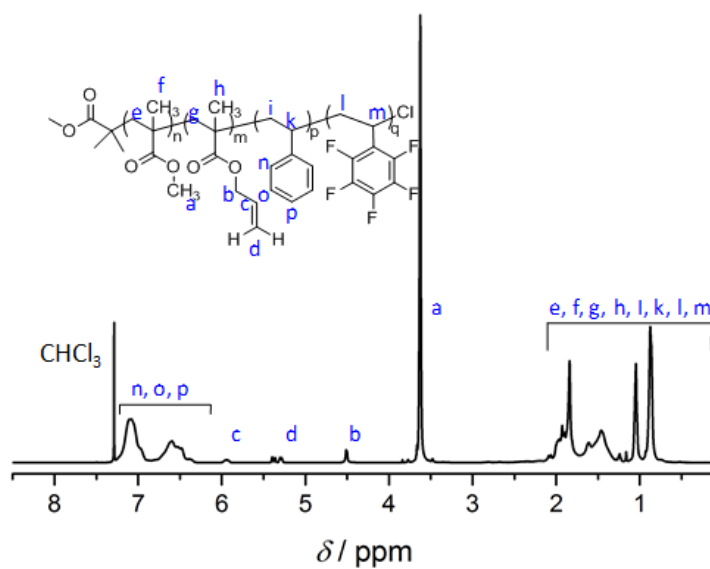


Figure 9.20 ¹H NMR spectrum of BCP[4].

9.3.3 PFTR and Thiol-Ene Occurring Separately on P(MMA-co-AMA)-b-P(S-co-PFS)

PFTR on P(MMA-co-AMA)-b-P(S-co-PFS) (C1): BCP[1] (300 mg) was dissolved in DMF (1.55 mL) in a 5 mL round-bottom flask. A stock solution was prepared by dissolving DBU (129.8 mg, 0.85 mmol) in 10 mL DMF. 1.5 mL of this DBU solution was injected into the aforementioned 5 mL flask, which provided 1 eq. of DBU (18.8 mg, 0.123 mmol) according to PFS units. Lastly, OT (107.4 μ L, 0.618 mmol, 5 equiv according to PFS units) was added to the flask and it was sealed with a rubber septum. After 2 min, a 50 μ L aliquot was withdrawn and the reaction was quenched by directly introducing it into an NMR tube filled with CDCl₃ (0.5 mL). The rest of the product was precipitated into cold methanol and **C1** was recovered as a white powder. SEC (THF): $M_n = 21\,900\text{ g mol}^{-1}$; $\mathcal{D} = 1.15$.

Thiol-Ene Reaction on P(MMA-co-AMA) (C2): BCP[2] (300 mg) was dissolved in 3 mL DMF in a 5 mL round-bottom flask. BDK (11.1 mg, 0.044 mmol, 0.5 equiv according to double bonds) and OT (75.5 μ L, 0.44 mmol, 5 eq. according to double bonds) were added and the flask was sealed with a rubber septum. The content was purged with nitrogen for 30 min and subsequently irradiated for by UV light ($\lambda = 366\text{ nm}$) at 2 cm distance for 30 min. The reaction was stopped by placing the flask in the dark. The product **C2** was precipitated into cold methanol and recovered as a white powder. SEC (THF): $M_n = 18\,800\text{ g mol}^{-1}$; $\mathcal{D} = 1.17$.

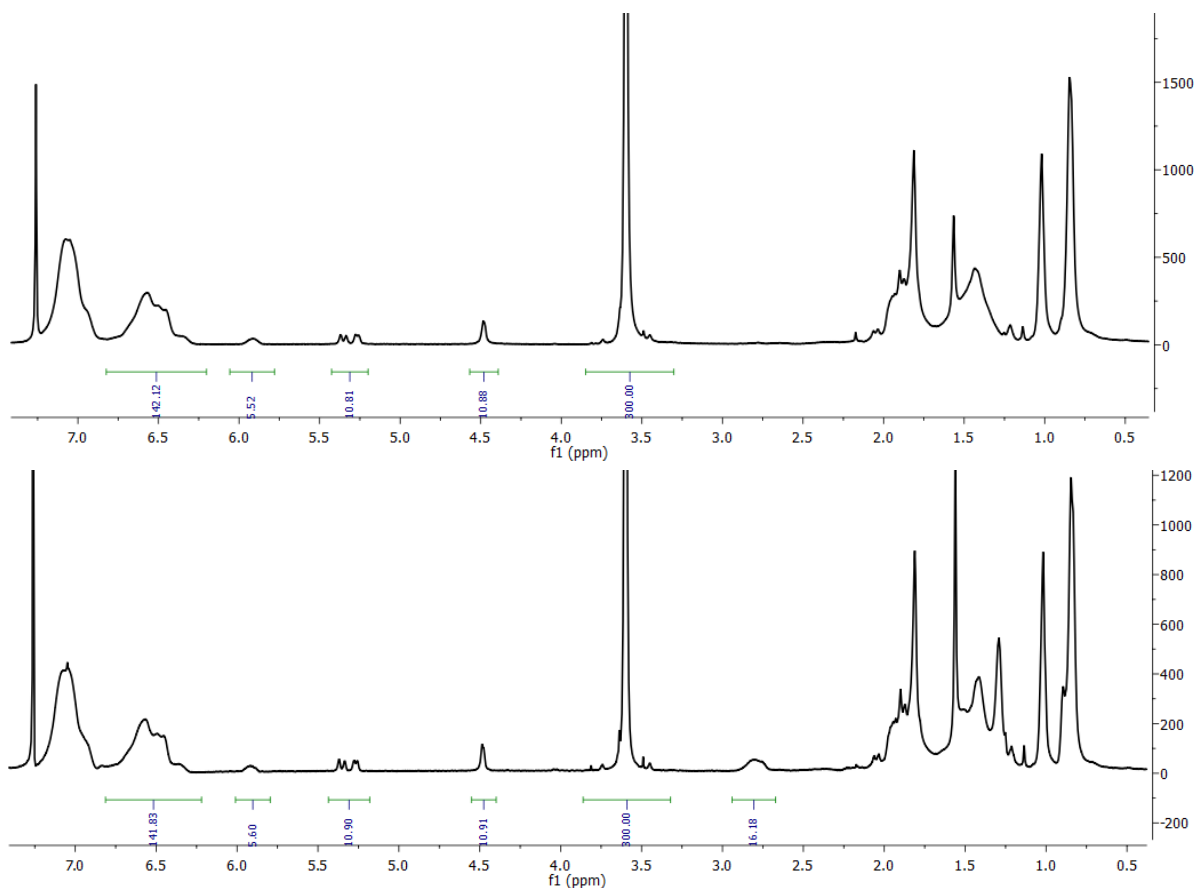


Figure 9.21 ¹H NMR spectra with integration values of BCP[1] (top) and compound **1** (bottom).

9.3.4 Dual Functionalization with Intermediate Purification

Synthesis of C3: C1 (300 mg) was dissolved in DMF (3 mL) in a 5 mL round-bottom flask. BDK (10.4 mg, 0.042 mmol, 0.5 eq. according to double bonds) and mercaptoethanol (28.5 μ L, 0.42 mmol, 5 equiv according to double bonds) were added. Afterwards, the content was purged with nitrogen for 30 min and then the mixture was irradiated with UV light for 30 min. The product was concentrated under vacuum, dissolved in acetone and precipitated in cold methanol. Compound C3 was recovered as a white powder. SEC (THF): $M_n = 22100 \text{ g mol}^{-1}$; $D = 1.17$.

Synthesis of C4: C2 (300 mg) was dissolved in 1.6 mL DMF in a 5 mL round-bottom flask. An aliquot of the aforementioned stock solution of DBU in DMF (1.4 mL) was added to this flask providing 1 eq. of DBU according to PFS units (18.2 mg, 0.12 mmol). Mercaptoethanol (42 μ L, 0.59 mmol, 5 equiv according to PFS units) was lastly added. After 2 min of reaction time, the residue was concentrated under vacuum, dissolved in a minimum amount of acetone and

Experimental Procedures

precipitated in cold methanol. Product **C4** was recovered as a white powder. SEC (THF): $M_n = 21\,210\text{ g mol}^{-1}$; $D = 1.13$.

Control Experiment of PFTR in the presence of ethanol

BCP[2] (67 mg) was dissolved in DMF (190 μL). To this, ethanol (8 μL , 0.135 mmol, 5 equivalents according to PFS) was added. DBU (17 mg) was dissolved in DMF (2 mL). From this DBU+DMF mixture, 484 μL were taken and added to the reaction flask providing 1 eq. DBU (4.1 mg, 0.027 mmol) according to PFS into the medium. Reaction was monitored for 3 hours. Eventually, it was shown that -OH group of ethanol did not react with PFS under these conditions.

Synthesis of C1' and C4': This synthesis was carried out the same way as for **C1** with mercaptoethanol as a thiol instead of OT. The reactive block copolymer was in this case **BCP[5]**. After purification, **C1'** underwent thiol-ene reaction with the same procedure described for the synthesis of **C3**, but with OT instead of mercaptoethanol resulting in compound **4'**.

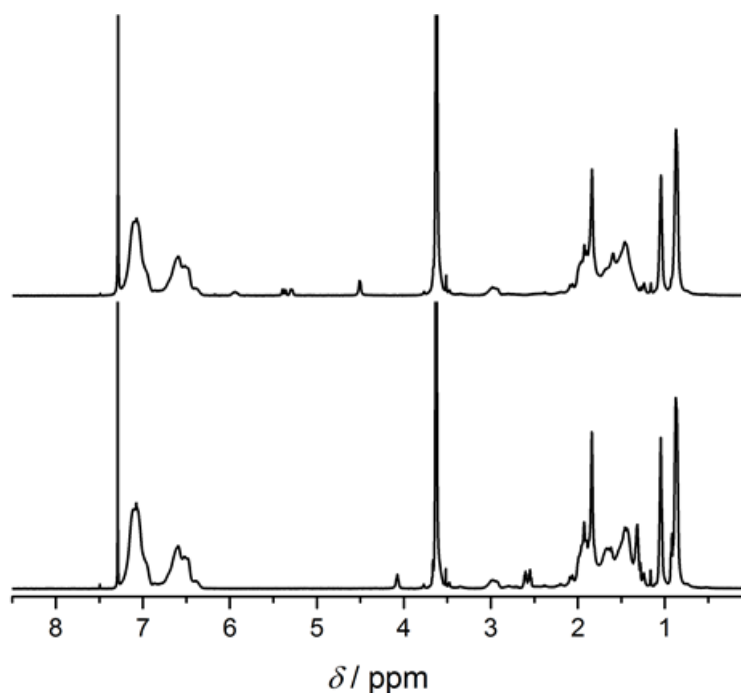


Figure 9.22 ^1H NMR spectrum of **C1'** (top) and **C4'** (bottom).

9.3.5 One-Pot Dual Functionalizations

During one-pot reaction investigations, two identical flasks were prepared at the same time: one for monitoring and analysis of the first step and the other for completing the entire sequence.

9.3.5.1 One-Pot Type 1

Synthesis of C5 and C6: In a 10 mL round-bottom flask, compound **BCP[3]** (400 mg) was dissolved in DMF (3.25 mL) and BDK (15.6 mg, 0.061 mmol, 0.5 equiv according to double bonds) was added to this. A stock solution of DBU (129.8 mg, 0.85 mmol) in DMF (10 mL) was previously prepared and an aliquot of it was added to the main flask (752 μ L, corresponding to 9.76 mg DBU, 0.064 mmol, 0.4 equiv according to PFS units). The final volume of DMF in the main flask was 4 mL. Finally, OT (137.6 μ L, 0.79 mmol, 5 equiv according to PFS units) was added and the contents were purged with nitrogen for 30 min in an ice bath. The end of deoxygenation was recorded as time zero. Product **C5** was purified by precipitating the content of the first flask into cold methanol. SEC (THF): $M_n = 17\,500\text{ g mol}^{-1}$; $D = 1.14$.

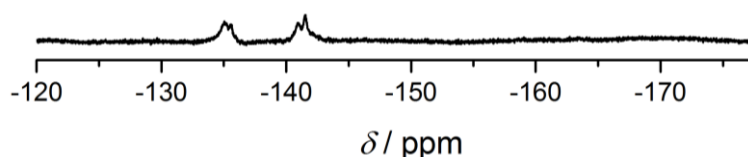


Figure 9.23 ^{19}F NMR spectrum of **C5**.

After completion of the first step, the second (parallel running) flask was irradiated with UV light without any purification. After 30 min, the UV lamp was switched off and **C6** was recovered as a white powder by precipitation in cold methanol. SEC (THF): $M_n = 18\,400\text{ g mol}^{-1}$; $D = 1.18$.

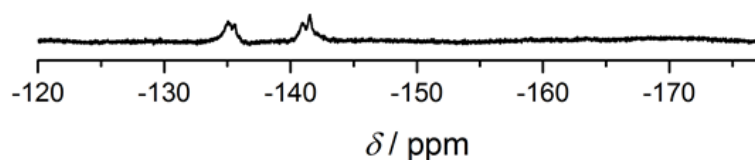


Figure 9.24 ^{19}F NMR spectrum of **C6**.

9.3.5.2 One-Pot Type 2

Synthesis of C7 and C8: BCP[4] (100 mg) was dissolved in DMF (950 μ L) in a 5 mL round-bottom flask. BDK (3.55 mg, 0.014 mmol, 0.5 equiv according to double bonds) and OT (37.6 mL, 0.22 mmol, 5 eq. according to PFS) were subsequently added and the mixture was purged with nitrogen for 30 min. The flasks were irradiated with UV light with the aforementioned conditions for 15 min. Product **C7** was recovered as a white powder after precipitation of the content of the first flask in cold methanol. SEC (THF): $M_n = 18\,500\text{ g mol}^{-1}$; $D = 1.17$.

In parallel, DBU (6.5 mg, 0.04 mmol, 1 eq. with respect to PFS) dissolved in DMF (50 μ L) was added to the second flask. A sample was withdrawn 2 min later and diluted in CDCl_3 to prove the completion of PFTR. **C8** was recovered as a white powder by precipitation in cold methanol. SEC (THF): $M_n = 20\,100\text{ g mol}^{-1}$; $D = 1.15$.

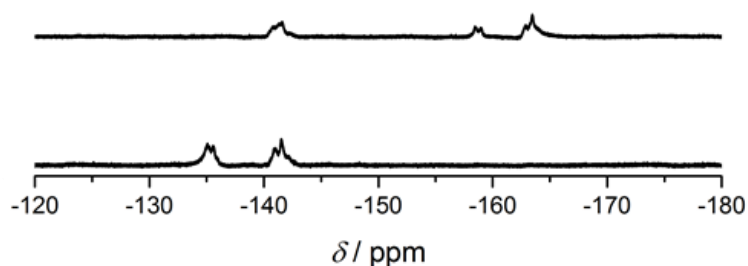


Figure 9.25 ^{19}F NMR spectrum of **C7** (top) and **C8** (bottom).

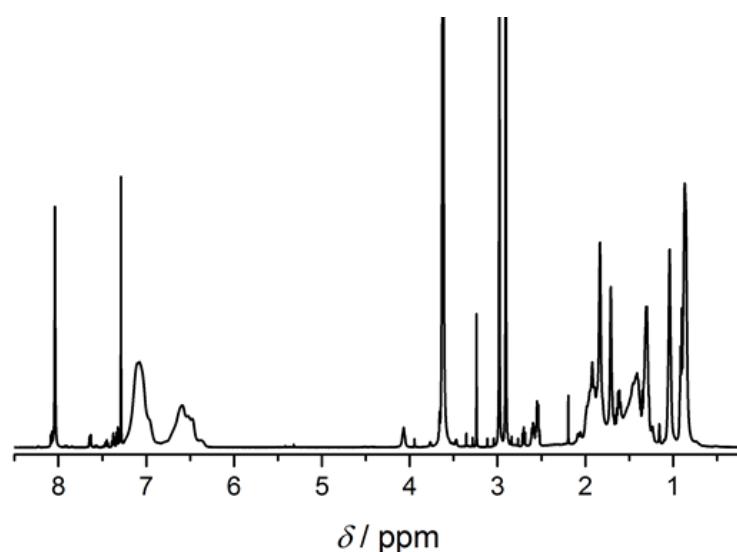


Figure 9.26 ^1H NMR spectrum of **C7** crude.

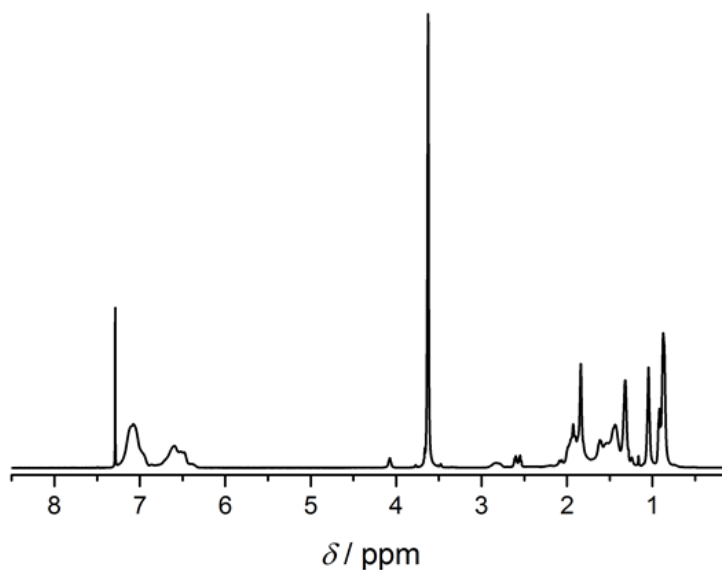


Figure 9.27 ^1H NMR spectrum of **C8**.

9.3.5.3 One-Pot Type 3

Synthesis of C9 and C10: BCP[2] (464 mg) was dissolved in DMF (2.4 mL) in a 5 mL round-bottom flask. BDK (17.2 mg, 0.067 mmol, 0.5 equiv according to double bonds) and OT (25.6 μL , 0.147 mmol, 1.1 equiv according to double bonds) were successively added. An aliquot (1.2 mL) of this mixture (containing 229 mg of the polymer) was placed into another round-bottom flask and both flasks were purged with nitrogen for 30 min. The first flask was used for sampling to monitor thiol-ene addition reaction for 2.5 h (81% conversion). At the end of this time, product **C9** was obtained by precipitation in cold methanol. SEC (THF): $M_n = 19\,250\text{ g mol}^{-1}$; $\mathcal{D} = 1.16$.

A solution of DBU and mercaptoethanol was prepared in DMF. An aliquot of this mixture (1138 μL), which provided 1 eq. of DBU (13.8 mg, 0.09 mmol) and 5 eq. of mercaptoethanol (32 μL , 0.45 mmol according to PFS units), was added to the second (parallel running) flask at the end of 3h of irradiation (thiol-ene addition step, 88% conversion). 2 min later, a sample was withdrawn and diluted in CDCl_3 to provide evidence of completion of PFTR. Product **C10** was recovered as a white powder after precipitation in cold methanol. SEC (THF): $M_n = 20\,110\text{ g mol}^{-1}$; $\mathcal{D} = 1.15$.

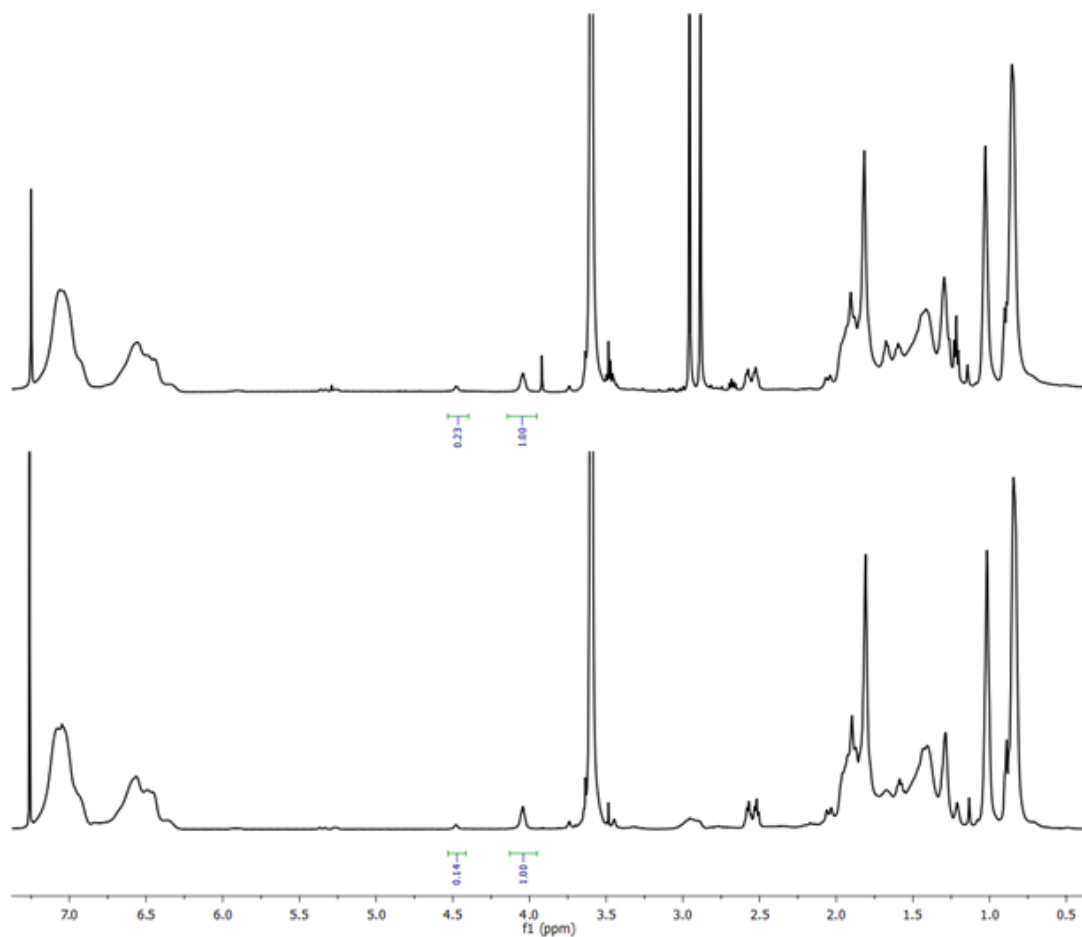


Figure 9.28 ^1H NMR spectra of **C9** (crude) recorded at the end of 2.5 hours exposure to UV light, 81% conversion (top) and of **C10** after 3 hours of UV exposure, 88% conversion, followed by subsequent PFTR (bottom).

9.4 PFTR in Water

9.4.1 Synthesis of Poly(DMAAm-co-PFS)

DMAAm (5.00 g, 50.4 mmol, 129 eq.) and PFS (0.49 g, 2.5 mmol, 6.4 eq.) and 5.8 mL toluene were taken in a 25-mL round-bottom flask. MAMA-SG1 (150 mg, 0.39 mmol, 1 eq.), free SG1 (17.3 μ L, 0.039 mmol, 0.1 eq.) and 1,3,5-trioxane (0.4 g, 4.4 mmol) were added and the flask was sealed with a rubber septum. A t_0 sample was withdrawn and the mixture was purged with nitrogen for 45 minutes. The flask was then placed in a preheated oil bath at 120 °C and. After 5h, the flask was cooled to ambient temperature. A t_{end} sample was taken for conversion calculation. Toluene was evaporated. The polymer was redissolved in THF, and precipitated twice in cold diethyl ether for purification. The product was obtained in the form of a white powder which was finally dried under vacuum. (DMAAm conv. 75%, PFS conv. 95% SEC (DMAc): $M_n = 9700 \text{ g mol}^{-1}$; $\mathcal{D} = 1.35$).

9.4.2 PFTR Experiments in Solution

Preparation of the Buffered Solutions

The buffered solutions were prepared by mixing the below listed components:

pH 11: 0.1 M NaOH (5.5 mL) + 0.05 M Na_2HPO_4 (100 mL); resulting in a pH value of 10.98.

pH 12: 0.1 M NaOH (53.8 mL) + 0.05 M Na_2HPO_4 (100 mL); resulting in a pH value of 11.99.

pH 12.5: 0.1 M NaOH (100 mL) + a solution of glycine (7.52 g L^{-1}) and NaCl (5.86 g L^{-1}) (60 mL); resulting in a pH value of 12.50.

pH 13: 0.4 M NaOH (90 mL) + 140 mL of a solution of glycine (7.52 g L^{-1}) and NaCl (5.86 g L^{-1}) (140 mL); resulting in a pH value of 13.04

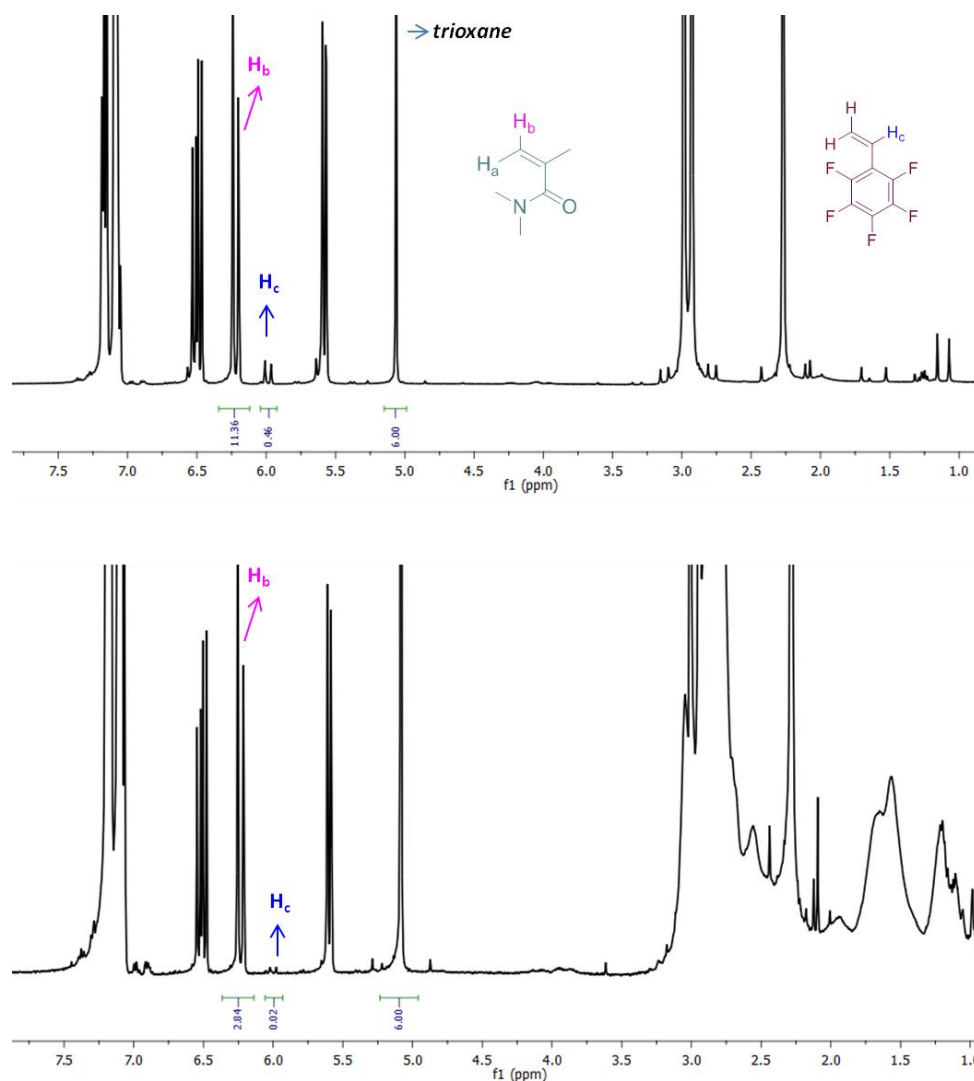


Figure 9.29 ^1H NMR spectra of (top) the t_0 sample (top) and (bottom) t_{end} sample of synthesis of **1**. The PFS content in **1** was calculated indirectly – due to the absence of non-overlapping characteristic proton for PFS units – by regarding the original feed and the independent monomer consumption.

PFTR on Poly(DMAAm-co-PFS) using buffered pH 12: Poly (DMAAm-co-PFS) (compound **1**) (68 mg, 9.3 wt% PFS, 1 eq.) was dissolved in pH 12 buffer (3.6 mL) in a 5-mL round-bottom flask and stirred for 15 minutes at room temperature until complete dissolution. Mercaptoethanol (25.9 μL , 0.368 mmol, 10 eq. with respect to PFS units) was added. The flask was then sealed with a rubber septum and placed in an ice bath. The mixture was deoxygenated by purging with nitrogen for 30 minutes and then placed in a pre-heated oil bath at 40 $^\circ\text{C}$. Samples were withdrawn regularly with deoxygenated syringes (1 mL per sample). The

reaction was quenched by adding 0.2 mL of pH 1 solution to each 1 mL sample taken from the reaction flask. They were then dried overnight prior to ^{19}F -NMR measurements.

The rest of the experiments were set up as described above with the related pH solutions, temperatures and quantities of the thiol. Samples (1 mL each) withdrawn from pH 13 solutions were quenched with 2 mL of pH 1 and those taken from pH 11 solutions were quenched with 0.02 mL of pH1 solutions. A separate experiment was carried out at pH 13 and 40 °C in a bigger batch in order to allow purification of the final product by precipitation. For this purpose, after completion of the reaction, the solution was dried. The residue was dissolved in THF, filtered, and precipitated twice in cold diethyl ether that was recovered as a white powder (compound **2**)($M_n = 10\,800\text{ g mol}^{-1}$; $D = 1.36$).

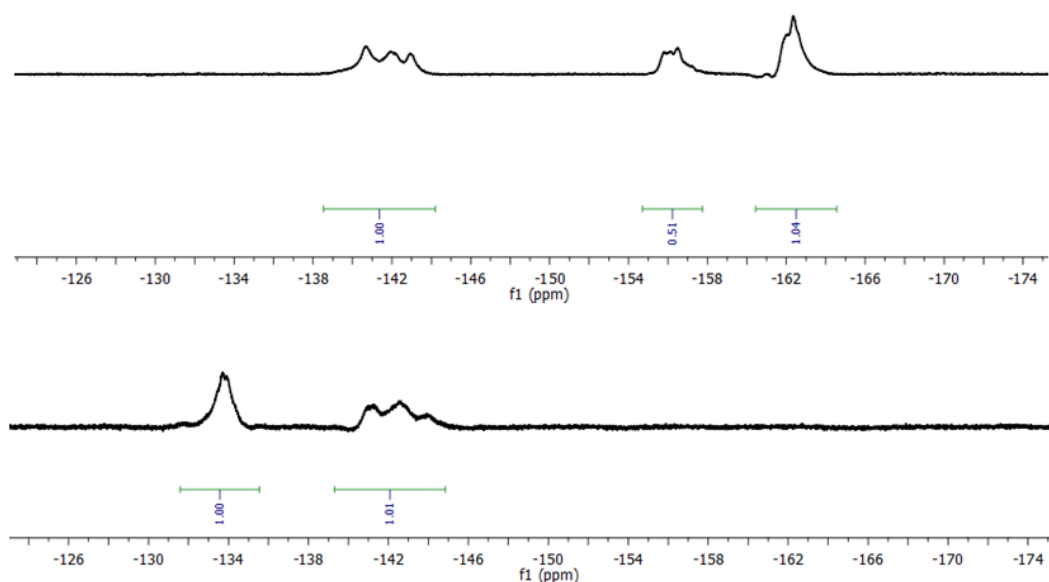


Figure 9.30 ^{19}F NMR spectra of (top) **1** and (bottom) **2** with peak integrations

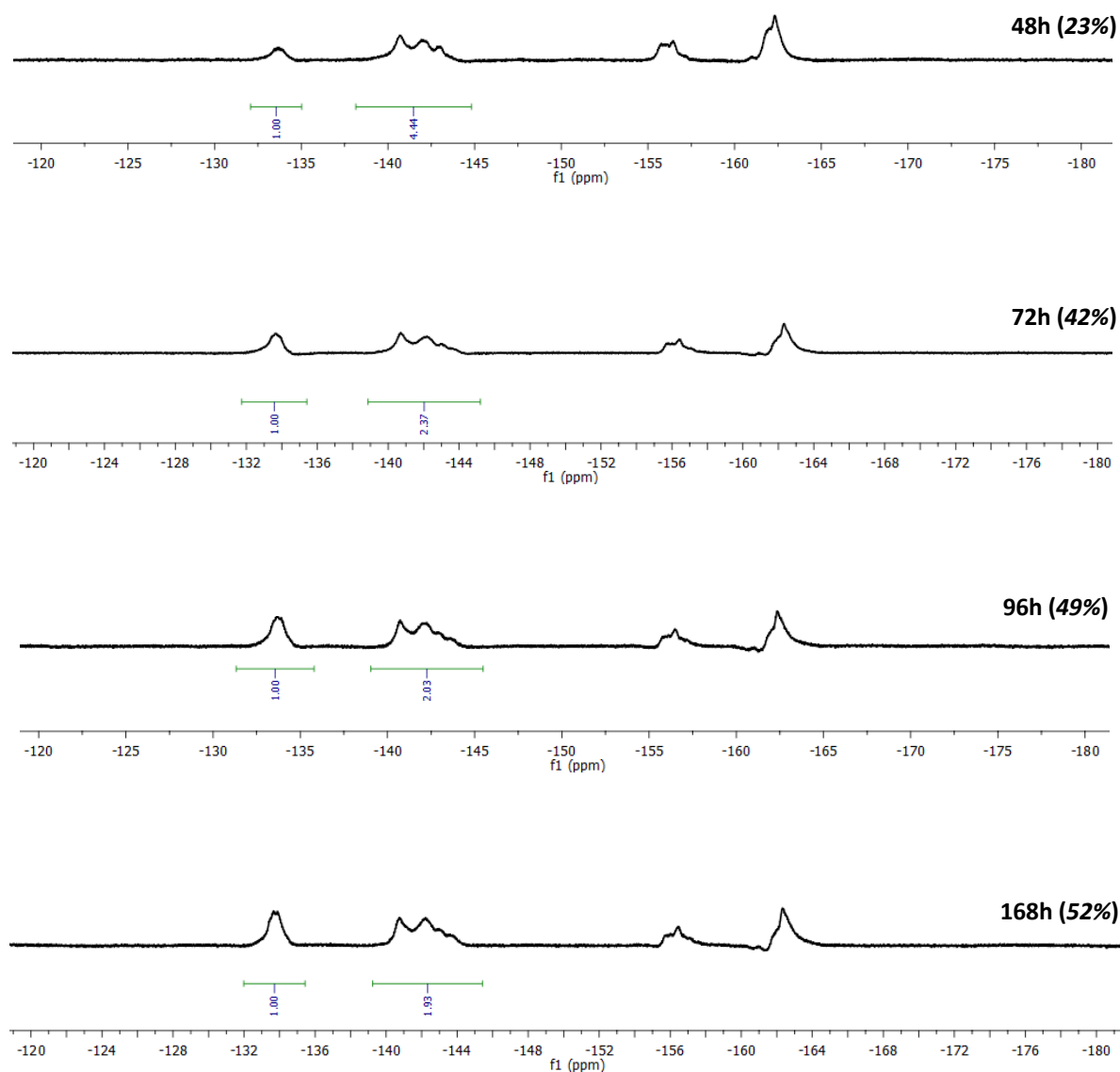


Figure 9.31 ^{19}F NMR spectra of samples withdrawn from PFTR conducted at pH 11, 40 °C using 10 eq. of mercaptoethanol with peak integrations showing 23% to 52% conversions.

Control Experiment of PFTR with Ethanol: Poly (DMAAm-co-PFS) (30 mg) was dissolved in pH 13 buffer (1.6 mL) in a 5 mL round-bottom flask and stirred for 15 minutes at room temperature until complete dissolution. Secondly, ethanol (9.5 μL , 0.16 mmol, 10 eq. with respect to PFS units) was added and the flask was sealed with a rubber septum. The flask was placed in an ice bath and the content was purged with nitrogen for 30 minutes and then it was run at RT for 4 days. At the end of 4 days, water was removed under vacuum.

9.4.3 PFTR Experiments on Surfaces

Modification of PS Petri Dishes via Photografting: 4-benzoyl benzylamine hydrochloride (24.7 mg, 0.01 mol) was mixed with poly(DMAAm-co-PFS) (100 mg) in water (1 mL). This solution was poured homogenously onto a Petri dish using a syringe. For the control experiment, only 100 mg of poly(DMAAm-co-PFS) was dissolved in 1 mL water and it was placed on a second petri dish. Both substrates were irradiated with a PL-L lamp (310-400 nm, max. 350 nm) for 30 min in a custom built UV reactor. After the reaction, solutions were removed from the Petri dishes and they were rinsed thoroughly with water. To remove unspecific adsorption, an excessive washing step was applied followingly. Each petri dish was placed in a separate beaker (250 mL) filled with 150 mL water and placed on a benchtop shaker at 150 rpm. Water was changed 3 times in 24 hours. At the end of 24 h, samples were dried with an air gun. The photo-modified Petri dishes were cut into pieces (ca. 1x1 cm²) for the next step.

Synthesis of the Peptide: Peptide synthesis was done on an automated peptide synthesizer (Syro II, Multisynth) using Fmoc/O^tBu solid phase peptide synthesis protocols described previously.^[376, 396] Cysteine-modified PGLa (Cys-PGLa: H₂N-C-GMASKAGAIAGKIAKVALKAL-CONH₂amide) was synthesized on a rink amide MBHA resin as described previously, yet with an additional Cys residue which was coupled at the *N*-terminus. Peptides were cleaved from the resin using TFA:TIS:H₂O (92:4:4 v/v/v) and were purified on a C18 semi-preparative HPLC column using water:acetonitrile gradients, each containing 5 mM HCl, as previously described.^[376]

Peptide Grafting on Modified Petri Dishes: A solution of the Cys-PGLa was prepared in pH 12 buffer (1 mg/mL). 100 µL of it was placed on a piece which was cut from the previously modified Petri dish. For the control experiment, 1 mg of the same peptide was dissolved in 1 mL of neutral water and it was placed on another piece of the modified Petri dish with similar dimensions. Both samples were left on benchtop at room temperature for 24 h, covered with Al foil. Afterwards, both pieces were first rinsed with water for 10-20 seconds. Tween 20 surfactant (0,01% by volume) was used to wash the surfaces in order to remove unspecific adsorption of the peptide. Each sample was placed into a 5 mL vial, filled with the surfactant and sonicated for 5 minutes (× 3). Eventually, the samples were sonicated with pure water for 5 min and and dried in a stream of air.

Bibliography

- [1] M. Luo, T. H. Epps, *Macromolecules* **2013**, *46*, 7567-7579.
- [2] A.-V. Ruzette, L. Leibler, *Nat. Mater.* **2005**, *4*, 19-31.
- [3] F. S. Bates, Fredrickson, G. H., *Physics Today* **1999**, 32-38.
- [4] III T. H. Epps, R. K. O'Reilly, *Chem. Sci.* **2016**, *7*, 1674-1689.
- [5] B. Basnar, I. Willner, *Small* **2009**, *5*, 28-44.
- [6] A. P. Marencic, R. A. Register, *Annu. Rev. Chem. Biomol. Eng.* **2010**, *1*, 277-297.
- [7] F. W. Speetjens, M. C. D. Carter, M. Kim, P. Gopalan, M. K. Mahanthappa, D. M. Lynn, *ACS Macro Lett.* **2014**, *3*, 1178-1182.
- [8] I. C. Reynhout, G. Delaître, H.-C. Kim, R. J. M. Nolte, J. J. L. M. Cornelissen, *J. Mater. Chem. B* **2013**, *1*, 3026-3030.
- [9] H. Tran, K. Ronaldson, N. A. Bailey, N. A. Lynd, K. L. Killops, G. Vunjak-Novakovic, L. M. Campos, *ACS Nano* **2014**, *8*, 11846-11853.
- [10] J. Stadermann, M. Riedel, H. Komber, F. Simon, B. Voit, *J. Polym. Sci., Part A: Polym. Chem.* **2012**, *50*, 1351-1361.
- [11] J. Stadermann, M. Riedel, B. Voit, *Macromol. Chem. Phys.* **2013**, *214*, 263-271.
- [12] L. Dumas, E. Fleury, D. Portinha, *Polymer* **2014**, *55*, 2628-2634.
- [13] C. Ott, R. Hoogenboom, U. S. Schubert, *Chem. Commun.* **2008**, 3516-3518.
- [14] K. Babiuch, C. R. Becer, M. Gottschaldt, J. T. Delaney, J. Weisser, B. Beer, R. Wyrwa, M. Schnabelrauch, U. S. Schubert, *Macromol. Biosci.* **2011**, *11*, 535-548.
- [15] K. Matyjaszewski, Davis T., *Handbook of Radical Polymerization*, John Wiley & Sons New Jersey, **2002**.
- [16] K. Matyjaszewski, J. Spanswick, *Mater. Today* **2005**, *8*, 26-33.
- [17] J. Carles E. Carraher, *Introduction to Polymer Chemistry*, CRC Press Taylor&Francis Group, New York, **2010**.
- [18] M. Szwarc, *Nature* **1956**, *178*, 1168-1169.
- [19] M. H. Stenzel, C. Barner-Kowollik, *Materials Horizons* **2016**.
- [20] H. Fischer, *Chem. Rev.* **2001**, *101*, 3581-3610.
- [21] T. Fukuda, T. Terauchi, A. Goto, K. Ohno, Y. Tsujii, T. Miyamoto, S. Kobatake, B. Yamada, *Macromolecules* **1996**, *29*, 6393-6398.
- [22] J. Nicolas, Y. Guillaneuf, C. Lefay, D. Bertin, D. Gigmes, B. Charleux, *Prog. Polym. Sci.* **2013**, *38*, 63-235.

- [23] M. K. Georges, R. P. N. Veregin, P. M. Kazmaier, G. K. Hamer, *Macromolecules* **1993**, *26*, 2987-2988.
- [24] R. E. Solomon DH, Cacioli P, *Polymerization process and polymers produced thereby*, CSIRO, **1986**.
- [25] C. J. Hawker, G. G. Barclay, A. Orellana, J. Dao, W. Devonport, *Macromolecules* **1996**, *29*, 5245-5254.
- [26] C. J. Hawker, *J. Am. Chem. Soc.* **1994**, *116*, 11185-11186.
- [27] C. J. Hawker, A. W. Bosman, E. Harth, *Chem. Rev.* **2001**, *101*, 3661-3688.
- [28] F. Minisci, *Acc. Chem. Res.* **1975**, *8*, 165-171.
- [29] M. Asscher, D. Vofsi, *J. Chem. Soc.* **1963**, 3921-3927.
- [30] M. S. Kharasch, E. V. Jensen, W. H. Urry, *Science* **1945**, *102*, 128-128.
- [31] M. J. W. Taylor, W. T. Eckenhoff, T. Pintauer, *Dalton Trans.* **2010**, *39*, 11475-11482.
- [32] J. S. Wang, Matyjaszewski, K., *J. Am. Chem. Soc.* **1995**, *117*, 5614-5615.
- [33] M. Kato, Kamigaito, M., Sawamoto, M., Higashimura, T., *Macromolecules* **1995**, *28*, 1721-1723.
- [34] V. Percec, B. Barboiu, *Macromolecules* **1995**, *28*, 7970-7972.
- [35] K. Matyjaszewski, *Macromolecules* **2012**, *45*, 4015-4039.
- [36] W. A. Braunecker, K. Matyjaszewski, *Prog. Polym. Sci.* **2007**, *32*, 93-146.
- [37] A. J. D. Magenau, Y. Kwak, K. Schröder, K. Matyjaszewski, *ACS Macro Lett.* **2012**, *1*, 508-512.
- [38] Q. Lou, D. A. Shipp, *ChemPhysChem* **2012**, *13*, 3257-3261.
- [39] Y. Inoue, K. Matyjaszewski, *Macromolecules* **2004**, *37*, 4014-4021.
- [40] K. Matyjaszewski, B. E. Woodworth, X. Zhang, S. G. Gaynor, Z. Metzner, *Macromolecules* **1998**, *31*, 5955-5957.
- [41] C. M. Wager, D. M. Haddleton, S. A. F. Bon, *Eur. Polym. J.* **2004**, *40*, 641-645.
- [42] N. V. Tsarevsky, K. Matyjaszewski, *J. Polym. Sci., Part A: Polym. Chem.* **2006**, *44*, 5098-5112.
- [43] T. Pintauer, K. Matyjaszewski, *Chem. Soc. Rev.* **2008**, *37*, 1087-1097.
- [44] W. Jakubowski, Matyjaszewski K., *Angew. Chem. Int. Ed. Engl* **2006**, *45*, 4482-4486.
- [45] K. Min, H. Gao, K. Matyjaszewski, *Macromolecules* **2007**, *40*, 1789-1791.
- [46] W. Jakubowski, K. Min, K. Matyjaszewski, *Macromolecules* **2006**, *39*, 39-45.
- [47] J. Chiefari, Y. K. Chong, F. Ercole, J. Krstina, J. Jeffery, T. P. T. Le, R. T. A. Mayadunne, G. F. Meijs, C. L. Moad, G. Moad, E. Rizzardo, S. H. Thang, *Macromolecules* **1998**, *31*, 5559-5562.
- [48] G. Moad, E. Rizzardo, S. H. Thang, *Aust. J. Chem.* **2005**, *58*, 379-410.

- [49] C. Barner-Kowollik, *Handbook of RAFT Polymerization*, Wiley- WCH, Weinheim, Germany, **2008**.
- [50] G. Johnston-Hall, A. Theis, M. J. Monteiro, T. P. Davis, M. H. Stenzel, C. Barner-Kowollik, *Macromol. Chem. Phys.* **2005**, *206*, 2047-2053.
- [51] G. Moad, E. Rizzardo, S. H. Thang, *Aust. J. Chem.* **2009**, *62*, 1402-1472.
- [52] S. Kulkarni, C. Schilli, A. H. E. Müller, A. S. Hoffman, P. S. Stayton, *Bioconjugate Chem.* **2004**, *15*, 747-753.
- [53] M. G. F. H. C. Kolb, K. B. Sharpless, *Angew. Chem. Int. Ed. Engl* **2001**, *40*.
- [54] R. K. Iha, K. L. Wooley, A. M. Nyström, D. J. Burke, M. J. Kade, C. J. Hawker, *Chem. Rev.* **2009**, *109*, 5620-5686.
- [55] B. S. Sumerlin, A. P. Vogt, *Macromolecules* **2010**, *43*, 1-13.
- [56] C. R. Becer, R. Hoogenboom, U. S. Schubert, *Angew. Chem. Int. Ed.* **2009**, *48*, 4900-4908.
- [57] P. L. Golas, K. Matyjaszewski, *Chem. Soc. Rev.* **2010**, *39*, 1338-1354.
- [58] C. J. Hawker, K. L. Wooley, *Science* **2005**, *309*, 1200-1205.
- [59] W. H. Binder, R. Sachsenhofer, *Macromol. Rapid Commun.* **2008**, *29*, 952-981.
- [60] C. J. Hawker, V. V. Fokin, M. G. Finn, K. B. Sharpless, *Aust. J. Chem.* **2007**, *60*, 381-383.
- [61] C. Barner-Kowollik, A. J. Inglis, *Macromol. Chem. Phys.* **2009**, *210*, 987-992.
- [62] C. Barner-Kowollik, F. E. Du Prez, P. Espeel, C. J. Hawker, T. Junkers, H. Schlaad, W. Van Camp, *Angew. Chem. Int. Ed.* **2011**, *50*, 60-62.
- [63] H. Durmaz, A. Dag, O. Altintas, T. Erdogan, G. Hizal, U. Tunca, *Macromolecules* **2007**, *40*, 191-198.
- [64] H. Turgut, G. Delaittre, *Chem. Eur. J.* **2016**, *22*, 1511-1521.
- [65] H. Nandivada, X. Jiang, J. Lahann, *Adv. Mater.* **2007**, *19*, 2197-2208.
- [66] G. s.-S. c. Dajana, S. c. Marija, *Curr. Org. Chem.* **2016**, *20*, 2211-2221.
- [67] G. Hizal, U. Tunca, A. Sanyal, *J. Polym. Sci., Part A: Polym. Chem.* **2011**, *49*, 4103-4120.
- [68] G. Florian, *Curr. Org. Chem.* **2016**, *20*, 2222-2253.
- [69] C. Kevin, K. Maria, L. Marie-Christine, M. Dean, *Curr. Org. Chem.* **2016**, *20*, 2254-2281.
- [70] B. A. Burkett, C. L. L. Chai, *Tetrahedron Lett.* **1999**, *40*, 7035-7038.
- [71] X. Zhang, W. Xi, C. Wang, M. Podgórski, C. N. Bowman, *ACS Macro Lett.* **2016**, *5*, 229-233.
- [72] Z. Q. Liu, Z. Wei, X. L. Zhu, G. Y. Huang, F. Xu, J. H. Yang, Y. Osada, M. Zrínyi, J. H. Li, Y. M. Chen, *Colloids Surf, B* **2015**, *128*, 140-148.
- [73] S. Chatani, T. Gong, B. A. Earle, M. Podgórski, C. N. Bowman, *ACS Macro Lett.* **2014**, *3*, 315-318.
- [74] D. P. Nair, M. Podgórski, S. Chatani, T. Gong, W. Xi, C. R. Fenoli, C. N. Bowman, *Chem. Mater.* **2014**, *26*, 724-744.
- [75] O. Diels, K. Alder, *Justus Liebigs Annalen der Chemie* **1928**, *460*, 98-122.

- [76] K. K. Oehlenschlaeger, J. O. Mueller, J. Brandt, S. Hilf, A. Lederer, M. Wilhelm, R. Graf, M. L. Coote, F. G. Schmidt, C. Barner-Kowollik, *Adv. Mater.* **2014**, *26*, 3561-3566.
- [77] C. Barner-Kowollik, F. Georg Schmidt, *Macromol. Chem. Phys.* **2012**, *213*, 129-130.
- [78] Z. P. Demko, K. B. Sharpless, *Org. Lett.* **2001**, *3*, 4091-4094.
- [79] R. Huisgen, G. Szeimies, L. Möbius, *Chem. Ber.* **1967**, *100*, 2494-2507.
- [80] R. Huisgen, *Pure Appl. Chem.* **1989**, *61*, 613.
- [81] V. Aureggi, G. Sedelmeier, *Angew. Chem. Int. Ed.* **2007**, *46*, 8440-8444.
- [82] B. H. M. Kuijpers, S. Groothuys, A. R. Keereweer, P. J. L. M. Quaedflieg, R. H. Blaauw, F. L. van Delft, F. P. J. T. Rutjes, *Org. Lett.* **2004**, *6*, 3123-3126.
- [83] G. Molteni, C. L. Bianchi, G. Marinoni, N. Santo, A. Ponti, *New J. Chem.* **2006**, *30*, 1137-1139.
- [84] H. A. Orgueira, D. Fokas, Y. Isome, P. C. M. Chan, C. M. Baldino, *Tetrahedron Lett.* **2005**, *46*, 2911-2914.
- [85] B. H. Lipshutz, B. R. Taft, *Angew. Chem. Int. Ed.* **2006**, *45*, 8235-8238.
- [86] S. C. Luza, H. C. Speisky, *Am. J. Clin. Nutr.* **1996**, *63*, 812S-820S.
- [87] J. Dommerholt, S. Schmidt, R. Temming, L. J. A. Hendriks, F. P. J. T. Rutjes, J. C. M. van Hest, D. J. Lefeber, P. Friedl, F. L. van Delft, *Angew. Chem. Int. Ed.* **2010**, *49*, 9422-9425.
- [88] J. S. Clovis, A. Eckell, R. Huisgen, R. Sustmann, *Chem. Ber.* **1967**, *100*, 60-70.
- [89] A. A. Poloukhtine, N. E. Mbua, M. A. Wolfert, G.-J. Boons, V. V. Popik, *J. Am. Chem. Soc.* **2009**, *131*, 15769-15776.
- [90] C. W. Tornøe, C. Christensen, M. Meldal, *J. Org. Chem.* **2002**, *67*, 3057-3064.
- [91] L. Barner, T. P. Davis, M. H. Stenzel, C. Barner-Kowollik, *Macromol. Rapid Commun.* **2007**, *28*, 539-559.
- [92] H. B. Wolfgang, K. Christian, *Curr. Org. Chem.* **2006**, *10*, 1791-1815.
- [93] B. Voit, *New J. Chem.* **2007**, *31*, 1139-1151.
- [94] P. Wu, A. K. Feldman, A. K. Nugent, C. J. Hawker, A. Scheel, B. Voit, J. Pyun, J. M. J. Fréchet, K. B. Sharpless, V. V. Fokin, *Angew. Chem. Int. Ed.* **2004**, *43*, 3928-3932.
- [95] H. C. Kolb, K. B. Sharpless, *Drug Discov. Today* **2003**, *8*, 1128-1137.
- [96] S. Dedola, S. A. Nepogodiev, R. A. Field, *Org. Biomol. Chem.* **2007**, *5*, 1006-1017.
- [97] R. Zirbs, F. Kienberger, P. Hinterdorfer, W. H. Binder, *Langmuir* **2005**, *21*, 8414-8421.
- [98] L. Gonzalez-Macia, S. Griveau, F. d'Orlyé, A. Varenne, C. Sella, L. Thouin, F. Bedioui, *Electrochem. Commun.* **2016**, *70*, 78-81.
- [99] A. Lucena-Serrano, C. Lucena-Serrano, R. Contreras-Cáceres, A. Díaz, M. Valpuesta, C. Cai, J. M. López-Romero, *Appl. Surf. Sci.* **2016**, *360*, Part A, 419-428.
- [100] L. Li, X.-X. Deng, Z.-L. Li, F.-S. Du, Z.-C. Li, *Macromolecules* **2014**, *47*, 4660-4667.
- [101] G. A. Hudalla, W. L. Murphy, *Langmuir* **2009**, *25*, 5737-5746.

- [102] N. K. Devaraj, J. P. Collman, *QSAR Comb. Sci.* **2007**, *26*, 1253-1260.
- [103] J.-M. Noy, M. Koldevitz, P. J. Roth, *Polym. Chem.* **2015**, *6*, 436-447.
- [104] C. Yin, F. Huo, J. Zhang, R. Martinez-Manez, Y. Yang, H. Lv, S. Li, *Chem. Soc. Rev.* **2013**, *42*, 6032-6059.
- [105] C. E. Hoyle, A. B. Lowe, C. N. Bowman, *Chem. Soc. Rev.* **2010**, *39*, 1355-1387.
- [106] S. Ata, P. Dhara, R. Mukherjee, N. K. Singha, *Eur. Polym. J.* **2016**, *75*, 276-290.
- [107] S. Caillol, M. Desroches, S. Carlotti, R. Auvergne, B. Boutevin, *Green Materials* **2013**, *1*, 16-26.
- [108] B. Yao, J. Sun, A. Qin, B. Z. Tang, *Chin. Sci. Bull.* **2013**, *58*, 2711-2718.
- [109] R. Hoogenboom, *Angew. Chem. Int. Ed.* **2010**, *49*, 3415-3417.
- [110] S. Knoppe, T. Bürgi, *Acc. Chem. Res.* **2014**, *47*, 1318-1326.
- [111] A. B. Lowe, *Polymer* **2014**, *55*, 5517-5549.
- [112] A. B. Lowe, J. W. Chan, in *Functional Polymers by Post-Polymerization Modification*, Wiley-VCH Verlag GmbH & Co. KGaA, **2012**, pp. 87-118.
- [113] P. Lindemann, A. Schade, L. Monnereau, W. Feng, K. Batra, H. Gliemann, P. Levkin, S. Brase, C. Woll, M. Tsotsalas, *J. Mater. Chem., A* **2016**, *4*, 6815-6818.
- [114] R. M. Hensarling, V. A. Doughty, J. W. Chan, D. L. Patton, *J. Am. Chem. Soc.* **2009**, *131*, 14673-14675.
- [115] B. M. Rosen, G. Lligadas, C. Hahn, V. Percec, *J. Polym. Sci., Part A: Polym. Chem.* **2009**, *47*, 3940-3948.
- [116] T. Posner, *Berichte der deutschen chemischen Gesellschaft* **1905**, *38*, 646-657.
- [117] R. M. J. V. Braun, *Ber Dtsch Chem Ges (A B Series)* **1926**, *59*, 1202-1209.
- [118] A. Dondoni, *Angew. Chem. Int. Ed.* **2008**, *47*, 8995-8997.
- [119] C. E. Hoyle, T. Y. Lee, T. Roper, *J. Polym. Sci., Part A: Polym. Chem.* **2004**, *42*, 5301-5338.
- [120] A. B. Lowe, *Polym. Chem.* **2010**, *1*, 17-36.
- [121] M. J. Kade, D. J. Burke, C. J. Hawker, *J. Polym. Sci., Part A: Polym. Chem.* **2010**, *48*, 743-750.
- [122] D. Y. S. Christiana Rissing, *Main Group Chem.* **2009**, *8*, 251-262.
- [123] S. P. S. Koo, M. M. Stamenović, R. A. Prasath, A. J. Inglis, F. E. Du Prez, C. Barner-Kowollik, W. Van Camp, T. Junkers, *J. Polym. Sci., Part A: Polym. Chem.* **2010**, *48*, 1699-1713.
- [124] J. W. Chan, B. Yu, C. E. Hoyle, A. B. Lowe, *Polymer* **2009**, *50*, 3158-3168.
- [125] K. Griesbaum, *Angew. Chem. Int. Ed.* **1970**, *9*, 273-287.
- [126] C. R. Morgan, F. Magnotta, A. D. Ketley, *Polym. Sci., Polym. Chem. Ed.* **1977**, *15*, 627-645.
- [127] L. M. Campos, K. L. Killips, R. Sakai, J. M. J. Paulusse, D. Damiron, E. Drockenmuller, B. W. Messmore, C. J. Hawker, *Macromolecules* **2008**, *41*, 7063-7070.
- [128] M. M. Ozmen, Q. Fu, J. Kim, G. G. Qiao, *Chem. Commun.* **2015**, *51*, 17479-17482.
- [129] V. S. Khire, T. Y. Lee, C. N. Bowman, *Macromolecules* **2007**, *40*, 5669-5677.

- [130] A. V. Bordoni, M. V. Lombardo, A. Wolosiuk, *RSC Advances* **2016**, *6*, 77410-77426.
- [131] B. Colak, J. C. S. Da Silva, T. A. Soares, J. E. Gautrot, *Bioconjugate Chem.* **2016**.
- [132] N. Cakir, U. Tunca, G. Hizal, H. Durmaz, *Macromol. Chem. Phys.* **2016**, *217*, 636-645.
- [133] L. A. W. W. J. Plummer, *J. Res. Nat. Bur. Stand.* **1959**, *63A*, 167.
- [134] C. R. Becer, K. Babiuch, D. Pilz, S. Hornig, T. Heinze, M. Gottschaldt, U. S. Schubert, *Macromolecules* **2009**, *42*, 2387-2394.
- [135] A. Wild, K. Babiuch, M. Konig, A. Winter, M. D. Hager, M. Gottschaldt, A. Prokop, U. S. Schubert, *Chem. Commun.* **2012**, *48*, 6357-6359.
- [136] C. S. Gudipati, C. M. Greenlief, J. A. Johnson, P. Prayongpan, K. L. Wooley, *J. Polym. Sci., Part A: Polym. Chem.* **2004**, *42*, 6193-6208.
- [137] H. Hussain, B. H. Tan, K. Y. Mya, Y. Liu, C. B. He, T. P. Davis, *J. Polym. Sci., Part A: Polym. Chem.* **2010**, *48*, 152-163.
- [138] M. Suzuki, S. Shimizu, J.-Y. Shin, A. Osuka, *Tetrahedron Lett.* **2003**, *44*, 4597-4601.
- [139] R. Kiebooms, P. Adriaensens, D. Vanderzande, J. Gelan, M. J. Swann, D. Bloor, C. J. Drury, G. M. Brooke, *Synth. Met.* **1997**, *84*, 189-190.
- [140] R. D. Chambers, D. Close, D. L. H. Williams, *J. Chem. Soc., Perkin Trans. 2* **1980**, 778-780.
- [141] P. Battioni, O. Brigaud, H. Desvaux, D. Mansuy, T. G. Traylor, *Tetrahedron Lett.* **1991**, *32*, 2893-2896.
- [142] X. Chen, L. Hui, D. A. Foster, C. M. Drain, *Biochemistry* **2004**, *43*, 10918-10929.
- [143] V. A. Olshevskaya, A. V. Zaitsev, A. L. Sigan, E. G. Kononova, P. V. Petrovskii, N. D. Chkanikov, V. N. Kalinin, *Dokl. Chem.* **2010**, *435*, 334-338.
- [144] D. Samaroo, C. E. Soll, L. J. Todaro, C. M. Drain, *Org. Lett.* **2006**, *8*, 4985-4988.
- [145] D. Samaroo, M. Vinodu, X. Chen, C. M. Drain, *J. Comb. Chem.* **2007**, *9*, 998-1011.
- [146] S. J. Shaw, K. J. Elgie, C. Edwards, R. W. Boyle, *Tetrahedron Lett.* **1999**, *40*, 1595-1596.
- [147] H. R. A. Golf, H.-U. Reissig, A. Wiehe, *Eur. J. Org. Chem.* **2015**, *2015*, 1548-1568.
- [148] A. Wild, A. Winter, M. D. Hager, H. Görls, U. S. Schubert, *Macromol. Rapid Commun.* **2012**, *33*, 517-521.
- [149] J. Chen, L. Dumas, J. Duchet-Rumeau, E. Fleury, A. Charlot, D. Portinha, *J. Polym. Sci., Part A: Polym. Chem.* **2012**, *50*, 3452-3460.
- [150] J. Chen, J. Duchet, D. Portinha, A. Charlot, *Langmuir* **2014**, *30*, 10740-10750.
- [151] J. Chen, D. Vuluga, B. Crousse, J. Legros, J. Duchet-Rumeau, A. Charlot, D. Portinha, *Polymer* **2013**, *54*, 3757-3766.
- [152] F. S. Bates, G. H. Fredrickson, *Annu. Rev. Phys. Chem.* **1990**, *41*, 525-557.
- [153] H.-C. Kim, S.-M. Park, W. D. Hinsberg, *Chem. Rev.* **2010**, *110*, 146-177.
- [154] F. S. Bates, *Science* **1991**, *251*, 898-905.
- [155] M. J. Fasolka, A. M. Mayes, *Annu. Rev. Mater. Res.* **2001**, *31*, 323-355.

- [156] Y. Matsushita, K. Mori, R. Saguchi, Y. Nakao, I. Noda, M. Nagasawa, *Macromolecules* **1990**, *23*, 4313-4316.
- [157] G. Hadziioannou, A. Skoulios, *Macromolecules* **1982**, *15*, 258-262.
- [158] Y. Matsushita, A. Noro, M. Inuma, J. Suzuki, H. Ohtani, A. Takano, *Macromolecules* **2003**, *36*, 8074-8077.
- [159] C. M. Bates, M. J. Maher, D. W. Janes, C. J. Ellison, C. G. Willson, *Macromolecules* **2014**, *47*, 2-12.
- [160] M. W. Matsen, M. Schick, *Phys. Rev. Lett.* **1994**, *72*, 2660-2663.
- [161] M. W. Matsen, M. Schick, *Macromolecules* **1994**, *27*, 6761-6767.
- [162] M. W. Matsen, F. S. Bates, *Macromolecules* **1996**, *29*, 1091-1098.
- [163] E. Helfand, *J. Chem. Phys.* **1975**, *62*, 999-1005.
- [164] L. Leibler, *Macromolecules* **1980**, *13*, 1602-1617.
- [165] G. H. Fredrickson, E. Helfand, *J. Chem. Phys.* **1987**, *87*, 697-705.
- [166] D. A. Hajduk, P. E. Harper, S. M. Gruner, C. C. Honeker, G. Kim, E. L. Thomas, L. J. Fetters, *Macromolecules* **1994**, *27*, 4063-4075.
- [167] M. W. Matsen, *J. Phys.: Condens. Matter* **2002**, *14*, R21.
- [168] R. A. Segalman, *Mater. Sci. Eng. R* **2005**, *48*, 191-226.
- [169] K. Kimishima, T. Koga, T. Hashimoto, *Macromolecules* **2000**, *33*, 968-977.
- [170] T. P. Russell, *Curr. Opin. Colloid Interface Sci.* **1996**, *1*, 107-115.
- [171] M. W. Matsen, *J. Chem. Phys.* **1997**, *106*, 7781-7791.
- [172] A. Böker, A. H. E. Müller, G. Krausch, *Macromolecules* **2001**, *34*, 7477-7488.
- [173] H. Huang, F. Zhang, Z. Hu, B. Du, T. He, F. K. Lee, Y. Wang, O. K. C. Tsui, *Macromolecules* **2003**, *36*, 4084-4092.
- [174] D. W. Schubert, T. Dunkel, *Mater. Res. Innovations* **2003**, *7*, 314-321.
- [175] I. W. Hamley, *Prog. Polym. Sci.* **2009**, *34*, 1161-1210.
- [176] X.-s. Jin, Y.-y. Pang, S.-x. Ji, *Chin. J. Polym. Sci.* **2016**, *34*, 659-678.
- [177] J. N. L. Albert, T. H. Epps Iii, *Mater. Today* **2010**, *13*, 24-33.
- [178] S. H. Anastasiadis, T. P. Russell, S. K. Satija, C. F. Majkrzak, *Phys. Rev. Lett.* **1989**, *62*, 1852-1855.
- [179] L. H. Radzilowski, B. L. Carvalho, E. L. Thomas, *J. Polym. Sci., Part B: Polym. Phys.* **1996**, *34*, 3081-3093.
- [180] T. Geisinger, M. Müller, K. Binder, *J. Chem. Phys.* **1999**, *111*, 5251-5258.
- [181] M. J. Fasolka, D. J. Harris, A. M. Mayes, M. Yoon, S. G. J. Mochrie, *Phys. Rev. Lett.* **1997**, *79*, 3018-3021.
- [182] G. T. Pickett, A. C. Balazs, *Macromolecules* **1997**, *30*, 3097-3103.
- [183] H.-C. Kim, W. D. Hinsberg, *J. Vac. Sci. Technol., A* **2008**, *26*, 1369-1382.

- [184] D. Liu, T. Wang, J. L. Keddie, *Langmuir* **2009**, *25*, 4526-4534.
- [185] D. Borah, M. Ozmen, S. Rasappa, M. T. Shaw, J. D. Holmes, M. A. Morris, *Langmuir* **2013**, *29*, 2809-2820.
- [186] R. D. Peters, X. M. Yang, T. K. Kim, P. F. Nealey, *Langmuir* **2000**, *16*, 9620-9626.
- [187] J. Heier, J. Genzer, E. J. Kramer, F. S. Bates, S. Walheim, G. Krausch, *J. Chem. Phys.* **1999**, *111*, 11101-11110.
- [188] E. Delamarche, B. Michel, C. Gerber, D. Anselmetti, H. J. Guentherodt, H. Wolf, H. Ringsdorf, *Langmuir* **1994**, *10*, 2869-2871.
- [189] P. Mansky, Y. Liu, E. Huang, T. P. Russell, C. Hawker, *Science* **1997**, *275*, 1458-1460.
- [190] E. Han, K. O. Stuen, Y.-H. La, P. F. Nealey, P. Gopalan, *Macromolecules* **2008**, *41*, 9090-9097.
- [191] I. In, Y.-H. La, S.-M. Park, P. F. Nealey, P. Gopalan, *Langmuir* **2006**, *22*, 7855-7860.
- [192] D. Y. Ryu, J.-Y. Wang, K. A. Lavery, E. Drockenmuller, S. K. Satija, C. J. Hawker, T. P. Russell, *Macromolecules* **2007**, *40*, 4296-4300.
- [193] D. Y. Ryu, K. Shin, E. Drockenmuller, C. J. Hawker, T. P. Russell, *Science* **2005**, *308*, 236-239.
- [194] J. Bang, J. Bae, P. Löwenhielm, C. Spiessberger, S. A. Given-Beck, T. P. Russell, C. J. Hawker, *Adv. Mater.* **2007**, *19*, 4552-4557.
- [195] E. Han, I. In, S. M. Park, Y. H. La, Y. Wang, P. F. Nealey, P. Gopalan, *Adv. Mater.* **2007**, *19*, 4448-4452.
- [196] E. Han, K. O. Stuen, M. Leolukman, C.-C. Liu, P. F. Nealey, P. Gopalan, *Macromolecules* **2009**, *42*, 4896-4901.
- [197] E. Han, P. Gopalan, *Langmuir* **2010**, *26*, 1311-1315.
- [198] S. Ji, G. Liu, F. Zheng, G. S. W. Craig, F. J. Himpfel, P. F. Nealey, *Adv. Mater.* **2008**, *20*, 3054-3060.
- [199] M. E. Galvin, *Macromolecules* **1991**, *24*, 6354-6356.
- [200] K. Sparnacci, D. Antonioli, V. Gianotti, M. Laus, F. Ferrarese Lupi, T. J. Giammaria, G. Seguíni, M. Perego, *ACS Appl. Mater. Interfaces* **2015**, *7*, 10944-10951.
- [201] S. Ham, C. Shin, E. Kim, D. Y. Ryu, U. Jeong, T. P. Russell, C. J. Hawker, *Macromolecules* **2008**, *41*, 6431-6437.
- [202] C. J. Hawker, E. Elce, J. Dao, W. Volksen, T. P. Russell, G. G. Barclay, *Macromolecules* **1996**, *29*, 2686-2688.
- [203] K. Kubo, A. Goto, K. Sato, Y. Kwak, T. Fukuda, *Polymer* **2005**, *46*, 9762-9768.
- [204] B. K. Denizli, J.-F. Lutz, L. Okrasa, T. Pakula, A. Guner, K. Matyjaszewski, *J. Polym. Sci., Part A: Polym. Chem.* **2005**, *43*, 3440-3446.

- [205] H. Liu, C. T. O'Mahony, F. Audouin, C. Ventura, M. Morris, A. Heise, *Macromol. Chem. Phys.* **2012**, *213*, 108-115.
- [206] K. Sparnacci, D. Antonioli, V. Gianotti, M. Laus, G. Zuccheri, F. Ferrarese Lupi, T. J. Giammaria, G. Seguini, M. Ceresoli, M. Perego, *ACS Appl. Mater. Interfaces* **2015**, *7*, 3920-3930.
- [207] B. H. Kim, D. H. Lee, J. Y. Kim, D. O. Shin, H. Y. Jeong, S. Hong, J. M. Yun, C. M. Koo, H. Lee, S. O. Kim, *Adv. Mater.* **2011**, *23*, 5618-5622.
- [208] T. L. Morkved, M. Lu, A. M. Urbas, E. E. Ehrichs, H. M. Jaeger, P. Mansky, T. P. Russell, *Science* **1996**, *273*, 931-933.
- [209] H. Yokoyama, E. J. Kramer, M. H. Rafailovich, J. Sokolov, S. A. Schwarz, *Macromolecules* **1998**, *31*, 8826-8830.
- [210] Z. Di, D. Posselt, D.-M. Smilgies, C. M. Papadakis, *Macromolecules* **2010**, *43*, 418-427.
- [211] S. H. Kim, M. J. Misner, T. Xu, M. Kimura, T. P. Russell, *Adv. Mater.* **2004**, *16*, 226-231.
- [212] K. A. Cavicchi, K. J. Berthiaume, T. P. Russell, *Polymer* **2005**, *46*, 11635-11639.
- [213] A. Knoll, R. Magerle, G. Krausch, *J. Chem. Phys.* **2004**, *120*, 1105-1116.
- [214] Y. Xuan, J. Peng, L. Cui, H. Wang, B. Li, Y. Han, *Macromolecules* **2004**, *37*, 7301-7307.
- [215] Y.-H. Wu, T.-Y. Lo, M.-S. She, R.-M. Ho, *ACS Appl. Mater. Interfaces* **2015**, *7*, 16536-16547.
- [216] X. Chevalier, C. Nicolet, R. Tiron, A. Gharbi, M. Argoud, C. Couderc, G. Fleury, G. Hadziioannou, I. Iliopoulos, C. Navarro, in *SPIE Advanced Lithography Vol. 9049*, **2014**, pp. 1-13.
- [217] X. Zhang, K. D. Harris, N. L. Y. Wu, J. N. Murphy, J. M. Buriak, *ACS Nano* **2010**, *4*, 7021-7029.
- [218] D. Borah, R. Senthamaraikannan, S. Rasappa, B. Kosmala, J. D. Holmes, M. A. Morris, *ACS Nano* **2013**, *7*, 6583-6596.
- [219] C. Harrison, P. M. Chaikin, D. A. Huse, R. A. Register, D. H. Adamson, A. Daniel, E. Huang, P. Mansky, T. P. Russell, C. J. Hawker, D. A. Egolf, I. V. Melnikov, E. Bodenschatz, *Macromolecules* **2000**, *33*, 857-865.
- [220] S. Ouk Kim, H. H. Solak, M. P. Stoykovich, N. J. Ferrier, J. J. de Pablo, P. F. Nealey, *Nature* **2003**, *424*, 411-414.
- [221] S. Werner, D. Pospiech, D. Jehnichen, K. Eckstein, H. Komber, P. Friedel, A. Janke, F. Näther, U. Reuter, B. Voit, R. Taurino, M. Messori, *J. Polym. Sci., Part A: Polym. Chem.* **2011**, *49*, 926-937.
- [222] H. Yabu, T. Jinno, K. Koike, T. Higuchi, M. Shimomura, *J. Polym. Sci., Part B: Polym. Phys.* **2011**, *49*, 1717-1722.
- [223] J. Z. Li, Y. Wang, Z. Hong Wang, D. Mei, W. Zou, A. Min Chang, Q. Wang, M. Komura, K. Ito, T. Iyoda, *Ultramicroscopy* **2010**, *110*, 1338-1342.

- [224] Y.-L. Loo, R. A. Register, D. H. Adamson, *J. Polym. Sci., Part B: Polym. Phys.* **2000**, *38*, 2564-2570.
- [225] G. Goizueta, T. Chiba, T. Inoue, *Polymer* **1993**, *34*, 253-256.
- [226] T. P. Russell, *Mater. Sci. Rep.* **1990**, *5*, 171-271.
- [227] M. D. Foster, *Crit. Rev. Anal. Chem.* **1993**, *24*, 179-241.
- [228] G. Coulon, J. Daillant, B. Collin, J. J. Benattar, Y. Gallot, *Macromolecules* **1993**, *26*, 1582-1589.
- [229] D. E. Aspnes, *J. Vac. Sci. Technol., A* **2013**, *31*, 058502.
- [230] W. Jakubowski, A. Juhari, A. Best, K. Koynov, T. Pakula, K. Matyjaszewski, *Polymer* **2008**, *49*, 1567-1578.
- [231] I. W. Hamley, V. Castelletto, *Prog. Polym. Sci.* **2004**, *29*, 909-948.
- [232] A. Gutsche, N. Dingenouts, X. Guo, M. Meier, H. Nirschl, *J. Appl. Crystallogr.* **2016**, *49*, 15-23.
- [233] A. Guinier, G. Fournet, *Small-Angle Scattering of X-Rays*, New York: John Wiley and Sons New York, **1955**.
- [234] V. Goertz, N. Dingenouts, H. Nirschl, *Part. Part. Syst. Charact.* **2009**, *26*, 17-24.
- [235] D. Fairén-Jiménez, F. Carrasco-Marín, D. Djurado, F. Bley, F. Ehrburger-Dolle, C. Moreno-Castilla, *J. Phys. Chem. B* **2006**, *110*, 8681-8688.
- [236] H. Fischer, M. de Oliveira Neto, H. B. Napolitano, I. Polikarpov, A. F. Craievich, *J. Appl. Crystallogr.* **2010**, *43*, 101-109.
- [237] S. Skou, R. E. Gillilan, N. Ando, *Nat. Protocols* **2014**, *9*, 1727-1739.
- [238] S. Hölzer, T. N. Büttner, R. Schulze, M. M. L. Arras, F. H. Schacher, K. D. Jandt, U. S. Schubert, *Eur. Polym. J.* **2015**, *68*, 10-20.
- [239] J. Park, K. S. Lee, C. Choi, J. Kwak, H. C. Moon, J. K. Kim, *Macromolecules* **2016**, *49*, 3647-3653.
- [240] M. C. D. Carter, J. Jennings, F. W. Speetjens, D. M. Lynn, M. K. Mahanthappa, *Macromolecules* **2016**, *49*, 6268-6276.
- [241] A. Malek, N. Dingenouts, T. F. Beskers, U. Fehrenbacher, L. Barner, M. Wilhelm, *Eur. Polym. J.* **2013**, *49*, 2704-2720.
- [242] K. Almdal, K. A. Koppi, F. S. Bates, K. Mortensen, *Macromolecules* **1992**, *25*, 1743-1751.
- [243] A. Andrea, F. Paolo, *Meas. Sci. Technol.* **2005**, *16*, R65.
- [244] R. N. Jagtap, A. H. Ambre, *Indian J. Eng. Mater. Sci.* **2006**, *13*, 368-384.
- [245] G. Binnig, H. Rohrer, *Rev. Mod. Phys.* **1987**, *59*, 615-625.
- [246] G. Binnig, H. Rohrer, C. Gerber, E. Weibel, *Phys. Rev. Lett.* **1982**, *49*, 57-61.
- [247] M. S. Marek Szklarczyk, K. Bieńkowski, in *Modern Aspects of Electrochemistry* (Ed.: C. Vayenas), Springer, New York, **2008**.

- [248] F. J. Giessibl, *Rev. Mod. Phys.* **2003**, *75*, 949-983.
- [249] G. Binnig, C. F. Quate, C. Gerber, *Phys. Rev. Lett.* **1986**, *56*, 930-933.
- [250] G. Meyer, N. M. Amer, *Appl. Phys. Lett.* **1988**, *53*, 1045-1047.
- [251] Q. Zhong, D. Inniss, K. Kjoller, V. B. Elings, *Surf. Sci.* **1993**, *290*, L688-L692.
- [252] J. Tamayo, R. García, *Langmuir* **1996**, *12*, 4430-4435.
- [253] N. Jalili, K. Laxminarayana, *Mechatronics* **2004**, *14*, 907-945.
- [254] E. Casero, L. Vazquez, A. M. Parra-Alfambra, E. Lorenzo, *Analyst* **2010**, *135*, 1878-1903.
- [255] NanoAndMore GmbH, Retrieved from <http://www.nanoandmore.com/> on 13.09.2016.
- [256] E. Nagao, J. A. Dvorak, *J. Microsc.* **1998**, *191*, 8-19.
- [257] J. A. Last, P. Russell, P. F. Nealey, C. J. Murphy, *Invest. Ophthalmol. Vis. Sci.* **2010**, *51*, 6083-6094.
- [258] B. Smith (2015, March), *The Differences Between Atomic Force Microscopy and Scanning Electron Microscopy*, in *Azo Materials*. Retrieved from <http://www.azom.com/> on 14.09.2016.
- [259] J. Bang, U. Jeong, D. Y. Ryu, T. P. Russell, C. J. Hawker, *Adv. Mater.* **2009**, *21*, 4769-4792.
- [260] P. Mansky, C. K. Harrison, P. M. Chaikin, R. A. Register, N. Yao, *Appl. Phys. Lett.* **1996**, *68*, 2586-2588.
- [261] M. Park, C. Harrison, P. M. Chaikin, R. A. Register, D. H. Adamson, *Science* **1997**, *276*, 1401-1404.
- [262] F. H. Schacher, P. A. Rugar, I. Manners, *Angew. Chem. Int. Ed.* **2012**, *51*, 7898-7921.
- [263] M. Ulbricht, *Polymer* **2006**, *47*, 2217-2262.
- [264] K.-V. Peinemann, V. Abetz, P. F. W. Simon, *Nat. Mater.* **2007**, *6*, 992-996.
- [265] A. C. Edrington, A. M. Urbas, P. DeRege, C. X. Chen, T. M. Swager, N. Hadjichristidis, M. Xenidou, L. J. Fetters, J. D. Joannopoulos, Y. Fink, E. L. Thomas, *Adv. Mater.* **2001**, *13*, 421-425.
- [266] I. Botiz, S. B. Darling, *Mater. Today* **2010**, *13*, 42-51.
- [267] S. Lyu, T. D. Jones, F. S. Bates, C. W. Macosko, *Macromolecules* **2002**, *35*, 7845-7855.
- [268] S. Förster, M. Antonietti, *Adv. Mater.* **1998**, *10*, 195-217.
- [269] J. F. Ciebien, R. T. Clay, B. H. Sohn, R. E. Cohen, *New J. Chem.* **1998**, *22*, 685-691.
- [270] T. L. Morkved, P. Wiltzius, H. M. Jaeger, D. G. Grier, T. A. Witten, *Appl. Phys. Lett.* **1994**, *64*, 422-424.
- [271] W. A. Lopes, H. M. Jaeger, *Nature* **2001**, *414*, 735-738.
- [272] Y. N. C. Chan, G. S. W. Craig, R. R. Schrock, R. E. Cohen, *Chem. Mater.* **1992**, *4*, 885-894.
- [273] S. Watanabe, R. Fujiwara, M. Hada, Y. Okazaki, T. Iyoda, *Angew. Chem. Int. Ed.* **2007**, *46*, 1120-1123.

- [274] C. Huang, G. Wen, J. Li, T. Wu, L. Wang, F. Xue, H. Li, T. Shi, *J. Colloid Interface Sci.* **2016**, *478*, 236-245.
- [275] V. Sankaran, C. C. Cummins, R. R. Schrock, R. E. Cohen, R. J. Silbey, *J. Am. Chem. Soc.* **1990**, *112*, 6858-6859.
- [276] R. S. Kane, R. E. Cohen, R. Silbey, *Langmuir* **1999**, *15*, 39-43.
- [277] M. J. Robb, L. A. Connal, B. F. Lee, N. A. Lynd, C. J. Hawker, *Polym. Chem.* **2012**, *3*, 1618-1628.
- [278] K. T. Kim, J. J. L. M. Cornelissen, R. J. M. Nolte, J. C. M. van Hest, *Adv. Mater.* **2009**, *21*, 2787-2791.
- [279] S. Chae, J.-H. Kim, P. Theato, R. Zentel, B.-H. Sohn, *Macromol. Chem. Phys.* **2014**, *215*, 654-661.
- [280] A. P. Marencic, R. A. Register, *Annu. Rev. Chem. Biomol. Eng.* **2010**, *1*, 277-297.
- [281] C. M. Kolodziej, H. D. Maynard, *Chem. Mater.* **2012**, *24*, 774-780.
- [282] S. A. Alang Ahmad, L. S. Wong, E. ul-Haq, J. K. Hobbs, G. J. Leggett, J. Micklefield, *J. Am. Chem. Soc.* **2011**, *133*, 2749-2759.
- [283] M. Montague, R. E. Ducker, K. S. L. Chong, R. J. Manning, F. J. M. Rutten, M. C. Davies, G. J. Leggett, *Langmuir* **2007**, *23*, 7328-7337.
- [284] H.-W. Li, B. V. O. Muir, G. Fichet, W. T. S. Huck, *Langmuir* **2003**, *19*, 1963-1965.
- [285] C. Park, J. Yoon, E. L. Thomas, *Polymer* **2003**, *44*, 6725-6760.
- [286] C. T. Black, R. Ruiz, G. Breyta, J. Y. Cheng, M. E. Colburn, K. W. Guarini, H. C. Kim, Y. Zhang, *IBM J. Res. Dev.* **2007**, *51*, 605-633.
- [287] N. Kumar, J.-i. Hahm, *Langmuir* **2005**, *21*, 6652-6655.
- [288] T. P. Lodge, *Macromol. Chem. Phys.* **2003**, *204*, 265-273.
- [289] A. P. Lane, M. J. Maher, C. G. Willson, C. J. Ellison, *ACS Macro Lett.* **2016**, *5*, 460-465.
- [290] J. Chai, J. M. Buriak, *ACS Nano* **2008**, *2*, 489-501.
- [291] H. Schönherr, C. L. Feng, N. Tomczak, G. J. Vancso, *Macromol. Symp.* **2005**, *230*, 149-157.
- [292] C. Minelli, I. Geissbuehler, C. Hinderling, H. Heinzlmann, H. Vogel, R. Pugin, M. Liley, *J. Nanosci. Nanotechnol.* **2006**, *6*, 1611-1619.
- [293] J. G. Kennemur, M. A. Hillmyer, F. S. Bates, *Macromolecules* **2012**, *45*, 7228-7236.
- [294] E. W. Cochran, F. S. Bates, *Macromolecules* **2002**, *35*, 7368-7374.
- [295] T. Hosoda, S. P. Gido, J. W. Mays, T. Huang, C. R. Park, T. Yamada, *J. Polym. Eng.* **2013**, *33*, 49-59.
- [296] S. Park, D. Y. Ryu, J. K. Kim, M. Ree, T. Chang, *Polymer* **2008**, *49*, 2170-2175.
- [297] Y. Noda, T. Kumada, T. Hashimoto, S. Koizumi, *J. Appl. Crystallogr.* **2011**, *44*, 503-513.
- [298] S.-Y. Chen, Y. Huang, R. C.-C. Tsiang, *J. Polym. Sci., Part A: Polym. Chem.* **2008**, *46*, 1964-1973.

- [299] T. Higuchi, M. Shimomura, H. Yabu, *Macromolecules* **2013**, *46*, 4064-4068.
- [300] H. Yabu, S. Sato, T. Higuchi, H. Jinnai, M. Shimomura, *J. Mater. Chem.* **2012**, *22*, 7672-7675.
- [301] D. Liu, C. A. Che Abdullah, R. P. Sear, J. L. Keddie, *Soft Matter* **2010**, *6*, 5408-5416.
- [302] X. Li, J. Guo, Y. Liu, H. Liang, *J. Chem. Phys.* **2009**, *130*, 074908.
- [303] S. H. Kim, K.-S. Kim, K. Char, S. I. Yoo, B.-H. Sohn, *Nanoscale* **2016**, *8*, 10823-10831.
- [304] P. N. Mogaddam, A. Entezami, *Chin. J. Polym. Sci.* **2004**, *22*, 55-61.
- [305] S. Harrisson, P. Couvreur, J. Nicolas, *Macromolecules* **2011**, *44*, 9230-9238.
- [306] U. Jeong, D. Y. Ryu, D. H. Kho, J. K. Kim, J. T. Goldbach, D. H. Kim, T. P. Russell, *Adv. Mater.* **2004**, *16*, 533-536.
- [307] U. Jeong, H.-C. Kim, R. L. Rodriguez, I. Y. Tsai, C. M. Stafford, J. K. Kim, C. J. Hawker, T. P. Russell, *Adv. Mater.* **2002**, *14*, 274-276.
- [308] E. L. Malins, S. Amabilino, G. Yilmaz, F. H. Isikgor, B. M. Gridley, C. R. Becer, *Eur. Polym. J.* **2015**, *62*, 347-351.
- [309] R. Breslow, M. Brandl, J. Hunger, N. Turro, K. Cassidy, K. Krogh-Jespersen, J. D. Westbrook, *J. Am. Chem. Soc.* **1987**, *109*, 7204-7206.
- [310] J. P. Tam, C. R. Wu, W. Liu, J. W. Zhang, *J. Am. Chem. Soc.* **1991**, *113*, 6657-6662.
- [311] J.-P. O'Shea, V. Solovyeva, X. Guo, J. Zhao, N. Hadjichristidis, V. O. Rodionov, *Polym. Chem.* **2014**, *5*, 698-701.
- [312] J. Brandrup, Immergut, E. H., Grulke, E. A., *Polymer Handbook, 4th Ed.*, John Wiley & Sons, Chicester, **1999**.
- [313] M. Dionisio, L. Ricci, G. Pecchini, D. Masseroni, G. Ruggeri, L. Cristofolini, E. Rampazzo, E. Dalcanale, *Macromolecules* **2014**, *47*, 632-638.
- [314] C. B. Roth, J. R. Dutcher, *Eur. Phys. J. E Soft Matter* **2003**, *12*, 103-107.
- [315] G. B. Kharas, E. Hanawa, A. B. Agpasa, T. O. Fedczynya, B. M. Flaherty, J. L. Fernandes, M. Liosatos, M. E. Lukowski, K. G. Skinner, R. N. Theiler, *Polym. Bull.* **2013**, *70*, 707-714.
- [316] V. Thirtha, R. Lehman, T. Nosker, *Polym. Eng. Sci.* **2005**, *45*, 1187-1193.
- [317] J. Liu, Q. Deng, Y. C. Jean, *Macromolecules* **1993**, *26*, 7149-7155.
- [318] C. Kow, M. Morton, L. J. Fetters, N. Hadjichristidis, *Rubber Chem. Technol.* **1982**, *55*, 245-252.
- [319] V. Jitchum, S. Perrier, *Macromolecules* **2007**, *40*, 1408-1412.
- [320] I. W. Hamley, *The Physics of Block Copolymers*, USA: Oxford University Press, USA, **1999**.
- [321] T. Hashimoto, K. Nagatoshi, A. Todo, H. Hasegawa, H. Kawai, *Macromolecules* **1974**, *7*, 364-373.
- [322] H. Hasegawa, T. Hashimoto, H. Kawai, T. P. Lodge, E. J. Amis, C. J. Glinka, C. C. Han, *Macromolecules* **1985**, *18*, 67-78.

- [323] C. Harrison, M. Park, P. M. Chaikin, R. A. Register, D. H. Adamson, N. Yao, *Polymer* **1998**, *39*, 2733-2744.
- [324] C. Harrison, M. Park, P. M. Chaikin, R. A. Register, D. H. Adamson, *J. Vac. Sci. Technol., B* **1998**, *16*, 544-552.
- [325] T. A. Mykhaylyk, O. O. Mykhaylyk, S. Collins, I. W. Hamley, *Macromolecules* **2004**, *37*, 3369-3377.
- [326] C. Lei, Ouzineb, K., Dupont, O., Keddie, J. L., *J. Colloid Interface Sci.* **2007**, *307*, 56-63.
- [327] M. J. Fasolka, P. Banerjee, A. M. Mayes, G. Pickett, A. C. Balazs, *Macromolecules* **2000**, *33*, 5702-5712.
- [328] J. Park, C. Lee, J. Jung, H. Kang, K.-H. Kim, B. Ma, B. J. Kim, *Adv. Funct. Mater.* **2014**, *24*, 7588-7596.
- [329] A. P. Marencic, R. A. Register, *Annu. Rev. Chem. Biomol. Eng.* **2010**, *1*, 277-297.
- [330] P. M. Mendes, C. L. Yeung, J. A. Preece, *Nanoscale Res. Lett.* **2007**, *2*, 373-384.
- [331] W. Senaratne, L. Andruzzi, C. K. Ober, *Biomacromolecules* **2005**, *6*, 2427-2448.
- [332] G. H. Fredrickson, F. S. Bates, *Annu. Rev. Mater. Sci.* **1996**, *26*, 501-550.
- [333] Q. Zhang, T. Xu, D. Butterfield, M. J. Misner, D. Y. Ryu, T. Emrick, T. P. Russell, *Nano Lett.* **2005**, *5*, 357-361.
- [334] J. Romulus, J. T. Henssler, M. Weck, *Macromolecules* **2014**, *47*, 5437-5449.
- [335] K. A. Günay, P. Theato, H.-A. Klok, *J. Polym. Sci., Part A: Polym. Chem.* **2013**, *51*, 1-28.
- [336] M. I. Gibson, E. Fröhlich, H.-A. Klok, *J. Polym. Sci., Part A: Polym. Chem.* **2009**, *47*, 4332-4345.
- [337] N. Mohr, M. Barz, R. Forst, R. Zentel, *Macromol. Rapid Commun.* **2014**, *35*, 1522-1527.
- [338] D. Varadharajan, G. Delaittre, *Polym. Chem.* **2016**, *7*, 7488-7499.
- [339] A. Das, P. Theato, *Chem. Rev.* **2016**, *116*, 1434-1495.
- [340] P. Theato, *J. Polym. Sci., Part A: Polym. Chem.* **2008**, *46*, 6677-6687.
- [341] K. Matyjaszewski, N. V. Tsarevsky, *Nat Chem* **2009**, *1*, 276-288.
- [342] G. Moad, E. Rizzardo, S. H. Thang, *Polymer* **2008**, *49*, 1079-1131.
- [343] P. Tao, Y. Li, A. Rungta, A. Viswanath, J. Gao, B. C. Benicewicz, R. W. Siegel, L. S. Schadler, *J. Mater. Chem.* **2011**, *21*, 18623-18629.
- [344] S.-J. Kim, W. J. Maeng, S. K. Lee, D. H. Park, S. H. Bang, H. Kim, B.-H. Sohn, *J. Vac. Sci. Technol., B* **2008**, *26*, 189-194.
- [345] T. Thurn-Albrecht, J. Schotter, G. A. Kästle, N. Emley, T. Shibauchi, L. Krusin-Elbaum, K. Guarini, C. T. Black, M. T. Tuominen, T. P. Russell, *Science* **2000**, *290*, 2126-2129.
- [346] J. Hahn, W. A. Lopes, H. M. Jaeger, S. J. Sibener, *J. Chem. Phys.* **1998**, *109*, 10111-10114.
- [347] T. Vu, N. Mahadevapuram, G. M. Perera, G. E. Stein, *Macromolecules* **2011**, *44*, 6121-6127.

- [348] D. Borah, S. Rasappa, R. SenthamaraiKannan, M. T. Shaw, J. D. Holmes, M. A. Morris, *J. Colloid Interface Sci.* **2013**, *393*, 192-202.
- [349] H. Turgut, A. C. Schmidt, P. Wadhvani, A. Welle, R. Mueller, G. Delaittre, **2016**, *Submitted Manuscript*.
- [350] C.-H. Wong, S. C. Zimmerman, *Chem. Commun.* **2013**, *49*, 1679-1695.
- [351] E. M. Sletten, C. R. Bertozzi, *Angew. Chem. Int. Ed.* **2009**, *48*, 6974-6998.
- [352] M. Mennicken, R. Nagelsdiek, H. Keul, H. Höcker, *Macromol. Chem. Phys.* **2004**, *205*, 2429-2437.
- [353] Q. Zhang, A. Anastasaki, G.-Z. Li, A. J. Haddleton, P. Wilson, D. M. Haddleton, *Polym. Chem.* **2014**, *5*, 3876-3883.
- [354] B. B. Uysal, U. S. Gunay, G. Hizal, U. Tunca, *J. Polym. Sci., Part A: Polym. Chem.* **2014**, *52*, 1581-1587.
- [355] S. B. Rahane, R. M. Hensarling, B. J. Sparks, C. M. Stafford, D. L. Patton, *J. Mater. Chem.* **2012**, *22*, 932-943.
- [356] J. Xu, C. Boyer, *Macromolecules* **2015**, *48*, 520-529.
- [357] P. Renaud, Giraud, L., *Synthesis* **1996**, 913-926.
- [358] N. Hoffmann, Bertrand, S., Marinkovic, S., Pesch, J., *Pure Appl. Chem.* **2006**, *78*, 2227-2246.
- [359] L. Yu, L.-H. Wang, Z.-T. Hu, Y.-Z. You, D.-C. Wu, C.-Y. Hong, *Polym. Chem.* **2015**, *6*, 1527-1532.
- [360] B. Thapa, H. B. Schlegel, *J. Phys. Chem. A* **2016**, *120*, 5726-5735.
- [361] I. Ugur, A. Marion, S. Parant, J. H. Jensen, G. Monard, *J. Chem. Inf. Model.* **2014**, *54*, 2200-2213.
- [362] J. R. Pliego, J. M. Riveros, *J. Phys. Chem., A* **2002**, *106*, 7434-7439.
- [363] J. W. Suggs, *Organic Chemistry*, Barron's International Series Inc. , New York, USA, **2002**.
- [364] H. Yuan, J. Zhang, *J. Comput. Chem.* **2015**, *36*, 1295-1303.
- [365] Y. Jin, K. H. Wong, A. M. Granville, *J. Colloid Interface Sci.* **2016**, *462*, 19-28.
- [366] S. Thawornchinsombut, J. W. Park, *J. Food Biochem.* **2004**, *28*, 135-154.
- [367] P. Tadpitchayangkoon, J. W. Park, J. Yongsawatdigul, *Food Chem.* **2010**, *121*, 1046-1052.
- [368] Y. Yang, W. V. Sweeney, K. Schneider, B. T. Chait, J. P. Tam, *Protein Sci.* **1994**, *3*, 1267-1275.
- [369] M. V. Trivedi, J. S. Laurence, T. J. Siahann, *Curr. Protein Pept. Sci.* **2009**, *10*, 614-625.
- [370] T. Matsuda, M. H. Litt, *Polym. Sci., Polym. Chem. Ed.* **1974**, *12*, 489-497.
- [371] E. Patrucco, S. Ouasti, C. D. Vo, P. De Leonardis, A. Pollicino, S. P. Armes, M. Scandola, N. Tirelli, *Biomacromolecules* **2009**, *10*, 3130-3140.
- [372] Z. Tang, Y. Akiyama, T. Okano, *Polymers* **2012**, *4*, 1478.

- [373] W. Tang, M. L. Becker, *Chem. Soc. Rev.* **2014**, *43*, 7013-7039.
- [374] S. Afonin, S. L. Grage, M. Ieronimo, P. Wadhvani, A. S. Ulrich, *J. Am. Chem. Soc.* **2008**, *130*, 16512-16514.
- [375] P. Tremouilhac, E. Strandberg, P. Wadhvani, A. S. Ulrich, *J. Biol. Chem.* **2006**, *281*, 32089-32094.
- [376] P. Wadhvani, R. F. Epand, N. Heidenreich, J. Bürck, A. S. Ulrich, R. M. Epand, *Biophys. J.* **2012**, *103*, 265-274.
- [377] E. K. U. Larsen, M. B. L. Mikkelsen, N. B. Larsen, *Biomacromolecules* **2014**, *15*, 894-899.
- [378] R. L. Thurlkill, G. R. Grimsley, J. M. Scholtz, C. N. Pace, *Protein Sci.* **2006**, *15*, 1214-1218.
- [379] L. B. Poole, *Free Radical Biol. Med.* **2015**, *80*, 148-157.
- [380] D. S. Mantus, B. D. Ratner, B. A. Carlson, J. F. Moulder, *Anal. Chem.* **1993**, *65*, 1431-1438.
- [381] M. S. Wagner, D. G. Castner, *Langmuir* **2001**, *17*, 4649-4660.
- [382] H. E. Canavan, D. J. Graham, X. Cheng, B. D. Ratner, D. G. Castner, *Langmuir* **2007**, *23*, 50-56.
- [383] U. T. Bornscheuer, *Angew. Chem. Int. Ed.* **2003**, *42*, 3336-3337.
- [384] U. Hanefeld, L. Gardossi, E. Magner, *Chem. Soc. Rev.* **2009**, *38*, 453-468.
- [385] S. Schoffelen, J. C. M. van Hest, *Soft Matter* **2012**, *8*, 1736-1746.
- [386] Y. H. P. Zhang, *Biotechnol. Adv.* **2011**, *29*, 715-725.
- [387] E. Ricca, B. Brucher, J. H. Schrittwieser, *Adv. Synth. Catal.* **2011**, *353*, 2239-2262.
- [388] L. Hlalele, B. Klumperman, *Macromolecules* **2011**, *44*, 6683-6690.
- [389] S. Harrisson, P. Couvreur, J. Nicolas, *Polym. Chem.* **2011**, *2*, 1859-1865.
- [390] C. J. Durr, S. G. J. Emmerling, P. Lederhose, A. Kaiser, S. Brandau, M. Klimpel, C. Barner-Kowollik, *Polym. Chem.* **2012**, *3*, 1048-1060.
- [391] V. Hong, S. I. Presolski, C. Ma, M. G. Finn, *Angew. Chem. Int. Ed.* **2009**, *48*, 9879-9883.
- [392] S. Beuermann, D. A. Paquet, J. H. McMinn, R. A. Hutchinson, *Macromolecules* **1996**, *29*, 4206-4215.
- [393] C. Strazielle, H. Benoit, O. Vogl, *Eur. Polym. J.* **1978**, *14*, 331-334.
- [394] K. L. Parry, A. G. Shard, R. D. Short, R. G. White, J. D. Whittle, A. Wright, *Surf. Interface Anal.* **2006**, *38*, 1497-1504.
- [395] J. H. Scofield, *J. Electron. Spectrosc. Relat. Phenom.* **1976**, *8*, 129-137.
- [396] G. B. Fields, R. L. Noble, *Int. J. Pept. Protein Res.* **1990**, *35*, 161-214.

Abbreviations

AGET	activators generated by electron transfer
AFM	atomic force microscopy
AIBN	azobisisobutyronitrile
AMA	allyl methacrylate
AMS	azidomethyl styrene
ARGET	activators regenerated by electron transfer
ATRP	atom transfer radical polymerization
BCB	benzocyclobutene
BCP	block copolymer
BDK	benzyl dimethyl ketal
BHT	butylated hydroxytoluene
BiPy	2,2'-bipyridine
BrS	bromostyrene
CMS	chloromethyl styrene
CDCl ₃	deuterated chloroform
CP	copolymer
CTA	chain transfer agent
CuAAC	copper catalyzed azide alkyne cycloaddition
<i>D</i>	polydispersity index
DBU	1,8-diazobicycloundec-7-ene
DMAAm	<i>N, N'</i> - dimethylacrylamide
DMAC	dimethylacetamide
DOPAT	2-(dodecylthiocarbonothioylthio)-propionic acid
DPN	dip-pen nanolithography
eq.	equivalents
<i>f</i>	volumic fraction
FRP	free radical polymerization
GMA	glycidyl methacrylate
HEBIB	2-hydroxyethyl 2-bromoisobutyrate
HEMA	2-hydroxyethyl methacrylate
HP	homopolymer
MBriB	methyl α -bromoisobutyrate
MI	macroinitiator
MMA	methyl methacrylate
NMP	nitroxide mediated polymerization
NMR	nuclear magnetic resonance
OT	octanethiol
PFP	pentafluorophenyl
PFPMA	pentafluorophenyl methacrylate

PFS	pentafluorostyrene
PFTR	<i>para</i> -fluoro thiol substitution reaction
PI	polyisoprene
PMDTA	<i>N,N,N',N'',N''</i> -pentamethyldiethylenetriamine
PMMA	poly(methyl methacrylate)
PS	polystyrene
RAFT	reversible addition-fragmentation chain transfer
RDRP	reversible deactivation radical polymerization
RT	room temperature
SAXS	small angle X-ray scattering
SEC	size exclusion chromatography
SEM	scanning electron microscopy
StCP	statistical copolymer
Sty	styrene
TBAF	tetrabutylammonium fluoride
TCPS	tissue culture polystyrene
TEA	triethylamine
TEM	transmission electron microscopy
THF	tetrahydrofuran
THTPA	tris(3-hydroxypropyltriazolylmethyl)amine
TMS	trimethylsilyl
ToF-SIMS	time-of-flight secondary ion mass spectrometry
χ	Flory-Huggins Interaction Parameter
XPS	X-ray photoelectron spectroscopy

List of Figures, Schemes, and Tables

Figures

1.1	Strategy applied in this dissertation – Block Copolymers as Patterning Platforms. Black and white domains are distinct parts of a BCP, purple and green are the functional moieties. Dark grey and light grey objects represent bio(molecule)s grafted on the functional points on the BCP film.	2
2.1	Examples of common nitroxides used in NMP.	8
2.2	Examples of commonly used initiators and ligands for ATRP: ethyl α -bromophenylacetate (EBPA), methyl α -bromoisobutyrate (MBriB), tris[2-(dimethylamino)ethyl]amine (Me6TREN) and tris(2-pyridylmethyl)amine (TPMA)	9
2.3	Guidelines to choose an suiTable RAFT agent. ^[48] Dashed lines represent poor control over the polymerization. MMA = methyl methacrylate, MA = methacrylate, St = styrene, AM = acrylamide, AN = acrylonitrile, VAc = vinylacetate.	13
2.4	One exemplary application of PFTR in the literature. Adapted with permission from ref ^[134] Copyright © 2009 American Chemical Society	20
2.5	Examples of BCP architectures. A and B represent distinct blocks.	21
2.6	(Left) Macrophase separation of homopolymers. (Right) BCPs microphase separation. Adapted with permission ^[154] . Copyright © 1991, 1990 by the American Association for the Advancement of Science.	22
2.7	Comparison of microdomain sizes obtained by BCPs with larger (Left) and narrower (Right) polydispersities. Adapted with permission. ^[158] Copyright © 2003, American Chemical Society	23
2.8	Self-consistent mean field theory ^[160-162] predicting lamellar (L), cylindrical (C), spherical (S), and gyroid (G) equilibrium morphologies. Adapted with permission. ^[162] Copyright ©1999 American Institute of Physics (top) Equilibrium morphologies predicted by the self consistent mean field theory (bottom)	24

2.9	Representation of different orientations of diblock, lamellar forming BCP films. A) Parallel orientation with symmetrical wetting. B) Parallel orientation with antisymmetrical wetting. C) Neutral wetting. D) Neutral wetting-mixed morphology. Adapted with permission from ref ^[176] Copyright © 2016, Chinese Chemical Society, Institute of Chemistry, Chinese Academy of Sciences and Springer-Verlag Berlin Heidelberg.	28
2.10	Chemical structures of various random copolymer brushes in the literature. Adapted with permission. ^[176] Copyright © 2016, Chinese Chemical Society, Institute of Chemistry, Chinese Academy of Sciences and Springer-Verlag Berlin Heidelberg.	31
2.11	SEM images of a self-assembled, 45 nm thick, symmetrical PMMA- <i>b</i> -PS (52-52 kg mol ⁻¹) film coated on OH-terminated random copolymer with different mole fractions ($F_{St} = 0.45-0.72$) (Top). Perpendicular window of a random copolymer layer bearing terminal-OH for PMMA- <i>b</i> -PS (52-52 kg mol ⁻¹) (Bottom). <i>Scale bar is 200 nm</i> . The gray region represents mixed orientation and the black region represents parallel orientation. Adapted with permission ^[190] Copyright © 2008 American Chemical Society.	32
2.12	SEM images demonstrating the evolution of the nanodomain orientation in BCP films deposited on top of a ~2 nm (top) and ~3 nm (bottom) thick StCP layer with different molar masses. Adapted with permission. ^[200] Copyright © 2015 American Chemical Society.	32
2.13	Schematic illustration of parallel orientation of a cylinder forming BCP (Left), perpendicular orientation of cylinders (Right). Adapted with permission. ^[168] Copyright © 2005 Elsevier B.V. All rights reserved.	33
2.14	a) Demonstration of placing a BCP coated substrate into a MW system. b) Representation of an exemplary surface neutralization with OH-terminated random copolymer followed by BCP coating, annealing, and successive selective etching of PMMA block. Adapted with permission. ^[218] Copyright © 2013 American Chemical Society.	35
2.15	A basic setup of SAXS. Adapted with permission. ^[237] Copyright © 2014 Nature Publishing Group.	37
2.16	Typical 2D scattering diagram of BCPs applied listed in Chapters 3 and 4.	38
2.17	Schematic representation of a typical AFM setup.	40
2.18	Schematic representation of the three modes of AFM: contact, non-contact and tapping modes.	41
2.19	Schematic representation of stimuli responsive bioreactors with a permeable membrane responsive to sugar and base. Adapted with permission. ^[278] Copyright	

© 2009 WILEY-VCH Verlag GmbH & Co. KGaA, Weinheim.....	44
2.20 Schematic representation of the process of amine patterning on a PS- <i>b</i> -PVDMA film. Adapted with permission. ^[7] Copyright © 2014 American Chemical Society ...	46
3.1 SEC traces of A) MI1 and BCP1 , B) MI2 and BCP2 , and C) MI3 , BCP3 , and BCP4	52
3.2 SEC traces of PI chain extension attempt from a PS-SG1: A) with a target of 30% conversion at [isoprene]/[PS-SG1] = 1025; B) with a target of 20% conversion at [isoprene]/[PS-SG1] = 1335. ($M_{n,SEC}$ (PS-SG1) = 23000 g mol ⁻¹).....	53
3.3 A) Representative repeating unit distribution for a PI block synthesized in the current study. B) ¹ H NMR peak assignments for the ethylenic protons present in the PI block of PS- <i>b</i> -PI derivatives.....	54
3.4 A) DSC thermographs and B) SAXS profiles of PS- <i>b</i> -PI derivatives BCP1-4	54
3.5 AFM phase images of A) BCP1 , B) BCP2 , C) BCP3 , and D) BCP4 . <i>Scale bar 300 nm</i> ..	56
3.6 (Top row) A) AFM phase images of a 33 nm-thick film of BCP1 spin-coated from a 0.3 wt% solution in toluene. B) 29 nm thick film of BCP1 spin-coated from a 0.3 wt% solution in toluene. C) 7 nm thick film of BCP1 spin-coated from a 0.2 wt% solution in toluene. (Bottom row) Schematic representations of D) PI wetting the surface in the case of thick films demonstrated on images A-B, E) BCP perpendicular orientation on Si wafer in the case of ultra thin films demonstrated on image. <i>Scale bar 200 nm</i>	57
3.7 Schematic representation of the grafting of alkynyl-PDMAAm on a BCP4 film via copper-catalyzed azide-alkyne coupling.....	58
3.8 N1s (Left) and S2p (Right) selected regions of XPS spectra of an as-coated BCP4 thin film (bottom, <i>reference</i>) and after incubation with Alkyne-PDMAAm in the presence (middle, <i>reaction sample</i>) or in the absence (top, <i>control sample</i>) of the copper-based catalytic system.....	59
3.9 AFM phase images of a BCP4 film before reaction (Left), after incubation with Alkyne-PDMAAm in the presence (Middle, <i>reaction sample</i>) or in the absence (Right, <i>control sample</i>) of the copper-based catalytic system. <i>Scale bar 300 nm</i>	60
3.10 AFM height images of BCP4 (Left), after azide-alkyne coupling (Middle), and control sample (Right).....	60
3.11 AFM phase (Left) and height (Right) images of a photocrosslinked BCP4 film after multiple washings and incubation with organic solvents. <i>Scale bar 300 nm</i>	61
4.1 General concept employed in this project.....	64
4.2 SEC traces of A) HP1 and RBCP B) CP2 , BCP-4 and BCP-5	69

4.3	A) Synthetic steps to obtain HEBIB and the StCP used in the first layer of the coating. B) SEC traces of the StCP.	70
4.4	AFM phase images of all 6 BCPs employed in this work. The order is as follows: Top row from left to right: RBCP , BCP-1 , BCP-2 . Bottom row from left to right: BCP-3 , BCP-4 , BCP-5 . <i>Scale bar 200 nm</i>	72
4.5	AFM height images of all 6 BCPs employed in this work. The order is as follows: Top row from left to right: RBCP , BCP-1 , BCP-2 . Bottom row from left to right: BCP-3 , BCP-4 , BCP-5	73
4.6	SAXS profiles of A) RBCP , BCP-1 and BCP-2 B) BCP-3 , BCP-4 , BCP-5	75
4.7	AFM phase image of (Left) BCP-3 after MW annealing, (Right) after thermal annealing. <i>Scale bar 200 nm</i>	75
4.8	AFM phase image of (Left) RBCP , (Middle) After incubation in water for 6 h at RT, (Right) after incubation in water for 2.5 days at RT. The insets of the top row depict the water contact angle images obtained for the respective films. <i>Scale bar 300 nm</i>	76
4.9	AFM phase image after incubation in water for 6 h of (Left) BCP-2 , (Middle) BCP-3 , and (Right) BCP-4 . <i>Scale bar 300 nm</i>	77
4.10	AFM phase image of (Left) BCP-3 after photo-crosslinking and (Right) BCP-2 after thermal crosslinking. <i>Scale bars 300 nm</i>	78
4.11	SAXS profiles of BCP-6 and BCP-7 with q , $2q$ and $3q$ values indicated with vertical dashed lines.	79
5.1	^{19}F NMR spectra of BCP (top), C1 (middle), and C2 (bottom)	86
5.2	A) ^1H NMR spectrum of BCP[1] after PFTR with OT (C1). B) ^1H NMR spectrum of BCP[2] after thiol-ene reaction with OT (C2)	86
5.3	A) ^1H NMR spectrum of C3 . B) SEC traces of BCP[1] , C1 , and C3 . C) ^1H NMR spectrum of C4 . D) SEC traces of BCP[2] , C2 , and C4	87
5.4	^{19}F NMR spectra of C3 (top) C4 (bottom)	89
5.5	^{19}F NMR spectrum obtained after the PFTR control experiment with ethanol.	89
5.6	A) ^{19}F NMR spectra of C1' (top) and C4' (bottom). B) SEC traces of BCP[5] , C1' , and C4'	90
5.7	A) ^1H NMR spectrum of BCP[3] after undergoing <i>Type 1</i> dual functionalization with OT (overall reaction time = 1 h, C6). B) Size-exclusion chromatograms of BCP before the reaction, after the <i>Type 1</i> PFTR step (30 min, C5), and after the complete	

	Type 1 dual functionalization (overall reaction time = 1 h, C6)	93
5.8	A) ¹⁹ F NMR spectra of (top) C9 and (bottom) C10 . B) SEC traces of BCP[4] , C7 , and C8 . C) ¹ H NMR spectrum of C10 . D) SEC traces of BCP[2] , C9 , and C10	95
6.1	A) Conversion vs. time plot for the PFTR on 1 in buffered and non-buffered pH 12 solutions, conducted at 40 °C with 10 eq. of mercaptoethanol. B) ¹⁹ F NMR spectra of 1 upon PFTR conducted at RT with (top) 5 eq. DBU and 1.1 eq. mercaptoethanol in deionized water, (middle) 1.1 eq. DBU and 1.1 eq. mercaptoethanol in methanol, and (bottom) 1.1 eq. DBU and 1.1 eq. mercaptoethanol in ethanol.	100
6.2	Exemplary kinetics monitored by ¹⁹ F NMR spectroscopy of the experiment conducted at pH 12 and 40 °C with 20 eq. of thiol. <i>For the spectrum of 2, the final sample of the experiment at 50 °C, pH 13, and 10 eq. thiol was plotted as a reference for full conversion.</i>	102
6.3	Kinetics studies for the PFTR of 1 with various quantities of mercaptoethanol, at 40 °C and pH 12 (buffered).	103
6.4	Kinetics studies for the PFTR of 1 at various pH values (buffered), with 10 equivalents of mercaptoethanol at 40 °C.	104
6.5	Kinetics studies for the PFTR of 1 at various temperatures, at pH 13 (buffered) and with 10 equivalents of mercaptoethanol.	105
6.6	A) Size-exclusion chromatograms of polymer precursor 1 and its counterpart 2 after full PFTR at pH 13 and 50 °C. B) ¹ H NMR spectra of 1 (top) and 2 (bottom). ...	106
6.7	¹⁹ F NMR spectra of 1 (top) and 1 after incubation during 4 days with 10 eq. ethanol at pH 13 and 40 °C (bottom)	107
6.8	Schematic representation of the surface modifications.	108
6.9	Secondary ion mass spectra obtained for the original TCPS Petri dish (grey, solid), after photografting of 1 (blue, solid), and the control experiment of the photografting step (blue, dashed). (Left) Pentafluorophenyl-specific region, theoretical <i>m/z</i> value (C ₆ F ₅ ⁻): 166.9. (Middle) First phosphonate-specific regions (PO ₂ ⁻), theoretical <i>m/z</i> value: (PO ₂ ⁻): 62.96. (Right) Second phosphonate specific region (PO ₃ ⁻), theoretical <i>m/z</i> value: (PO ₃ ⁻): 78.96.	108
6.10	Cysteine-specific regions of the secondary ion mass spectra obtained after photografting of 1 (blue plain line), PFTR with peptide Cys-PGLa (red plain line), and control of PFTR (red dashed line). (Left and middle) negative mode. (Right) positive mode. Theoretical <i>m/z</i> values: (S ⁻) 31.97; (HS ⁻) 32.98; (CHS ⁺) 44.98.	109
6.11	Secondary ion mass spectra obtained after photografting of 1 (blue, solid), PFTR with peptide Cys-PGLa (red, solid), and PFTR control (red, dashed). (Left) Lysine-specific region; theoretical <i>m/z</i> value (C ₅ H ₁₀ N ⁺) 84.08. (Right) Leucine/Isoleucine-	

	specific region; theoretical m/z value ($C_5H_{12}N^+$) 86.10.....	110
7.1	(Left) The Krebs cycle. (Right) Representation of enzyme cascades on a surface with a nanostructuration.....	114
9.1	1H NMR spectra of samples taken during the synthesis of MI2 at t_0 (top) and t_{end} (bottom), with integrals indicated that were used for conversion and comonomer composition calculation.....	123
9.2	^{19}F -NMR spectrum of BCP2	123
9.3	A) Synthetic route for the conversion of 4-chloromethylphenyl group into 4-azidomethylphenyl to obtain BCP4 from BCP3 . B) Selected region of the 1H NMR spectra of BCP 3 (top) and BCP4 (bottom) to show the shift of the methylene protons after chloride-to-azide transformation.....	125
9.4	1H NMR spectrum of BCP1-4 showing similar integral values for styrene and isoprene repeating units.....	126
9.5	1H NMR spectra of (top) TMS-Alkyne-PDMAAm (bottom) Alkyne-PDMAAm	128
9.6	SEC traces of TMS-Alkyne-PDMAAm and its deprotected counterpart Alkyne-PDMAAm	129
9.7	1H NMR spectrum of RBCP	132
9.8	1H NMR spectrum of BCP-1	133
9.9	SEC traces of (A) HP2 , BCP-2 , and BCP-7 ; (B) CP1 and BCP-3 ; and (C) CP2 and BCP-4	134
9.10	1H NMR spectrum of BCP-2	135
9.11	1H NMR spectrum of BCP-3	136
9.12	1H NMR spectrum of BCP-4	137
9.13	^{19}F NMR spectrum of BCP-4	137
9.14	1H NMR spectrum of BCP-5	138
9.15	^{19}F NMR spectrum of BCP-5	139
9.16	1H NMR spectrum of the StCP.....	140
9.17	Exemplary 1H NMR spectrum of a P(MMA- <i>co</i> -AMA) macroinitiator (P3).....	142
9.18	Exemplary 1H NMR spectra for the calculation of PFS content using BCP[4] initial (top) and final (bottom) raw polymerization mixtures.....	144

9.19	NMR spectrum of BCP[4] with peak integral values.....	145
9.20	¹ H NMR spectrum of BCP[4]	145
9.21	¹ H NMR spectra with integration values of BCP[1] (top) and compound 1 (bottom).	147
9.22	¹ H NMR spectrum of C1' (top) and C4' (bottom)	148
9.23	¹⁹ F NMR spectrum of C5	149
9.24	¹⁹ F NMR spectrum of C6	149
9.25	¹⁹ F NMR spectrum of C7 (top) and C8 (bottom)	150
9.26	¹ H NMR spectrum of C7 crude.....	150
9.27	¹ H NMR spectrum of C8	151
9.28	¹ H NMR spectra of C9 (crude) recorded at the end of 2.5 hours exposure to UV light, 81% conversion (top) and of C10 after 3 hours of UV exposure, 88% conversion, followed by subsequent PFTR (bottom)	152
9.29	¹ H NMR spectra of (top) the t_0 sample (top) and (bottom) t_{end} sample of synthesis of 1 . The PFS content in 1 was calculated indirectly – due to the absence of non-overlapping characteristic proton for PFS units – by regarding the original feed and the independent monomer consumption.....	154
9.30	¹⁹ F NMR spectra of (top) 1 and (bottom) 2 with peak integrations.....	155
9.31	¹⁹ F NMR spectra of samples withdrawn from PFTR conducted at pH 11, 40 °C using 10 eq. of mercaptoethanol with peak integrations showing 23% to 52% conversions.....	156

Schemes

2.1	The four elementary steps of the free radical polymerization mechanism.	5
2.2	NMP Equilibrium.	7
2.3	Exemplary NMP mechanism with TEMPO.	8
2.4	General mechanism of ATRP. Mt: metal, L: ligand, X: halide.	9
2.5	Proposed mechanism for regeneration of the copper(I) complex in ARGET ATRP. ...	10
2.6	Mechanism of RAFT polymerization. ^[48-49]	12
2.7	Examples of Modular Ligations.	14
2.8	Azide-alkyne cycloadditions. A) Thermally induced 1,3-dipolar cycloaddition. B) Copper catalyzed 1,3-dipolar cycloaddition.	15
2.9	Scheme and possible products of radical thiol-ene reaction.	17
2.10	General radical thiol-ene reaction mechanism.	18
2.11	Suggested mechanism for PFTR.	19
3.1	Chemical structures of the PS- <i>b</i> -PI derivatives employed in the current study and corresponding synthetic route. (a) NaN_3 , DMF, RT.	51
4.1	A) Synthesis of RBCP . B) Synthetic route to obtain functional BCPs. C) Functional monomers present in each BCP.	67
5.1	Synthesis of the doubly reactive platform: poly(MMA- <i>co</i> -AMA)- <i>b</i> -poly(styrene- <i>co</i> -PFS). MBriB: methyl 2-bromoisobutyrate, Me ₆ (TREN): tris[2-(dimethylamino)ethyl]amine, Sn(EH) ₂ : tin(II)2-ethylhexanoate.	83
5.2	Chemical routes to direct thiols towards either PFS units or allylic double bonds for the PFTR or thiol-ene addition, respectively. DBU: 1,8-diazabicyclo[5.4.0]undec-7-ene, BDK: benzyl dimethyl ketal.	85
5.3	Chemical routes towards dual functionalization by sequential PFTR and thiol-ene addition.	88
5.4	Synthetic conditions for obtaining C4' , equivalent product to C4 , with inversion of the reaction sequence and an intermediate purification step.	90

5.5	Representation of <i>Type 1</i> dual functionalization. (Top) Simplified cartoon. (Bottom) Synthetic route for the one-pot batch sequential procedure.....	92
5.6	Representation of <i>Type 2</i> dual functionalization. (Top) Simplified cartoon. (Bottom) Synthetic route for the one-pot batch sequential procedure.....	94
5.7	Representation of <i>Type 3</i> dual functionalization. (Top) Simplified cartoon. (Bottom) Synthetic route for the one-pot batch sequential procedure.....	96
6.1	Structure of poly(DMAAm-co-PFS) 1 and model reaction carried out in this work. ...	99
9.1	Synthetic route to obtain MI1 and BCP1	121
9.2	Synthetic route to obtain MI2 and BCP2	122
9.3	Synthetic route to obtain MI3 and BCP3	124
9.4	Synthetic route to obtain TMS-Alkyne PDAAm and Alkyne-PDAAm	127

Tables

2.1	Peak position of Bragg reflections for possible BCP structures. q is the scattering vector, q^* is the primary peak. Adapted with permission. ^[231] Copyright © 2004 Elsevier Ltd. All rights reserved.	37
3.1	Characteristics of the polymers reported in the present study.	52
4.1	Detailed information on the characteristics of the statistical copolymer (StCP), homopolymers (HP) and copolymers (CP).	68
4.2	Detailed information about the BCPs employed in this work.	68
4.3	Characteristics of BCP-6 and BCP-7	78
5.1	Detailed information on the reactive BCPs employed herein.	84
5.2	Conversions of PFTR with different amounts of DBU.	88
5.3	Thiol–ene reaction results with various quantities of TEA and BDK.	94
6.1	Conversion values for the PFTR of 1 in buffered and non-buffered pH 12 solutions at 40 °C with 10 eq. of mercaptoethanol.	101
6.2	Summary of all conditions applied in the present study for the PFTR of 1 with mercaptoethanol.	101
6.3	Conversion values for the PFTR of 1 with various quantities of mercaptoethanol, at 40 °C and 12 (buffered)	103
6.4	Conversion values for the PFTR of 1 at various pH values (buffered), with 10 equivalents of mercaptoethanol at 40 °C.	104
6.5	Chemical routes towards dual functionalization by sequential PFTR and thiol–ene addition.	105

Curriculum Vitae

Date of birth: 13.05.1988

Place of birth: Istanbul, Turkey

Nationality: Turkish

Education

09/2011 – 01/2013 **MSc in Materials Science and Nanotechnology** (CGPA: 3.81/4.00)

Bilkent University, Ankara, Turkey

09/2006 – 06/2011 **BSc in Chemistry** (CGPA: 3.60/4.00)

Middle East Technical University (METU), Ankara, Turkey

Work Experience

07/2013 – 12/2016 **PhD Research in Polymer Chemistry**

Supervisors: Guillaume Delaittre and Christopher Barner-Kowollik

Karlsruhe Institute of Technology (KIT), Karlsruhe, Germany

09/2011 – 01/2013 **Bilkent University, Ankara, Turkey**

MSC research under the supervision of Prof. Engin Umut Akkaya

Title: "Nitroolefin Functionalized BODIPY dyes for protein labeling"

07/2010 – 08/2010 **Summer Internship at Forensic Medicine, Ankara, Turkey**

Awards & Scholarships

1. **DAAD** travel grant for EUPOC 2016 (Europolymer conference)
2. **Poster prize** at EUPOC 2016
3. **Best Talk** award at the annual retreat of Biointerfaces International Graduate School (BIF-IGS), KIT (2015)
4. **Travel grant** from BIF-IGS conference fee contest (2014)
5. **MSc scholarship** from Bilkent University (09/2011-01/2013)
6. Graduation in **3rd place** from chemistry department, METU (2011)
7. Graduation in **1st place** from high school, Istanbul (2006)

Scientific Production

Publications Arising from This Dissertation

- H. Turgut, G. Delaittre, "On the Orthogonality of Two Thiol Based Modular Ligations", *Chem. Eur. J.* **2016**, *22*, 1511-1521.
- H. Turgut, A. C. Schmidt, P. Wadhvani, A. Welle, R. Müller, G. Delaittre, "Para-Fluoro Thiol Ligation in Water", **2016**, *Submitted Manuscript*.
- H. Turgut, N. Dingenouts, V. Trouillet, P. Krolla-Sidenstein, H. Gliemann, G. Delaittre, "Towards Chemical Patterning with Block Copolymer Thin Films", **2016**, *Submitted Manuscript*.
- H. Turgut, D. Varadharajan, N. Dingenouts, G. Delaittre, "Preservation of Phase Separation Upon Functionalization in PMMA-*b*-PS Thin Films", *Manuscript in Preparation*.

Other Publications

- A. C. Schmidt, H. Turgut, A. Beloqui, G. Delaittre, "Nitroxide-Mediated Polymerization (NMP) of Methacrylates in the Presence of a Small Amount of Functional Styrenics", *Manuscript in Preparation*

Oral Communications

- Functional Block Copolymers as Platforms for Patterned Immobilization. *EUPOC 2016: Block Copolymers for Nanotechnology Applications*, Gargnano, Italy (22-26 May 2016)
- Functional Block Copolymers as Platforms for Synthetic Enzyme Cascades. *KIT PhD Symposium*, Karlsruhe, Germany (11 September 2014)
- Functional Block Copolymers as Platforms for Patterned Immobilization. *BIF-IGS Annual Retreat*, Bad Homburg, Germany (27-29 July, 2015) (*Best Talk Award*)

Poster Presentations

- Thiol-Based Dual Functionalization of Distinct Block Copolymer Segments by Control of Chemical Orthogonality. *EUPOC 2016*, Gargnano, Italy (*Poster Prize*)
- Functional Block Copolymers as Platforms for Enzyme Immobilization. *Molecular Interaction Engineering (MIE) Project Evaluation Meeting*, Karlsruhe, Germany (23-24 November 2015)
- Functional Block Copolymers as Self-Assembling Units for Synthetic Enzyme Cascades. *BIF-IGS Annual Retreat*, Göltingen/Herrnberg, Germany (01-03 Sep, 2014)

Acknowledgements

My first and greatest thanks are to my dear supervisor Guillaume. The day I met him was definitely one of the luckiest times of my life. He has always been very supportive in all subjects, very open and very friendly. He is a kind-hearted human, a positive man, and a gentle boss... I have learnt not only about science but also about how to improve myself from him. Holding the pride of being his very first student, I am hoping not to be forgotten forever. It has been a tough journey from setting up the laboratory to publishing the first article. Nevertheless, if I am looking at the world from a little wider window now, I owe a big part of it to him. *Merci beaucoup Guillaume!*

I would like to acknowledge Prof. Christopher Barner-Kowollik for letting me be a part of this great group: Macroarc. I have always got inspiration from Christopher's passion and endless success. It was great experience.

Herein, I want to acknowledge my collaboration partners. First of all, I want to thank Nico Dingenouts for SAXS measurements and fruitful discussions. He is a great mind. Thanks Nico! Secondly, Vanessa Trouillet is thanked for XPS measurements and always creating time for me and having friendly dialogues. I would also like to thank Alex Welle for ToF-SIMS, Helena Hoerig for DSC, and Meike Koenig for ellipsometer. A big thank to Peter-Krolla Sidenstein and Markus Moosmann for AFM.

Plenty of thanks to my friends who made me have nice time in Germany, namely, Ozcan Altintas, Nicolas Zydziak, Zafer Soyler, Ozgul Demir Bulut, Andrea Au, Victoria Nedashkivska, Mevlana Levendoglu, Anna Popova, Hulya Karaagac and Divya Varadharajan. Special thanks to Konstantin Demir and his lovely mother Ursula for always giving me a warm welcome at their house.

Hartmut Gliemann and Cornelia Lee-Thedieck are acknowledged for meeting me as members of Thesis advisory committee several times during my PhD and giving me supportive ideas.

BIF-IGS is thanked for giving me courses throughout my PhD and a grant for attending a conference. MIE project suppliers are thanked for the financial support. In addition, DAAD is acknowledged for giving me a grant to attend a conference.

Finally, I would like to thank my father who doesn't really understand what I am doing but still supports me as every good father. I also want to thank my mother who heartfully supports me

wherever I go and whatever I do. My dear sister and her little daughter Melis are also thanked for always being there to cheer me up.

Last but not the least, I want to thank my zumba-class coaches Tony, Nicole, Elena and Romina for helping me to have the greatest times! I wouldn't survive without dancing!

Deep thanks to the members of Deloitte group and Macroarc! It was nice to meet you guys!

It was challenging to live in a foreign country though. Thank you Germany for teaching me a lot.

Tschüss!

